

National Library
of CanadaBibliothèque nationale
du Canada

Canadian Theses Division / Division des thèses canadiennes

Ottawa, Canada
K1A 0N4

60444

PERMISSION TO MICROFILM — AUTORISATION DE MICROFILMER

• Please print or type — Écrire en lettres moulées ou dactylographier

Full Name of Author — Nom complet de l'auteur

CLIVE HUGH REGINALD MACKAY

Date of Birth — Date de naissance

JANUARY 6, 1955

Country of Birth — Lieu de naissance

CANADA

Permanent Address — Résidence fixe

81 BARDIN CRESCENT
CHARLOTTETOWN, R.R. NO 7
P.E.I. C1A 7J9

Title of Thesis — Titre de la thèse

PERFORMANCE OF A SHAFT IN WEAK ROCK

University — Université

UNIVERSITY OF ALBERTA

Degree for which thesis was presented — Grade pour lequel cette thèse fut présentée

MASTER OF SCIENCE

Year this degree conferred — Année d'obtention de ce grade

1982

Name of Supervisor — Nom du directeur de thèse

Dr. P.K. KAISER

Permission is hereby granted to the NATIONAL LIBRARY OF CANADA to microfilm this thesis and to lend or sell copies of the film.

The author reserves other publication rights, and neither the thesis nor extensive extracts from it may be printed or otherwise reproduced without the author's written permission.

L'autorisation est, par la présente, accordée à la BIBLIOTHÈQUE NATIONALE DU CANADA de microfilmer cette thèse et de prêter ou de vendre des exemplaires du film.

L'auteur se réserve les autres droits de publication; ni la thèse ni de longs extraits de celle-ci ne doivent être imprimés ou autrement reproduits sans l'autorisation écrite de l'auteur.

Date

April 30, 1982

Signature

THE UNIVERSITY OF ALBERTA

PERFORMANCE OF A SHAFT IN WEAK ROCK

by



CLIVE HUGH REGINALD MACKAY

A THESIS

SUBMITTED TO THE FACULTY OF GRADUATE STUDIES AND RESEARCH

IN PARTIAL FULFILMENT OF THE REQUIREMENTS FOR THE DEGREE

OF M.SC.

IN

CIVIL ENGINEERING

EDMONTON, ALBERTA

FALL, 1982

CANADIAN THESES ON MICROFICHE

I.S.B.N.

THESES CANADIENNES SUR MICROFICHE



National Library of Canada
Collections Development Branch

Canadian Theses on
Microfiche Service

Ottawa, Canada
K1A 0N4

Bibliothèque nationale du Canada
Direction du développement des collections

Service des thèses canadiennes
sur microfiche

NOTICE

The quality of this microfiche is heavily dependent upon the quality of the original thesis submitted for microfilming. Every effort has been made to ensure the highest quality of reproduction possible.

If pages are missing, contact the university which granted the degree.

Some pages may have indistinct print especially if the original pages were typed with a poor typewriter ribbon or if the university sent us a poor photocopy.

Previously copyrighted materials (journal articles, published tests, etc.) are not filmed.

Reproduction in full or in part of this film is governed by the Canadian Copyright Act, R.S.C. 1970, c. C-30. Please read the authorization forms which accompany this thesis.

THIS DISSERTATION
HAS BEEN MICROFILMED
EXACTLY AS RECEIVED

AVIS

La qualité de cette microfiche dépend grandement de la qualité de la thèse soumise au microfilmage. Nous avons tout fait pour assurer une qualité supérieure de reproduction.

S'il manque des pages, veuillez communiquer avec l'université qui a conféré le grade.

La qualité d'impression de certaines pages peut laisser à désirer, surtout si les pages originales ont été dactylographiées à l'aide d'un ruban usé ou si l'université nous a fait parvenir une photocopie de mauvaise qualité.

Les documents qui font déjà l'objet d'un droit d'auteur (articles de revue, examens publiés, etc.) ne sont pas microfilmés.

La reproduction, même partielle, de ce microfilm est soumise à la Loi canadienne sur le droit d'auteur, SRC 1970, c. C-30. Veuillez prendre connaissance des formules d'autorisation qui accompagnent cette thèse.

LA THÈSE A ÉTÉ
MICROFILMÉE TELLE QUE
NOUS L'AVONS REÇUE

THE UNIVERSITY OF ALBERTA

RELEASE FORM

NAME OF AUTHOR CLIVE HUGH REGINALD MACKAY
TITLE OF THESIS PERFORMANCE OF A SHAFT IN WEAK ROCK
DEGREE FOR WHICH THESIS WAS PRESENTED M.SC.
YEAR THIS DEGREE GRANTED 1982

Permission is hereby granted to THE UNIVERSITY OF ALBERTA LIBRARY to reproduce single copies of this thesis and to lend or sell such copies for private, scholarly or scientific research purposes only.

The author reserves other publication rights, and neither the thesis nor extensive extracts from it may be printed or otherwise reproduced without the author's written permission.

(SIGNED)

Clive Mackay

PERMANENT ADDRESS:

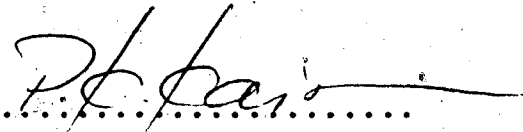
81 Bardin Crescent
Charlottetown, R.R.#7
P.E.I., C1A 7J9

DATED April 23, 1982

THE UNIVERSITY OF ALBERTA
FACULTY OF GRADUATE STUDIES AND RESEARCH

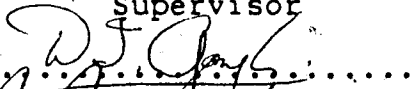
The undersigned certify that they have read, and recommend to the Faculty of Graduate Studies and Research, for acceptance, a thesis entitled PERFORMANCE OF A SHAFT IN WEAK ROCK submitted by CLIVE HUGH REGINALD MACKAY in partial fulfilment of the requirements for the degree of M.SC. in CIVIL ENGINEERING.

Dr. P.K. Kaiser


.....

Supervisor

Dr. D.I. Gough


.....

Dr. N.R. Morgenstern


.....

Dr. S. Thomson


.....

Date

April 23, 1982

TO MY PARENTS

ABSTRACT

The performance of a 235m deep by 4.3m diameter concrete lined circular shaft, excavated in weak rock (Bearpaw Formation) at Kipp, near Lethbridge, Alberta, for Petro Canada Exploration Ltd. is documented and analysed in this thesis.

A field program was undertaken during construction of the shaft to measure *in situ* stresses, the rock mass displacement field, the rock stress changes which occurred during the shaft advance and the stress build up on the liner.

Stressmeter measurements obtained near the advancing shaft bottom have been used to calculate the orientation and magnitude of the principal horizontal stresses. The *in situ* modulus of elasticity was estimated by coupling measured stress changes with the radial rock mass displacements which occurred between the shaft bottom and the liner installation.

The monitoring and *in situ* testing program has provided the necessary components required to evaluate the shaft performance through use of the Convergence-Confinement Method. Reasonable agreement was obtained between the measured and predicted support interaction points for the 152 and 180m levels.

ACKNOWLEDGEMENTS

This research programme was conducted under the supervision of Dr. P.K. Kaiser. I wish to thank Dr. Kaiser for his encouragement, support, and guidance over the past two years. I also wish to thank Dr. N.R. Morgenstern for originally suggesting this thesis topic, and for providing encouragement and guidance throughout this research.

The shaft instrumentation program was funded jointly by the University of Alberta and Petro Canada Exploration Inc., in cooperation with Thyssen Mining Construction of Canada. I am grateful for the cooperation received from Messrs. W. Buckley and C. Chiang of Petro Canada and Mr. J. McIntyre of TMCC. during the field program.

The personal support provided by the University of Alberta and the National Research Council of Canada is appreciated.

I am indebted to Messrs. K. Ellis and A. Muir for fabrication of the field and laboratory equipment. Mr. G. Cyre provided invaluable assistance during all parts of the field and laboratory program.

I wish to extend special thanks to my fellow graduate students in appreciation of the assistance in all parts of this thesis. Messrs. D. Hutchinson, F.M. Lieu, J. Sobkowicz and K. Sterne provided assistance in the field program. Mr. S. Maloney provided guidance in using ADINA. Special thanks are extended to Mr. P. McLellan who critically reviewed this thesis.

Finally, I wish to express my deepest appreciation to my family, who have always provided love, support and understanding.

LIST OF IMPORTANT SYMBOLS

- a radius of shaft
- A radius of shaft on computer plots
- E isotropic Young's modulus
- E horizontal Young's modulus
- E vertical Young's modulus
- K_o ratio of horizontal/vertical stress
- N ratio of minor/major principal horizontal stress
- $\sigma_1, \sigma_2, \sigma_3$
principal stresses
- σ_v vertical stress
- σ_h horizontal stress
- Sigma1
major principal stress on plots
- sigma3
minor principal stress on plots
- sigma-h(max)
maximum horizontal stress
- sigma-h(min)
minimum horizontal stress
- theta
orientation of maximum horizontal stress
- S major principal biaxial stress
- S* apparent major principal biaxial stress

Table of Contents

Chapter	Page
1. INTRODUCTION	1
1.1 General	1
1.2 Aim	3
1.3 Scope	3
2. GEOLOGY	5
2.1 Introduction	5
2.2 Bedrock Geology	5
2.2.1 Oldman Formation	6
2.2.2 Bearpaw Formation	8
2.3 Structural Geology	9
2.4 Surficial Geology	12
2.5 Hydrogeology	13
3. GEOTECHNICAL PROPERTIES OF THE BEARPAW FORMATION	15
3.1 Introduction	15
3.2 Results of Previous Testing	15
3.3 Laboratory Testing of Bearpaw Formation Samples ..	17
3.3.1 Sampling and Storage	17
3.3.2 Index Testing	18
3.3.3 Direct Shear Tests	20
3.3.3.1 Test Procedure	20
3.3.3.2 Sample Preparation and Description	20
3.3.3.3 Direct Shear Test Results	22
3.3.4 High Pressure Triaxial Tests	24
3.3.4.1 Test Equipment	24

3.3.4.2	Sample Preparation and Description	27
3.3.4.3	Test Procedure	28
3.3.4.4	High Pressure Triaxial Test Results	31
4.	SHAFT CONSTRUCTION AND INSTRUMENTATION	45
4.1	Introduction	45
4.2	Shaft Construction	45
4.3	Shaft Instrumentation	51
4.3.1	Introduction	51
4.3.2	Drilling Equipment	52
4.3.3	Instrumentation and Testing Locations	52
4.3.4	Instrument Descriptions and Installation Procedures	57
4.3.4.1	Extensometers	57
4.3.4.2	Embedment Gauges	65
4.3.4.3	Stressmeters	68
4.3.4.4	Piezometers	74
5.	EVALUATION OF THE <i>IN SITU</i> STRESS FIELD	75
5.1	Introduction	75
5.2	Evidence on the Orientation of the Regional Stress Field	75
5.3	<i>In situ</i> Stress Measurements by Overcoring	78
5.3.1	Introduction	78
5.3.2	Test Equipment and Procedure	78
5.3.3	Data Reduction and Analysis	84
5.4	Interpretation of <i>in situ</i> Stresses from Stressmeter Measurements	92
5.5	Conclusions on the <i>in situ</i> Stress Field	93
6.	ANALYSIS OF SHAFT INSTRUMENTATION	95

6.1	Introduction	95
6.2	Extensometers	95
6.2.1	Extensometer Data Reduction	95
6.2.2	Discussion of Errors	98
6.2.3	Extensometer Performance	99
6.2.4	Analysis of Extensometer Data	100
6.2.5	Comparison of Measured with Predicted Radial Displacements	106
6.2.6	Practical Recommendations Arising from Extensometer Measurements	109
6.3	Stressmeters	111
6.3.1	Stressmeter Data Reduction	111
6.3.2	Discussion of Errors	112
6.3.3	Estimation of the <i>in situ</i> Stress Field ...	114
6.3.3.1	Method of Analysis	114
6.3.3.2	Comparison of measured stress changes to Model	120
6.3.4	Stress Changes Associated With the Advancing Shaft Bottom	122
6.3.5	Practical Implications From Stressmeter Measurements	129
6.4	Embedment Gauges	130
6.4.1	Data Reduction	130
6.4.2	Factors Influencing Concrete Strain Measurements	130
6.4.2.1	Introduction	131
6.4.2.2	Compliance of the Embedment Gauge	131
6.4.2.3	Thermal Properties of the Concrete Lining	133
6.4.2.4	Shrinkage of the Concrete Lining	134

6.4.2.5	Creep of Concrete	137
6.4.3	Analysis of Embedment Gauge Data	138
6.4.3.1	Non-Uniform Response of the Lining to Applied Load	138
6.4.3.2	Interpretation of Lining Strains	139
6.4.3.3	Interpretation of Lining Stresses	144
6.4.4	Analysis of Field Stress on Lining	149
6.4.4.1	Introduction	149
6.4.4.2	Relative Stiffness Solution	150
6.4.4.3	Finite Element Analysis of Lining Stresses	154
6.4.4.4	Comparison of Finite Element Solution to Relative Stiffness Solution	159
6.4.5	Prediction of the Orientation and Magnitude of Stresses on the Shaft Lining	159
6.4.6	Practical Implications from Lining Strain Measurements	160
6.5	Piezometers	161
6.6	Conclusions from Instrumentation Analysis	162
7.	EVALUATION OF SHAFT LINING PERFORMANCE	165
7.1	Introduction	165
7.2	The Convergence-Confinement Method	165
7.2.1	The Ground Convergence Curve	167
7.2.2	The Support Reaction Curve	170
7.3	Application of the Convergence-Confinement Method to the Lethbridge Shaft	171
7.4	Discussion of Convergence-Confinement Curves	173
7.5	Conclusions From Convergence-Confinement Analysis	183

8. CONCLUSIONS	186
8.1 Introduction	186
8.2 Laboratory Testing	186
8.3 <i>In situ</i> Stress Field	187
8.4 Rock Mass Response to Shaft Sinking	188
8.5 Development of Lining Loads	190
8.6 Rock-Support Interaction Analysis	191
8.7 Implications for the Design of Future Adits	192
8.8 Implications for Future Monitoring Programs	192
REFERENCES	194
APPENDIX A	202
APPENDIX B	211
APPENDIX C	234
C.1 Radial Displacement Around a Circular Hole Formed in a Prestressed Thin Plate	234
C.2 Analysis of Stress Change Measurements Adjacent to Shaft	237
C.3 Evaluation of Elastic and Creep Strains in the Concrete Lining	243
C.4 Formulas for Determining <i>in situ</i> Stresses in Isotropic Rock	251
C.5 Formulas for Determining <i>in situ</i> Stresses in Anisotropic Rock	255

List of Tables

Table	Page
2.1 Shale and Sandstone Members of Bearpaw Formation (Crawford, 1947)	9
3.1 Summary of Laboratory Testing on Samples from Exploratory Drillholes on Site (after Dames and Moore, 1978)	16
3.2 Index Properties of Samples from Shaft at a Depth of 111 m.	19
3.3 Initial Properties of Triaxial Test Samples	29
4.1 Specifications of Concrete Used for Casting the Shaft Lining	46
5.1 Summary of Diametral Deformations from Overcore Tests	87
5.2 Comparison of Principal Biaxial Stresses Calculated from Isotropic and Anisotropic Analysis	89
5.3 Isotropic Analysis of Overcore Tests 2 and 4 Based on Assumption of $\sigma_v = \gamma h$	91
6.1 Measured Stress Changes for Shaft Bottom at 5 m and 55 m Below Plane of Gauges	119
6.2 Field Stress Orientation and Magnitude Predicted from Stressmeter Analysis	121
6.3 Percentage of Total Measured Tangential and Radial Stress Changes Occuring Ahead of Shaft Bottom and Before Installation of Lining	125
6.4 Evaluation of Strains at 152 m Depth, Assuming Zero Strain at 10 Days	146
6.5 Evaluation of Strains at 180 m Depth, Assuming Zero Strain at 10 Days	147
7.1 Input Parameters for Ground Convergence Curve	174
7.2 Input Parameters for Support Reaction Curves Calculated from Relative Stiffness Solution	175

Table

Page

C.1	Parameters for Development of Creep Function for Concrete Lining at t=450 Days	246
-----	--	-----

List of Figures

Figure	Page
1.1	Location of Kipp Mine2
2.1	Cross Section of Bedrock and Surficial Deposits Encountered in Shaft7
3.1	Mohr Envelope for Direct Shear Tests on Bearpaw Formation Siltstone23
3.2	Plot of the Peak Strength Mohr Envelope for Triaxial Tests34
3.3	Plot of the Ultimate Strength Mohr Envelope for Triaxial Tests36
3.4	Plot of Axial Stress vs. Confining Stress for Triaxial Tests37
3.5	Plot of the Ultimate Strength Mohr Envelope for Triaxial Tests Showing Dependence of Ultimate Strength on Strain Rate38
3.6	Principal Stress Plot Showing Hoek-Brown Failure Criterion Fitted to Triaxial Test Data40
3.7	Combined Plot of Deviatoric Stress vs. Strain for all Triaxial Tests41
3.8	Plot of Modulus of Elasticity vs. Log of the Axial Strain Rate for Triaxial Test Data43
4.1	Log of Shaft Sinking and Lining Through Bearpaw Formation48
4.2	Shaft Lining Schedule, Lethbridge Coal Project (after T.M.C.C., 1980)49
4.3	Cross-section of Shaft Showing Locations of Instrumentation and Testing54
4.4	Plan View of Extensometers at 111.3 m Depth55
4.5	Plan View of Embedment Gauges at 108 and 109 m Depth56
4.6	Plan View of Stressmeters at 152 m Depth58

Figure	Page
4.7 Section View of Stressmeters at 152 m Depth	59
4.8 Plan View of Extensometers at 180 m Depth	60
4.9 Plan View of Embedment Gauges at 180 m Depth	61
4.10 Borehole Extensometer with Single Anchor (after Irad Gage Inc.)	62
4.11 Vibrating Wire Embedment Gauge (after Irad Gage Inc.)	66
4.12 Photo and Section of Vibrating Wire Stressmeter with Soft Rock Platen (after Irad Gage Inc.)	70
5.1 Orientation of Major and Minor Principal Horizontal Stresses Interpreted from Oilwell Breakouts (after Gough and Bell, 1981)	76
5.2 U.S.B.M. Borehole Deformation Gauge (after Hooker and Bickel, 1974)	80
5.3 Plan View of Overcore Test Locations of 91 m Depth	81
5.4 Schematic Presentation of Relationship Between Overcored Depth and Measured Diametral Deformation (after Obert, 1966)	83
5.5 Estimated Field Stress Profile Adjacent to the Shaft	94
6.1 Normalized Radial Elastic Displacements at 111 m Depth for $\Theta = 60^\circ$	102
6.2 Normalized Radial Elastic Displacements at 111 m Depth for $\Theta = 30^\circ$	102
6.3 Normalized Radial Elastic Displacements at 180 m Depth for $\Theta = 20^\circ$	103
6.4 Normalized Radial Elastic Displacements at 180 m Depth for $\Theta = 80^\circ$	103
6.5 Normalized Data Plot for North Wall Extensometer at 111 m.	104

Figure	Page
6.6 Normalized Data Plot for Southeast Wall Extensometer at 111 m.	104
6.7 Normalized Data Plot for North Wall Extensometer at 180 m.	105
6.8 Normalized Data Plot for Southwest Wall Extensometer at 180 m.	105
6.9 Plot of Predicted Radial Elastic Stress Changes at $r/a=1.35$ Normalized to the Maximum Field Stress vs. Orientation of Maximum Field Stress	116
6.10 Plot of Predicted Radial Elastic Stress Changes at $r/a=1.50$ Normalized to the Maximum Field Stress vs. Orientation of Maximum Field Stress	116
6.11 Plot of Predicted Radial Elastic Stress Changes at $r/a=1.75$ Normalized to the Maximum Field Stress vs. Orientation of Maximum Field Stress	117
6.12 Plot of Predicted Radial Elastic Stress Changes at $r/a=1.95$ Normalized to the Maximum Field Stress vs. Orientation of Maximum Field Stress	117
6.13 Comparison of Measured and Predicted Tangential and Radial Stress Changes of $r/a = 1.5$ vs. Distance from Plane of Measurement	123
6.14 Plot of Predicted Tangential and Radial Stress Change at Tunnel Wall vs. Distance Behind Tunnel Face (after Hutchinson, 1982)	126
6.15 Schematic Representation of Thermal Strain Development in Concrete Lining	142
6.16 Development of the Dimensionless Stiffness Ratios for the Relative Stiffness Solution (after Schwartz and Einstein, 1980)	151
6.17 Notation and Formulas for No-Slip Case of Relative Stiffness Solution (after Schwartz and Einstein, 1980)	153

Figure	Page
6.18 Plot of Tangential Lining Strains Normalized to the Maximum Principal Stress vs. Orientation of the Minor Principal Stress, for the Relative Stiffness Solution at 152 m Depth	155
6.19 Plot of Tangential Lining Strains Normalized to the Maximum Principal Stress vs. Orientation of the Minor Principal Stress, for the Finite Element Analysis at 152 m Depth	155
6.20 Plot of Tangential Lining Strains Normalized to the Maximum Principal Stress vs. Orientation of the Minor Principal Stress, for the Relative Stiffness Solution at 180 m Depth	156
6.21 Plot of Tangential Lining Strains Normalized to the Maximum Principal Stress vs. Orientation of the Minor Principal Stress, for the Finite Element Analysis at 180 m Depth	156
6.22 Finite Element Mesh for Lining Strain Analysis	157
7.1 Schematic Convergence-Confinement Curves for a Nonuniformly Loaded Circular Shaft (after Kaiser et al, 1982)	166
7.2 Schematic Linear Ground Convergence Curves (after Kaiser, 1981)	169
7.3 Convergence-Confinement Curves for Shaft at 152 m Depth	176
7.4 Convergence-Confinement Curves for Shaft at 180 m Depth	177
7.5 Convergence-Confinement Curves for Shaft at 152 m Depth	178
A.1 Axial Strain and Confining Stress vs. Axial Stress for Triaxial Test No. 1	203
A.2 Axial Strain and Confining Stress vs. Axial Stress for Triaxial Test No. 2	204
A.3 Axial Strain and Confining Stress vs. Axial Stress for Triaxial Test No. 3	205

Figure	Page
A.4 Axial Strain and Confining Stress vs. Axial Stress for Triaxial Test No. 4	206
A.5 Axial Strain and Confining Stress vs. Axial Stress for Triaxial Test No. 5	207
A.6 Axial Strain and Confining Stress vs. Axial Stress for Triaxial Test No. 6	208
A.7 Axial Strain and Confining Stress vs. Axial Stress for Triaxial Test No. 7	209
A.8 Axial Strain and Confining Stress vs. Axial Stress for Triaxial Test No. 8	210
B.1 Depth-Displacement Plot for N. Wall Extensometer at 111 m Depth	212
B.2 Depth-Displacement Plot for S.E. Wall Extensometers at 111 m Depth	212
B.3 Depth-Displacement Plot for N. Wall Extensometer at 180 m Depth	213
B.4 Depth-Displacement Plot for S.E. Wall Extensometers at 180 m Depth	213
B.5 Time-Displacement Plot for N. Wall Extensometer at 111 m Depth	214
B.6 Time-Displacement Plot for S.E. Wall Extensometers at 111 m Depth	214
B.7 Time-Displacement Plot for N. Wall Extensometer at 180 m Depth	215
B.8 Time-Displacement Plot for S.E. Wall Extensometers at 180 m Depth	215
B.9 Stress Change-Time Plot for Stressmeters at 1.49 m from South Wall	216
B.10 Stress Change-Time Plot for Stressmeters at 2.65 m from South Wall	216
B.11 Stress Change-Time Plot for Stressmeters at 1.34 m from West Wall	217
B.12 Stress Change-Log Time Plot for Stressmeters at 1.49 m from South Wall	217

Figure	Page
B.13 Stress Change-Log Time Plot for Stressmeters at 2.65 m from South Wall	218
B.14 Stress Change-Log Time Plot for Stressmeters at 1.34 m from West Wall	218
B.15 Stress Change-Depth Plot for Stressmeters at 1.49 m from South Wall	219
B.16 Stress Change-Depth Plot for Stressmeters at 2.65 m from South Wall	219
B.17 Stress Change-Depth Plot for Stressmeters at 1.34 m from West Wall	220
B.18 Tangential Strain-Time Plot for Inside Embedment Gauge Ring at 108 m Depth	221
B.19 Tangential Strain-Time Plot for Outside Embedment Gauge Ring at 108 m Depth	221
B.20 Tangential Strain-Time Plot for Inside Embedment Gauge Ring at 109 m Depth	222
B.21 Tangential Strain-Time Plot for Outside Embedment Gauge Ring at 109 m Depth	222
B.22 Tangential Strain-Time Plot for Inside Embedment Gauge Ring at 152 m Depth	223
B.23 Tangential Strain-Time Plot for Outside Embedment Gauge Ring at 152 m Depth	223
B.24 Tangential Strain-Time Plot for Inside Embedment Gauge Ring at 180 m Depth	224
B.25 Tangential Strain-Time Plot for Outside Embedment Gauge Ring at 180 m Depth	224
B.26 Tangential Strain-Log Time Plot for Inside Embedment Gauge Ring at 108 m Depth	225
B.27 Tangential Strain-Log Time Plot for Outside Embedment Gauge Ring at 108 m Depth	225
B.28 Tangential Strain-Log Time Plot for Inside Embedment Gauge Ring at 109 m Depth	226

Figure	Page
B.29 Tangential Strain-Log Time Plot for Outside Embedment Gauge Ring at 109 m Depth	226
B.30 Tangential Strain-Log Time Plot for Inside Embedment Gauge Ring at 152 m Depth	227
B.31 Tangential Strain-Log Time Plot for Outside Embedment Gauge Ring at 152 m Depth	227
B.32 Tangential Strain-Log Time Plot for Inside Embedment Gauge Ring at 180 m Depth	228
B.33 Tangential Strain-Log Time Plot for Outside Embedment Gauge Ring at 180 m Depth	228
B.34 Plot of Diametral-Deformation vs. Overcored Depth for Overcore Test No. 1	229
B.35 Plot of Diametral-Deformation vs. Overcored Depth for Overcore Test No. 2	230
B.36 Plot of Diametral-Deformation vs. Overcored Depth for Overcore Test No. 3	231
B.37 Plot ²⁰ of Diametral-Deformation vs. Overcored Depth for Overcore Test No. 4	232
B.38 Plot of Diametral-Deformation vs. Overcored Depth for Overcore Test No. 5	233
C.1 Initial Biaxial Stress Conditions	238
C.2 Notation for Biaxial Stresses Adjacent to Shaft in Isotropic Elastic Ground	240
C.3 Creep Function vs. Time for t=450 days	248
C.4 View Down Borehole of a 60 Degree Deformation Rosette (Obert, 1966)	252
C.5 A Circular Hole in an Orthotropic Solid Subject to Biaxial Field	256

List of Plates

Plate	Page
3.1 MTS Test Frame with 14 MPa Pressure System	25
3.2 Hoek Cell in Test Frame with Pressure Transducer and L.V.D.T.	25
3.3 Triaxial Test Sample No. 4 After Failure	32
3.4 Triaxial Test Sample No. 7 After Failure	32

1. INTRODUCTION

1.1 General

Large areas of western Canada and the United States are underlain by soft and weak "shale" bedrock. The design of underground openings in these rocks has been primarily empirical. The dimensioning of the underground supports has often been based on rules developed for comparable rock types in other parts of the world. Little data has been collected to evaluate the performance of existing openings, and check the applicability of present empirical methods to local conditions.

The sinking of a vertical shaft at Kipp, near Lethbridge in southern Alberta, provided the opportunity to collect performance data during the construction and operation of the shaft. The mine site is located approximately 10 kilometres north-west of Lethbridge on the southern edge of the Alberta Plains (Figure 1.1). The mine is being developed by Petro Canada Exploration Inc. to exploit part of the extensive Lethbridge Coal Field.

Underground coal mining has been active in the Lethbridge area since the early 1880's. Closure of the last mine in the mid 1960's reflected the declining world demand and increasing costs of underground mining. Recent increases in coal prices, and advances in technology make underground mining once again potentially viable. One additional major

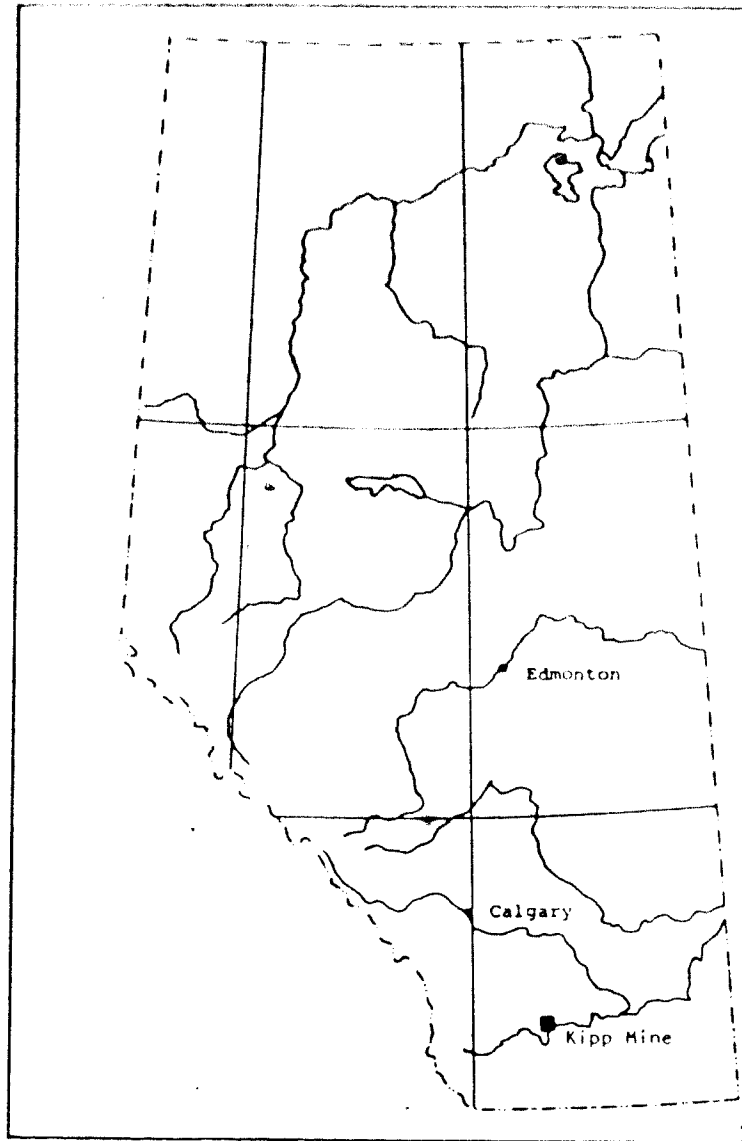


Figure 1.1 Location of Kipp Mine

project is presently under development in the area.

1.2 Aim

The sinking of the vertical shaft at Kipp provided an excellent opportunity to collect shaft performance data for the rational design of future adits to this coal mine. For this purpose, it was necessary to determine the *in situ* stress field, to observe the deformations near the opening, to determine the rock mass deformation properties, to determine the strength properties by laboratory tests, and to monitor load development on the support to verify the lining design.

1.3 Scope

Chapter 2 presents an overview of the local bedrock, surficial and structural geology in the Lethbridge area. Chapter 3 discusses the geotechnical properties of the Bearpaw Formation, including the results of high pressure triaxial tests. The construction procedure and instrumentation program are reviewed in Chapter 4, as well as the instrument installation procedures and locations. Chapter 5 discusses the regional evidence on the orientation and magnitude of the *in situ* stress field. The results of *in situ* stress measurements by overcoring, and stressmeter measurements ahead of the shaft face are compared with the regional stress model.

Chapter 6 contains the discussion of the performance of the instrumentation, and an analysis of field data using an appropriate model.

The overall performance of the lining is evaluated in Chapter 7 through the use of the convergence-confinement method. Ground reaction curves and support reaction curves are developed from measured field data. The long term performance of the shaft lining and possible alternate support systems are discussed.

Conclusions from this study are presented in Chapter 8. Laboratory test results are presented in Appendix A. Field test results are presented in Appendix B. Formulas used, instrumentation and *in situ* testing analysis are presented in Appendix C.

2. GEOLOGY

2.1 Introduction

Lethbridge lies on the western edge of the Alberta Plains which is characterised by a flat lying plain that has been deeply incised by the Oldman, Belly and St. Mary Rivers. The Lethbridge coalfield covers an area of about 1150 square kilometres within parts of Townships 8 to 11, Ranges 21 to 23, west of the fourth meridian.

The major report on the geology of the southern Alberta plains was conducted by Russel and Landes (1940). Crawford (1947) studied the geology and structure of the Lethbridge coalfield. Irish (1971) updated the bedrock geology map of the Southern Plains of Alberta.

2.2 Bedrock Geology

The bedrock cropping out in the Lethbridge area was deposited during the Upper Cretaceous Period as detrital sediments, in both continental and marine environments. Montmorillonite, formed from volcanic ash deposits, is found throughout the Upper Cretaceous sediments, both as pure bentonite beds, and as the dominant clay mineral in the fine-grained sediments (Byrne and Farvolden, 1959).

The Lethbridge Coal Zone is located in the uppermost beds of the non-marine Oldman Formation, the youngest formation of the Belly River Group. Conformably overlying

the Oldman Formation is the marine Bearpaw Formation. Discussion of the bedrock geology in this report will be restricted to the Bearpaw and Oldman Formations, the two formations encountered in sinking the shaft. Figure 2.1 presents a cross section of the bedrock and surficial deposits exposed in the shaft.

2.2.1 Oldman Formation

The Oldman Formation was deposited in a non-marine deltaic environment as an eastward-thinning sedimentary wedge (Holter and Chu, 1978). The Oldman Formation conformably overlies the non-marine Foremost Formation, the lower member of the Belly River Group. The contact between the Oldman and Foremost Formations is gradational and therefore is not precisely defined. The Oldman Formation is up to 180 m thick and is divided into an upper and lower member (Crawford, 1947). The upper member is about 24 m thick and is known as the Lethbridge coal member. The Oldman Formation is composed of interbedded light colored sandstones and shales with frequent coal beds in the upper member. The sandstones vary in color from light grey and green, to brown, and vary in river bank outcrops from uncemented massive beds to hard, lenticular and crossbedded sandstones (Crawford, 1947). The hard sandstones are cemented by calcite. The shale beds are generally light green, and highly plastic in weathered outcrops. Montmorillonite is found throughout the Oldman Formation.

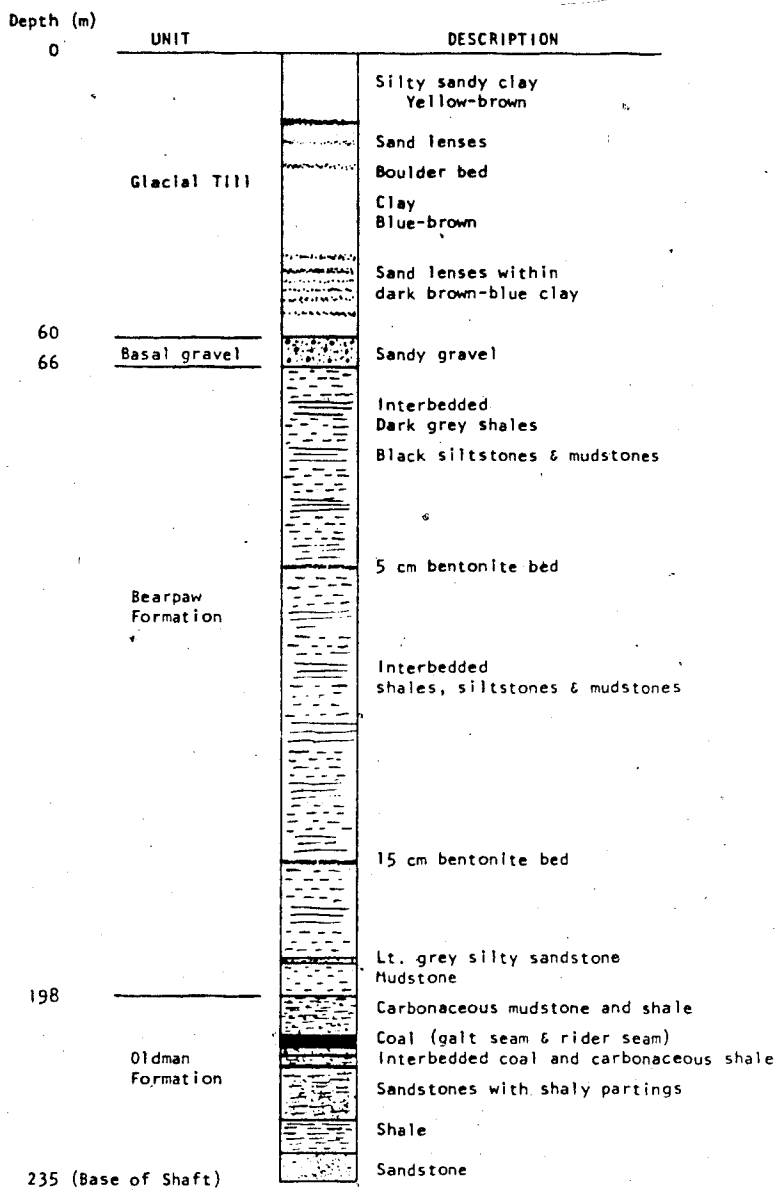


Figure 2.1 Cross Section of Bedrock and Surficial Deposits Encountered in Shaft

The coal beds found in the upper member of the Oldman Formation were deposited in fresh to brackish water on the edge of the transgressing Bearpaw Sea. The coal seams vary in thickness from 0.15 m to 2.1 m. The Lethbridge or Galt seam is the thickest seam, and this is the seam presently exploited by mining operations. The coal is a high volatile C bituminous coal (Crawford, 1947). Interbedded with the coal beds are dark grey to brown, sulfurous, gypsiferous and carbonaceous shales, with thin ironstone bands and concretions (Crawford, 1947). In the vicinity of the Kipp mine the Galt Seam varies in thickness from 1.1 to 1.8 m, and is located 4.6 to 7.6 m below the top of the 10.7 to 17 m thick coaly zone or coal bearing zone (Dames and Moore, 1978).

Directly overlying the Galt Seam are thinly bedded shales, mudstones, carbonaceous shales and a thin coal seam. Within 15 to 30 m above the Galt seam are interbedded black mudstones, shales with occasional thin beds of coal, bentonite and grey sandstone. Directly underlying the Galt seam is a black carbonaceous mudstone, with shales, some thin coal seams and occasional fine sandstone beds (Dames and Moore, 1978).

2.2.2 Bearpaw Formation

The transition between the non-marine Oldman Formation and the marine Bearpaw Formation is gradational indicating a slow transgression of the Bearpaw Sea over the area

(Crawford, 1947). The Lethbridge Coal zone is in the lower part of this transition zone. Up to 222 m of Bearpaw sediments are found in the Lethbridge area, with between 100 and 175 m overlying the Kipp mine site. Crawford (1947) subdivides the Bearpaw sediments in the Lethbridge area as shown in Table 2.1.

The sandstone members are fine-grained, poorly indurated and argillaceous. The remainder of the Bearpaw Formation consists of dark grey and green to black siltstones and fissile shales. Beds of bentonite up to 10 cm thick and occasional beds of clay ironstone are interspersed throughout the fine-grained members (Byrne and Farvolden, 1959).

2.3 Structural Geology.

The Lethbridge area is situated on the east limb of the Alberta syncline and the west limb of the Sweetgrass Arch, forming a west dipping monoclinial structure. The Sweetgrass Arch, a north-northeast trending anticlinal flexure, plunges 4 to 6 metres per kilometre to the north. Local bedrock dips near Kipp are about 20 m per kilometre to the west (Crawford, 1947). The bedrock structure of the Lethbridge coalfield consists of a series of gentle, low amplitude anticlines and synclines trending northwest-southeast and plunging gently to the northwest (Crawford, 1947). Associated with the folds are a number of faults of normal

Table 2.1 Shale and Sandstone Members of Bearpaw
Formation (Crawford, 1947)

	MEMBER	THICKNESS (m)
Top	Shale	25.6
	Ryegrass Sandstone	27.4
	Shale	44.5
	Kipp Sandstone	12
	Shale	29.5
	McGrath Sandstone	19
Bottom	Shale	64

and thrust displacement, traceable over several kilometres. The Monarch Fault Zone, located approximately 10 km west of the mine site in Sections 31 and 32, Township 9 and Section 6, Township 10, Range 23, is the major fault zone near the mine. This zone consists of a series of vertical to west dipping (20°) thrust faults striking $N 25^\circ E$ to $N 20^\circ W$. Crawford (1947) reported that there was no continuity of disturbance along strike.

Displacements of up to 30 m were measured on localized faults identified from mine plans (Crawford, 1947). Both normal and reverse dip slip faults were found in the coal field. Studies of fault orientations in the early underground mines and river valley exposures showed a distinct grouping in some of the mines, but a large scatter in other mines (Crawford, 1947). Single fault traces in some mines followed a particularly sinuous path with strikes varying over 90 degrees. Where groupings of fault orientations occurred, two major families were formed, one parallel to the major folding in the area, in a northwest-southeast direction, and the other perpendicular to the first, in a northeast-southwest orientation. Normal faults trending $N15^\circ W$ to $N15^\circ E$ have also been identified in several mines. Displacement on the faults is generally in the order of 1.2 m to 1.8 m, with up to 6 m observed. Dip of the faults was generally between 35° to 40° . Cleavage has developed in the coal in two major orientations, with the major cleavage at $N 50^\circ E$ and the minor cleavage at $N 40^\circ W$.

The structural features present in the Lethbridge coal field were largely formed during the Tertiary Period. Continental sediments were deposited in the area during the late Cretaceous and early Paleocene. The culmination of the Laramide Orogeny in the Eocene produced widespread uplift, crustal shortening and thrust faulting in the Rocky Mountains and renewed uplift of the Sweetgrass Arch in southwestern Alberta (McCrossan and Glaister, 1966).

The low amplitude folding and thrust faulting, trending northwest-southeast, are compatible with the high lateral compressive stresses developed in a northeast-southwest direction during the Laramide Orogeny. The relative age of the renewed uplift of the Sweetgrass Arch with respect to the period of high horizontal compressive stresses developed during the Laramide Orogeny is unknown. If the uplift of the Sweetgrass Arch occurred following the Laramide event, associated local crustal flexure could account for the development of the normal faults observed in the area.

2.4 Surficial Geology

Surficial deposits over the Kipp mine site vary in thickness between 60 and 85 metres with 70 m present at the shaft location. The present day Oldman River to the west of the mine cuts through the complete section of surficial deposits. A 10.5 m thick early Pleistocene sandy gravel deposit known as the "Saskatchewan Gravels" overlies bedrock

at the site. These gravels were deposited by the eastward flowing pre-glacial Oldman River (Stalker, 1963). Overlying the pre-glacial gravels are about 60 m of tills of Nebraskan to Classical Wisconsin Age. Stalker (1963) has noted up to 6 Laurentide tills in the area, each with distinctive colors, degree of consolidation and jointing patterns. Thin interglacial sand and gravel deposits usually separate the individual till sheets. The uppermost till in the area is a thin hummocky dead ice moraine overlain in places by Lacustrine and/or windblown silts (Stalker, 1963). A number of distinct till sheets and interglacial sands and gravels have been identified.

2.5 Hydrogeology

The hydrogeological conditions of the overburden and bedrock were important considerations in the shaft design and development of the mine. Previous mine records do not mention significant ground water problems (Robinson, Dames and Moore, 1980). Crawford (1947) reports minor seepage occurring along fault surfaces cutting the coal seams in some of the mines. Several wells have been developed in the coal seam within about a 10 km radius of the site producing up to 2800 l/min. (Geiger *et al.*, 1965).

Hydrological information gained from installing standpipe piezometers in the coal and at the base of the surficial gravels were unable to show the coal as

waterbearing.

During shaft sinking, an aquifer was encountered in the lower zone of the Saskatchewan Gravels at about 65 m depth. This extended into the underlying weathered bedrock, to a depth of about 77 m. Maximum inflow from this aquifer was 35 to 45 l/min in the 5.4 m diameter unfinished shaft. No further ground water inflow was encountered as shaft sinking progressed. Small amounts of moisture were observed on open joints in the shales overlying the coal seam. The coal seam is dry.

3. GEOTECHNICAL PROPERTIES OF THE BEARPAW FORMATION

3.1 Introduction

This chapter presents the results of the laboratory testing program on samples obtained from the shaft, plus some previously reported test results. The laboratory test program consisted of Index testing, direct shear and high pressure triaxial tests.

3.2 Results of Previous Testing

Bryne and Farvolden (1959), have shown from a detailed study of the clay mineralogy of Bearpaw Formation sediments, near Lethbridge that the mineralogy of the clay fraction is 55% montmorillonite, 27% illite and 18% Chlorite.

Dames and Moore (1978) report test results from drill core samples collected from two drill holes on the mine site. Core was collected over a 30 m interval above the Galt coal seam, and 6 m below the seam, using a 76 mm diameter plastic tubing lined core barrel. Table 3.1 presents a summary of the test results from the Dames and Moore study.

Table 3.1 Summary of Laboratory Testing on Samples from
Exploratory Drillholes on Site (Dames and Moore,
1978)

Material	Unconfined Compressive Strength [MPa]		Youngs Modulus [GPa]		Point Load Test Strength Index [MPa]		Anisotropy Ratio		Slake Durability Index 1st Cycle/2nd Cycle		Moisture Content (%)		Bulk Density γ_s [g/cm ³]
	Mean	Std.Dev.	Mean	Std.Dev.	Mean	Std.Dev.	Mean	Std.Dev.	Mean	Std.Dev.	Mean	Std.Dev.	
Coal	9.0	3.5	4.1	1.8	0.73	0.26	/	/	90/70	/	9.9	1.6	1.85
Black Carbonaceous Shale	9.0	4.8	1.7	1.9	0.83	0.46	11.9	11.9	60/13	22/22	9.3	3.6	2.50
Dark Grey Shale	5.5	9.7	1.7	1.9	0.83	0.46	11.9	11.9	60/13	22/22	9.3	3.6	2.45
Sandstone	20.8	8.3	4.6	2.3	1.31	0.58	12.1	12.1	96/92	/	6.6	1.2	2.60

3.3 Laboratory Testing of Bearpaw Formation Samples

3.3.1 Sampling and Storage

Samples for laboratory testing were obtained at depths of 91 and 111 m in the shaft, from horizontal diamond drill holes. Two 24.5 cm diameter by 40 cm long cores were recovered from the blast damaged rock adjacent to the shaft wall at the 91 m level. Continuous samples of 14.3 cm diameter core were obtained from a 7 m long drill hole in conjunction with the overcoring measurements at the 91 m level. Recovery of the 14.3 cm diameter core was 100 percent, with lengths of core often equal to the 71 cm long core barrel. All drilling for samples employed single walled masonry bits, using water to flush the cuttings. The core at the 91 m level was obtained from a 45 cm thick bed of dark grey-black mudstone. At the 91 m level, the rock was approximately horizontally bedded, and appeared massive between the bedding planes, which were separated at intervals of 20 to 45 cm. Random fractures oblique to bedding were attributed to blasting. Visual inspection of the 15 cm diameter drill hole indicated a zone of blast induced fracturing up to 35 cm thick was present. Several vertical fractures were observed in individual beds, but continuous vertical fractures between beds were not observed.

Following extraction from the corebarrel, samples were wiped dry, and wrapped with saran plastic, cheesecloth and

sealed with a layer of wax. All samples were given a further coating with wax after being transported to the University of Alberta. Samples were stored in a constant temperature moist room until tested.

Samples of the rock exposed to air drying developed a fine pattern of surface cracks within minutes of exposure.

3.3.2 Index Testing

Index tests were conducted on samples from the 91 and 111 m levels in conjunction with the direct shear and triaxial compression tests. Tests were conducted on selected samples to determine the grain size distribution, specific gravity, Atterberg limits, moisture content and bulk and dry density. Preparation of samples for grain size distribution, specific gravity and atterberg limit tests were conducted according to A.S.T.M. Standard D421-58. Grain size distribution was determined on cuttings from the swelling test samples, according to A.S.T.M. Standard D422-63. The specific gravity was determined according to A.S.T.M. Standard D854-58. Atterberg limits were determined according to A.S.T.M. Standards D423-66 and D424-59.

Index test results for two samples representative of the samples are presented in Table 3.2. Index test results from the triaxial tests are presented in Table 3.3.

Table 3.2 Index Properties of Samples from Shaft at a Depth of 111 m.

Sample No.	Bulk Density γ/γ_d [g/cm ³]	Moisture Content (%)	Specific Gravity	Atterberg Limits $\frac{w_L}{w_p}$	I_p	Type of Soils	Particle Sizes (%) Fine Sand Silt	Clay	Void Ratio	Porosity n	Saturation S (%)		
111-1	2/40/2.23	7.8 (wet cut)	2.80	55.2	22.5	32.7	CH	15	54	31	0.256	20.4	85.3
111-2	2.40/2.32	3.5 (dry cut)	2.77	53.5	22.9	30.6	CH	15	61	24	0.194	16.2	50.0

w_L = liquid limit
 w_p = plastic limit
 I_p = plasticity index
 CH = high plastic clay

3.3.3 Direct Shear Tests

3.3.3.1 Test Procedure

Direct shear tests were conducted on two samples of jointed siltstone, the first test on a smooth joint and the second on an open bedding plane. Tests were conducted on the modified direct shear machine described by Noonan (1972). Both samples were initially tested in a dry state and subsequently in a submerged state. Shear displacement rate of 0.275 mm/min. was constant for all samples. Normal loads for the dry tests were applied about one day prior to shearing, and about three days prior to shearing for the submerged tests. Samples were sheared for two cycles, forward and reverse for each normal load. Displacements of each cycle varied from 0.8 to 1.3 cm. Horizontal displacement of the shearbox and vertical movement of the load cap were measured with Linearly Variable Displacement Transducers (LVDT). Normal loads were added with a dead weight and lever hanging apparatus. Shear loads were measured with an 8.9 KN capacity load cell. An X-Y₁-Y₂ recorder was used to record shear load (Y₁) and vertical load cap displacement (Y₂) vs displacement (X) during the tests.

3.3.3.2 Sample Preparation and Description

The shear samples were cut from 14 centimetre diameter cores from the 91 and 111 metre depths. Sample No.1 was cut by saw from the core from the 111 metre depth. The sample

was prepared in two pieces, with a pre-cut smooth shearing surface. The lower half of the sample fitted tightly in the 5.08 cm by 5.08 cm box. The upper portion of the sample had a loose fit in the shear box, and a shearing area of 18.44 cm². Cuttings from the core during sample preparation had an initial moisture content of 3.5 percent. The final moisture content of Sample No.1 after testing was 10.1 percent as a result of swelling during the submerged stage of the test. Sample No.1 was a dark grey siltstone with numerous micro cracks indicating a disturbed state of the sample. The low initial moisture content compared with an average moisture content of about 8 percent indicates the sample had dried between sampling and testing. The pre-cut plane was positioned such that it was in the centre of the 1.0 mm gap between the two halves of the shear box. At normal loads higher than the first two normal loads, the pre-cut plane was depressed below the top of the lower half of the shear box, resulting in an unacceptable shearing mode. Results from testing Sample No.1 are restricted to the first two normal loads.

Sample No. 2, cut by saw from drill core from 91 m depth, was sheared along a slightly undulating open bedding plane. The upper and lower halves of the sample were cut separately to the approximate size of the shearbox, and cast in sulfa-set to provide a rigid perfect fit of the irregular shaped samples. The lower half of the sample had a larger area than the upper half of the sample, thus during

shearing, the contact area was constant at 26.50 cm². The sample had an initial moisture content of 6.4 percent and a bulk density of 2.38 g/cm.³ Sample No.2 was a dark grey siltstone but less fractured and easier to prepare for shearing than sample No.1. An air-dried block of sample No.2 was placed in a beaker of distilled water and disintegrated within 1 hour. Undulations on the shearing surface were about 5 mm from trough to crest. The halves of the shearbox were separated by 7 millimetres to allow free movement of the shearing surfaces.

3.3.3.3 Direct Shear Test Results

Figure 3.1 presents a Mohr-Coulomb plot of the ultimate shearing resistance of the two tested samples. Sample No.2 shows an angle of shearing resistance of 20 degrees on a precut plane in a dry state during shearing and a subsequent reduction of the friction angle after wetting to 17 degrees. The submerged sample was affected by excessive extrusion of material between the halves of the shearbox, thus new material was constantly being sheared. This could indicate that the residual angle of shearing resistance on material subjected to several cycles of shearing is less than 17 degrees. An angle of shearing resistance of 26 degrees was obtained for the dry natural undulating joint. No correction was added to the measured angle of shearing resistance to correct for dilation along the uneven surface.

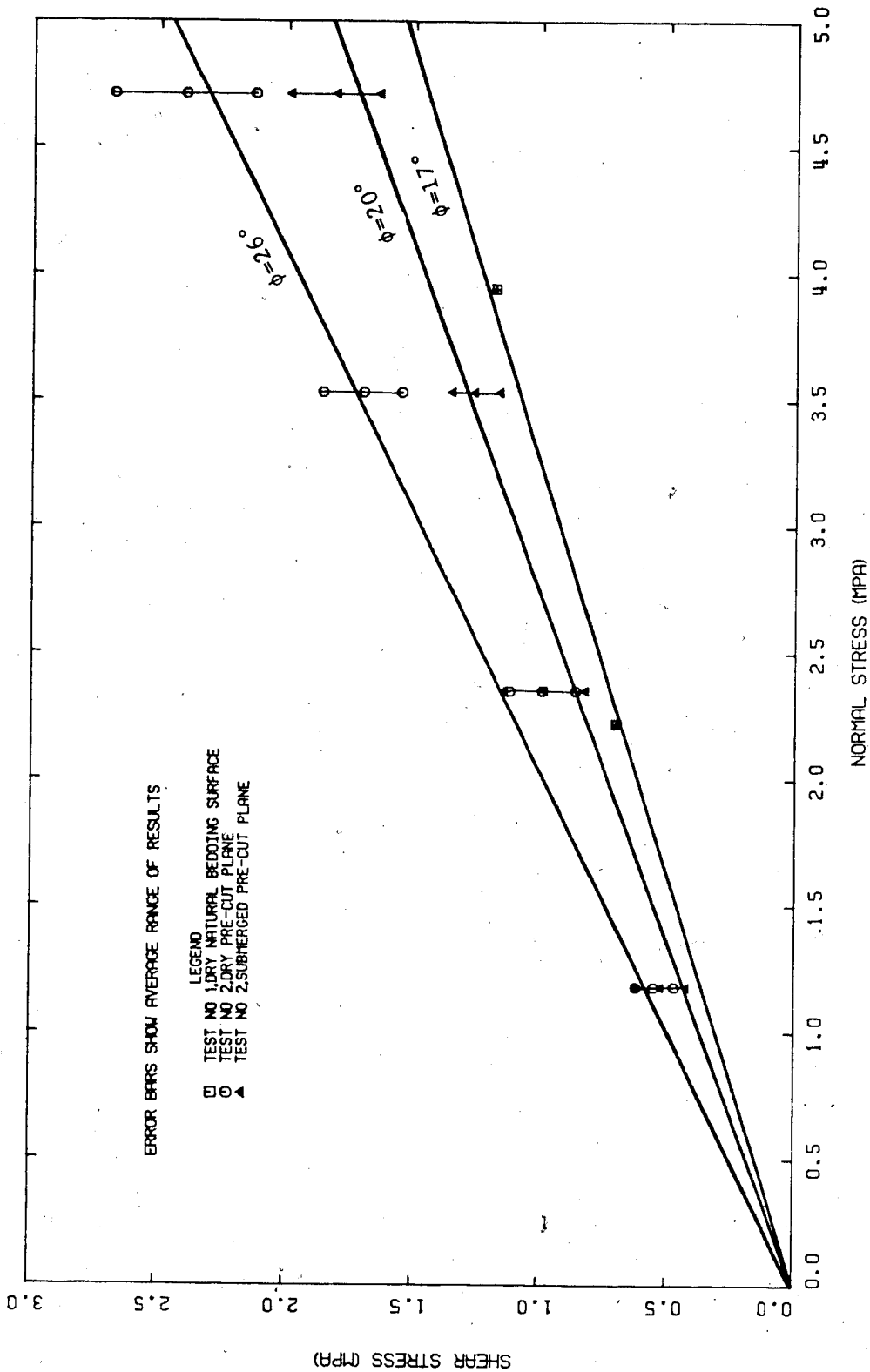


Figure 3.1 Mohr Envelope for Direct Shear Tests on Bearpaw Formation Siltstone

The direct shear tests were conducted independently by Mr. F. M. Lieu, a visiting student from the Republic of China. The test results represent two samples from a massive siltstone bed, and may not be representative of the shear strength in shale beds with a higher clay content. Difficulties in sample preparation and testing indicate the results should be viewed with caution. Drying and cracking of the samples during preparation resulted in alteration of the rock properties. Binding of the samples on the walls of the upper half of the shear box was observed, and indicates that the actual applied normal force at the shear plane may be lower than assumed.

3.3.4 High Pressure Triaxial Tests

3.3.4.1 Test Equipment

High pressure triaxial tests were conducted in the Department of Mineral Engineering at the University of Alberta, using a 600,000 lb (2.67 MN) MTS servo-controlled stiff testing machine. The MTS system as shown in Plate 3.1 is equipped with a programmable function generator capable of generating a variety of load functions. Only the ramp load function was used in the present test program. An internal LVDT and load cell for measuring axial displacement and load respectively are incorporated into the system.

Samples of NX size core (5.40 cm \emptyset x 10.8 cm long) were tested using the Hoek-Franklin triaxial cell (Hoek and

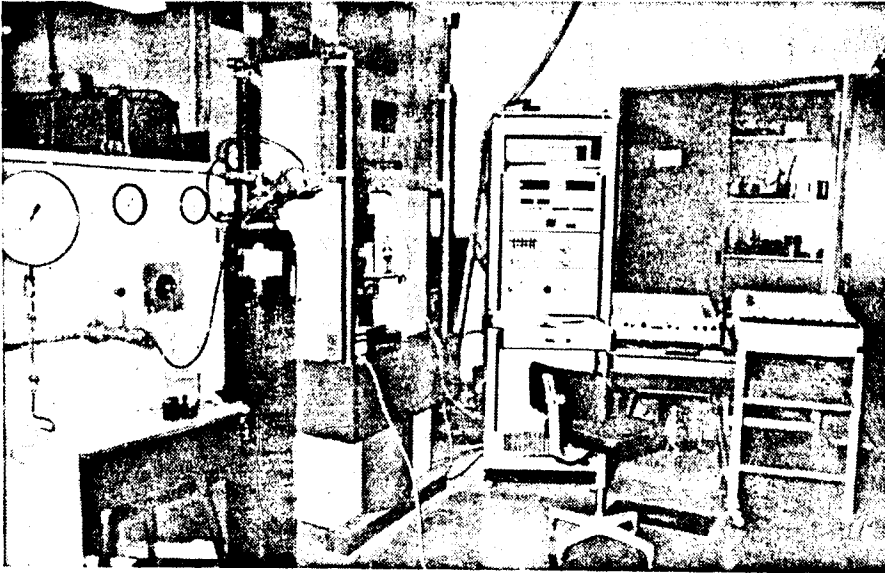


Plate 3.1 MTS Test Frame with 14 MPa Pressure System

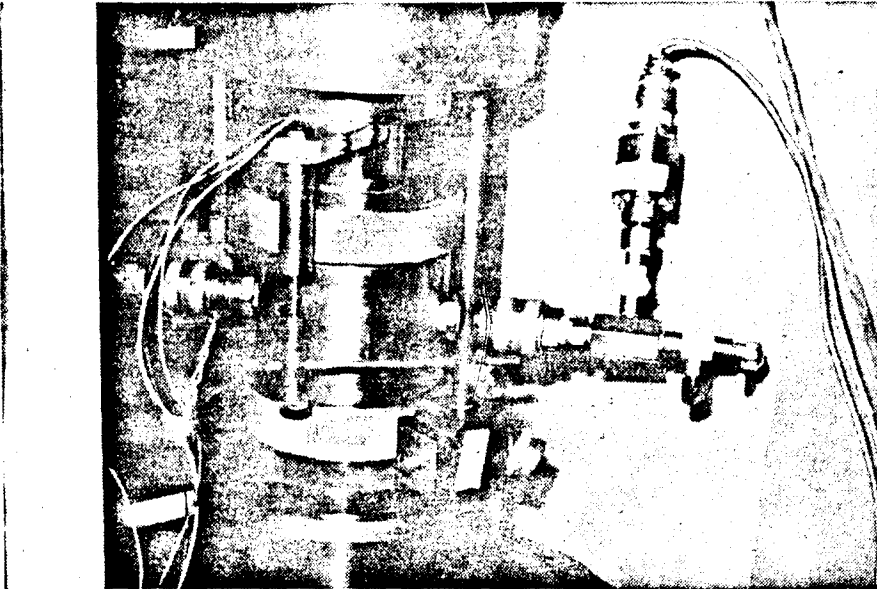


Plate 3.2 Hoek Cell in Test Frame with Pressure Transducer and L.V.D.T.

Franklin, 1968, Franklin and Hoek, 1970). Features of the cell which make it particularly suited for performing rapid triaxial tests on rock are the incorporation of an adiprene rubber sealing sleeve in the cell. The rubber sleeve seals the hydraulic oil from the sample and allows the removal of the sample from the cell without draining the hydraulic fluid at the end of a test. The durability of the sleeve allows multiple reuse. Plate 3.2 shows the triaxial cell in the MTS load frame during a test. The two ports at the sides of the cell are connected to the hydraulic pressure system and pressure transducer respectively.

The pressure system was capable of generating 13.8 MPa cell pressure. A nitrogen bottle, initial pressure about 17 MPa, provided the gas pressure, which was regulated at the bottle, with a standard 0-17.2 MPa regulator, and a second gas pressure regulator (Hooke Type) on the console board. (Plate 3.1, left hand side). A hydraulic accumulator converted nitrogen pressure to fluid pressure. Cell fluid pressure was measured on the console with a 0-2000 psi (0-13.8 MPa) Budenberg Gauge.

Two X-Y recorders were used during the tests to continuously plot axial load vs axial displacement and axial load vs cell pressure. A Fluke model 2240 B data-logger with paper tape and a Techtron model 8410 cassette recorder were used to record cell pressure, external LVDT and internal MTS-LVDT displacements, MTS axial load, and time during each test. Data from the LVDT's, load cell and pressure

transducers was recorded as a voltage. Test data recorded on the magnetic cassette tapes was transferred into storage files on the university computer, and converted into the respective units of stress, strain, etc. through use of Fortran programs.

3.3.4.2 Sample Preparation and Description

Two sets of four samples, (5.40 cm diameter x 10.8 cm long) were prepared from two 70 cm long sections of 14.3 cm diameter core obtained from the 7 m long horizontal drill hole at the 91 m level. The 14.3 cm diameter core used for the triaxial samples was obtained from a depth of 4 to 5 metres from the shaft wall, well beyond the zone influenced by blasting. The NX size samples were drilled with a portable commercial concrete diamond drill using a single barrel diamond core barrel. Compressed air was used to flush cuttings away from the diamond bit, to minimize the disturbance of the samples, the 14.3 cm \emptyset core was oriented and clamped on the drill table such that the bedding planes were vertical, or parallel to the cylindrical axis of the NX core. The ends of the samples were cut normal to the cylindrical axis in a diamond saw, also using air to flush cuttings. Samples were sealed in plastic bags and stored at room temperature until testing. Samples for moisture content determination were taken from the remains of the 14.3 cm \emptyset cores.

An attempt was made to use bonded strain gauges on samples of triaxial tests No.1-4, to measure simultaneously axial and circumferential strain. Several types of two-component epoxies, from fast to slow curing, were used to bond gauges to the samples. In all cases the gauges failed to bond to a clean surface. It appears moisture migration within the samples prevented bonding of the gauges to the samples.

All samples were dark grey massive siltstone with an average initial moisture content between 6.7 and 7.2 percent. Samples tended to form small irregular surface cracks after being uncovered for short periods at room temperature. Longer exposure produced continuous cracks along bedding planes. Table 3.3 presents the initial properties of the triaxial samples.

3.3.4.3 Test Procedure

The two main objectives of the triaxial testing program were: a) to determine the peak and ultimate strength of the samples in triaxial compression, and b) to determine the modulus of deformation of the rock under triaxial compression as a function of loading rate. To achieve these objectives testing was divided into two series of 4 samples each. The first series of triaxial tests, (Samples 1-4) were conducted using the procedure outlined by Kovari and Tisa, (1975) classed as the Multiple Failure State Test. In this test, several points are determined for both the peak and

Table 3.3 Initial Properties of Triaxial Test Samples

Sample No.	Height [cm]	Diameter [cm]	Volume [cm ³]	Weight [g]	Moisture Content [%]	Bulk Density $\frac{\gamma}{\text{g/cm}^3}$	Initial Saturation [%]	Atterberg Limits			
								WL [%]	WP [%]	IP [%]	
1	10.44	5.22	223.42	552.0	7.2	2.47	2.29	100	48.2	24.7	23.5
2	10.65	5.27	232.28	556.5	7.2	2.43	2.26	89.5	49.4	27.2	22.2
3	10.49	5.27	228.79	553.4	7.2	2.42	2.25	87.9	48.5	29.2	19.3
4	10.63	5.24	229.29	562.5	7.2	2.45	2.27	96.6	47.5	28.1	19.4
5	10.57	5.28	231.48	560.2	6.7	2.42	2.27	81.6	48.1	27.2	20.9
6	10.60	5.29	232.97	565.2	6.7	2.42	2.27	81.6	46.0	23.9	22.1
7	10.53	5.31	233.19	560.9	6.7	2.40	2.25	77.9	45.4	20.8	24.6
8	10.55	5.31	231.00	556.7	6.7	2.41	2.26	79.7	50.7	21.2	30.5

$G_s = 2.79$ (from tests on direct shear samples)

ultimate failure surfaces in contrast to the conventional triaxial test where a single point is determined for the peak and possibly the ultimate failure surface. Basically the test is run like a conventional triaxial test, with a σ_3 applied and the sample sheared at a constant rate of axial strain. Tests 1-4 were run at a strain rate of 5.5×10^{-4} /sec. The two X-Y plotters described in Section 2.3.7.1 displayed the axial stress vs axial strain plot and σ_1 vs σ_3 plot. As a sample approaches failure, the σ_1 - ϵ_1 plot will show the inception of non-linear behavior. At this point in the test, σ_3 is rapidly increased, without stopping the test, to a higher value of σ_3 , and the test is allowed to continue. When the σ_1 - ϵ_1 plot again shows the beginning of non-linear behavior, σ_3 increased again. This procedure is repeated until the desired σ_3 for failure is reached, at which time the sample is allowed to fail. In the post-peak stress strain curve, the ultimate shearing resistance for a given cell pressure is reached when the shearing resistance remains constant with continued axial straining. At this point in the test, σ_3 may be increased or decreased, and the ultimate shearing resistance for the new σ_3 determined. Given sufficient remaining axial strain, the ultimate shearing resistance may be determined over the range of interest from a single sample. The σ_1 vs σ_3 plot provides a plot of the failure surface of the ultimate strength formed by the locus of points from the stepwise ultimate shearing resistance tests, and an estimate of the peak failure

surface from the several tests loaded to near failure in the pre-peak loading.

The second series of tests, (Samples 4-8) were conducted over the stress range to failure with constant σ_3 . Strain rates were maintained constant for a sufficient interval to define a linear stress-strain curve. Up to four strain rates were used in the elastic loading portion of each test. About 5 seconds were required to change the strain rate on the MTS. Dependence of the ultimate shearing resistance on strain rate was investigated in Tests 6, 7 and 8.

The effects of saturating a fractured but intact triaxial sample on the ultimate shearing resistance were investigated on Samples 6 and 8. Following peak strength testing, both samples were flooded under a back pressure of about 15 KPa for 48 hours, while remaining confined in the cell. Test results indicated the saturated samples were not sheared under drained conditions. As pore pressure measurements could not be made under the present set-up of the Hoek-Franklin cell, the results of these tests were difficult to interpret.

3.3.4.4 High Pressure Triaxial Test Results

Plates 3.3 and 3.4 show the mode of failure typical of the samples tested. Failure planes developed as a single continuous failure surface, with or without one or two secondary parallel failure surfaces. The angle between the

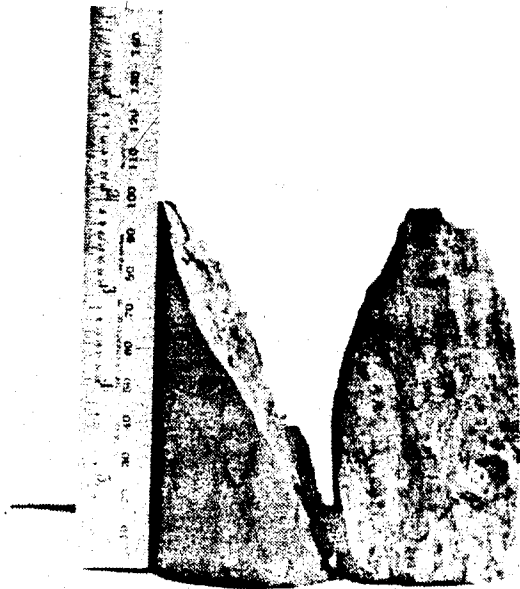


Plate 3.3 Triaxial Test Sample No. 4 After Failure

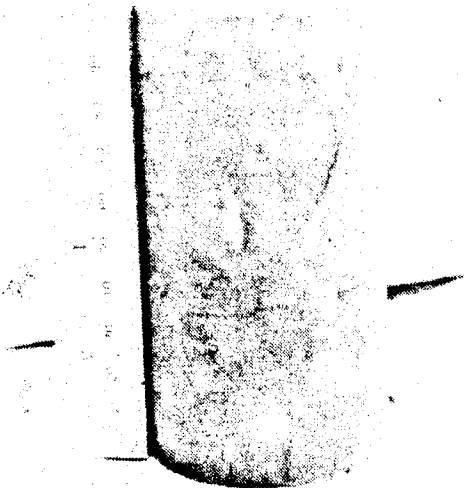


Plate 3.4 Triaxial Test Sample No. 7 After Failure

core axis and the failure plane varied from 25° to 30° .

The stress-strain and principal stress plots for the triaxial tests are presented in Appendix A (Figures A.1 to A.8). Notation on each plot indicates the cell pressure and strain rates applied over different parts of the tests. The principal stress plots show the loading-unloading relationship of each test.

Figure 3.2 shows the peak strength Mohr envelope plot for the eight tests. Tests 4 to 8 are each represented by a single point. The measured response for the Multiple Failure State Tests (MFST) shows a range of peak strengths. This range increases with increasing average normal stress. The success of running the MFST depends on the response of the operator, in increasing the confining pressure at the inception of non-linear behavior on the stress-strain plot obtained during the test. The marked non-linear response observed for the last point on tests 2 and 4, and the last 6 points on test 3, indicate the samples have started to yield. These points will lie somewhere between the stress space defined by the peak and ultimate failure surfaces for that sample. Care must be exercised in choosing a peak failure envelope for MFST data, to avoid using data points obtained when the sample was strained beyond peak. The findings of Kovari and Tisa (1975) on Buchberg sandstone and Carrara marble, indicated that there was negligible decrease in peak strength with increasing numbers of successive failure states produced from a single sample. This is not

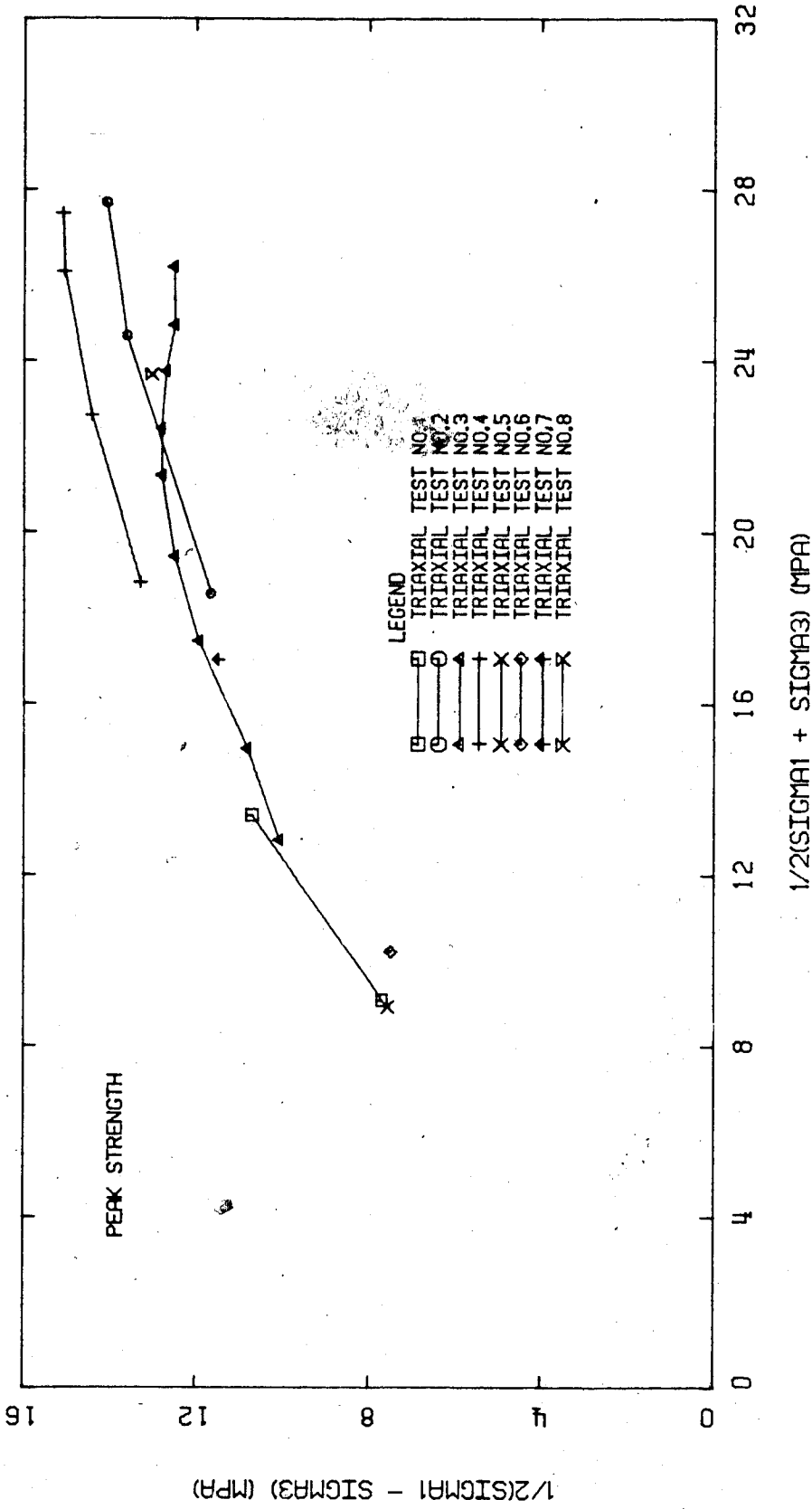


Figure 3.2 Plot of the Peak Strength Mohr Envelope for Triaxial Tests

directly applicable to the Bearpaw Formation siltstones.

Figure 3.3 shows considerable scatter in the ultimate failure envelope increasing with increasing confining pressure. As shown in Appendix A, the strain rates for Tests 1 and 4 were constant, while Tests 5 to 8 were conducted at various rates. Figure 3.4 shows the combined principal stress state plots for all of the tests. The influence of strain rate on the ultimate strength was investigated on Samples 6, 7 and 8 with each sample loaded at three different strain rates. Each sample was tested at a different confining pressure. The results of these tests are shown on Figure 3.5. Each sample showed a decrease in the ultimate strength with a reduction in strain rate. The comparison of the tests shown on Figure 3.5 should not be taken to indicate that the ultimate failure envelope becomes horizontal at low strain rates, but rather that the decrease in ultimate strength over a range of decreasing strain rates becomes more significant with increasing confining pressure.

The peak and ultimate failure envelopes can be defined in a number of ways. Hoek and Brown (1980) developed an empirical non-linear strength relationship between the principal stresses at failure, given by equation 3.1.

$$\sigma_1 = \sigma_3 + \sigma_c \sqrt{\frac{M \cdot \sigma_3}{\sigma_c} + S}$$

Eq. 3.1

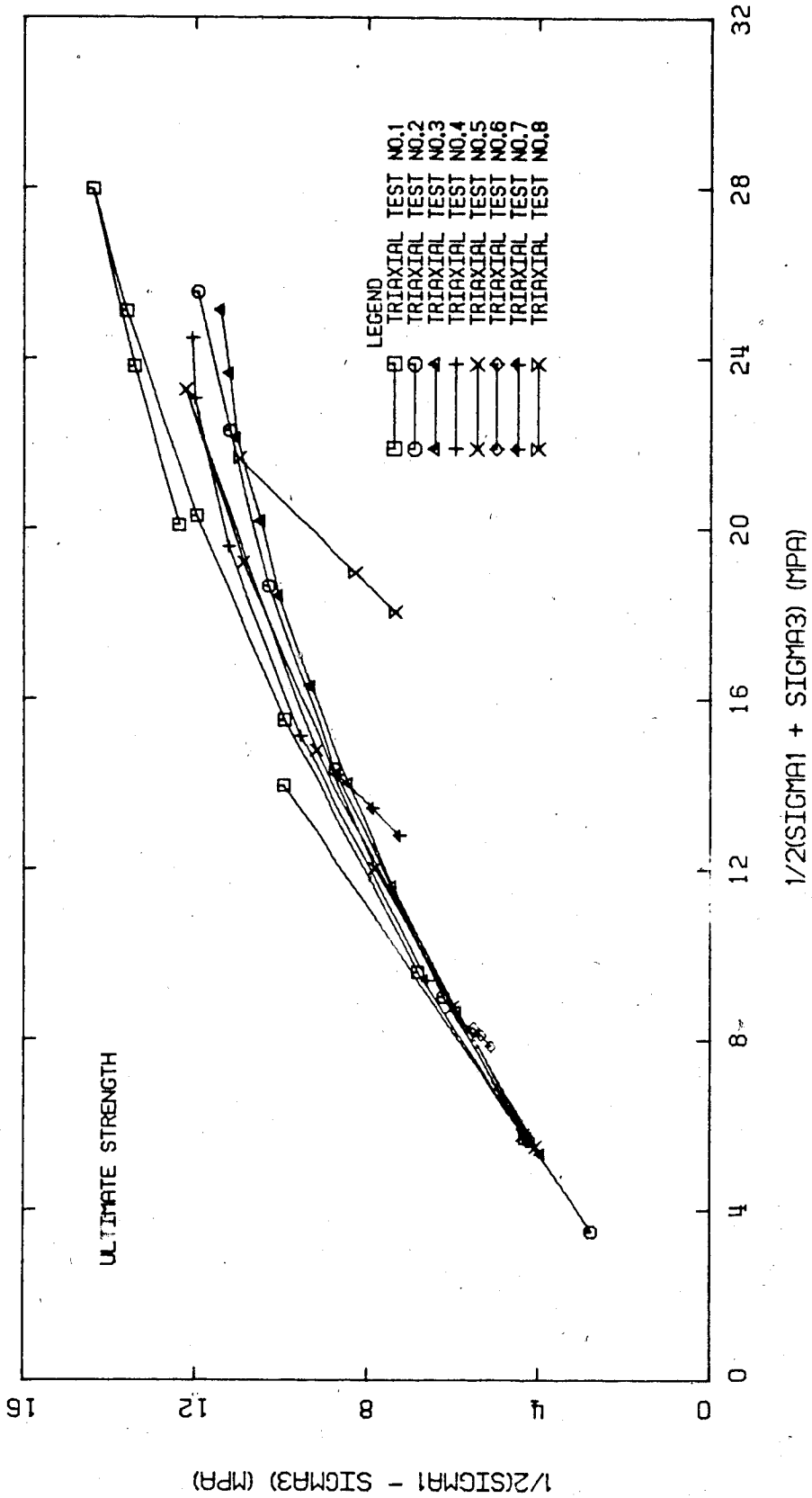


Figure 3.3 Plot of the Ultimate Strength Mohr Envelope for Triaxial Tests

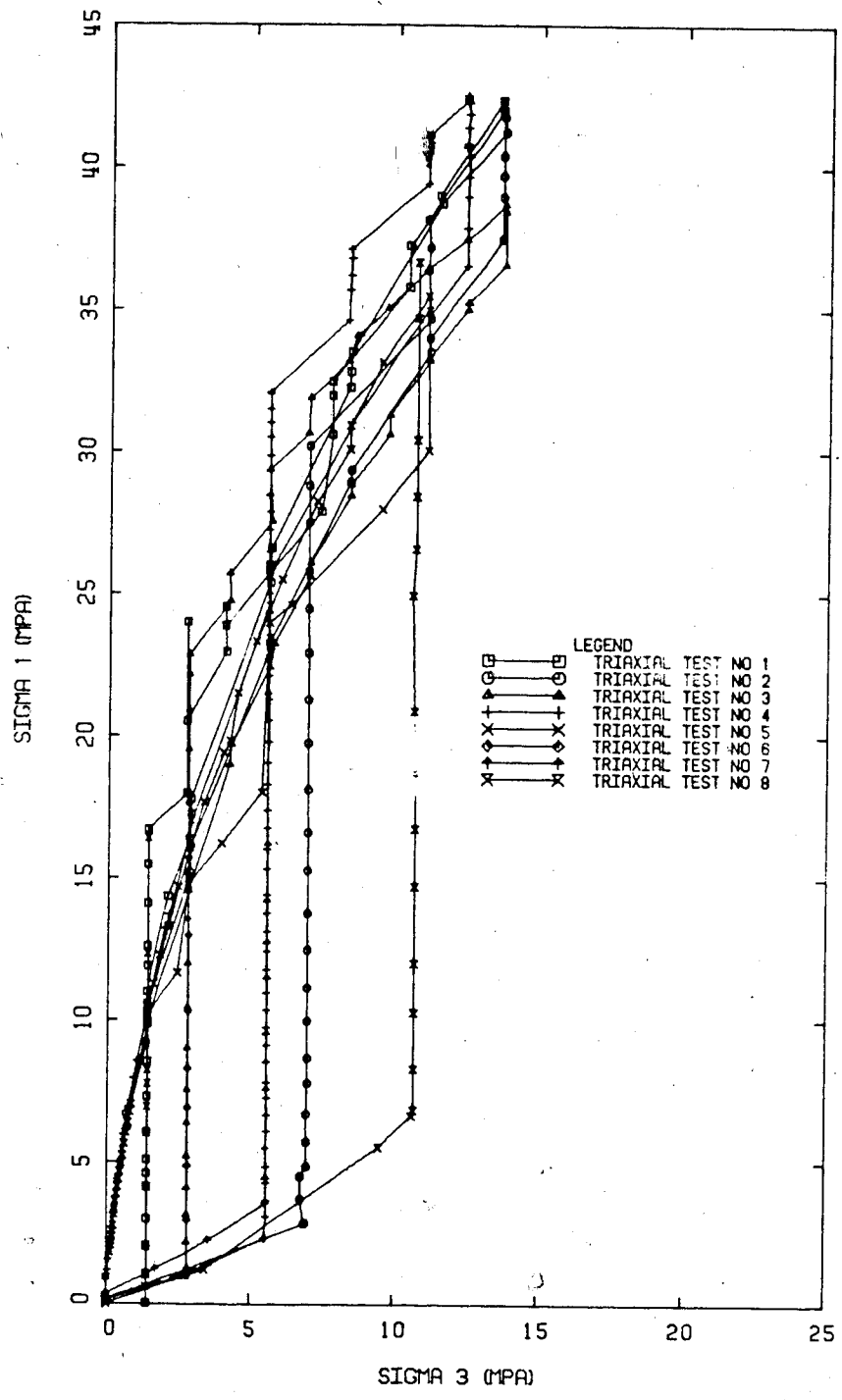


Figure 3.4 Plot of Axial Stress vs Confining Stress for Triaxial Tests

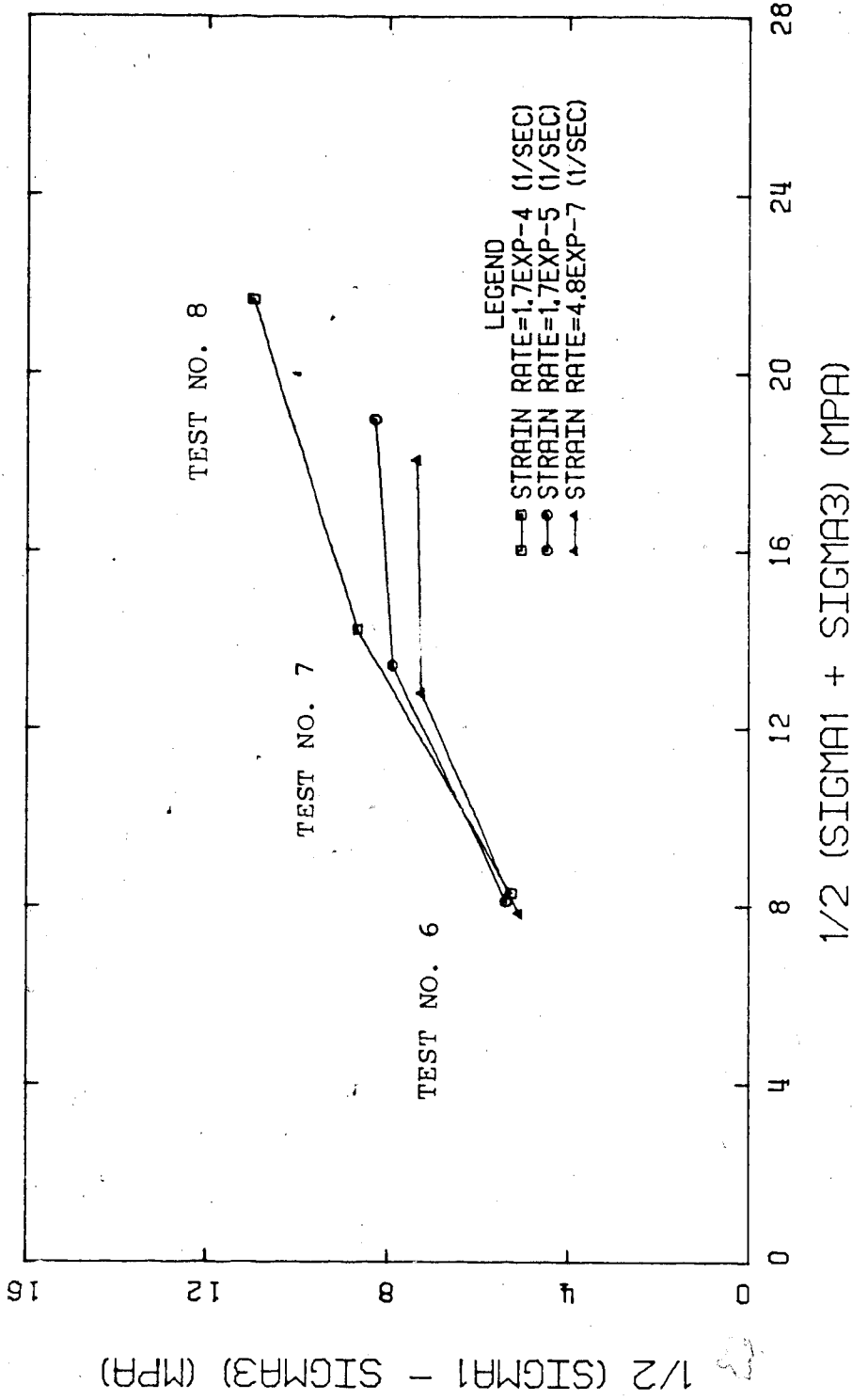


Figure 3.5 Plot of the Ultimate Strength Mohr Envelope for Triaxial Tests Showing Dependence of Ultimate Strength on Strain Rate

where

σ_1 = the major principal stress at failure

σ_3 = the minor principal stress at failure

σ_c = the uniaxial compressive strength of the intact rock

m & s are constants which depend on the rock properties

Figure 3.6 presents the Hoek and Brown (1980) relationship fitted to the triaxial test data. The points on the curve corresponding to estimated peak were obtained by increasing the value of σ_3 measured for the initial yielding for the MFST, to an estimated σ_3 , which would occur if the sample were allowed to fail at that confining pressure. Equations 3.2 and 3.3 describe the selected peak strength and ultimate strength relationships, respectively, for the samples tested.

$$\sigma_1 = \sigma_3 + 12 \sqrt{\frac{7\sigma_3}{12} + 1} \quad \text{Eq. 3.2}$$

$$\sigma_1 = \sigma_3 + 12 \sqrt{\frac{3.5\sigma_3}{12} + 0.01} \quad \text{Eq. 3.3}$$

where σ_1 and σ_3 are in MPa.

Figure 3.7 presents the pre-failure portion of the deviatoric stress-strain curve for the eight triaxial tests. The strain rates for Tests 1 to 4 were constant throughout the tests at 5.5×10^{-6} /sec. The modulus of elasticity

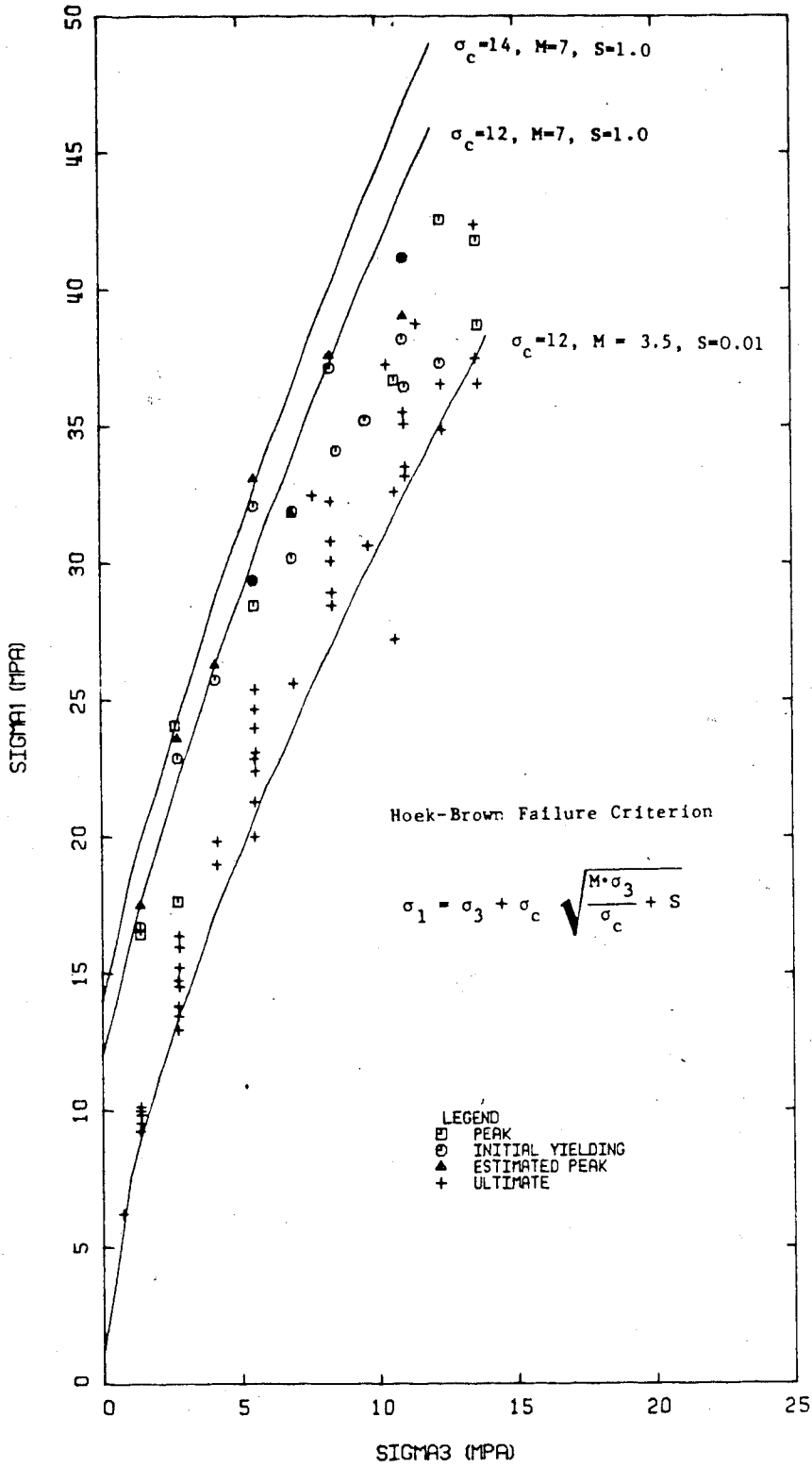


Figure 3.6 Principal Stress Plot Showing Hoek-Brown Failure Criterion Fitted to Triaxial Test Data

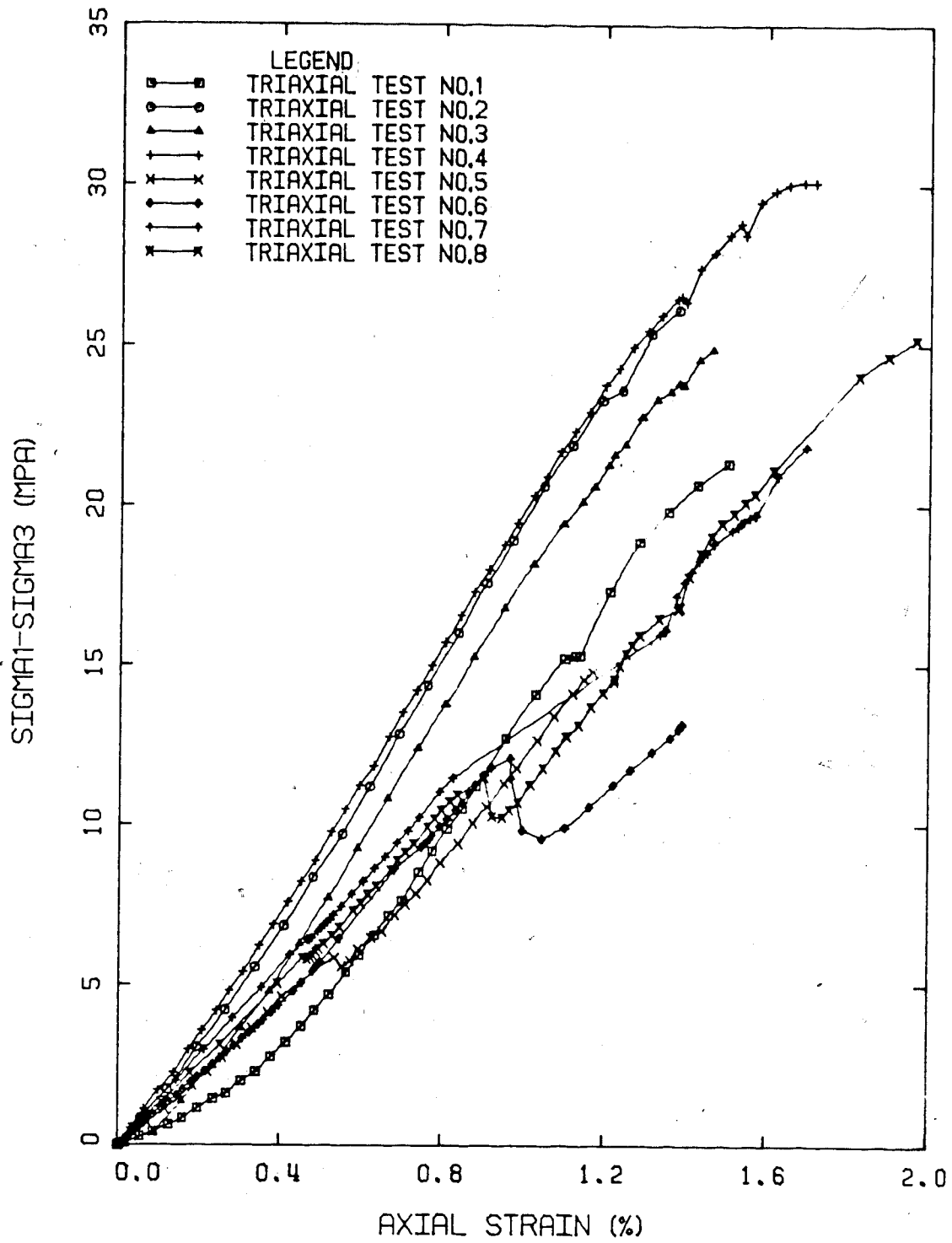


Figure 3.7 Combined Plot of Deviatoric Stress vs. Strain for all Triaxial Tests

obtained from Tests 1 to 4 ranged from 1.9 to 2.1 GPa, with Samples 2, 3 and 4 showing a very similar response on the deviatoric stress-strain curve. The initial strain stiffening behavior of Sample No.1 may reflect closure of micro fractures during the initial stages of loading. Tests 5 to 8 were conducted as variable strain rate tests. The axial strain rate was varied between 4.8×10^{-4} to 1.7×10^{-4} strain/sec. The modulus of elasticity measured in these tests ranged from 1.1 to 1.7 GPa. Figure 3.8 shows a plot of the tangent modulus of elasticity of the eight tests vs strain rate. The plot shows two opposite trends for the variable strain rate tests. A decrease in stiffness with increasing strain rate is shown for tests 5 and 8, whereas tests 6 and 7 show an increasing stiffness with increasing strain rate. Bieniawski (1970) has shown that a higher strain rate before failure results in a higher modulus of elasticity. This is generally observed when identical samples are tested under different but constant strain rates to failure. In variable strain rate tests, the load history significantly influences the stress-strain behavior at any instant in time. The tangent modulus as determined from the initial loading state of Tests 1 to 4 (tested under constant strain rate) showed an increase in the tangent modulus with increasing confining pressure, as shown on Figure 3.8.

The secant modulus dependence on strain rate is shown on Figure 3.7. Tests 2 to 4 show relatively little secant modulus dependence on confining pressure. The nonlinear

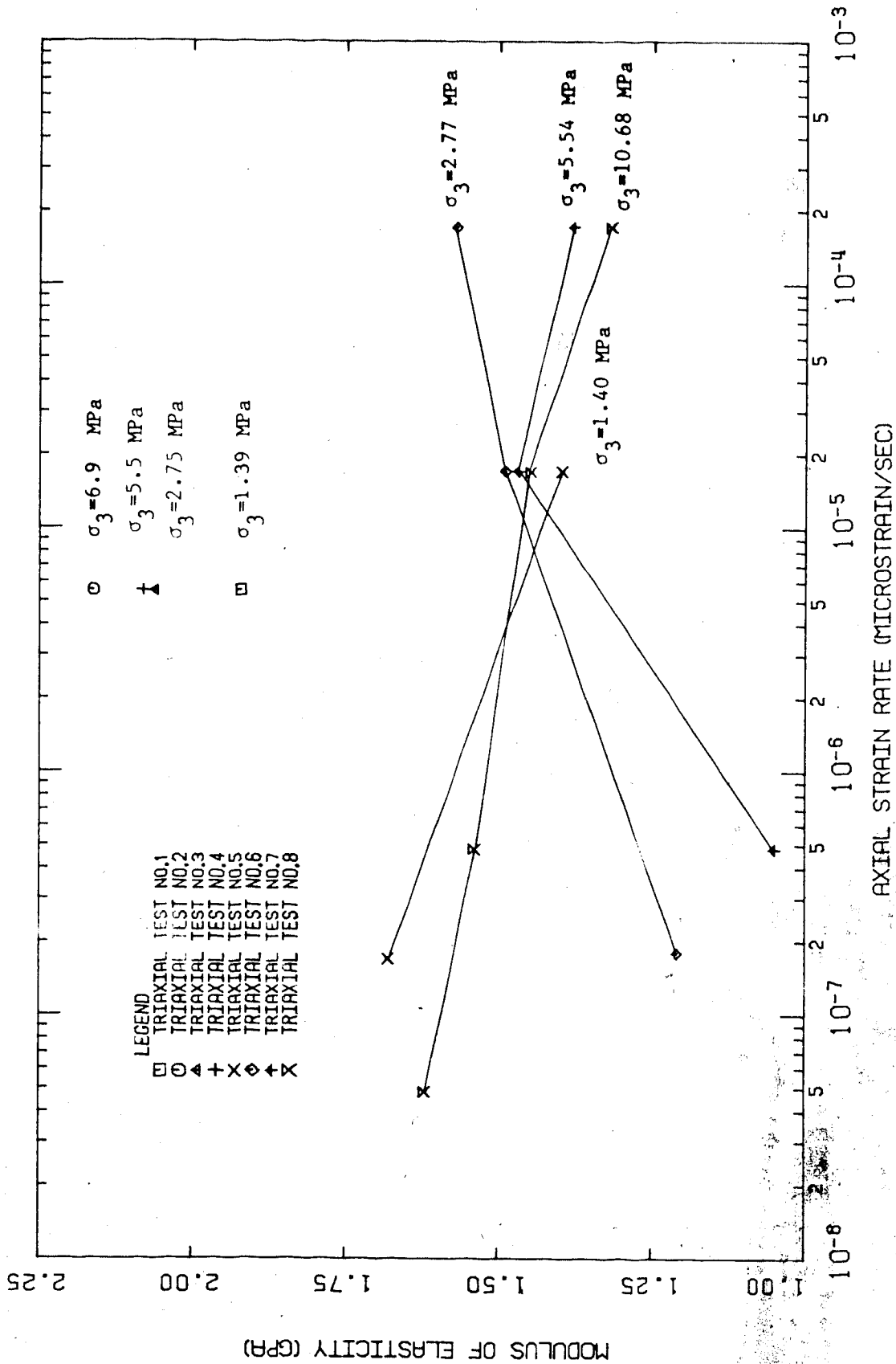


Figure 3.8 Plot of Modulus of Elasticity vs. Log of the Axial Strain Rate for Triaxial Test Data

behavior of Test 1 reflects the initial nonlinear seating of the sample and the nonlinear strain experienced at the end of the first loading stage. The variable strain rate tests, Tests 4 to 8, show a secant modulus dependence on strain rate. A change in strain rate during a test results in an increase or decrease in the secant modulus depending on whether the strain rate was increased or decreased, respectively. For example, Test 6 showed a significant decrease in the secant modulus when the strain rate was reduced from 1.75×10^{-5} microstrain/sec to 1.8×10^{-7} . The strain rate dependence of the secant modulus has not been determined quantitatively for the present analysis.

4. SHAFT CONSTRUCTION AND INSTRUMENTATION

4.1 Introduction

The Number One shaft at the Kipp mine was sunk between February and November of 1980 to a depth of 235 m using conventional sinking and lining methods. Instrumentation was installed at three depths (110, 152 and 180 m) in the Bearpaw Formation to measure:

- radial rock mass displacements,
- stress changes in the rock mass during sinking,
- tangential strains in the concrete lining, and
- water pressures at the rock/lining interface.

4.2 Shaft Construction

The shaft is a 4.32 m finished diameter circular shaft with a cast in place concrete lining. The surficial deposits were excavated using backhoe, clamshell and pneumatic chippers in order of increasing depth below the surface. Below about 8 m depth, the loosened material was loaded into muck buckets by a Cryderman clam, a pneumatic clamshell excavator suspended from a hoist cable and anchored to the shaft wall. When excavation using the mechanical chippers became too difficult, the drill and blast method was used. Each blast took approximately one half of the full shaft bottom in a 1.8 to 2.4 m deep bench. East and west benches were blasted alternately, with each blast followed by a

mucking period to remove the rubble. Progress of sinking and lining of the shaft through the Bearpaw Formation is shown on Figure 4.1. Shaft construction followed a schedule of 10 working days and 4 resting days. The concrete for the lining was obtained on demand from a local cement company and mixed to the specifications given in Table 4.1. The shaft lining schedule is shown on Figure 4.2.

The lining form consists of a segmented steel ring bolted together in 0.76 m high sections. Any number of sections could be bolted together to give the desired height of pour. The top and bottom rings have special features to permit the stage-wise downward construction of the lining. The lower ring or curb ring has an outside ledge through which six equally spaced vertical (25 m) threaded rebar rods are bolted. These rods, suspended from threaded rebar couplers in the previous pour, initially carry the entire weight of the form, plus concrete. Sand bags and boards supported by removable steel bars, are placed over the gaps between the curb ring ledge and the shaft wall to stop concrete loss during pouring. The upper ring or match ring has an expanded upper edge to allow concrete to be poured to fit with the bottom of the previous pour. During the sinking of the Kipp No. 1 shaft, a minimum of two sections were used through the till to give a 1.52 m high pour. Where unstable sand lenses were encountered within the till, the normal procedure of exposing 2 to 3 metres of self supporting till was abandoned in favour of using forepoling, and

Table 4.1 Specifications of Concrete Used for Casting
the Shaft Lining

Components for 1.m ³ of concrete	
Cement Type:50	340 kilograms
20 mm Aggregate	806 kilograms
10 mm Aggregate	268 kilograms
Concrete Sand	854 kilograms
Mix Proportion	1:2.51:3.16
(cement:fine aggregate:coarse aggregate)	
Water	114 kilograms
W/C Ratio	0.34
Average Unit Weight	23 kN/m ³
Average 28 day strength 35 MPa	
Not Air Entrained, No Admixtures	

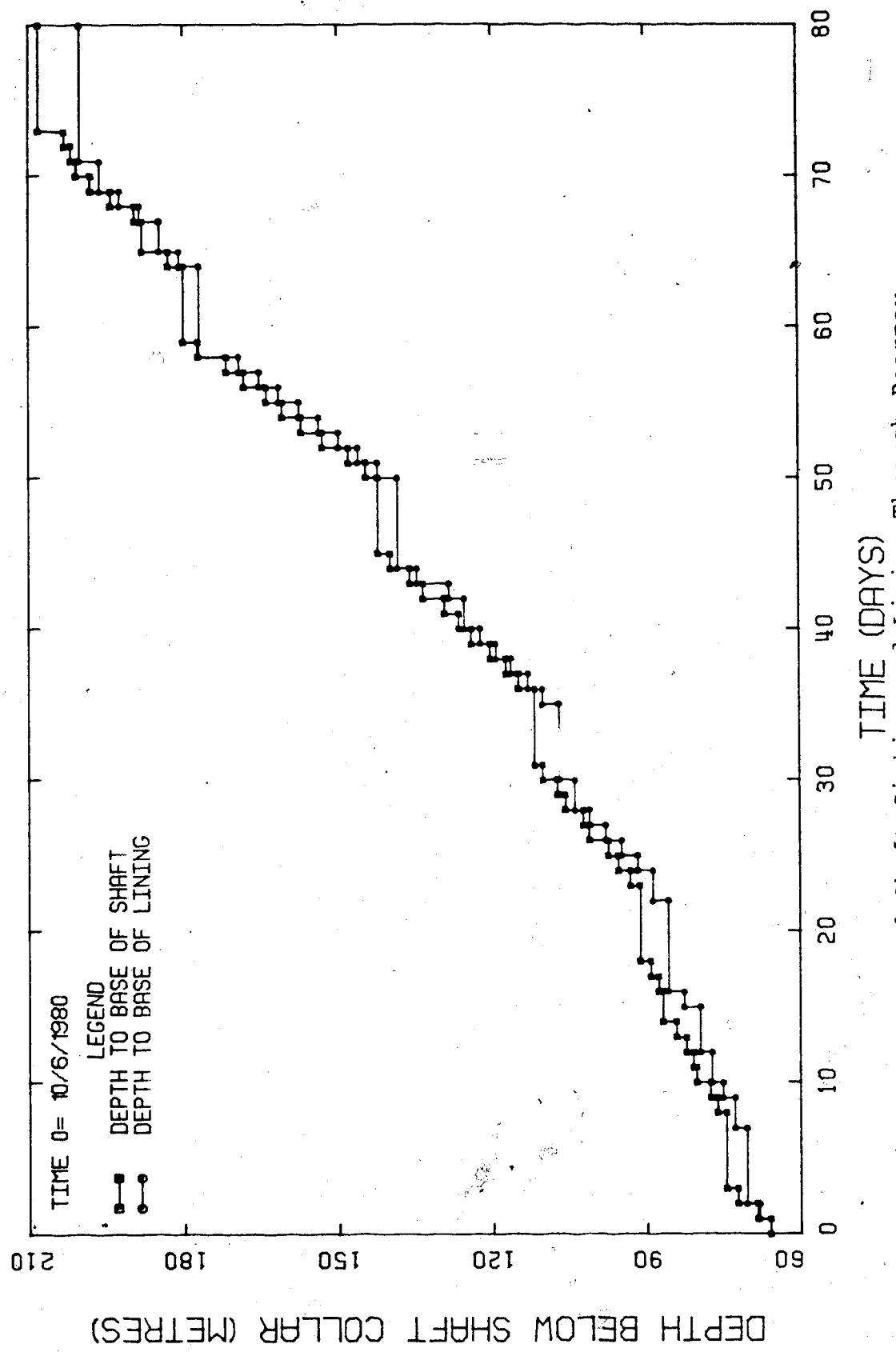


Figure 4.1 Log of Shaft Sinking and Lining Through Bearpaw Formation

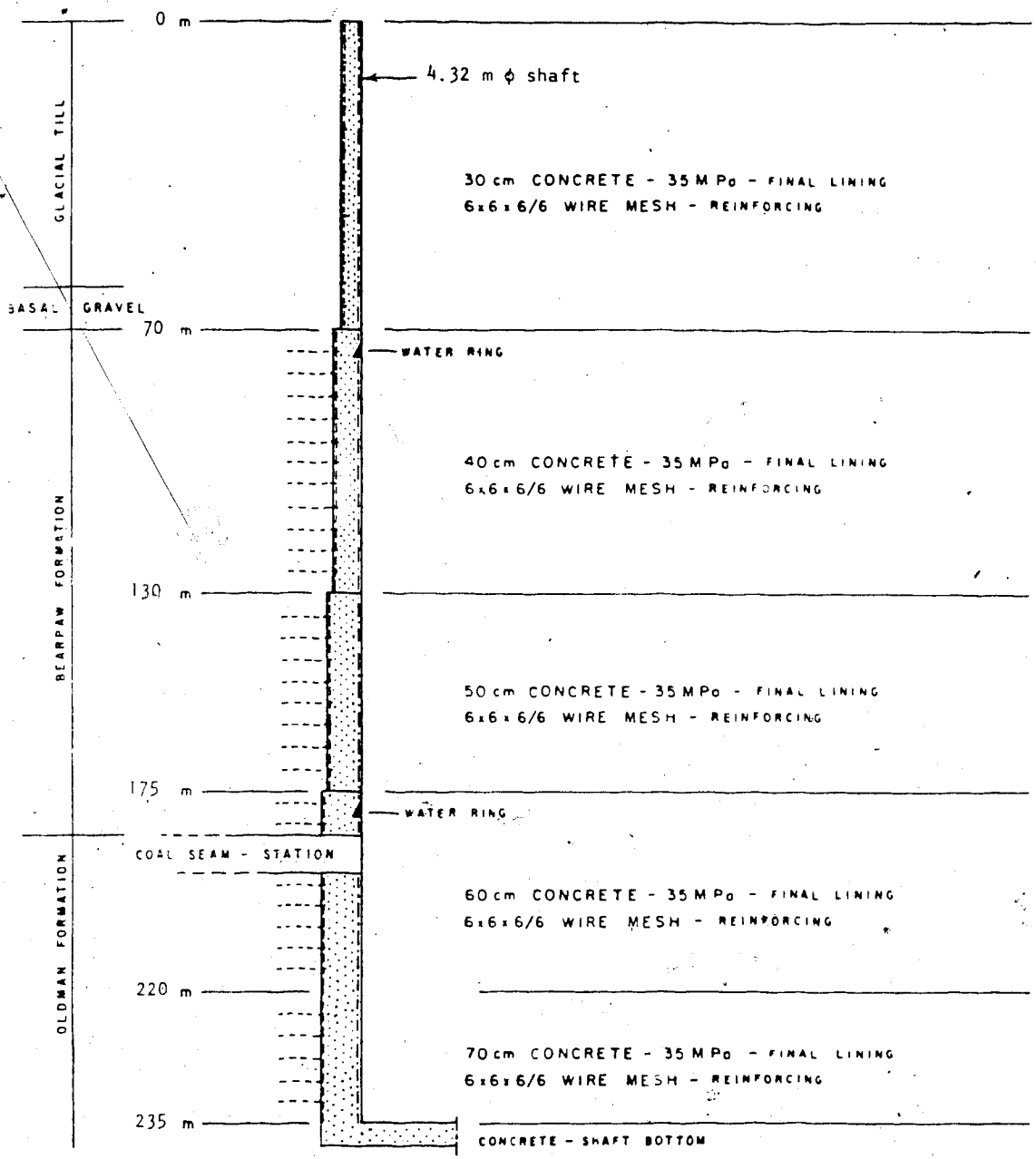


Figure 4.2 Shaft Lining Schedule, Lethbridge Coal Project (after T.M.C.C., 1980)

backsheeting to wall off the sand. Rebar reinforcement was used to hold the backsheeting in place, and the lining was poured as close to the bottom as possible to prevent wall collapse. In the lower section of the till, 2.3 m high pours were used and 3.05 and 3.81 m high pours were used as the shaft sinking progressed through the Bearpaw Formation. The higher the lift poured, the faster the overall progression of shaft sinking. When single pours reached heights of 3.05 and 3.81 m the pour was made in three lifts to ensure the concrete was adequately vibrated to avoid formation of honeycomb structure which would lower the concrete strength. Work during the lining operation was managed from the three deck galoway stage. Concrete was lowered in a hopper bucket and placed behind the forms through a large rubber funnel. While steady shaft sinking was in progress, concrete was being poured once a day. When loose ground conditions were encountered, a 15 cm square wire mesh reinforcement was placed about 15 cm inside the form. Vibration of the concrete was relatively uniform over the width of the lining, thus producing a relatively uniform concrete.

With the continuous cycle of sinking and lining, the height of exposed rock was always less than about two shaft diameters, or about 10 m, and for normally less than 8 hours. Usually the sinking proceeded only to a depth where enough wall was exposed after the last blast to lower the forms and pour the lining. By keeping the lining close to the shaft bottom, temporary support to protect the men from

falling rock was not required.

Where overbreak occurred either from blasting or subsequent slabbing and spalling, the thickness of the lining was increased.

4.3 Shaft Instrumentation

4.3.1 Introduction

The prime objective of the shaft instrumentation and the *in situ* testing program was to evaluate the response of the Cretaceous bedrock to conventional shaft sinking methods and to document the performance of the cast in place concrete lining. To achieve this goal the field program had six objectives:

1. To measure the *in situ* stress field using the U.S.B.M. deformation gauge and the overcoring technique;
2. To install borehole stressmeters in the wall rock ahead of the face to measure the stress change associated with advancing shaft;
3. To install horizontal multipoint borehole extensometers close to the shaft bottom to measure radial convergence associated with shaft advancement;
4. To install embedment gauges in the concrete lining to measure tangential strain resulting from the rock/lining interaction;
5. To install piezometers behind the lining to measure

- water pressures at the lining/rock interface; and
6. To obtain core samples for index testing and laboratory testing to determine the shear strength and elastic properties of the rock.

This section includes a description of the shaft instrumentation program.

4.3.2 Drilling Equipment

A Boyles Brothers J.V.A. air driven underground drill provided by TMCC was suitable for drilling, and met coal mines safety regulations. The J.V.A. drill has a twin-vee air driven motor, operated from the shaft air supply. The combined features of the J.V.A. drill, including an A.W. rod chuck, mechanical feed screw, variable speed gear box, and a separate water swivel, made it particularly suited for the overcoring operation.

With the varied testing and instrumentation requirements of the program, a selection of drill rods and bits was required. Experimentation with drill bits, hole reamers, rods and rod stabilizers, allowed the optimization of the drilling rate and drill hole quality.

4.3.3 Instrumentation and Testing Locations

The geotechnical investigation of the shaft was organized to coincide with the bi-monthly four day rest periods. The research budget allowed for four weekends of testing and installation. The planned instrumentation and

testing program for each weekend was ultimately modified as slow drilling progress, and drilling equipment and instrument failures consumed precious time. Figure 4.3 shows the locations of the four levels of instrumentation and the overcoring tests.

The initial stage of the investigation was conducted between June 29, 1980 and July 1, 1980 with the shaft base at a depth of about 91.3 metres. Work completed during this period consisted of five overcoring tests in a single horizontal borehole. The overcoring program is described in Section 5.3.

The second period of investigation was conducted between July 11 and 14, 1980, with the shaft base at 111.7 metres depth. Three horizontal multipoint borehole extensometers were installed at a depth of 111.4 metres. Each extensometer had five anchor points extending from 1.5 metres to 10.7 metres from the shaft wall as shown on Figure 4.4. Sixteen vibrating wire embedment strain gauges were placed in the concrete at depths of 108 and 109 m, during the first concrete pour following the work period on July 15, 1980. Figure 4.5 shows the location of the embedment gauges.

The shaft base was at a depth of 142.2 metres on the third work period between July 25 and 28, 1980, when seven vibrating wire borehole stressmeters were installed at a depth of 152.2 m in three steeply inclined boreholes. The instruments were located between 1.2 m and 2.7 m from the

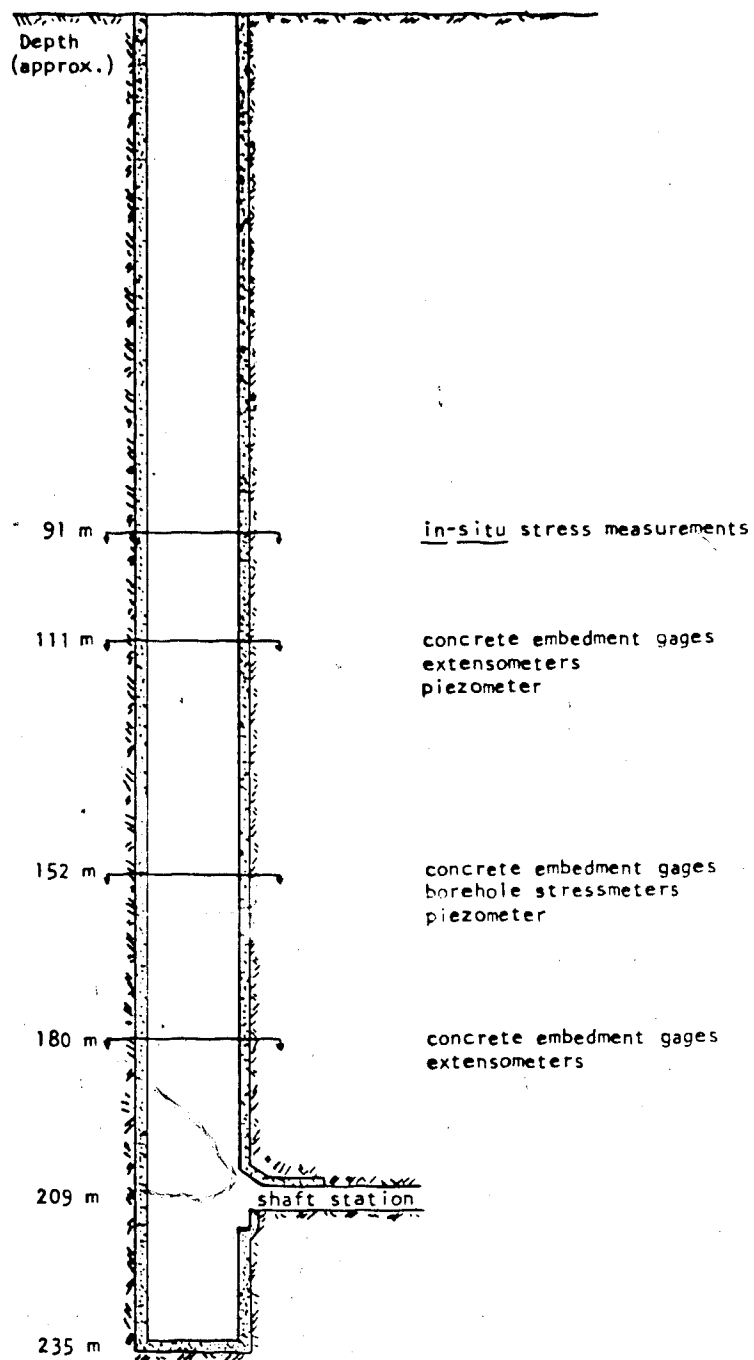


Figure 4.3 Cross-section of Shaft Showing Locations of Instrumentation and Testing

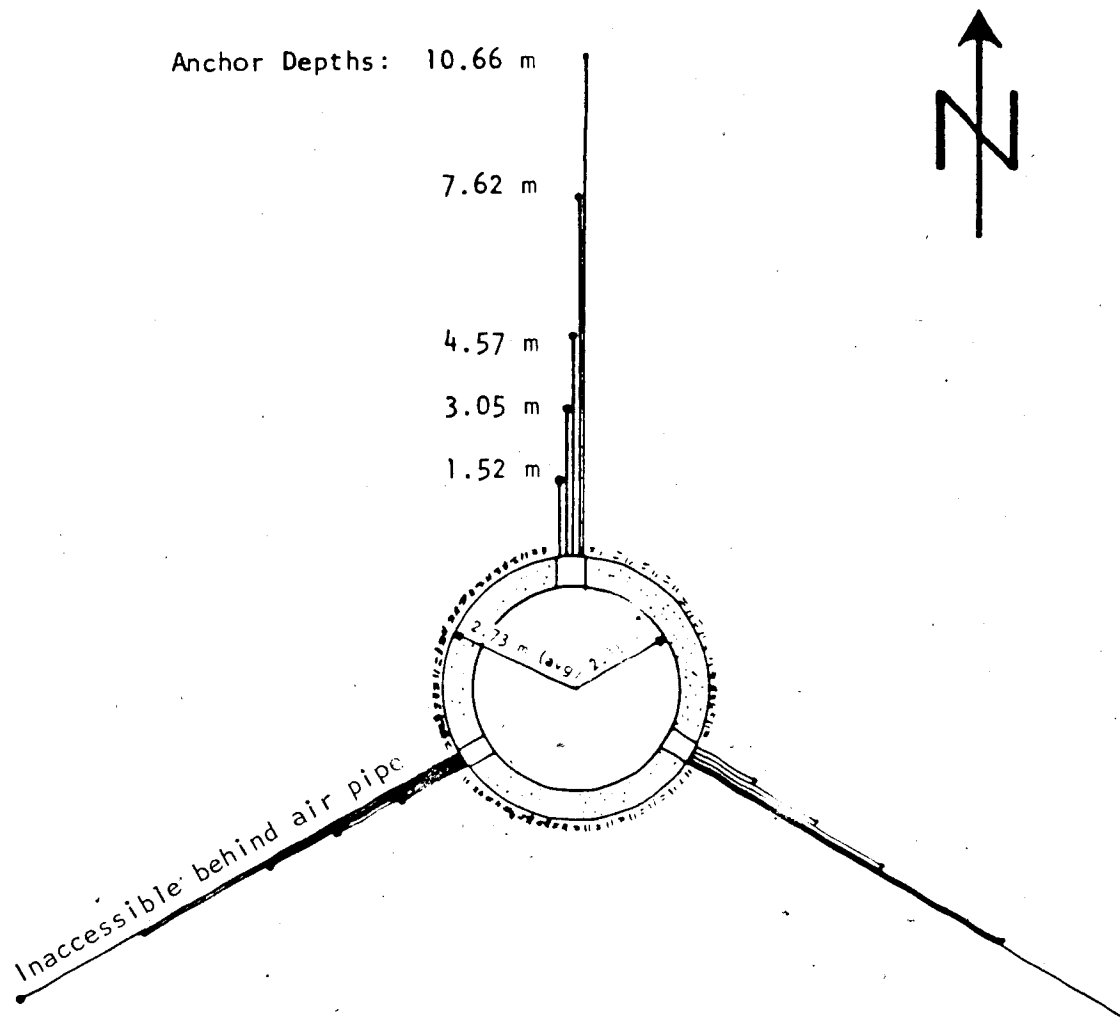


Figure 4.4 Plan View of Extensometers at 111.3 m Depth

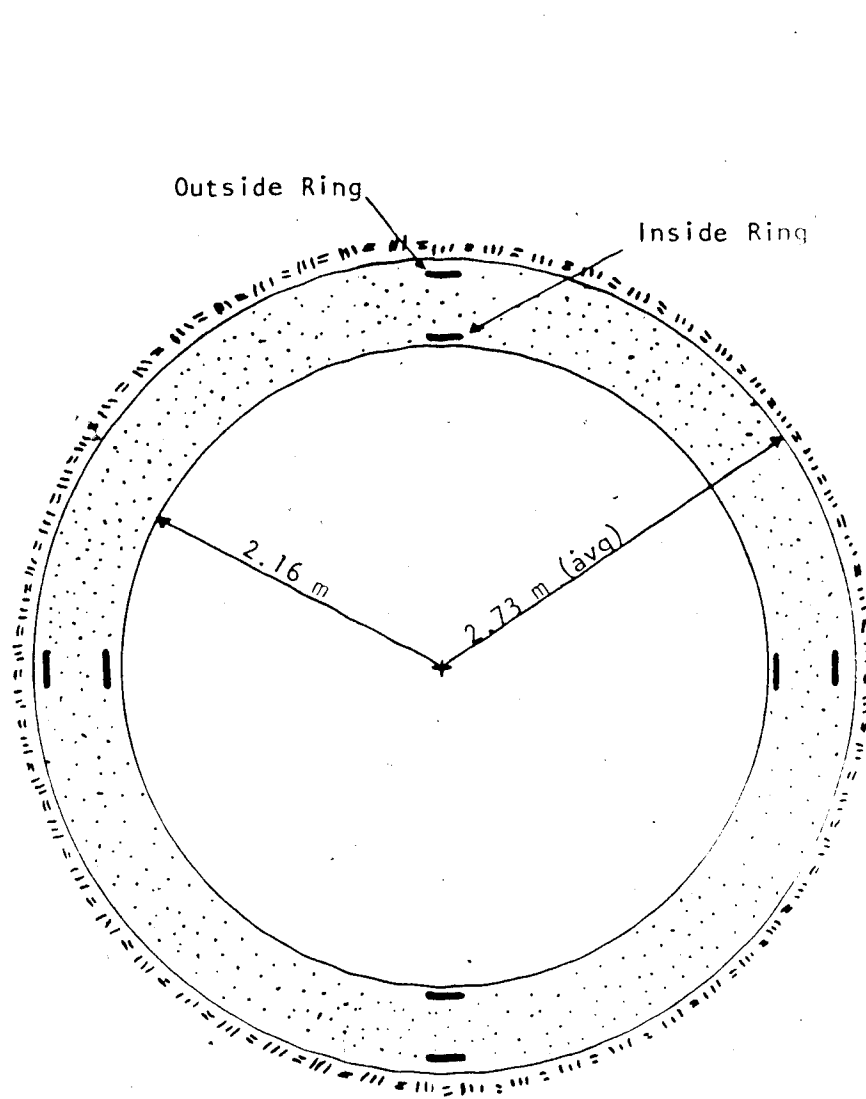


Figure 4.5 Plan View of Embedment Gauges at 108 and 109 m Depth

shaft wall, as shown on Figures 4.6 and 4.7. Eight vibrating wire embedment strain gauges were installed in the concrete lining at the 152 m depth on August 2, 1980, when the lining for that section of shaft was being poured.

The lowest level of instrumentation was installed at a depth of 179.8 metres, on the weekend of August 8 to 11, 1980. Three multipoint borehole extensometers were installed in horizontal boreholes. Each extensometer had 5 anchor points located between 10.7 m and 0.6 m from the shaft wall as shown on Figure 4.8. Eight vibrating wire embedment strain gauges were installed at the 180 m level on August 13, 1980 as that section of lining was being poured. Figure 4.9 shows the location of the embedment gauges.

4.3.4 Instrument Descriptions and Installation Procedures

4.3.4.1 Extensometers

Description and Specifications:

Extensometers were a mechanical multipoint borehole type manufactured by the Irad Gage Inc. and modified in the University of Alberta, at the Civil Engineering machine shop. Each extensometer was installed with five anchors. Each anchor was attached to a threaded stainless steel rod and extended to the extensometer head as shown on Figure 4.10. The anchors were expansion rock bolt anchors with two welded wings which allowed activation in a nominal 76 mm diameter borehole. Connecting rods were of 6.35 mm diameter

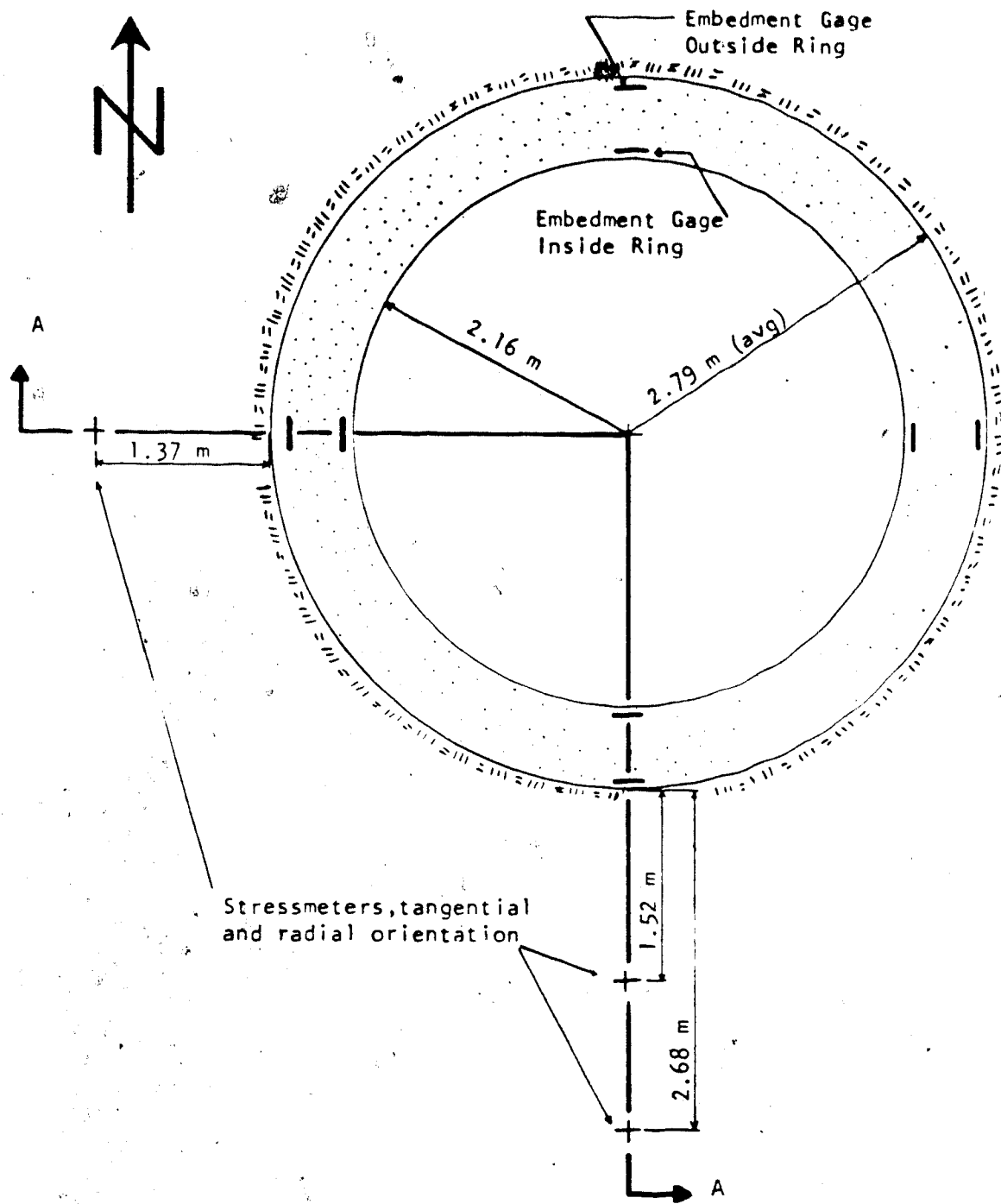


Figure 4.6 Plan View of Stressmeters at 152 m Depth

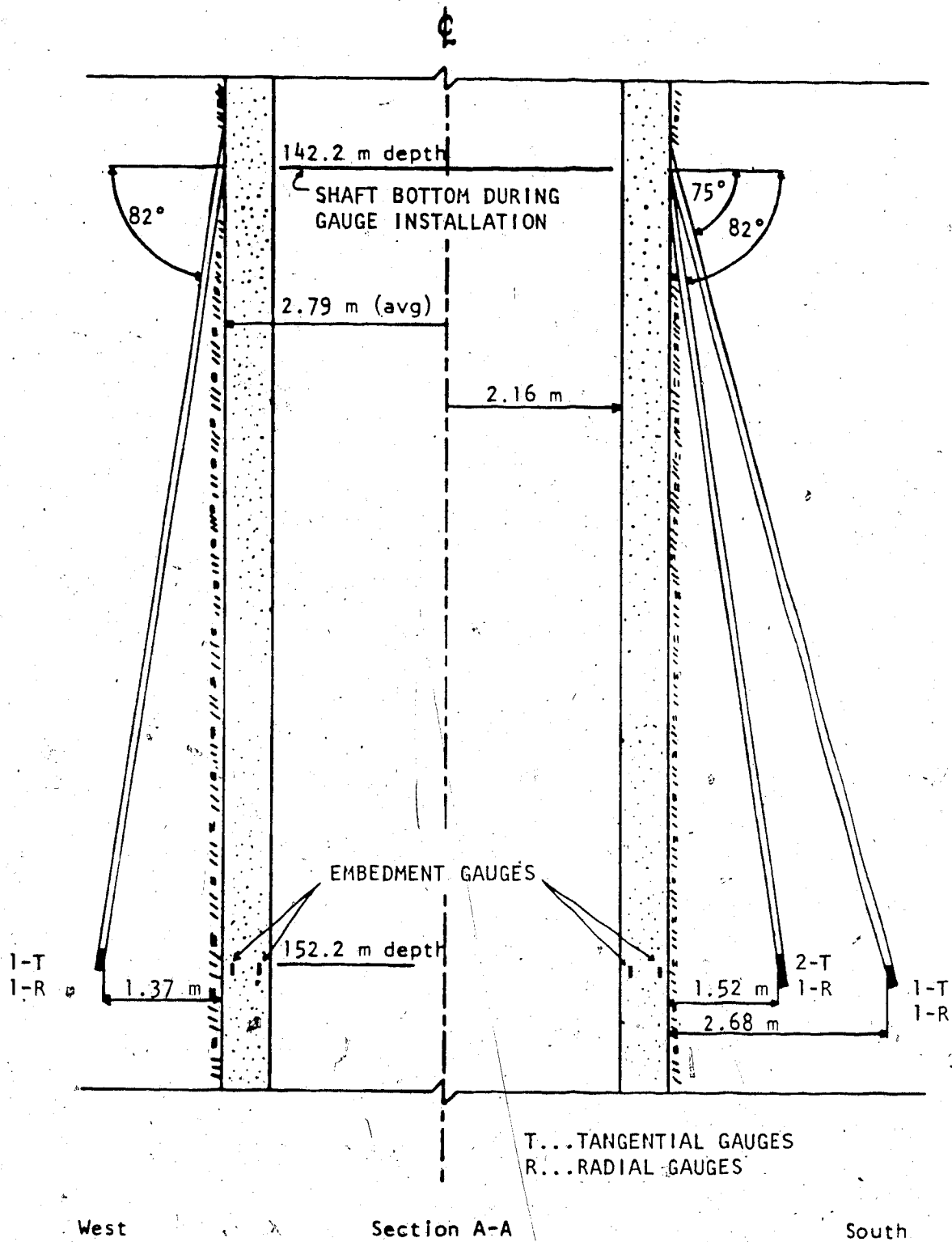


Figure 4.7 Section View of Stressmeters at 152 m Depth

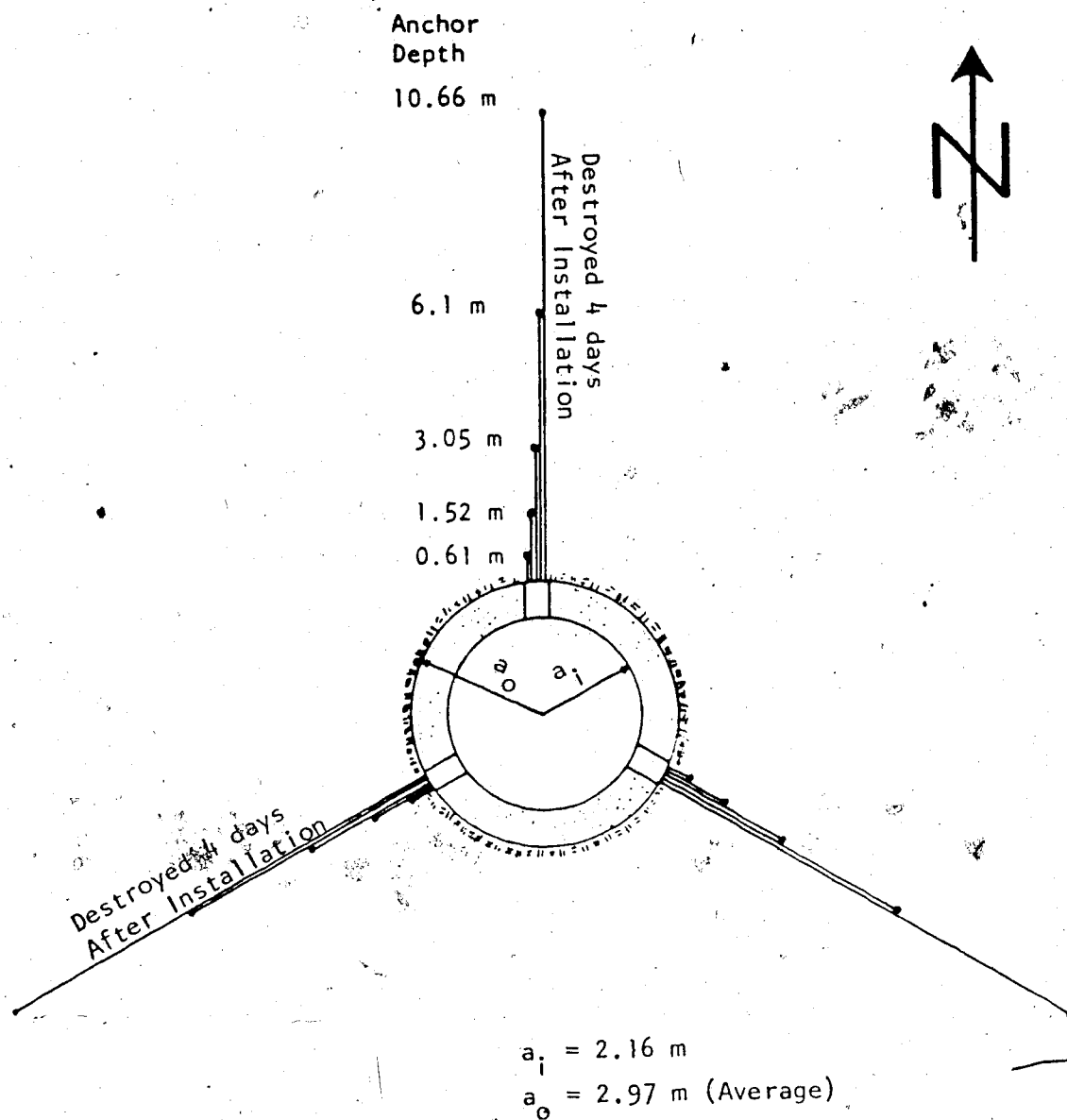


Figure 4.8 Plan View of Extensometers at 180 m Depth

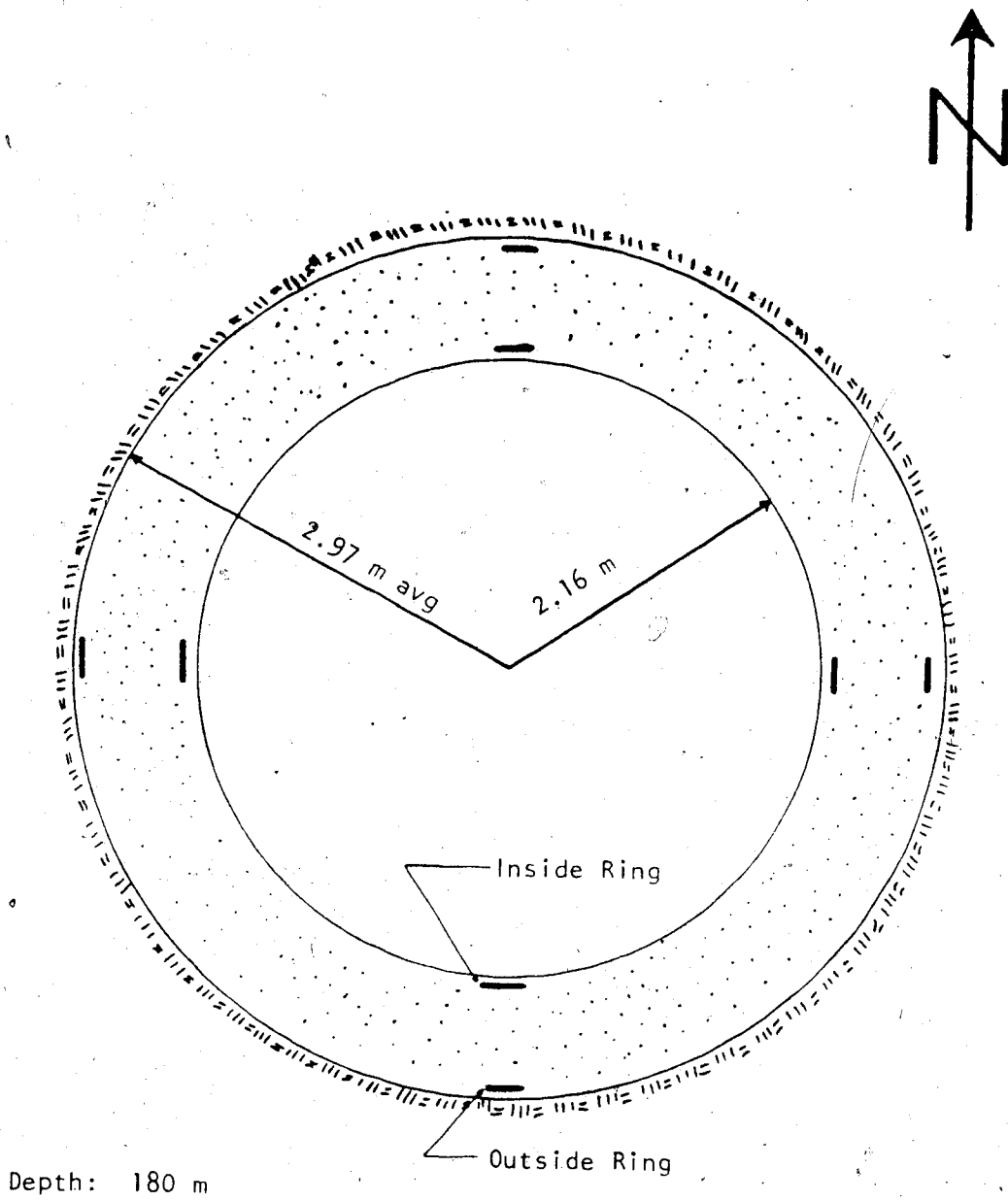


Figure 4.9 Plan View of Embedment Gauges at 180 m Depth

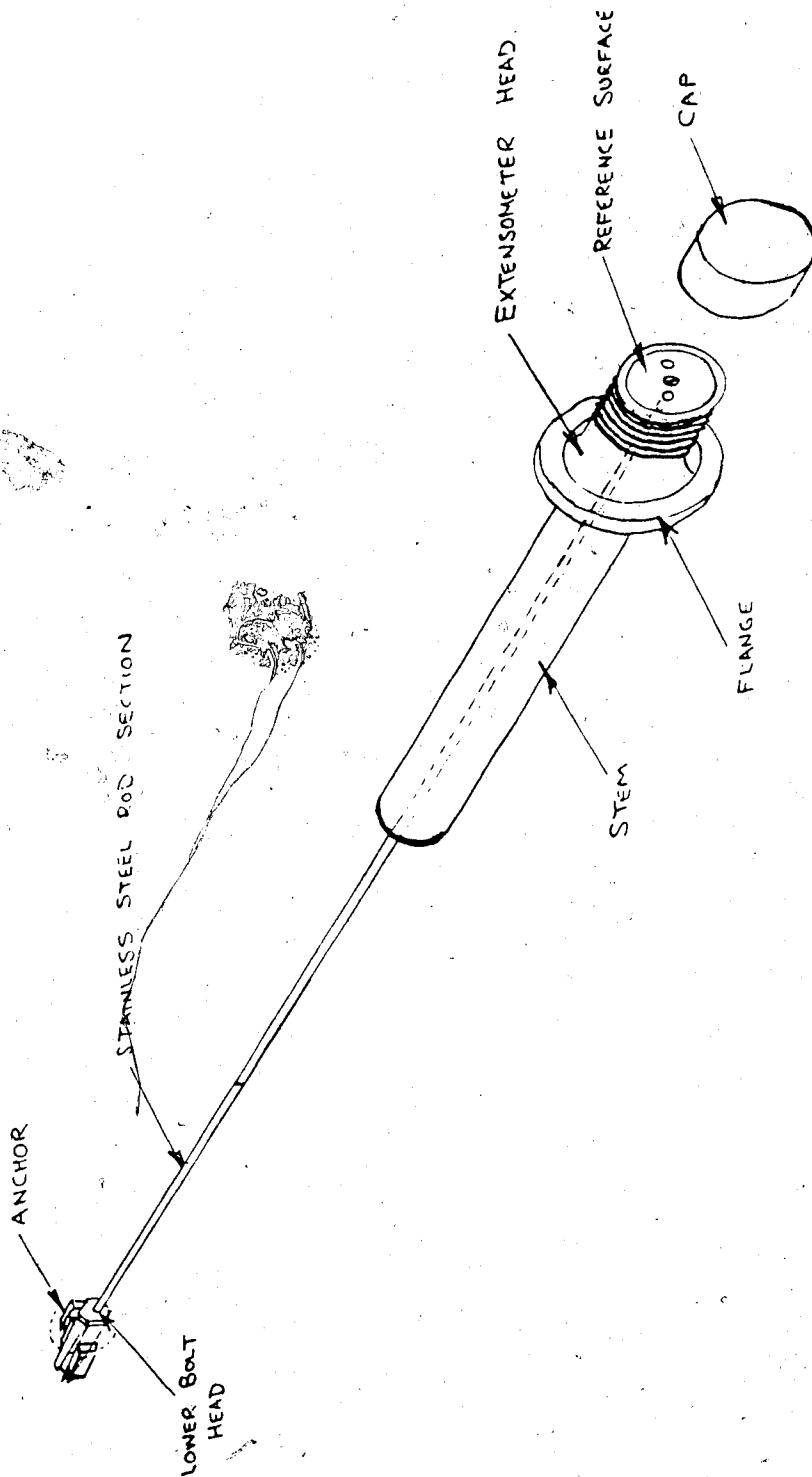


Figure 4.10 Borehole Extensometer with Single Anchor (Irad Gage Inc.)

stainless steel. A P.V.C. extensometer head was provided by Irad Gage. A second extensometer head was constructed in the machine shop to allow extension of the extensometer head through the concrete lining. A stainless steel plate forming a flat end on each extensometer head was used as a reference surface to measure the depth to the anchor rods.

Installation Procedure

Extensometers were installed in horizontal drill holes oriented radially outward from the shaft centre. The three extensometers installed at each level were spaced equally around the shaft circumference. At the 152 m depth, anchors were installed at a distance of 1.52 m, 3.05 m, 4.57 m, 7.62 m and 10.66 m from the shaft wall. At 180 m depth, anchors were installed at depths of 0.61 m, 1.52 m, 3.05 m, 6.1 m and 10.66 m from the shaft wall. In each hole the anchors were installed sequentially, starting from the deepest end of the drill hole. A socket wrench welded to a 19 mm threaded pipe was used to activate the anchor against the side of the borehole. The rods for each successive anchor were installed under the rods from the deeper anchors. Breakout on the top and bottom of the boreholes on level 4 increased the difficulty in setting the anchors, and horizontal orientation of the anchor wings was required.

Positioning of the extensometer heads became a critical problem during installation. To obtain accurate convergence readings the anchor head should be fixed as close as possible to the shaft wall. Installation of the

extensometers within 1 metre of the shaft base left the extensometer heads exposed to potential blast damage. Damage to the extensometer heads could occur in two ways, the first as direct impact from flying rock and the second as the adjacent wall rock sloughed off after blasting. Wall recession of about 15 cm at 152 m and 30 cm at 180 m occurred between installing the extensometer and pouring the lining. The extensometer heads were countersunk in 20 cm deep holes at level two and 30 cm deep holes at level four. Extensometer heads were grouted along the outer 250 mm of the borehole and protected by 12 mm thick steel plates welded to 15 cm diameter, 15 cm long steel pipe sections. The steel plates were secured by removable rock bolts. One of the six P.V.C. extensometer heads was damaged by the blast.

The cast in place concrete lining thickness was about 0.5 m at 152 m and about 0.8 m at 180 m. Extension heads for the extensometers were devised to allow continued data collection following the lining placement. The extensions consisted of a large diameter protective outer tube (15 cm at 152 m and 25 cm at 180 m), an extension head, and extension rods. Success in extending the extensometer heads was limited. One extension was successful, three extensometer heads were accessible through the outer tubes, and two of the outer tubes at 180 m were crushed under the weight of the concrete pour. At the completion of the project in addition to the two extensometers covered by

concrete, one extensometer at 152 m was inaccessible, because it was behind a 15 cm steel air supply pipe.

4.3.4.2 Embedment Gauges

Specifications

Concrete strain was measured using Irad Gage Inc. model EM-5 vibrating wire embedment strain gauge. Figure 4.11 shows the gauge and its basic components. The gauge specifications give a normal range of 3,000 microstrain and a sensitivity of ± 1 microstrain. Gauges will operate normally between -40° and 71°C .

Vibrating wire strain gauges are based on the principle of the fundamental frequency of vibration of a wire tensioned between two points. As a tensioned wire is strained, the fundamental frequency changes. The strain is proportional to the difference in the squares of the fundamental frequencies. The measured strain in the concrete is averaged over the embedded portion of the gauge.

The relationship given in equation 4.1 is used for strain determination (Irad Gage, 1979):

$$\epsilon = 1.0156 \times 10^{11} \left(\frac{1}{T_1^2} - \frac{1}{T_2^2} \right) \quad (\mu \text{ strain}) \quad \text{Eq. 4.1}$$

where: ϵ is the strain

T_1 and T_2 are the initial and subsequent frequency readings taken from the readout.

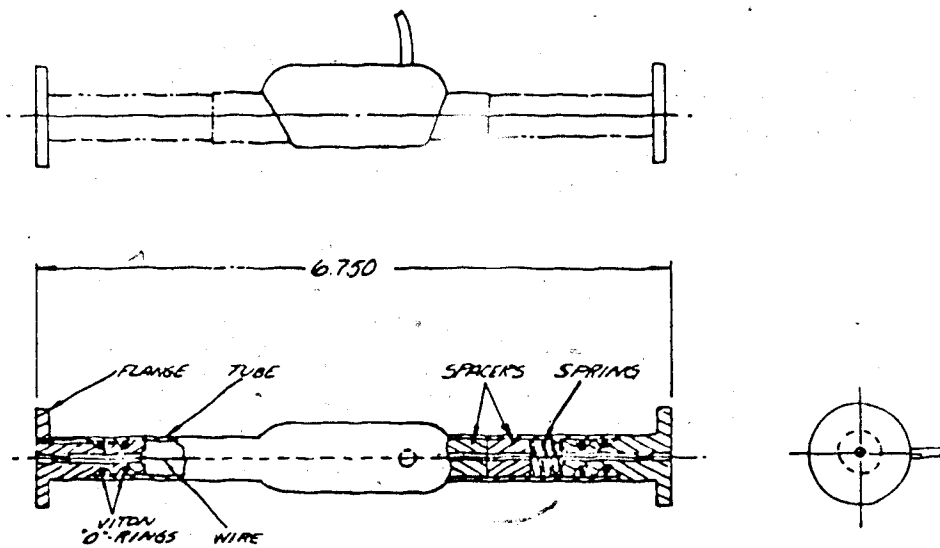
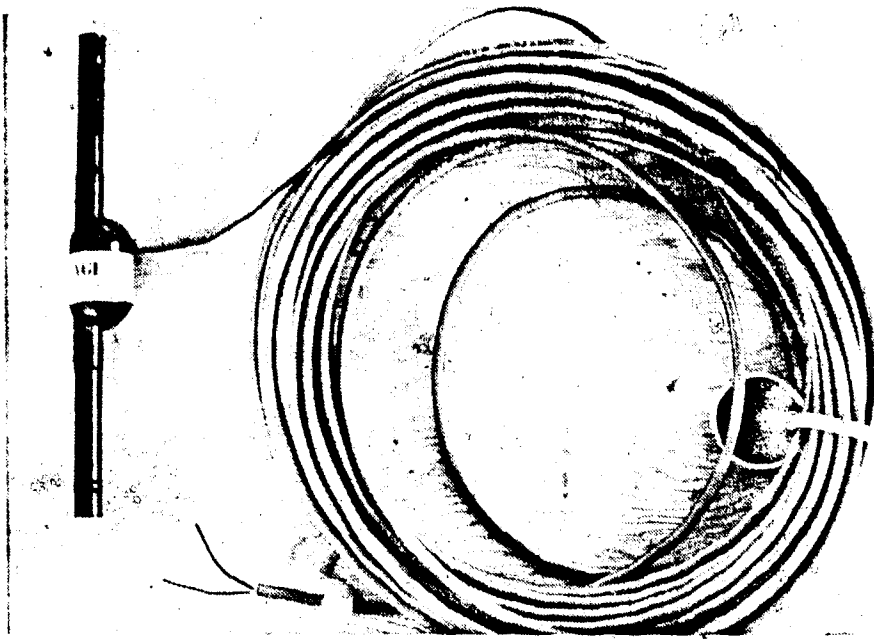


Figure 4.11 Vibrating Wire Embedment Gauge (Irada Gage Inc.)

Readings were obtained from the Irad Gage Inc. model MB-6 readout. The readout displays values of T, where:

$$T = 10^7/2F \quad \text{Eq. 4.2}$$

F = fundamental frequency of vibration.

Installation Procedure

A total of thirty-two gauges were cast in the concrete lining, and operated successfully throughout the project. The gauges were initially cast in concrete briquet blocks made from the same mix proportions as used in the lining concrete, but without the aggregate greater than 12 mm in diameter. The blocks were cast in a 10.1 cm x 10.1 cm x 22.9 cm mold, using wires to centre the gauges. Samples were cast on a vibrating table to eliminate voids around the gauge platens and cured in a constant temperature moist room. Readings were taken regularly during curing to check for shrinkage strains. As the gauges were installed during the pouring of the concrete lining, the installation procedure was streamlined as much as possible to cause minimal interference with the pouring operations.

Two levels of gauges were installed at the upper level of instrumentation (at 108 and 109 m), and one set on each of the lower two levels. Each set of gauges consisted of eight gauges, four along the inside of the lining, adjacent to the inside shaft wall and four along the outside of the lining, about 10 cm from the concrete rock interface. Gauges were located on the north-south and east-west diameters, and orientated to measure tangential strains. Wires from the

gauges were collected in an electrical junction box on the north wall. The box was mounted flush with the finished lining wall, and accessible by hand from the muck bucket. On level three, lead wires from the embedment gauges were fed through a 5 cm diameter water pipe to the panel box located about 10 m above.

Two methods of placing the gauges in the concrete were used. For the upper levels, gauges were hung on rock bolts inserted in pre-drilled holes. This process was time consuming, and also the orientations of the blocks could change if they were hit directly with falling concrete. A much faster method of placing the blocks was used for the lower two levels. After pouring the initial or curb ring lift, the blocks were placed in the desired location and orientation in the concrete. Lead wires were attached to re-bar hanging rods or wire mesh with quick-loc ties to keep the wires from being ripped during the pouring of the remaining concrete.

4.3.4.3 Stressmeters

Description and Specifications

The vibrating wire borehole stressmeters were manufactured by Irad Gage Inc. The gauge was developed under contract to the U.S.B.M. to provide a low cost system to obtain long term readings of stress change in rock (Hawkes and Bailey, 1973). In addition to the initial development report, there are several papers, (Hawkes and Hooker, 1974,

and Sellers, 1977) which briefly describe the background theory and some applications in underground mining and excavations.

Figure 4.12 shows an assembled gauge and a section through a gauge body. Hawkes and Bailey (1973) provide a complete description of the gauge, its specifications, installation techniques, and data analysis. In brief, the gauge consists of a hollow steel cylinder which is activated diametrically across a 38.1 mm diameter borehole by wedging the gauge body and platens apart. The steel cylinder of the gauge flexes elastically, in the manner of a proving ring. Associated with the deformation of the gauge body is a corresponding deformation of a highly tensed steel wire in line with the loading axis. The change in length and tension of the tensioned steel wire is accompanied by a change in the fundamental frequency of vibration. The fundamental frequency is determined by causing the wire to oscillate with an electro-magnetic field. The MB6 readout was also used to read the stressmeters.

A distinct advantage of the vibrating wire instruments over other electrical instruments is the allowable freedom in selecting a lead wire length. Readings are taken as frequencies, not resistances, and therefore the lengths of the lead wires may be changed following gauge installation without affecting data. Very long lead wires may be used to collect data from a safe or accessible place.

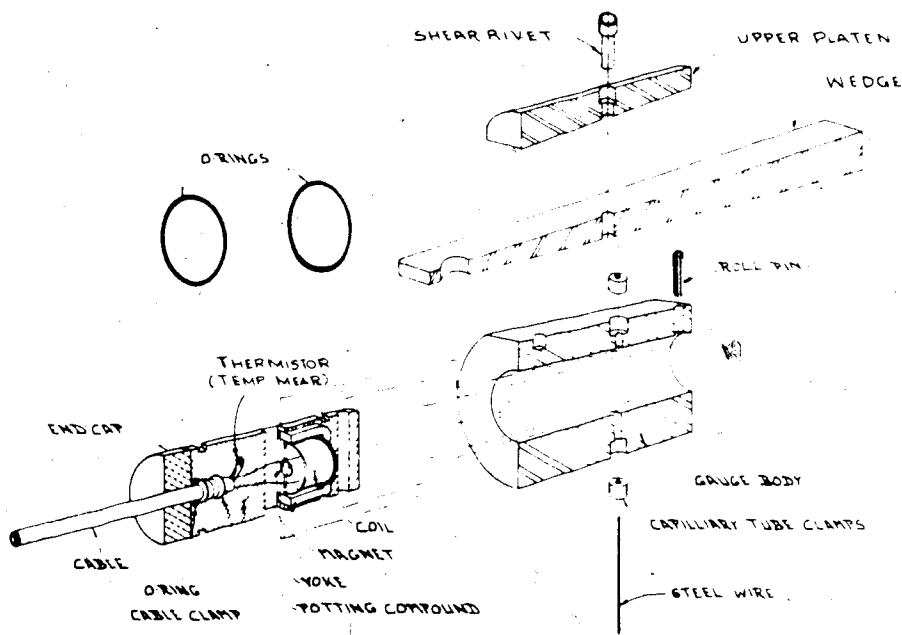
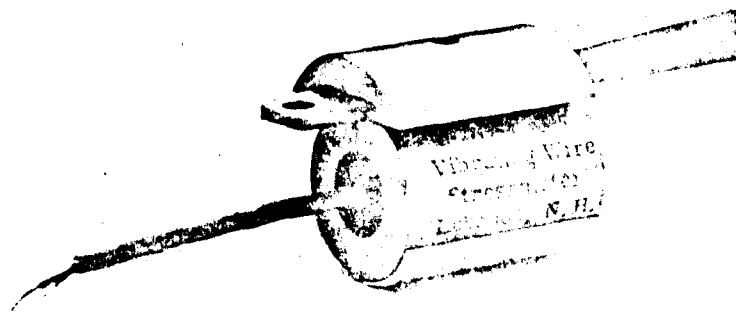


Figure 4.12 Photo and Section of Vibrating Wire Stressmeter with Soft Rock Platen (Irad Gage Inc.)

The stressmeters installed in the shaft were fitted with special wide platens and gauge shoes as shown in Figure 4.12 (soft rock type), which distribute the contact stresses on the borehole walls. In softer rocks the narrow platens of the hard rock model develop higher contact stresses on the borehole walls, which may result in yielding and relaxation of stresses.

Installation Procedure

The initial plan called for eight stressmeters to be set in four steeply inclined boreholes from a depth of 142.2 m. The boreholes were spudded at the shaft wall, two on the south wall and two on the west wall, with all holes oriented radially outward from the shaft centre. One hole at each location plunged from the horizontal at 82 degrees and the other at 75 degrees. Gauges were set in the boreholes between 10.4 and 11 metres from the shaft bottom. The gauges were set within 1.3 and 2.7 m from the excavation line, as shown on Figure 4.5 and 4.6. Drill holes were advanced from 0 to 10 m with a 75 mm diameter carbide tipped wing bit. Wing bits were found to be much more efficient in advancing the boreholes than tri-cone bits. The lower 0.6 to 1 m of the drill holes were cored with a double walled EWG core barrel with a carbide tipped bit. Recovery was poor, and therefore selection of the gauge sites on the basis of fracture location was not possible. The critical factor in successfully installing the borehole stressmeters is obtaining a circular borehole within the allowable diametral

tolerance. The EWG core barrel, fitted with a new carbide embedded reaming shell and carbide tipped bit produced an oversize hole. Taper in the hole also developed from vibration of the core barrel during drilling. Following completion of drilling, the holes were flushed and air dried to remove cuttings. A "go/no go" gauge was used to determine the section of the 38.1 mm diameter hole within the allowable tolerance. Two of the holes were oversize and were extended using the EWG core barrel with a worn carbide tipped bit and reaming shell.

Detailed installation procedures are outlined in the instruction manual (Hawkes and Bailey, 1973). Gauges were activated in the desired position and orientation, using a hydraulic setting tool.

Several problems developed during the stressmeter installation. The first concerned the small tolerance in hole diameter over which a gauge could be properly activated. This was probably due to the limited travel of the hydraulic setting tool piston. A second problem was the tendency for the sharp end of the setting tool to shear off the lead wires of the gauge during the release of the tool after activation of the gauge. This was overcome by applying sufficient activation pressure to shear the eye of the wedge, thus eliminating the necessity of following the recommended procedure to release the tool from the gauge. The final problem with the gauges arose from poor bonding of the soft rock shoe to the gauge. Several shoes detached from

the gauge body in the drill hole during installation attempts. The remaining gauges were rebonded to the soft rock shoe using strain gauge cement.

The drill hole plunging at 75 degrees on the west wall became blocked with gauge platens and wedges from unsuccessful installation attempts. A total of seven gauges were successfully installed in the three remaining test holes as shown on Figure 4.7. Each of these drill holes had one gauge in a tangential orientation and one gauge in a radial orientation. The hole plunging at 82 degrees on the south wall had one additional gauge in a tangential orientation.

Lead wires from the gauges were protected inside threaded 3 metre sections of 38 mm diameter steel water pipe. The protective pipe was lowered to the bottom of the 75 mm diameter section of the drill holes and grouted in place with quick set concrete. The exposed section of pipe was extended to the base of lining form, and was anchored to the wall with steel plates and expansion head rock bolts.

Between the time the shaft sinking resumed and the first concrete pour was made, five benches were blasted. The blasting sheared all the exposed protective pipes at the upper threaded coupling. The gauge lead wires were also severed. The lead wires were re-attached just prior to pouring the next level of lining. All gauges continued to function.

4.3.4.4 Piezometers

Specifications

Irada Gage type PW vibrating wire piezometers were used to measure water pressure of the rock lining interface. The piezometers had a range of 0-500 psi (0-3448 kPa) with a sensitivity of ± 0.5 psi (3.5 kPa). The Irada Gage MB6 vibrating wire readout was used to take readings from the piezometers.

Installation Procedure

Piezometers were initially intended to be installed in short drill holes (20 cm x 15 cm diameter) in the shaft wall at each level of investigation (Levels 2, 3 and 4). Time shortage associated with installing the embedment gauges and panel boxes required modification of the initial plan. Piezometers were later installed at the 109 and 152 m levels by drilling 38 mm diameter holes through the liner into the shaft wall. Holes were drilled with a jack leg percussion drill. A water soaked sponge was placed in front of the gauge. The water in the sponge would fill the small cavity in front of the piezometers diaphragm, to minimize equalization time. Lead wires were collected at the adjacent panel box, and the drill hole was sealed with grout.

5. EVALUATION OF THE *IN SITU* STRESS FIELD

5.1 Introduction

The purpose of this chapter is to evaluate the *in situ* stress field adjacent to the shaft. Regional evidence on the orientation and relative magnitudes of the principal stresses is discussed. The results of *in situ* stress measurements from a single borehole in the shaft are presented and discussed. The results of stressmeter measurements are interpreted to determine the magnitude and orientation of the major principal horizontal stresses.

5.2 Evidence on the Orientation of the Regional Stress Field

The concept of subdividing large areas of the continent into stress provinces, on the basis of current orientations and magnitudes of the principal stresses, has been advanced by Zoback and Zoback (1980). Synthesis of available data both from direct measurements, and qualitative indicators, has shown that many areas, within a given physiographic province, having the same recent tectonic history, have the same principal stress orientations and magnitudes.

Bell and Gough (1979) have shown from a regional study in Alberta and north-eastern British Columbia, that the major principal horizontal stress is approximately normal to the Rocky mountains, in a NE-SW direction (Figure 5.1). Interpretation of the orientation of the principal

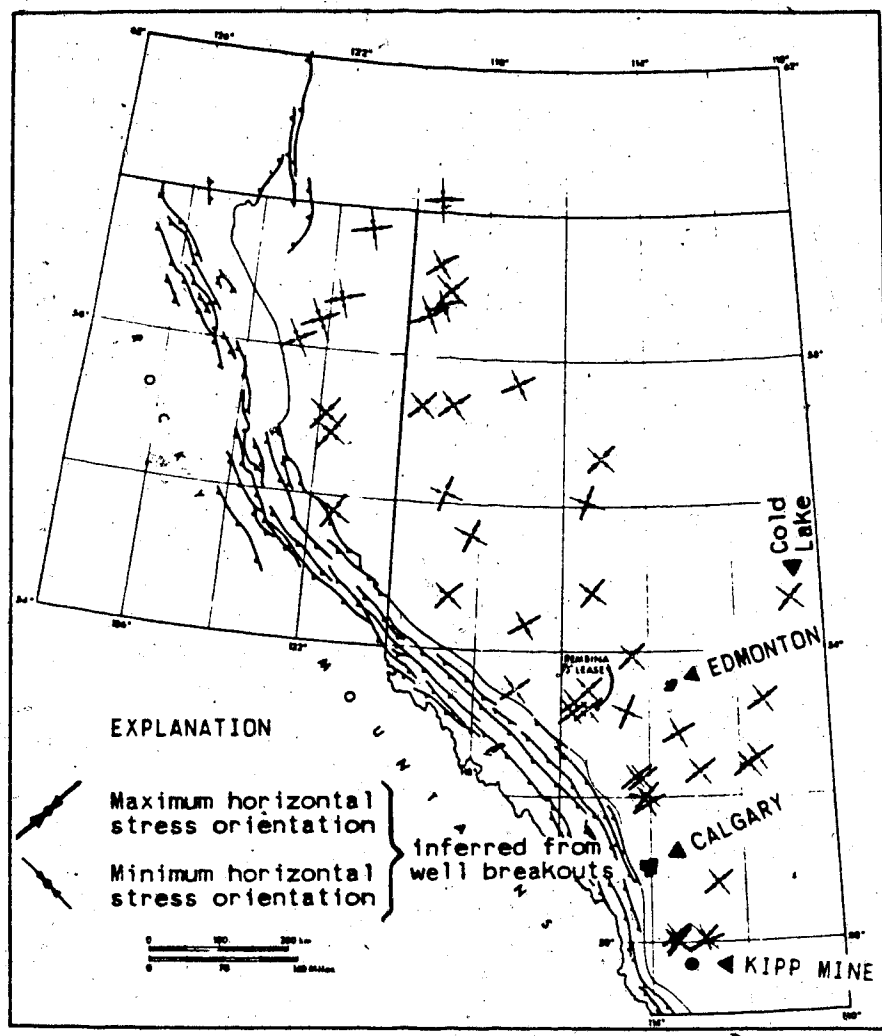


Figure 5.1 Orientation of Major and Minor Principal Horizontal Stresses Interpreted from Oilwell Breakouts (after Gough and Bell, 1981)

horizontal stresses, is based on a regional study of breakouts occurring on the walls of uncased oilwells. Measured by a four arm caliper probe, the breakouts occur as diametral elongated grooves continuous over tens of metres. The breakouts can be explained by considering the oil well to be analagous to a circular hole in a thin plate subjected to an uneven biaxial stressfield. When the maximum tangential stresses around the circular hole are greater than the uniaxial compressive strength of the material, yielding will occur. The maximum compressive tangential stresses are developed at 90° to the major principal stress direction. Babcock (1978) reported measuring 41 breakouts, between depths of 1280 and 2194 m in 5 wells in the Lethbridge area, indicating the major principal horizontal stress orientation was about $N 30^\circ E$. Gough and Bell (1981) report breakouts in oilwells occurring as shallow as 480 m. Given that the depth of casing in oilwells is often several hundred metres, the opportunity of finding breakouts at shallow depths is rare.

Results of hydraulic fracturing tests in the Pembina field, and steam injection tests at Cold Lake have been interpreted by Gough and Bell (1981) as indicating the minor principal stress is horizontal, i.e. $K_0(\min) \leq 1$. Peterson (1954) interpreted K_0 as 1.5 in the Bearpaw Formation at the South Saskatchewan River Dam site. Long term horizontal and vertical plate load tests in a test adit indicated that with time the stress on the plates in the vertical direction

approached the expected overburden pressure, while the horizontal stress became steady at about $1.5 \sigma_v$.

Gough and Bell (1981) have interpreted the regional field stresses as fitting either a thrust stress field (σ_1 and σ_2 horizontal and σ_3 vertical) or a strike slip stress field (σ_1 and σ_2 horizontal, σ_3 vertical). The previously cited evidence of σ_1 horizontal suggests the strike slip stress field may be appropriate, with σ_1 northeast-southwest and σ_2 northwest-southeast.

5.3 *In situ* Stress Measurements by Overcoring

5.3.1 Introduction

In situ stress measurements by overcoring were planned as part of the shaft instrumentation program. The initial objective was to determine the complete stress tensor. As a result of slow drilling and limited time, testing was restricted to 5 tests in a single horizontal borehole. The operation was nevertheless considered successful, as the method was shown to be practical in the weak bedrock underlying much of the prairies.

5.3.2 Test Equipment and Procedure

The technique of overcoring a small diameter borehole containing a diametral borehole deformation gauge was developed in the early 1960's by the United States Bureau of

Mines. Hooker and Bickel (1974) describe the method used to determine rock stresses with the current generation of U.S.B.M. borehole deformation gauges. The U.S.B.M. deformation gauge used in the program shown in Figure 5.2 measured borehole deformations on ~~2.5 meters~~ 60° apart in the same plane. The torpedo shaped gauge is centered in a 38 mm diameter borehole with 6 tungsten carbide tipped plungers at the front of the gauge, and 3 springs at the rear of the gauge. The 6 plungers are each in contact with a strain gauged beryllium copper cantilever. The cantilevers are wired in diametral pairs to give 3 diametral deformation readings. Hooker *et al.* (1974) describe the features, specifications, and performance characteristics of the 3 component deformation gauge. The gauges used in the testing were model BG-2 gauges, manufactured by Irad Gage Inc. Deformation readings were recorded by a Vishay model P-350A portable strain indicator.

A 0.3 m thick massive siltstone bed was selected for the location of the horizontal test hole, to optimize core recovery. Figure 5.3 shows the orientation of the test hole and the positions of the overcoring tests, located at a depth of 91 m below the surface. The drill hole was orientated so the biaxial plane of measurement was coincident with the expected maximum horizontal principal stress.

A 147 mm diameter starter hole was drilled to a depth of 0.71 m, to the location of the first test, with a thin

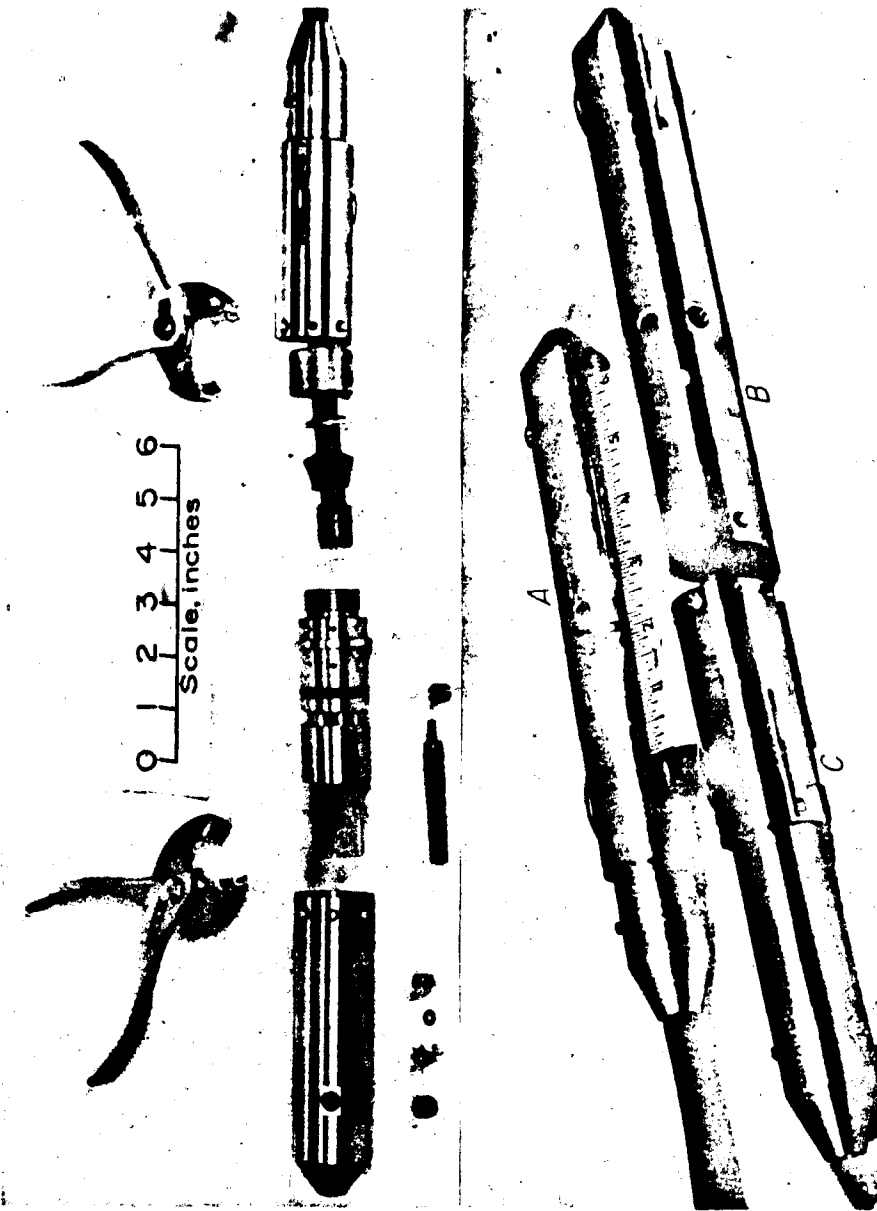


Figure 5.2 U.S.B.M. Borehole Deformation Gauge (after Hooker and Bickel, 1974)

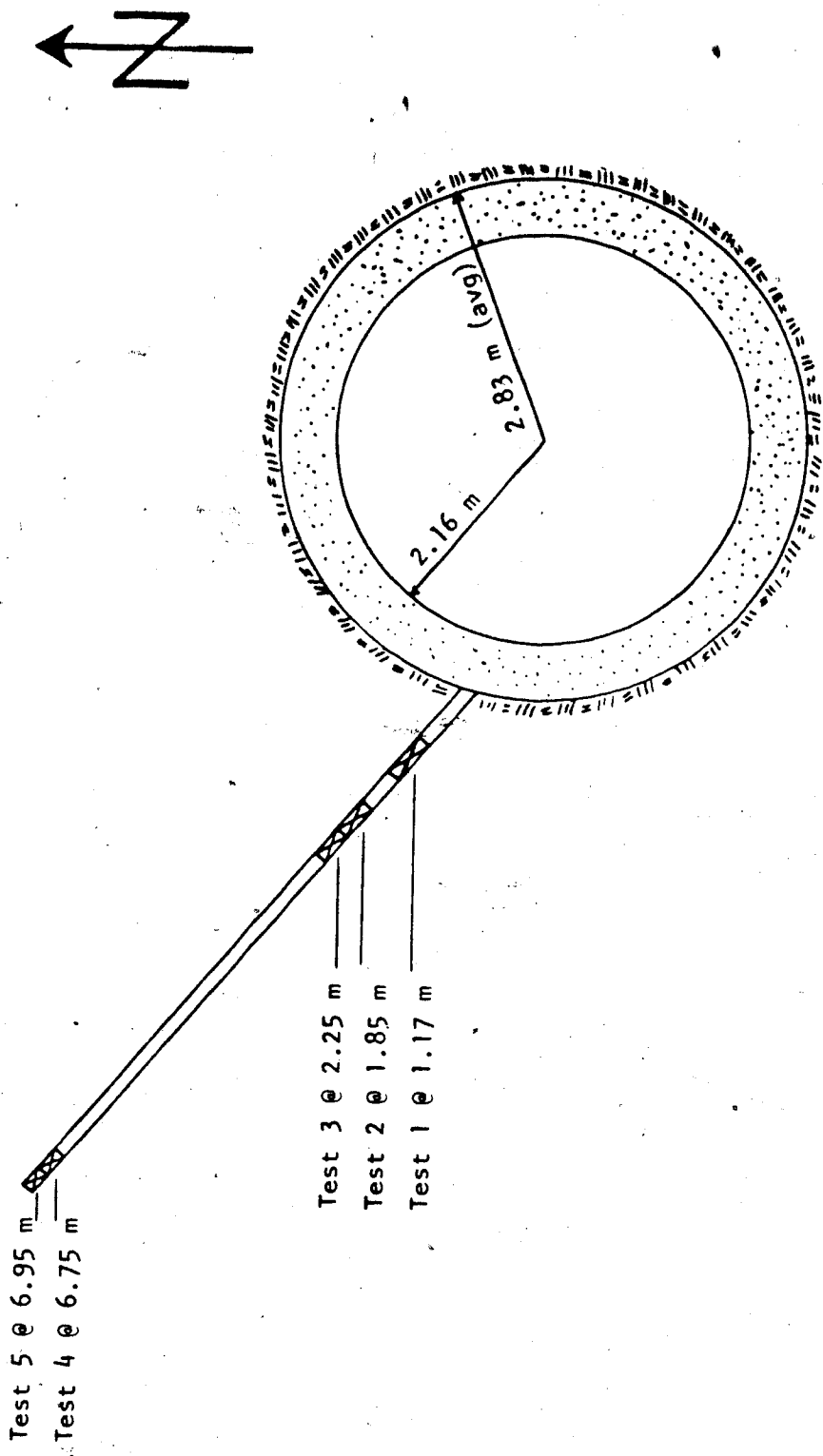


Figure 5.3 Plan View of Overcore Test Locations of 91 m Depth

walled masonry core barrel. A centred 38 mm diameter borehole was cored a further 0.6 m past the end of the starter hole. A double walled Acker-E.W.G. corebarrel with a tungsten carbide tipped drill bit was used for the 38 mm diameter hole.

The E.W.G. core was examined to identify zones of jointing or fracturing to select the location for gauge placement. The U.S.B.M. deformation probe was inserted in the 38 mm diameter hole in a joint free section. The lengths of the 6 plungers were adjusted to obtain acceptable zero deformation readings. The probe was set and oriented with extendable setting rods. The probe lead wires were conducted through the drill string annulus and a specially fitted water swivel. A waterproof connection at the water swivel allowed continuous deformation measurements during the overcoring test. Overcoring consisted of cutting a core with the 147 mm diameter core barrel at a rate of about 125 mm/min, past the plane of measurement of the probe, as shown schematically in Figure 5.4. Readings were taken at 125 mm intervals as overcoring proceeded. After overcoring, first the probe and then the 147 mm diameter core was removed. The above procedure was followed for all 5 tests. Sections between tests were cored and the core was saved for lab testing. Steel stabilizers designed by the U.S.B.M. (Hooker and Bickel, 1974) and fabricated in the machine shop, were used to minimize rod vibrations and to centre the B.Q. wireline drill rods.

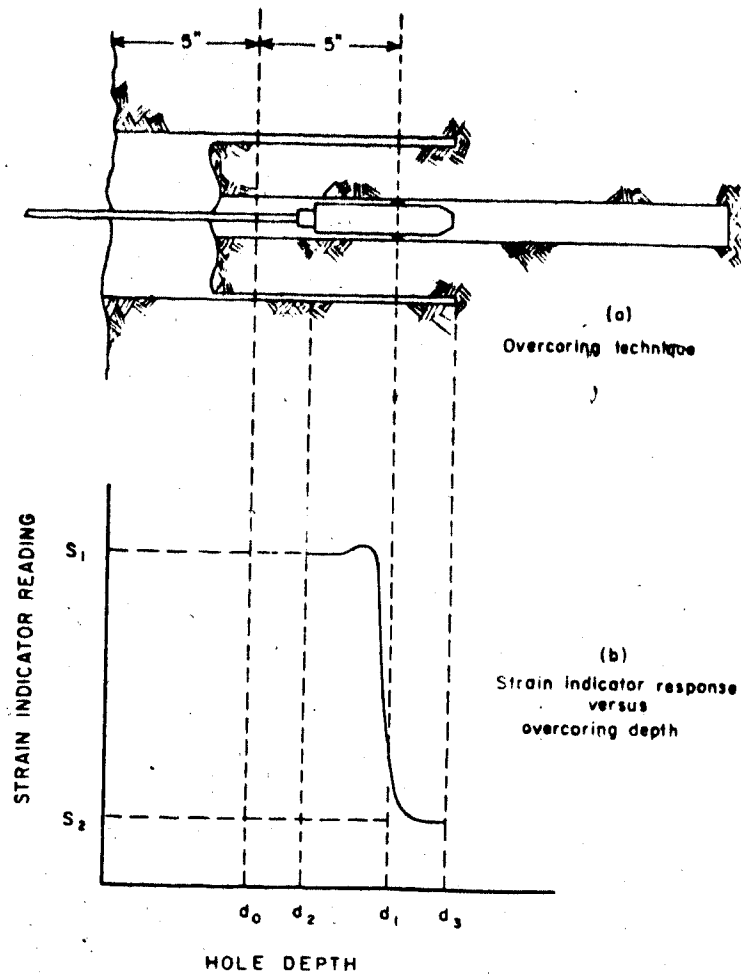


Figure 5.4 Schematic Presentation of Relationship Between Overcored Depth and Measured Diametral Deformation (after Obert, 1966)

Reduction of the borehole deformation data to values of *In situ* stress requires a knowledge of the Young's Modulus of the rock. The standard procedure for the overcoring test is to reload the core from each test in a biaxial pressure cell, and to measure the radial pressure vs internal bore deformation relationship. The biaxial cell provided by Irad Gage Inc. designed by the U.S.B.M. failed to work in the intended manner. Instead of applying a uniform radial stress along the embedded portion of the core to create approximate plane stress loading conditions, the cell pressure was concentrated along the centre of the cell and caused failure of the rock core in tension. Experimentation with the biaxial cell later, resulted in a solution to the problem. It is recommended that the core be wrapped with one or two layers of a thick flexible plastic sheeting, such as mylar or linoleum, to increase the diameter of the core to the inside diameter of the cell.

5.3.3 Data Reduction and Analysis

Figures B.34 to B.38 show the overcoring depth versus diametral deformation plots for the five tests. Four of the five tests were relatively successful. The data from Test 1 is incomplete, as shown on Figure B.34. The test was aborted before the overcoring bit had completely passed the plane of measurement. The overcored rock contained an open joint oblique to the core axis, which allowed the core and probe to spin with the core barrel. If the probe had been set at a

shallower depth, Test 1 would have been successful. Tests 2 through 5 provided complete overcore depth-diametral deformation curves. The shape of each curve is unique, reflecting somewhat the non-isotropic behavior and nonuniform stress distribution of the regularly jointed rock mass. The core from each of Tests 3 and 5 contained open fractures which were along a bedding plane in the sample from Test 3 and concave in the sample from Test 5. Both fractures were in the outer portions of the core, extending for about 30 cm along the core. Grob *et al.* (1975) show that open discontinuities in the vicinity of the plane of measurement cause errors in diametral deformations due to uneven stress gradients. The effect of the open bedding planes has not been evaluated. Displacements in the direction normal to bedding were much larger in the overcoring tests on the fractured rock than in the tests on the intact rock. It is possible that the open fractures cause the rock to behave like an anisotropic body, with a lower modulus in the direction of the bedding plane.

The initial positive, displacements shown on Figures B.34 to B.37 for Tests 1 through 4 are diametral strains resulting from concentrations of tensile stresses in the plane of the drill bit, as it advances toward the plane of measurement (Blackwood, 1978). When the drill bit has cut a short distance past the plane of measurement, the tensile stress concentrations and their effect on diametral deformations drops rapidly. At this point, a steady state

plane strain condition should exist. Slow response of the plungers, or time dependent strain recovery in the rock mass results in continued deformations after drilling has stopped.

Table 5.1 presents the diametral deformations for Tests 2 to 5. Further analysis of the data is restricted to Tests 2 and 4 because of reasons cited earlier. Two closed form solutions have been considered in calculating the *in situ* biaxial stress from the overcore tests. Both are based on linear elastic models. The first assumes the rock mass is isotropic, and the second assumes the rock mass is anisotropic. Grob *et al.* (1975) show that significant error is introduced into the calculation of the *in situ* stresses if the rock is assumed to behave linearly elastic, when it is behaving non-linearly or has developed a plastic zone around the pilot hole during overcoring. Triaxial test results show the stress/strain behavior in the elastic loading stage are linear during testing with a constant strain rate. The observations of Grob *et al.* (1975) have practical implications on the range of conditions where the technique can be applied without considering the effect of yielding on diametral deformations and the stress strain response of the rock.

Equations for the isotropic plane strain solution are presented in Appendix C.4. The Poisson's ratio of the rock is assumed to be 0.25 for all analysis. The Young's Modulus for the initial isotropic analysis was selected from the

Table 5.1 Summary of Diametral Deformations from Overcore Tests

Test No.	Test Depth (m)	Diametral Deformation, u , [$\text{cm} \times 10^6$]		
		Counterclockwise Angle from Vertical $u_1=0^\circ$	$u_2=60^\circ$	$u_3=120^\circ$
2	1.85	3500	11400	4700
3	2.16	14000	12000	13000
4	6.60	5400	6500	13250
5	6.88	12900	9750	11600

triaxial test results. The assumption of isotropic elasticity is seldom strictly true for sedimentary rocks. It is generally more realistic to consider layered rocks as a transversely isotropic material with isotropic horizontal layers. Becker (1968) and Becker and Hooker (1969) present an elastic solution for determining *in situ* stresses from overcoring measurements in anisotropic rock. The formulas for the anisotropic solution are presented in Appendix C.5. The solution requires that the axis of the circular hole (drill hole) lie along one of the orthotropic axis of the material. The horizontal drill hole meets this criterion if it is assumed that the horizontal plane is a plane of elastic symmetry (i.e. is isotropic), and that $E_h \neq E_v$. Tests have not been conducted on the Bearpaw shale to determine the ratio of E_h/E_v , but, based on personal experience in similar rock from another overcoring project, it will be assumed that $E_h/E_v = 1.6$. Table 5.2 presents the principal biaxial stresses calculated for tests 2 and 4 for the isotropic and anisotropic analysis. The isotropic analysis indicates the major principal stress is $\pm 26^\circ$ from horizontal while the anisotropic analysis reduces the range to $\pm 20^\circ$. The orientation of the major principal stress as calculated is strongly influenced by the orientation and ratio of the anisotropic modulus of elasticity. A maximum estimated error of ± 15 degrees is possible in determining the orientation of the gauge, a result of the technique used to set the gauge. This problem has been corrected by

Table 5.2 Comparison of Principal Biaxial Stresses
Calculated from Isotropic and Anisotropic Analysis

Test No.	Isotropic Elastic Analysis				Anisotropic Elastic Analysis			
	P [MPa]	Q [MPa]	Q/P	θ [degrees]	P [MPa]	Q [MPa]	Q/P	θ [degrees]
2	1.65	0.75	0.45	+64	2.27	0.90	0.40	+70
4	1.99	1.09	0.55	-64	2.73	1.29	0.47	-70

Note: E = 1.4 GPa for Isotropic analysis

$E_v = 1.4$ GPa and $E_h = 2.2$ GPa for Anisotropic analysis

θ = Positive measured counterclockwise from vertical axis

P = major principal biaxial stress

Q = minor principal biaxial stress

adopting a level to the setting rods. From the error allowance, it will be assumed that the major principal biaxial stress is approximately horizontal.

The vertical stress component for both methods of analysis are significantly lower than the estimated overburden pressure. Synthesis of a number of studies (Hoek and Brown, 1980) has shown that in non-mountainous areas, the vertical stress component can be approximated by the overburden pressure. If the ratio of P/Q from Tests 2 and 4, given by the isotropic analysis, is assumed to be correct, then the horizontal stresses for each test can be calculated by assuming vertical stress is equal to the overburden pressure of about 1.9 MPa. A correction must also be applied to P calculated by this method to account for the tangential stress concentration adjacent to the shaft. The tangential stress concentration factors were calculated on the assumption that the biaxial plane of measurement is about 90° from the orientation of the major principal stress and N , the ratio of ($\sigma_h(\max)$ to $\sigma_h(\min)$) is about 0.7. Appendix C.2 presents the necessary equations. Table 5.3 presents the results of this exercise, with the estimated horizontal field stresses, K_0 , and the equivalent isotropic modulus of elasticity. An average K_0 of 1.5 and E of 3.2 GPa is produced by this analysis.

Table 5.3 Isotropic Analysis of Overcore Tests 2 and 4
Based on the Assumption of $\sigma_v = \gamma_h$

Test No.	r/a	$\frac{\sigma_\theta}{\sigma_h}$	$(\frac{Q}{P})_{\text{isotropic}}$	P (1) [MPa]	σ_h (2) [MPa]	K_o	$E_{\text{(apparent)}}$ [GPa]
2	1.59	1.65	0.45	4.22	2.56	1.35	3.55
4	3.25	1.1	0.55	3.45	3.14	1.65	2.44

Notes:

r/a = position of test normalized to shaft radius

σ_θ/σ_h = tangential stress concentration factor in horizontal plane predicted by linear elasticity

$(Q/P)_{\text{isotropic}}$ = measured ratio of principal biaxial stresses for isotropic analysis.

(1) Principal biaxial stress calculated from assumption: $Q = \sigma_v = \gamma_h$

(2) $\sigma_h = P/(\sigma_\theta/\sigma_h)$: Correction for tangential stress concentration

$$K_o = \sigma_h/\sigma_v$$

$$E_{\text{(apparent)}} = \sigma_h/\epsilon_v$$

5.4 Interpretation of *In situ* Stresses from Stressmeter Measurements

Section 6.3 discusses in detail the method used to calculate the magnitude and orientation of the major principal horizontal stresses from stressmeter measurements. The method could be considered to be an "undercoring" test, where the principal biaxial stresses are calculated from measurement of the tangential and radial stress changes in the wall rock which occur as the stress state changes from a virgin stress field, to the steady state stress field after the shaft bottom influence is negligible. The calculated field stresses are reduced from the true field stresses by a factor proportional to the difference between the true field stress and the radial support pressure which develops on the liner. Analysis of the lining stress data indicates the short term (6 day) radial support pressure P (max) is about 0.25 MPa. The most likely field stresses and range calculated in Section 6.3 from the observed stress changes are:

$$\text{Sigma-H(max)} = 4.50 \pm 0.5 \text{ MPa}$$

$$N = 0.5 - 0.8$$

$$\text{theta} = \text{S } 40^\circ \text{ W } \pm 20^\circ$$

5.5 Conclusions on the *In Situ* Stress Field

The hypothesis advanced by Gough and Bell (1981) is supported by the results of the two overcoring tests, and the stressmeter data. As measurement of the complete stress tensor was not possible, interpretation of the *in situ* stresses must reflect a judgement on the fit of the data. Subsequent analysis in this thesis will be based on the assumption that the principal stresses are horizontal and vertical, and have a relationship with depth as shown on Figure 5.5.

Although time limited the number of overcoring tests possible, the results demonstrate the method is a practical tool for measuring *in situ* stresses in weak bedrock.

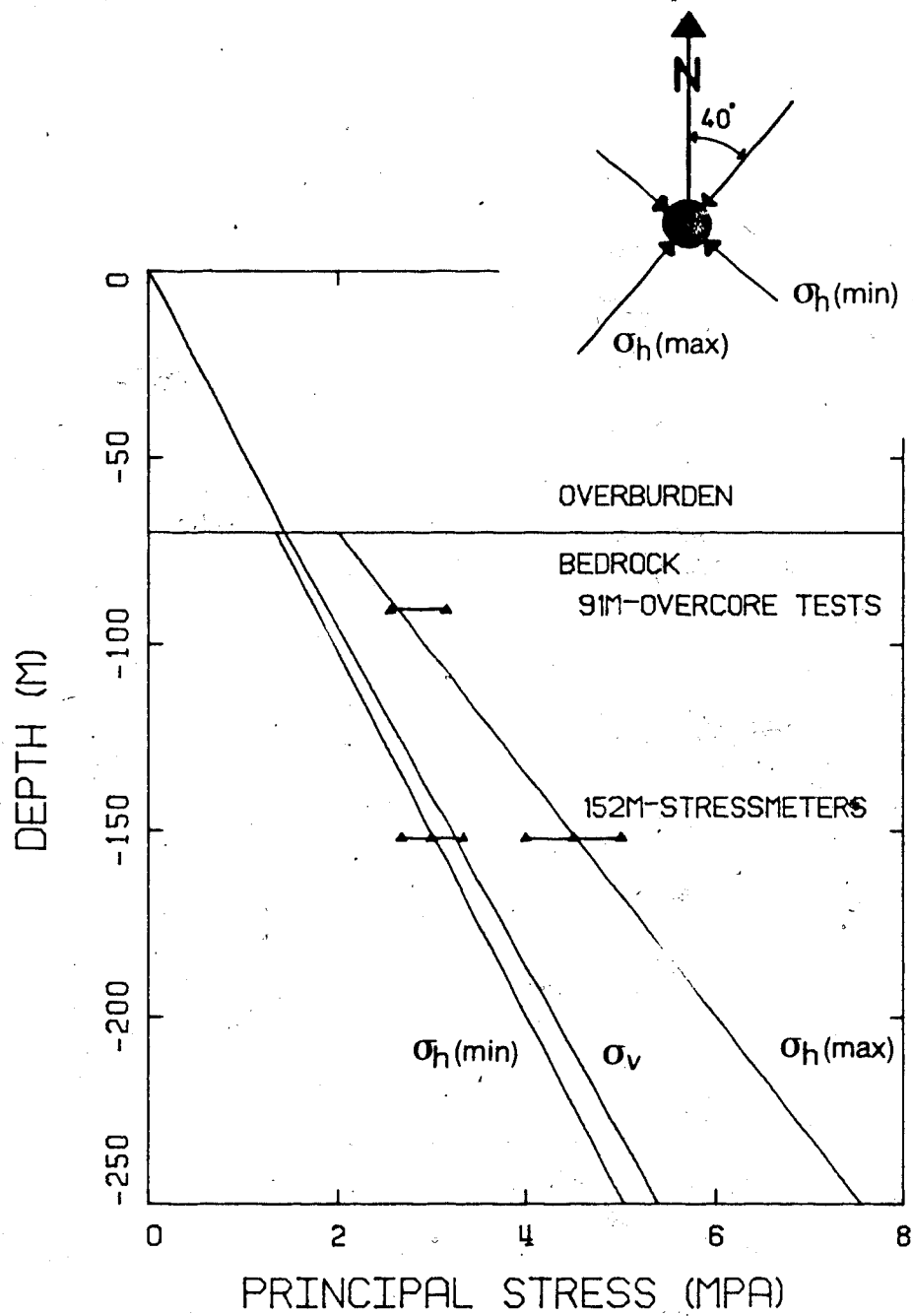


Figure 5.5 Estimated Field Stress Profile Adjacent to the Shaft

6. ANALYSIS OF SHAFT INSTRUMENTATION

6.1 Introduction

This chapter covers the reduction and analysis of data obtained from extensometer, stressmeter and embedment gauge measurements. The factors influencing the response, and sensitivity of the instruments and potential errors are discussed. Plots of the field data are presented in Appendix B. The data has been interpreted from comparison of the field data with normalized theoretical curves generated from an appropriate model.

6.2 Extensometers

6.2.1 Extensometer Data Reduction

Extensometers were installed in horizontal boreholes near the shaft bottom, to measure the magnitude and distribution of radial rock mass displacements accompanying the shaft sinking. The positions of the extensometers installed at the 111 m and 180 m levels are given on Figures 4.3 and 4.7 respectively. At each level, one of the three extensometers recorded almost no movement. Malfunction of these gauges could have been caused by:

1. binding of the rods against other rods and anchors, and
2. bonding of the rods to the reference head by excess grout extruded between the borehole and the reference

head.

The two remaining extensometers at the 180 m level were destroyed when the concrete lining was poured at that level. The two extensometers at the 111 m level were accessible after the lining was poured over that section.

Extensometer measurements were obtained at the 111 m level following each bench blast, while the extensometers were exposed on the shaft wall below the lining. Access to the extensometers at the 180 m level was restricted to the shutdown period when the extensometers were installed, and just prior to pouring the lining over that section of the shaft.

Extensometer readings were taken by measuring the distance from the reference head mounted at the shaft wall, to the ends of the anchor rods. Measurements were taken with a Mitutoyo depth micrometer, calibrated to ± 0.001 inches (± 0.0254 mm). The last set of measurements of the two operational extensometers at the 111 m level were taken with an L.V.D.T. mounted on a P.V.C. holder to act as an electrical depth micrometer. Readings on the L.V.D.T. were obtained with a portable "Fluke" digital voltmeter. A 6 volt battery was used to excite the L.V.D.T. The L.V.D.T. depth micrometer was found to have a repeatability of ± 0.005 inches (± 0.127 mm).

Extensometer data is presented as recommended by Cording *et al.* (1975), in the form of depth-displacement diagrams, and time-displacement diagrams. Figures B.1

through B.8 present the extensometer data.

The time-displacement diagrams show the displacement distribution between the reference head and each anchor with respect to time. An increase in the distance between the reference head and the anchors is shown as positive. Time-displacement diagrams allow correlation of displacement rates to construction events. The depth-displacement diagrams show the distribution of movement within the measured section. Extensometer measurements were taken as the displacement of each anchor with respect to the reference head mounted on the shaft wall, as outlined by Cording *et al.* (1975). For data analysis the inward displacement (convergence) of the shaft wall was taken as the measured displacement between the reference head and the deepest anchor. On the depth-displacement diagrams this displacement was plotted at the shaft wall. The measured displacement between the reference head and each of the intermediate anchors was subtracted from the measured displacement between the deepest anchor and the reference head, and plotted as the displacement of that anchor (towards the shaft). This method produces a displacement distribution relative to the deepest anchor. For data presentation purposes the displacement of the deepest anchor is shown to be zero.

6.2.2 Discussion of Errors

A possible error of ± 0.0254 mm was introduced into each extensometer reading obtained with the Mitutoyo depth micrometer and ± 0.127 mm for the reading obtained with the L.V.D.T. When the displacement at the depth of an anchor relative to the deepest anchor is calculated for the depth displacement diagrams, the error is doubled. Therefore on the depth-displacement diagrams a possible error of ± 0.0508 mm is associated with each reading obtained with the Mitutoyo depth micrometer at each anchor depth, and ± 0.0254 mm for the displacement between the deepest anchor and the extensometer head. For the two extensometers at the 180 m level, where less than 0.32 mm of total movement was recorded at the deepest 4 anchors, the possible error is greater than $\pm 16\%$ of the measured movement. This estimate of the possible errors is conservative, as all readings were taken by the same person using a consistent measurement technique.

A second type of error introduced into the results is from the nonuniform response of the extensometer head to movement at the shaft wall. Any rotation of the extensometer head would result in a nonuniform and indeterminable error on the measurements. The grouted length of 25 cm along the stem would tend to keep rotation of the head to a minimum. Sticking of the connecting rod between the extensometer head and the anchor appears to have caused a jump in the measured displacement at one anchor at the 111 m level. A small

amount of grout on the connecting rod at the back of the reference head could explain the sticking.

6.2.3 Extensometer Performance

Figures B.5 and B.6 show between 20 and 30 percent of the total measured movement at the 111 m level occurred while the shaft bottom was stationary at about 1 m below the extensometers, (between $t=0$ and 43.5 hr). The largest movements between readings at level 2 spanned the first blast, with smaller displacements associated with each of the 3 subsequent blasts prior to pouring the lining over that section of wall. The four benches blasted in this time accounted for a shaft bottom advancement of about 4.6 m, with each blast taking a bench 2.3 m deep by half the shaft bottom. In the time between pouring the lining at level 2 and the first reading taken through the lining (at $t=326$ hr) an additional 0.4 to 0.5 mm of closure occurred. This was about 25 percent of the total closure measured. No measurable closure occurred in the intervening 4 month period between August and December, 1980. In total, between 1.6 and 2.0 mm of inward radial displacement was measured after instrument placement at the 111 m level. This does not include the movement which occurred ahead of the shaft bottom and before installation of the extensometer.

At the 180 m level, radial closure during the period when the shaft bottom was stationary (from 0 to about 50 hours) was between 55 and 83 percent of the total measured

closures of 0.66 and 0.61 mm respectively as shown on Figures B.3, B.4, B.7 and B.8. The time-displacement diagrams for the 180 m extensometers show a radial closure which is almost independent of the shaft face advancement. Four benches were blasted following the 4-day idle period, before the lining was poured at the 180 m level, giving a shaft bottom advancement of about 4.6 m.

6.2.4 Analysis of Extensometer Data

Analysis of extensometer results is based on a two dimensional plane strain isotropic, linear elastic model. Appendix C.1 presents the formula for radial displacements around the circular hole, after Kruse (1969). Poisson's ratio was assumed to be 0.25 in the rock mass for analysis. Comparison of the measured depth-displacement extensometer curves from the two levels to the predicted depth displacement curves has yielded an estimation of the orientation of the major principal horizontal stress, the ratio of the principal horizontal stresses (N), and the ratio of the apparent principal horizontal field stress to the modulus of elasticity of the rock mass (S^*/E). S^* , the apparent principal horizontal field stress, corresponds to the magnitude of the stress change which occurs when extensometer measurements are recorded. Normalized plots have been used for presentation of both measured and theoretical displacements, to facilitate comparison. The distance from the shaft centre to the point in question, R ,

is normalized to the shaft radius, A on the abscissa of each plot. The ordinate presents the radial displacements, u , normalized to the variables S , A , and E in the form SxA/E . Equation C.1.5 (Appendix C) gives the true radial displacement distribution. To allow comparison of the theoretical with the measured displacement distributions, the theoretical displacement distribution must be adjusted to a value of zero displacement at the depth of the deepest anchor, by shifting the ordinate axis to zero at the deepest anchor. A set of 10 normalized theoretical curves was produced for each level, corresponding to a 90° arc in the field stress, in 10 ree increments. Each curve displays the radial displacements for values of N from 0.5 to 0.9. Figures 5.1 to 5.4 present the two curves from each level which best fit the measured results. The curves for $N \geq 0.8$ show little sensitivity to θ , the angle to the major principal stress, whereas the curves for $N=0.5$ and 0.6 are highly sensitive to θ .

A second set of normalized curves was produced from the extensometer data at the 111 and 180 m levels, (Figures 6.5 to 6.8) for the latest recorded displacements. A set of curves was produced for each extensometer plot, by normalizing the measured displacements to the ratio E/S^* , from 1500 to 3000 and 1500 to 4000 at the 111 m and 180 m levels respectively and the shaft radius A . The best fit for each level was obtained between the theoretical and measured curves for the variables N , E/S^* and the geodetic

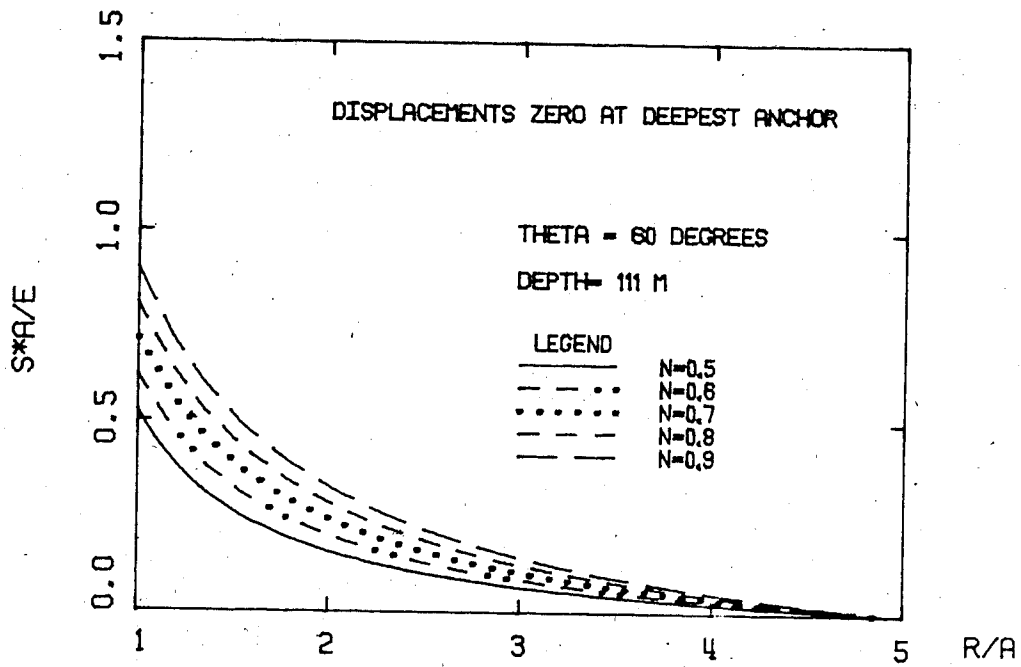


Figure 6.1 Normalized Radial Elastic Displacements at 111 m Depth for Theta = 60°

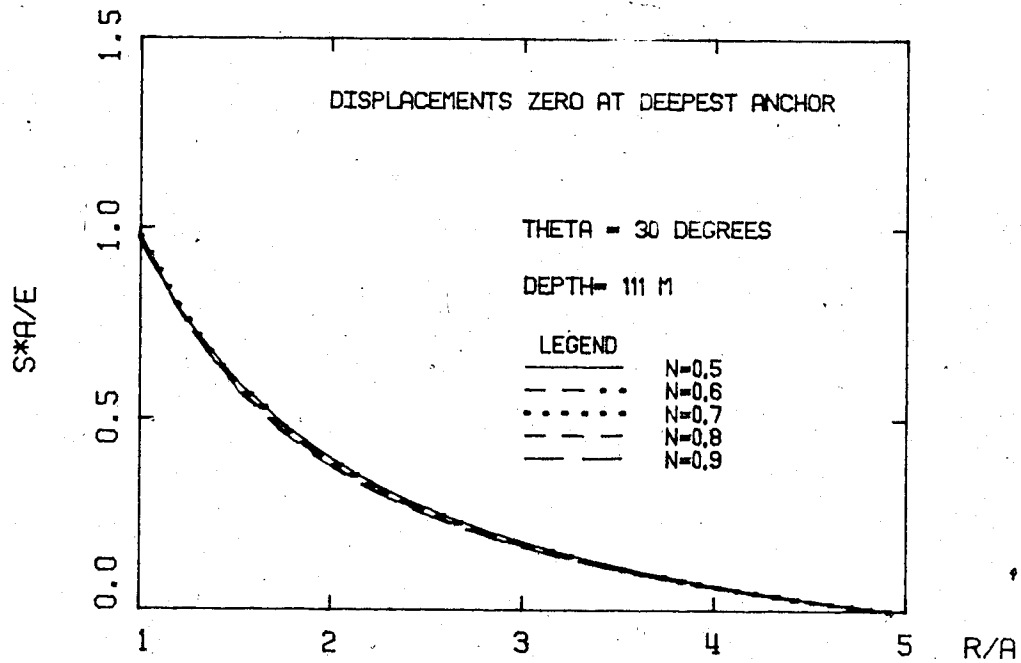


Figure 6.2 Normalized Radial Elastic Displacements at 111 m Depth for Theta = 30°

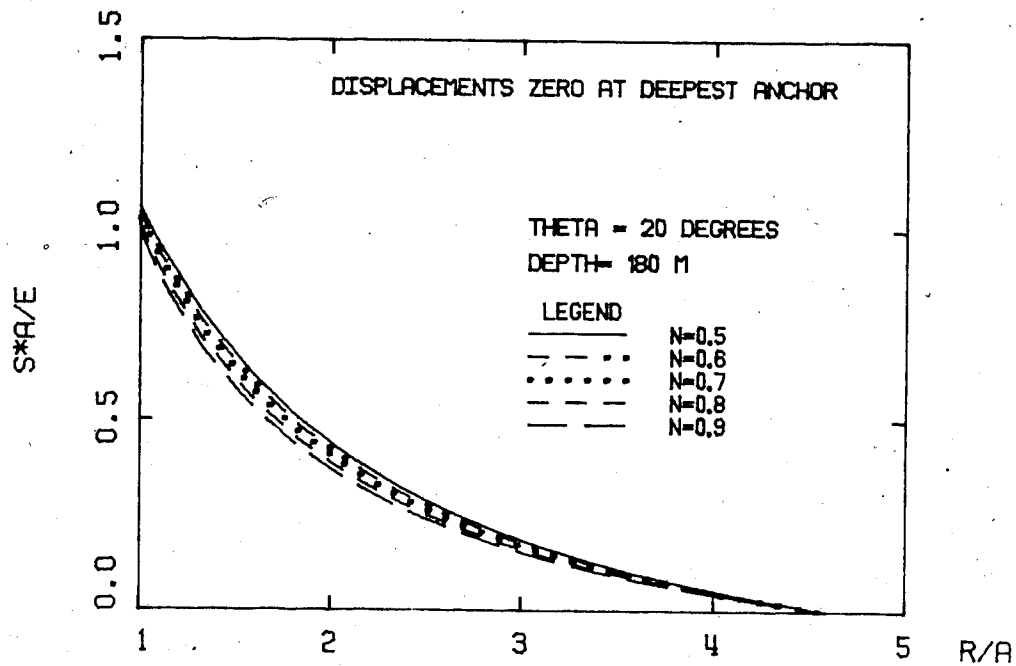


Figure 6.3 Normalized Radial Elastic Displacements at 180 m Depth for Theta = 20°

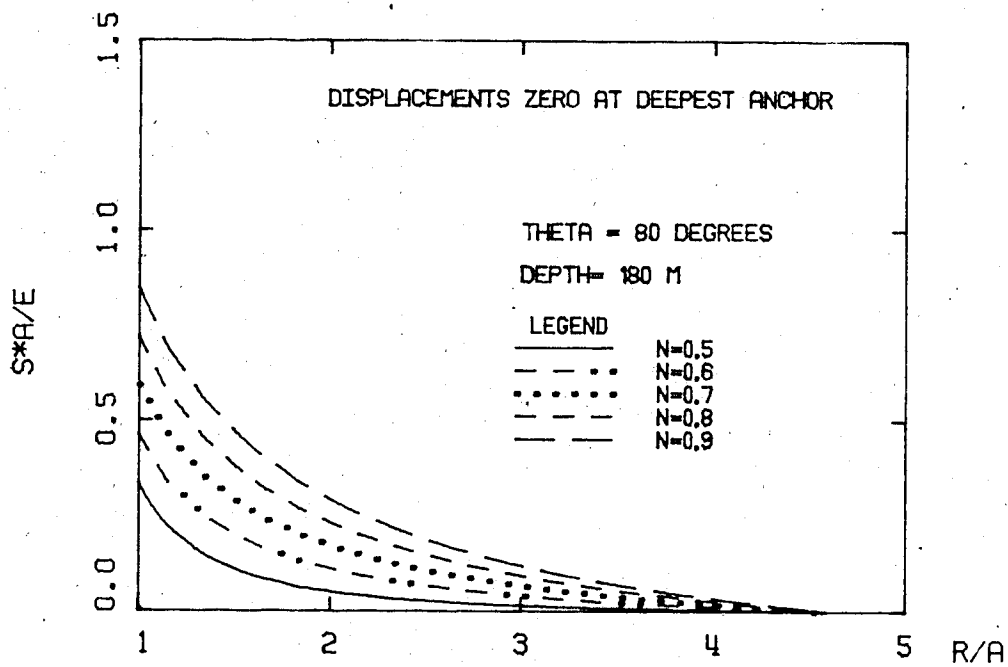


Figure 6.4 Normalized Radial Elastic Displacements at 180 m Depth for Theta = 80°

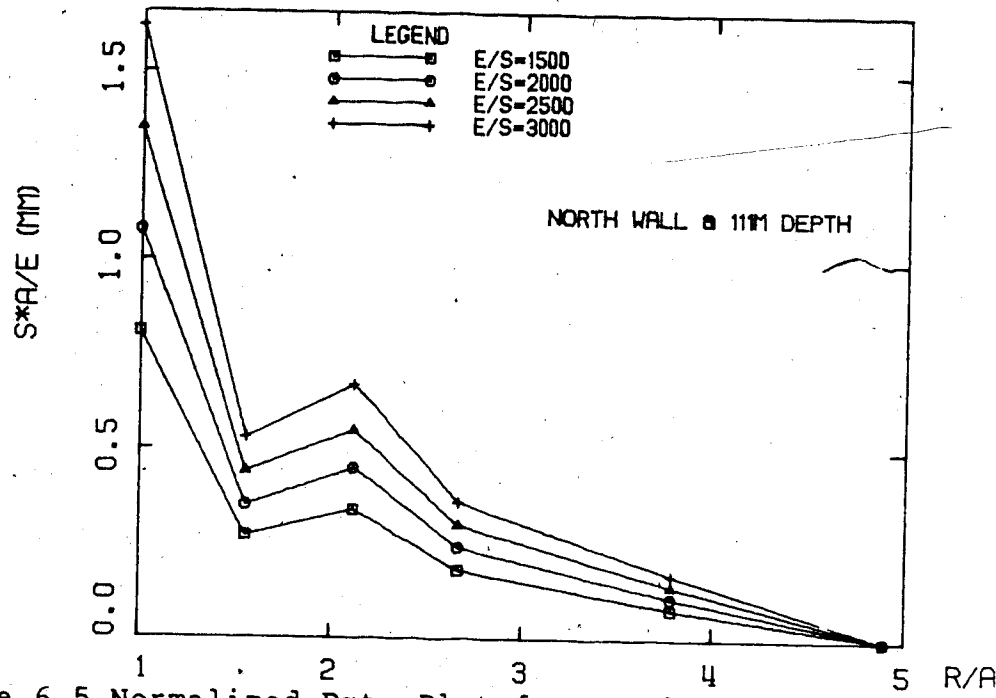


Figure 6.5 Normalized Data Plot for North Wall Extensometer at 111 m.

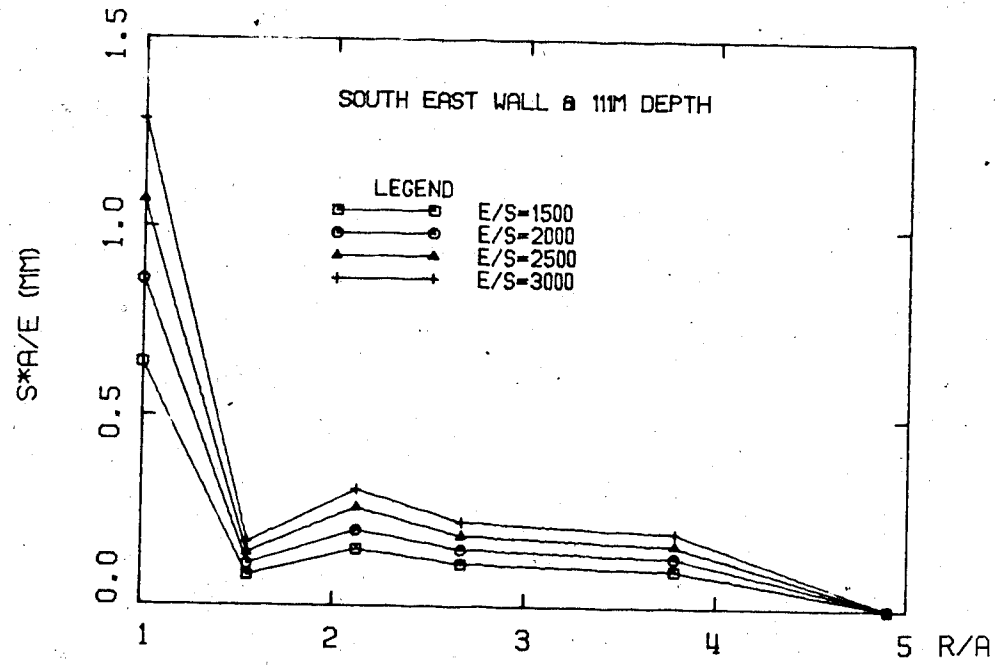


Figure 6.6 Normalized Data Plot for Southeast Wall Extensometer at 111 m.

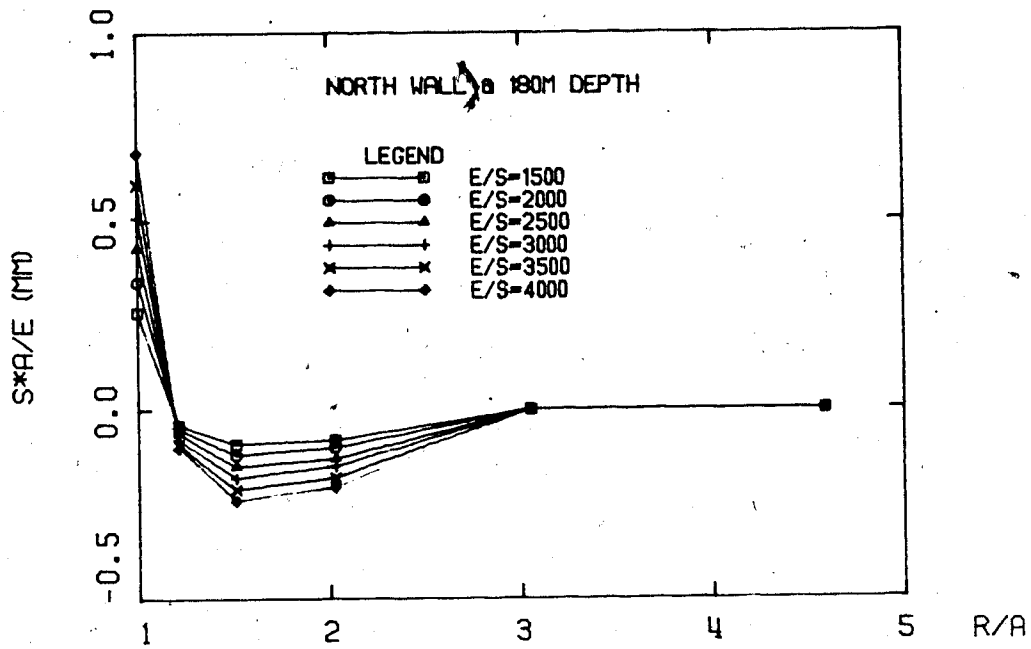


Figure 6.7 Normalized Data Plot for North Wall Extensometer at 180 m.

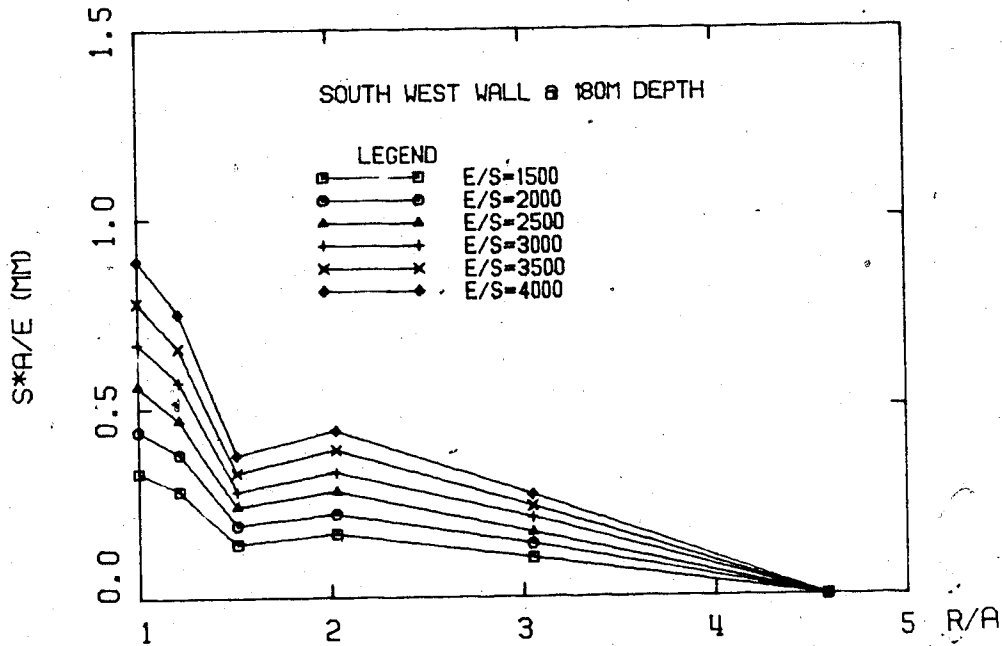


Figure 6.8 Normalized Data Plot for Southwest Wall Extensometer at 180 m.

orientation of the field stress (i.e. the azimuth of S).

6.2.5 Comparison of Measured with Predicted Radial Displacements

Comparison of measured displacement distribution curves with theoretical curves, in a normalized format, allows for the simultaneous evaluation of a number of independent variables. At best, the analysis allows an estimation of the variables, within a given range. An erroneous response of one of the two extensometers at either of the levels would influence the analysis significantly.

Fitting of the measured to predicted radial displacement curves has produced the following results.

111 m Level.

$$N = 0.8 (0.7-0.9)$$

$$E/S = 2000$$

orientation of S = 0-90° (indeterminable)

180 m Level.

$$N = 0.6$$

$$E/S = 3500-4500$$

orientation of S = N80°E±10°

This analysis is in agreement with that reported by Kaiser *et al.* (1982) for the 180 m level extensometers. Comparison of the measured displacements to the normalized curves indicates loosening adjacent to the shaft wall may not be a significant process. The embedded depth of extensometer shaft may also make the extensometer

insensitive to movement in the first 0.3 m of rock adjacent to the shaft where loosening would be dominant. Confidence in the overall extensometer response may be gained from the similar response of the pair of extensometers at each level, and the difference in the magnitude of displacement between the two levels, (i.e. approximately 0.6 mm at 180 m compared to about 2.0 mm at 111m). The similar shape of the depth displacement curves at 111 m indicated an N of about 0.8 and good confidence in E/S^* , but because of the relatively high N, it was difficult to estimate the orientation of the field stress. Conversely, the very different response of the 180 m extensometers indicated with reasonable confidence the orientation of the field stress. The very flat response of the north wall extensometer at 180 m (Figure 5.7) away from the shaft, indicates strongly that $N = 0.5-0.6$ (or possibly even lower). It was difficult to predict E/S^* closer than the given range.

A common feature on all of the depth displacement plots (Figures B.1 to B.4) is the development of a radial displacement trough at a depth of about 1.5 m. The trough is about 0.4 and 0.2 mm deep at the 111 and 180 m levels respectively when compared to a uniform radial displacement curve. The trough was identifiable at the 180 m level on the earliest set of readings, taken 6 hours after gauge installation. The trough was not apparent at the 111 m level until about 43 hours after installation. The north wall extensometer at the 180 m level shows a trough extending

from about 1.5 to 4.0 m from the shaft wall. The trough for this plot shows the rock in the trough zone is in compression with respect to the initial state.

Interpretation of the depth-displacement curves indicates the rock mass is not behaving as a homogeneous isotropic material, but rather as if the rock has developed three concentric zones of different material properties around the shaft. The first zone extending from r/a between 1 and 1.3 would have a modulus equal to or slightly lower than the initial modulus in undisturbed rock mass. The second zone extending between r/a of 1.3 and 2.0 would have a higher modulus than the undisturbed rock mass. The third zone at a depth greater than $r/a = 2.0$ would have an unchanged modulus from the initial state. This speculation could not be confirmed, but it is a possible explanation and it corresponds to observations of "protective zones" adjacent to tunnels reported by Vardar (1977).

The average modulus of elasticity of the rock mass at the 91 m level was estimated to be about 3.0 GPa as determined from back calculation of overcoring tests (Section 5.3.3). Table 5.3 shows the back calculated modulus for tests 2 and 4. The modulus from test 2, $r/a = 1.59$ is about 45% higher than the modulus at test 4, ($r/a = 3.25$). This supports the view that the rock in the intermediate zone around the shaft ($1.3 < r/a < 2.0$) has a higher modulus than the initial rock mass, but two values obtained by indirect calculation cannot be considered as hard evidence.

The modulus of elasticity measured in the laboratory varied from 1.1 to 2.1 GPa with an average modulus of 1.5 GPa. Qualitative assessment of the rock quality at 91, 111 and 180 m would indicate a lower modulus. The higher confining pressures at the 180 m level could counter the effect of a poorer rock quality to give a similar modulus. Calculation of S^* at the 111 and 180 m levels based on the assumed modulus of elasticity of 2.5 gives the following stresses:

At 111 m, $S^* = 1.25$ MPa.

At 180 m, $S^* = 0.55$ to 0.71 MPa.

The maximum principal stresses at the 111 and 180 m levels are estimated to be about 3.5 and 5.4 MPa respectively. The stress change S^* which occurred during the extensometer measurements would be about 35% and 12% of the field stress. About 14% and 7% of the total tangential and radial stress changes respectively, which were measured by the stressmeters (Section 6.3.4), occurred between the shaft bottom and lining installation. The higher percentage at the 111 m level reflects the additional radial displacements which occurred after the lining was installed. Comparison of the measured stress change to the observed displacement profile confirms that the *in situ* E is about 2.5 GPa.

6.2.6 Practical Recommendations Arising from Extensometer Measurements

Interpretation of extensometer data requires the *in situ* modulus of deformation of the rock mass. The modulus

must be obtained from either *in situ* testing by a pressuremeter or similar instrument, or from on-site testing of large samples immediately after sample recovery. Modulus profiling in a horizontal borehole away from the shaft using a pressuremeter would be one way of testing the modulus zoning hypothesis.

Installation of extensometers adjacent to a drill and blast face requires special measures to protect the reference head. Ideally the extensometers should be installed as close as possible to the face (shaft bottom), and as soon as possible, to allow maximum deformation measurement. Speed of installation could be increased significantly by using a rotary percussion drill over a diamond drill. Optimal orientation of the extensometers is important for interpreting the orientation of the field stress and N , the ratio of the principal horizontal stresses. Four extensometers would be ideal, with the radial orientations at 0° , 30° , 60° and 90° to the expected major principal biaxial stress. An extensometer oriented at 30 degrees to the major principal stress is insensitive to N , and therefore is best for estimating E/S^* . The extensometer oriented at 90 degrees to the major principal biaxial stress will show the greatest sensitivity to N . Estimation of the orientation of the major principal stress is almost impossible for N between 0.8 and 1.0 . Measurements from extensometers after the lining has been poured give the radial displacement from concrete shrinkage and thermal

contraction. The radial closure at the 108 m level after the lining was poured, was about 0.53 mm.

6.3 Stressmeters

6.3.1 Stressmeter Data Reduction

The purpose of installing the vibrating wire stressmeters, was to measure the stress change in the wall rock associated with the advancing shaft. To obtain the maximum practical measurable stress changes, the gauges were installed about 10 m or 3.8 radii ahead of the shaft bottom, and as close to the projected blast line as possible, as shown on Figures 4.5 and 4.6. The orientation of the gauges, in radial and tangential positions with respect to the shaft, was selected for ease of data interpretation.

Equation 6.1 presents the theoretical relationship between the uniaxial stress change and the readout frequency, developed by Hawkes and Bailey, (1973).

$$\sigma_r = \frac{\left[\frac{422400}{T_o}\right]^2 \left[1 - \left(\frac{T_o}{T}\right)^2\right]}{11.4 - 0.66 \times 10^{-6} E_r} \quad \text{Eq. 6.1}$$

where:

σ_r = uniaxial stress change (psi)

T_o = previous reading

T = current reading

E_r = Young's Modulus of rock (psi)

The Young's Modulus was assumed to be 1.5 GPa. Zero or base level drift was observed in the gauges following activation against the walls of the borehole, when the shaft bottom was stationary. The drop in pressure between the gauge platens and the borehole walls resulted from yielding at the bedrock/platen contacts. A nearly linear relationship of the data collected during the stationary period on a plot of stress change vs. log time was used to estimate the zero reading on the gauges when shaft blasting resumed. Gauge leads were inaccessible after installation period, until the concrete forms were lowered to pour the next lift. Significant stress changes did not occur during this period, as shown in Figures B.15 - B.17. Stress change data is presented in Figures B.9 to B.17, as time-stress change plots and shaft depth-stress change plots. Both arithmetic and log-time plots are shown.

6.3.2 Discussion of Errors

It is appropriate to discuss the limitations involved in calculating stress changes from stressmeter measurements. There are two major sources of error or uncertainty in interpreting these results. The first relates to the error in determining the exact location of the gauge with respect to the shaft wall. Gauge locations shown on Figures 4.5 and 4.6 were obtained from calculations based on the measured plunge of the drill holes ($\pm 2^\circ$), the length of the drillholes and the distance from the centre of the shaft (measured from

the laser plumb) to the drill hole collar. A $\pm 2^\circ$ uncertainty in the plunge of the drill hole would result in about ± 0.35 m radial error at a depth of 10 m. Thus there is the potential for a 0.35 m error in calculating the r/a value used in interpreting the stress change data. The shaft radius at the depth where the gauges were installed was calculated as the average outside radius from the volume of concrete poured over a 3.9 m length of shaft. The actual radius of the plane containing the gauges may have deviated from the average, and from a circular cross section as a result of irregular overbreak. Near the 152 m level, irregular overbreak was observed to be up to 0.3 m greater than the excavation perimeter, but generally overbreak was within 0.15 m of the average perimeter.

The second source of error concerns the response of the gauges to stress changes in the rock. When the gauges are installed the radius of curvature of the gauge platens (soft rock type) is less than the borehole radius. In softer rocks, full platen contact only develops after some yielding around the platens or rock. Pariseau and Eitani (1977) found from finite element studies, that for both elastic and elastic-perfectly plastic rock behavior, the response of the gauge to uniaxial stress change was insensitive to both the Young's Modulus of rock and the contact angle of the platens. Creep was assumed negligible due to the short loading history. They also found from hollow cylinder triaxial tests on coal, that the sensitivity of a soft rock

gauge under realistic loading conditions in the sample annulus was close to the response predicted by the finite element analysis, and the calibration provided by the manufacturer. The behavior of the gauges under conditions of constant load in time dependent rocks is unknown, and has not been studied to date.

The variation in tangential stress changes measured by the two gauges installed about 0.3 m apart in the inside drill hole on the south wall (Figure B.9), may have resulted from real differences in the stress changes in the rock, or from the gauge response to the same stress change. Unequal stress changes in the rock could result by installing one gauge in a siliceous concretion, or across a bedding plane, joint, or bentonite seam. On the other hand the variation may have resulted from the loss of the soft rock shoe from the gauge body, resulting in different response characteristics of the two gauges. The gauge response under uniform stress change conditions may be influenced by the magnitude of the prestress level.

6.3.3 Estimation of the *in situ* Stress Field

6.3.3.1 Method of Analysis

Analysis of stressmeter data has been divided into two areas. The first concerns the analysis and interpretation of the *in situ* stress field from stress change measurements. The second studies the influence of the shaft bottom on

stress changes in the shaft. For the *in situ* stress analysis the measured radial and tangential stress changes were compared to the predicted radial and tangential stress changes to obtain an estimate of the magnitude, degree of nonuniformity and geodetic orientation of the *in situ* stress field. Stress changes were calculated for two cases, an intact case assuming no rock damage and a second by assuming 0.3 m of broken wall rock. The shaft radius was assumed to be 0.3 m larger for the latter case with no support from the broken rock. A plane strain elastic analysis was used to calculate the radial and tangential stress changes which occur at the gauge locations during excavation of the shaft. Appendix C.2 presents the derivation of the formulas used to calculate the radial and tangential stress changes.

A linear elastic model was chosen for this section of the stressmeter analysis for two reasons. First, the model provides a simple analysis with minimal knowledge of the field conditions and material properties. Second, observations of the tangential stress changes and extensometer movements did not indicate that the rock was yielding around the gauges.

Figures 6.9 to 6.12 present normalized predicted stress change curves for the two cases considered (intact and 0.3 m broken), for two r/a positions of the gauges. The *in situ* field stress ratio was N , the magnitude of the stress, and the orientation of the major principle stress was estimated by normalizing the measured radial and tangential stress

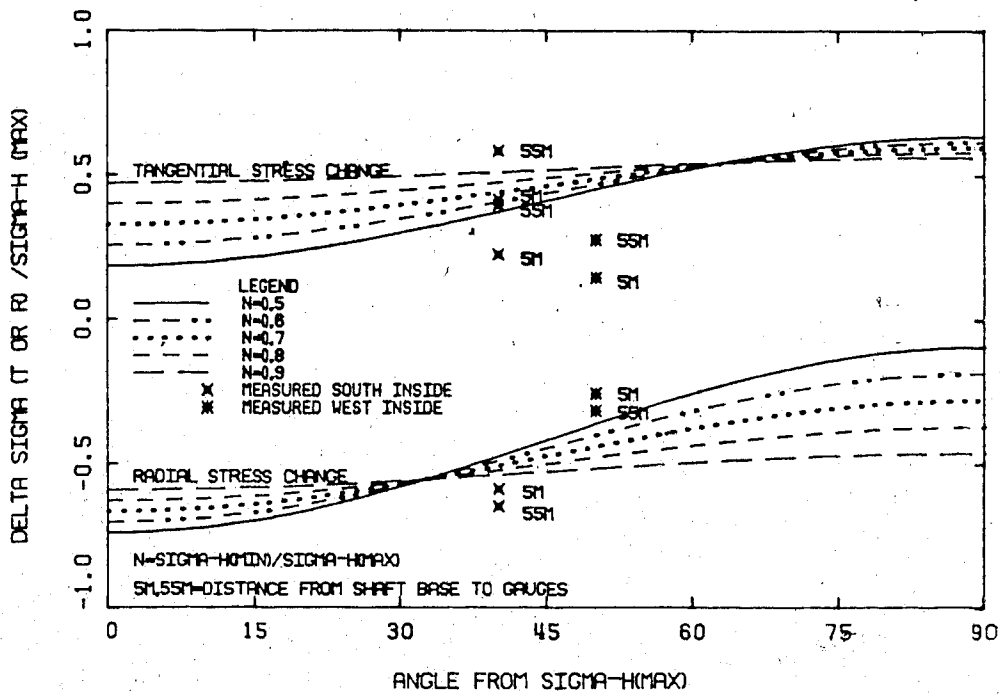


Figure 6.9 Plot of Predicted Radial Elastic Stress Changes at $r/a=1.35$ Normalized to the Maximum Field Stress vs. Orientation of Maximum Field Stress

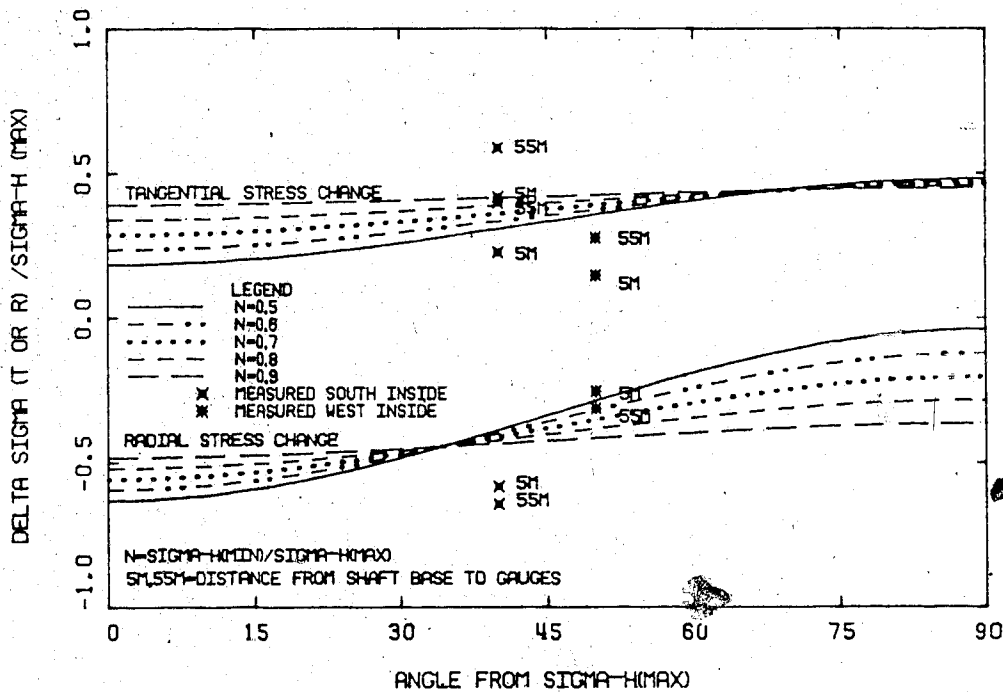


Figure 6.10 Plot of Predicted Radial Elastic Stress Changes at $r/a=1.50$ Normalized to the Maximum Field Stress vs. Orientation of Maximum Field Stress

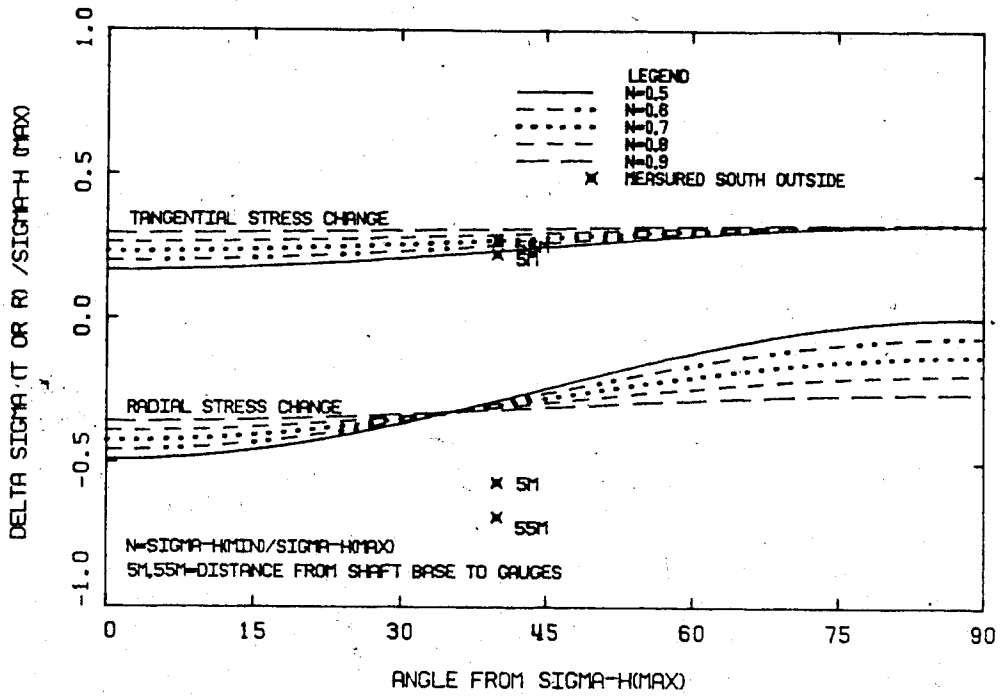


Figure 6.11 Plot of Predicted Radial Elastic Stress Changes at $r/a=1.75$ Normalized to the Maximum Field Stress vs. Orientation of Maximum Field Stress

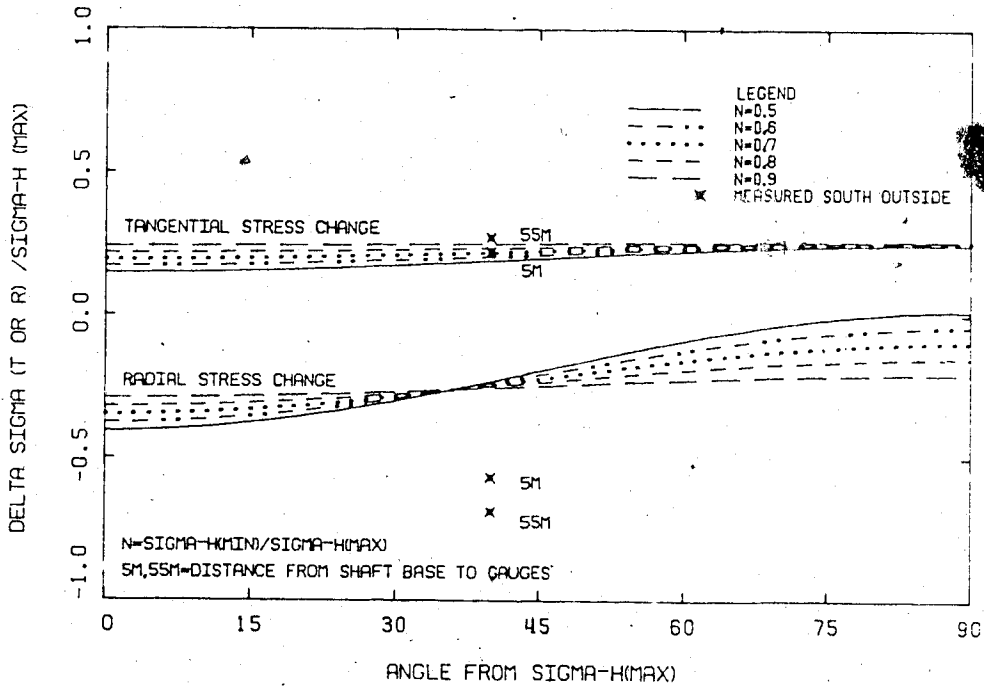


Figure 6.12 Plot of Predicted Radial Elastic Stress Changes at $r/a=1.95$ Normalized to the Maximum Field Stress vs. Orientation of Maximum Field Stress

changes to the assumed major principle field stress and checking the fit on the proper curve. Figures 6.9 to 6.12 show the measured stress changes normalized to the best estimate of the field stress and plotted at the estimated field stress orientation. Table 6.1 gives the values of the measured stress changes used for the *in situ* stress calculations, measured when the shaft bottom was 5 m and 55 m, respectively, below the plane of measurement.

The relatively flat response of the tangential stress change curves with respect to N , and the rotation of the major principle stress shown on Figures 6.9 to 6.12 limits the use of tangential stress change measurements in interpreting the orientation of the major principle stress. This leaves the tangential stress change measurements suited to estimating the magnitude of the major principal stress. The increase in the sensitivity of the tangential stress change to N as r/a decreases adds to the difficulty in predicting the major principal field stress. The greater sensitivity of the radial stress change curves to N and the orientation of the major principal field stress allows the tangential and radial stress change measurements to be used in pairs to estimate all three unknowns. However in most cases the combined analysis predicts unreasonable values of N , θ and σ_h (max).

Table 6.1 Measured Stress Changes for Shaft Bottom at 5 m and 55 m Below Plane of Gauges

Gauge Location	r/a for Assumed Wall Condition		Gauge Orientation	Measured Stress Change [MPa]	
	Intact	0.3 m Broken		@ 5 m	@ 55 m
West Wall	1.50	1.35	Radial	-1.05	-1.34
			Tangential	0.67	1.19
South Wall Inside	1.50	1.35	Radial	-2.45	-2.73
			Tangential	0.98	1.68
			Tangential	1.82	2.50
South Wall Outside	1.95	1.75	Radial	-2.43	-2.93
			Tangential	0.95	1.15

6.3.3.2 Comparison of measured stress changes to Model

Table 6.2 presents an estimate of the field stress parameters from fitting the stress change measurement to the normalized curves. It will be shown that the estimates of the field stress from the stress change measurements are only the apparent field stress or the portion of the field stress which is released. The remaining portion of the field stress acts to produce a load on the shaft lining.

Reasonable agreement of the tangential stress change measurements produced an average value of $\sigma_h(\max) = 4.25$ MPa. The wider band width between $N = 0.5$ to 0.9 for the tangential stress change curves for low theta values (Figures 6.9 to 6.12) allows for about ± 1 MPa deviation in the estimation of $\sigma_h(\max)$. Matching of the combined radial and tangential measurements to estimate N and the geodetic orientation of the maximum field stress was successful to varying degrees for the three gauge locations as shown in Table 5.2. To obtain a fit of both radial and tangential measurements for the south outside location required $\sigma_h(\max) = 5.8$ MPa. The response of the radial gauge on the south outside does not fit in with the overall stressmeter analysis and may reflect a release of a portion of the prestressed load in excess of the elastic stress change. Based on the preceding analysis only the following conclusions on the *in situ* stresses can be made:

$$\sigma_h(\max) = 4.25 \pm 0.5 \text{ MPa}$$

$$N = 0.5 \text{ to } 0.8$$

Table 6.2 Field Stress Orientation and Magnitude Predicted from Stressmeter Analysis

Gauge Location	Assumed Wall Condition	Estimated Parameters			Comment on Fit
		$\sigma_{h(\max)}$ (MPa)	N	$\theta_1^{\circ} \sigma_{h(\max)}$	
West Inside	Intact $r/a=1.30$	3.5	0.5-0.6	N43°E to N47°E	Good fit on both radial and tangential gauges.
	Broken $r/a=1.35$	3.0	0.5-0.6	N45°E to N52°E	Good fit.
South Inside	Intact $r/a=1.50$	4.25	0.5-0.6	N.S. to N15°E	Good fit.
	Broken $r/a=1.95$	4.25	0.5-0.6	N to N30°E	Good fit.
South Outside	Intact $r/a=1.95$	4.25	0.5-1.0	?	$\Delta\sigma_T$ fit only.
	Broken $r/a=1.75$	5.8	0.5	N to N10°E	Poor fit with radial gauge.

$$\sigma\text{-h(max)} = S40^{\circ}W \pm 20^{\circ}$$

The results of this analysis differ from the results of the preliminary analysis reported by Kaiser *et al.* (1982). The initial interpretation indicated the same magnitude and ratio of the principal stresses, but interpreted the orientation of $\sigma\text{-h(max)}$ as approximately east-west.

6.3.4 Stress Changes Associated With the Advancing Shaft Bottom

The second avenue of analysis of stressmeter data was with respect to the influence of the advancing shaft bottom. Figures B.15 to B.17 present radial and tangential stress changes observed at the three stressmeter locations, with respect to the distance from the plane of measurement. No readings were taken when the shaft bottom was between -5 m and the plane of measurement, as the gauge leads were inaccessible behind the lining form. Figure 4.1 shows the log of shaft bottom advancement and lining installation through the Bearpaw Formation. Figure 6.13 compares the observed stress change, normalized to a uniform horizontal field stress of 4.25 MPa, to the stress change predicted by Hutchinson (1982), for $r/a=1.5$. Hutchinson (1982) used an axisymmetric linear elastic finite element analysis to study the influence of construction and lining sequences on stresses and displacements near the working face. Two finite element models were used to predict the tangential and radial stress changes associated with the advancing shaft

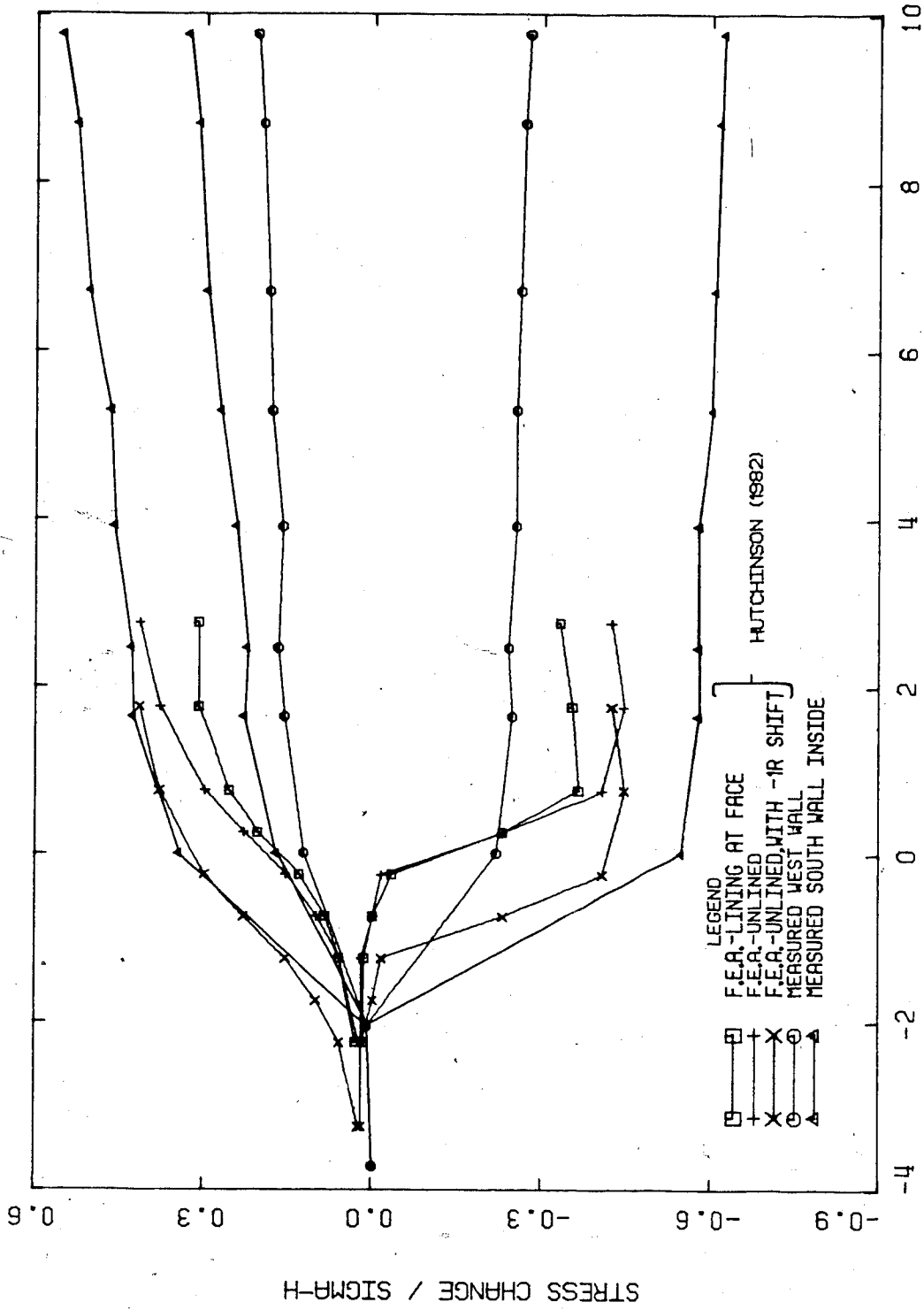


Figure 6.13 Comparison of Measured and Predicted Tangential and Radial Stress Changes of $r/a = 1.5$ vs. Distance from Plane of Measurement

bottom, a lined and an unlined case. In both cases the analysis simulated a full bench excavation with an excavation length of one radius at each excavation step with intact rock adjacent to the shaft. In the lined case the lining was placed to the shaft bottom, prior to excavation of the next step. The unlined case was completely unsupported. The lined case does not accurately model the actual sequence, as the lining was generally placed about 1.5 to 2 radii above the shaft bottom. Comparison of the two F.E.A. curves shows a decrease in the maximum stress change for the lined case compared to the unlined case of 21% for the radial and 25% for the tangential gauges.

The curves for both the lined and unlined cases have the same characteristic shape. Figure 6.14 (after Hutchinson, 1982) shows the tangential and radial stress change curves superimposed. The gradual change in tangential stress from about $-2R$ to $+3R$ contrasts the sharp drop in radial stress occurring between $-0.25R$ and $+0.5R$. Comparison of the measured and predicted stress change curves (Figure 6.13), shows a sudden radial stress change in the field data, similar to the radial stress change in the predicted curves. The gradual development of tangential stress changes in the field also has the same shape as the predicted stress change curve. Table 6.3 summarizes the development of radial and tangential and radial stress changes adjacent to the plane of measurement as a percentage of the stress change measured when the shaft bottom was 55 m below the gauges.

Table 6.3 Percentage of Total Measured Tangential and Radial Stress Changes Occuring Ahead of Shaft Bottom and Before Installation of Lining

Instrument Location	South Inside	South Outside	West Inside
<u>Radial Stress Change:</u>			
a) Ahead of face.	85%	76%	74%
b) Before liner installed at about 10 m.	90%	87%	78%
<u>Tangential Stress Change:</u>			
a) Ahead of face.	42% 49%	72%	43%
b) Before liner installed at about 10 m.	63% 79%	78%	50%

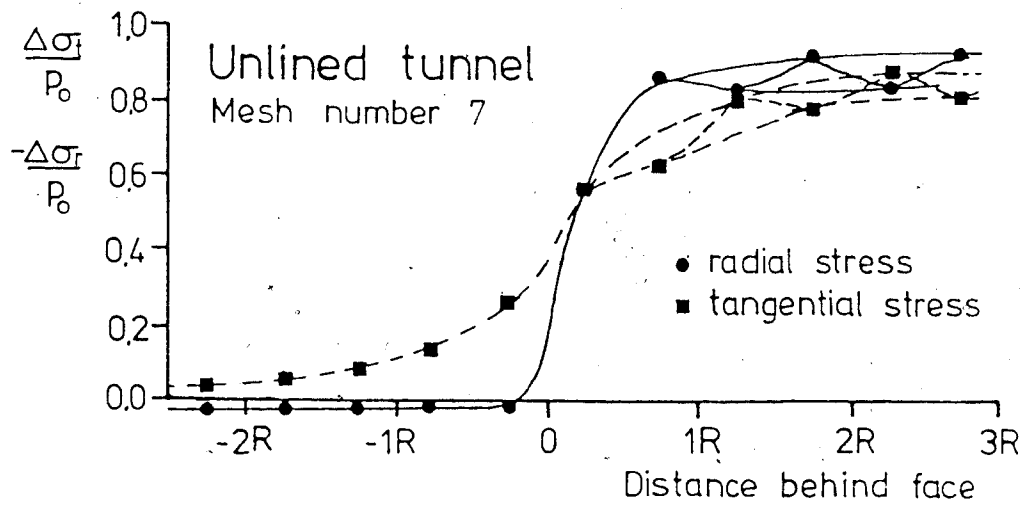


Figure 6.14 Plot of Predicted Tangential and Radial Stress Change at Tunnel Wall vs. Distance Behind Tunnel Face (after Hutchinson, 1982)

About 78% of the radial stress change and 54% of the tangential stress change occurs ahead of the shaft bottom while about 85% of the radial and 68% of the tangential stress change was recorded before the liner was installed. Because of the slow development of tangential stresses, stress change measurements used to predict *in situ* stresses will only give meaningful results when they are obtained after the face is about 10 to 20 r beyond the gauges or are adjusted to account for the delayed development of the tangential stress. In the Lethbridge shaft where a delay of 1.5 to 2.0 R in installing the lining was common, the lining would carry much less than the 25% of the field stress predicted from the lined case of Hutchinson (1982), in short term loading.

The gap in field readings between $-2r$ and the face makes it difficult to interpret the stress changes which occurred directly ahead of the face. An excellent fit of the measured stress changes was obtained with the unlined finite element model for the F.E.M. curve shifted one radius to the left on Figure 6.13. The finite element analysis used a model with a planar face surrounded by intact elastic material. A model with a semi-spherical face, or a blast damaged zone ahead of the face (modelled by a reduced modulus) would produce a leftward ($-r$) shift of the predicted tangential and radial stress change curves. Matching of the measured stress change curves to the finite element curves, indicates that some degree of stress release

has occurred at about $1r$ ahead of the shaft bottom. As described in section 4.2; the shaft bottom was advanced in half bottom rounds of $0.65r$ to $0.85r$. Data records are not detailed enough to show the round by round influence on stress changes adjacent to the face. The stress relief zone ahead of the face of about one radius may result from the initial stress relief as the first half bottom is blasted from an even floor.

The difference in response of tangential and radial stress changes (both predicted and measured) is related to the rotation of principal stresses adjacent to the face. A simple mechanistic explanation for the rapid response of the radial stress compared to the gradual response of the tangential stresses may lie in the boundary conditions governing the stresses in each direction. In the radial direction, a stress free boundary is exposed in close proximity to a point in the shaft wall, normal to the direction of measurements, providing a rapid change in the stress field. In the tangential direction the gradual increase in tangential stresses at a point in the shaft wall with the approach of the shaft face is controlled by the decreasing radial stress, but restrained from paralleling the radial stress change by the tangential stresses in adjacent material in a longitudinal direction.

6.3.5 Practical Implications From Stressmeter Measurements

Optimization of gauge locations is a function of both distance from shaft wall (r/a) and location of the drillholes with respect to the orientation of the major principal horizontal stress direction. Ideally, the gauges should be installed as close as possible to the wall/rock interface to measure the greatest stress changes. Practically the distance from the gauge to the wall is controlled by the drilling conditions and excavation method. The inside ring gauges at an r/a of about 1.5 were installed as close as practical to the shaft wall, given the restriction that the drillhole be contained entirely within the wall rock. As it was, about 3 m of the inside gauge holes were exposed after blasting, with gauge wires cut in the process. Having chosen a reasonable r/a for the gauges, a plot of stress change vs. orientation of the field stress can be developed, as shown by Figure 6.10.

Figure 6.10 shows the tangential and radial stress changes are insensitive to N at about 70° and 35° respectively to the major principal biaxial stress direction. If radial and tangential oriented gauges are installed in a drillhole at an r/a of 1.5 and oriented at 35° to σ_H (max) the major principal stress can be estimated from the radial stress change measurements, normalized to fit the curve. The variable N can then be estimated by normalizing the measured tangential stress change to σ_H (max), and observing the fit on the curve.

The same procedure could be followed for a drillhole at about 70° to $\sigma\text{-H}(\text{max})$, with the tangential stress change measurement used to estimate $\sigma\text{-H}(\text{max})$. As a measure of redundancy, gauges should be installed in diametrically opposed drillholes, therefore a total of four drillholes would be needed.

The nonuniform behavior of the gauges loading and unloading should be investigated in laboratory tests to aid in the interpretation of test sections.

6.4 Embedment Gauges

6.4.1 Data Reduction

Embedment gauge measurements were converted directly from the vibrating wire frequency, to relative strain over the length of the gauge using the relationship given in Equation 4.1. No corrections were applied to the measurements. Both arithmetic and semi-log plots of time vs tangential strain are presented in Figures B.18 to B.33. Tensile strains are shown as positive and compressive strains as negative.

6.4.2 Factors Influencing Concrete Strain Measurements

6.4.2.1 Introduction

The measurement of strain in concrete is complicated by development of strain from creep, shrinkage and temperature changes. Furthermore, the compliance of the strain measuring device must be known. Each of these factors can only be evaluated on the basis of empirical methods developed through testing and observation of the behavior of concrete. A qualitative evaluation of the effect of these factors on the strain measurements of the shaft lining is included in this section.

6.4.2.2 Compliance of the Embedment Gauge

An embedment strain measuring device must have sufficient length to accurately measure representative strain within the structure. Hornby and Noltingk (1974) recommended that the length of concrete embedment gauges be at least four times the diameter of the largest aggregate size. The Irad gauges had a length to largest aggregate size ratio of about 7. As a precaution against erroneous readings resulting from large aggregate lying against the gauges, or trapping air voids adjacent to the ends of the gauges, the gauges were cast in blocks as described in section 4.4.2. The blocks were cast in lots of 5 over a period of several weeks, and allowed to cure in a moisture room. Blocks were transported and stored on site in a cool dry room until installed. Upon installation in the lining the blocks would tend to swell initially at a relatively rapid rate in the

wet mix. This process would stop or become imperceptible within about 12 to 18 hours after installation, as the free moisture in the concrete decreases during hydration. The concrete would also provide a restraint to swelling after about 12-18 hours as it rapidly gained rigidity. Because of the initial stiffness contrast between the gauge block and the concrete, there would be some error in the strains measured by the gauge. The stiffness contrast will become insignificant as the concrete gains stiffness with time. The problem of the stiffness contrast between the concrete and the gauge block is complex and will be discussed later in relation to calculation of stress in the concrete at a young age.

Probably the most important factor to be evaluated with respect to the compliance of the gauge is the difference in the coefficients of thermal expansion of the gauge and the concrete. The coefficient of thermal expansion of the gauge is about 12.5 micro strain/C° (Irada Gage, 1979). A difference between the coefficient of thermal expansion of the gauge and concrete will result in the measurement of strain by the gauges, due to a change in temperature. A higher coefficient of thermal expansion of the gauge with respect to the concrete would result in measurement of increasing compressive strains with increasing temperatures.

6.4.2.3 Thermal Properties of the Concrete Lining

The coefficient of thermal expansion of concrete is largely dependent on the type and amount of aggregate used, and to a lesser degree on the type and amount of cement in the mix. Cement pastes have a higher coefficient of thermal expansion than most normal aggregates. The variation of the coefficient of thermal expansion over the range of cement contents found in normal concretes is not as significant an influence as the type of coarse aggregate used (Mindess and Young, 1981). They give a range for the coefficient of thermal expansion of concrete from 7.4 to 13.1 microstrain/C°. Quartzite used as a coarse aggregate will increase the coefficient of thermal expansion of the concrete to the upper quoted range, whereas limestone as a coarse aggregate reduces the coefficient to the lower quoted range. Intrusive igneous rocks (granites, etc.) used as aggregate would give intermediate concrete coefficients. Aggregate used for the concrete lining mix was obtained from local river gravel deposits and contained mostly quartzite and granitic gravel with minor quantities of limestone gravel. An estimate would place the coefficient of thermal expansion of the concrete between 9 and 11 microstrain/C°, or from 1.5 to 3.5 microstrain/C° below the gauge coefficient.

Thermal effects on the lining are significant during the first few days when high temperatures are generated by the heat of hydration, and during the winter when cold air

circulated through the shaft cools the concrete. Temperature measurements were not taken during the investigation.

The ambient rock temperature about 100 m below the ground surface is about 10°C. Concrete temperatures during initial curing stage when the mix starts to gain rigidity are estimated to be in the range of 50± C° for the 0.6 to 0.8 m thick lining. Neglecting any thermal response in the rock mass, the cooling of the concrete from about 50°C to 10°C would result in about (40°Cx10 microstrain/C°) 400 microstrain. The gauges would only record from 40 to 100 microstrain extension during a temperature drop of 40°C.

6.4.2.4 Shrinkage of the Concrete Lining

Volume change due to moisture content changes (shrinkage and swelling) are related to the loss or absorption of water by the cement. Swelling of the lining can be largely ruled out at the three instrumented sections. The inside wall of the lining was kept dry except over a period of a couple of week period in December 1980, when water was allowed to run down the inside wall from the water ring at 87 m. Very minimal amounts of water flowed down behind the lining at the rock/lining interface from the aquifer at about 75 m depth, as indicated by moisture present along the circumferential cracks between successive pours (cold joints).

A knowledge of the drying shrinkage is important for two reasons: to predict the diametral change at the

rock/lining interface, and to estimate the effect of shrinkage on the gauge blocks. Many factors affect the ultimate drying shrinkage. These include paste parameters (water/cement ratio), concrete parameters (aggregate stiffness), environmental parameters (relative humidity) and geometry of the structure (length of perimeter exposed to air per unit cross sectional area) (Mindess and Young, 1981). Orchard (1979) quotes ultimate shrinkage values for a W/C ratio of 0.34, and a 1 : 2.5 : 3.2 mix of about 400 microstrain (0.04%), and in another plot, estimates the ultimate shrinkage is about 200 microstrain (0.02%) for concrete with 115 kg H₂O/m³ concrete. Orchard (1979) gives the following values for the development of shrinkage with time.

Time	% of 20 Year Shrinkage
2 weeks	14-34
3 months	40-80
2 years	66-85

The Comite Euro-International du Beton (1978) presents an empirical relationship to determine shrinkage in concrete structures based on the notional thickness, relative humidity of curing, and temperature conditions. For the Lethbridge shaft the relationship is given by equation 6.2.

$$\epsilon_s(t, t_0) = - 294 \times 10^{-6} [\beta_s(t) - \beta_s(t_0)] \quad \text{Eq. 6.2}$$

where

$\epsilon_s(t, t_0)$ = the shrinkage strain developed in time interval

$(t-t_0)$

- t = the age of the concrete at time considered
- t_0 = the age of the concrete when shrinkage influence is considered
- β = a time varying function relating the change of shrinkage with time, largely dependent on the notional thickness

Because of the relatively high ratio of cross sectional area to exposed perimeter, the shaft lining has a high notional thickness and thus a significant delay in shrinkage with respect to structures with much lower notional thicknesses. This high value of notional thickness results in an estimated (t, t_0) at 450 days of about 29 microstrain. The long term ($t > 10,000$ days) would range between 250 and 300 microstrain.

The influence of shrinkage on lining strain measured by the embedment gauges will be neglected because of the difficulty in evaluating the effect. The gauge blocks were slightly dry when installed, and the swelling of the blocks shortly after installation would tend to offset the compression on the blocks due to shrinkage of the concrete mass.

The combined effect of thermal contraction on the initial cooling of the lining and shrinkage results in a decrease in the outside diameter of the lining. Extensometer measurements at 111 m depth indicated about

0.5 mm decrease in the shaft radius, which is equivalent to about 200 microstrain shrinkage plus thermal contraction. Estimation of the corresponding reduction in the radius at the 152 and 180 m levels is about 0.6 and 0.8 mm respectively.

6.4.2.5 Creep of Concrete

Creep strains are developed in concrete under sustained loads. Assuming all other factors remain constant an applied load on a concrete structure will result in instantaneous elastic deformation and a time dependent component of inelastic creep deformation. The rate at which concrete creeps is a function of the age of the concrete and the magnitude of the applied load. Laboratory tests have shown that the slope of the creep strain vs. time plot decreases with time, and for a given applied load the ultimate creep strain decreases with increasing age of concrete when loaded (Jones, 1961).

The main problem in calculating stress from strain measurements in concrete is to evaluate the creep strain component. No creep tests were run on samples of the concrete. The stress calculations were based on the assumption of typical concrete behavior.

Neville (1970) and Branson (1977) discuss the possible methods available to predict creep strains. One of the more reliable methods of predicting creep for normal concrete cured under normal conditions is presented by the the Comite

Euro-International du Beton (1978)(C.E.B.). Both Branson (1977) and Neville (1970) show good agreement between the observed and predicted creep by the C.E.B. method. A range of uncertainty of $\pm 20\%$ is suggested by C.E.B. Appendix C.3 presents the basic equations of the C.E.B. method and the calculations for determining the creep strains in the shaft lining at an age of 450 days. This time represents the age of the concrete at the 180 m level when the most recent set of measurements were taken (Nov. 20, 1981). Evaluation of the creep component of the measured strains at $t=450$ days is presented in Tables 6.4 and 6.5.

6.4.3 Analysis of Embedment Gauge Data

6.4.3.1 Non-Uniform Response of the Lining to Applied Load

In order to separate the elastic and creep strains from the total measured strains, a certain degree of subjective interpretation had to be applied to the data.

The response of diametrically opposed gauges, in the same position and orientation in the lining with respect to the inside shaft margin, should be the same if the lining has a uniform thickness and modulus of elasticity, and if it is subjected to a distantly applied biaxial stress field by an isotropic rock mass. The observed variation in the outside lining radius was generally about ± 0.15 m or $\pm 5\%$ for an average outside radius of 2.9 m. Also a variation in the location of the gauges of ± 8 cm is possible due to movement

during initial placement and vibration in the mix. Some rotation of the gauges could have occurred.

Some variation in the lining modulus must be expected because of non-uniform concrete placement. Vibration of the concrete over restricted sections around the lining perimeter during placement could give denser and thus stiffer concrete compared to the non-vibrated pour.

Non-uniform overbreak in the rock mass will produce zones of broken rock with lower moduli of elasticity than the surrounding rock mass and may cause stress concentrations at other locations. If the zones of overbreak are not continuous around the shaft, but related in space to the blast geometry, the non-uniform zones of lower rock would exist. The zones of lower moduli would produce apparent non-uniformities in the stress field around the shaft, at least in the early loading stages.

Strains measured in diametrically opposed pairs were considered to represent the limits of the actual strains at the position where the gauges were installed. Unusually high or low strains on a single gauge were interpreted as an indication that the gauge block had moved significantly from its initial position.

6.4.3.2 Interpretation of Lining Strains

Between the time the gauges were installed and the first set of readings which were taken about 24 hours later, all gauges developed compressive strains, varying between -8

and -84 microstrains. This initial strain development may have resulted from two sources. The first is from compression of the blocks by external loading of the concrete, and the second is from thermal contraction of the gauge block and gauge. Hydrostatic pressure of the fluid concrete would result in 2 to 3 microstrain compression of the gauges. Section 6.4.2.2 describes the effect of having the coefficient of thermal expansion of the gauge about 1 microstrain/C° higher than the coefficient of thermal expansion of the concrete. The development of concrete strains during the first week is best shown on the log time plots, Figures B.26 to B.33.

It is estimated that the maximum temperature developed in the concrete due to the heat of hydration will occur at 1 to 2 days and cool to ambient temperature conditions in the shaft after about 5 or 6 days. Estimates of the maximum temperatures developed in the concrete are between 40° and 60°C. The effect of the relatively thick lining (0.6 to 0.8 m) with cooling effectively only through the centre annulus, is to restrict the hydration temperature development near the inside shaft wall. Near the inside gauge ring the maximum temperature should develop 18 to 24 hours after placement, to about 40°C. Near the outer shaft margin (outside gauge ring), the maximum hydration temperatures would be higher, and cool at a slower rate. Maximum temperatures are estimated to be in the range of 55° to 60°C and developing about 2 days after placement and cooling to

ambient temperatures at about 6 days. This hypothesis on the curing of the lining qualitatively matches the observed behavior of the lining during the first week. The coefficient of thermal expansion of the gauge is estimated to be about 1 microstrain/C° higher than the concrete, as described in section 6.4.2.3. Therefore an increase in temperature produces compressive strains in the concrete. Figure 6.15 shows schematically the thermally generated strain response and superimposed loading strains at a typical gauge. The maximum thermally generated compressive strains are developed at about one and two days at the inside and outside gauge rings respectively. Cooling of the concrete is shown by the recovery of the initial compressive strains over the following 4 to 6 days, with the outside ring cooling at a slower rate. The nonuniform cooling of the unloaded lining ring will result in thermally induced moments in the ring, with tensile strains and possibly cracking developing on the inside margin. Figure 6.15 shows the inside ring developing tensile strains after cooling to ambient temperatures, while the outside ring strains return to zero. Within this model thermally induced strains are considered fully reversible. As external loading of the lining develops, the elastic and creep strains are superimposed on the thermally induced strains as shown on Figure 6.15. After the initial cooling period of about 10 days, the strains should ideally represent the strains due to loading. Figures B.26 to B.31 show the initial

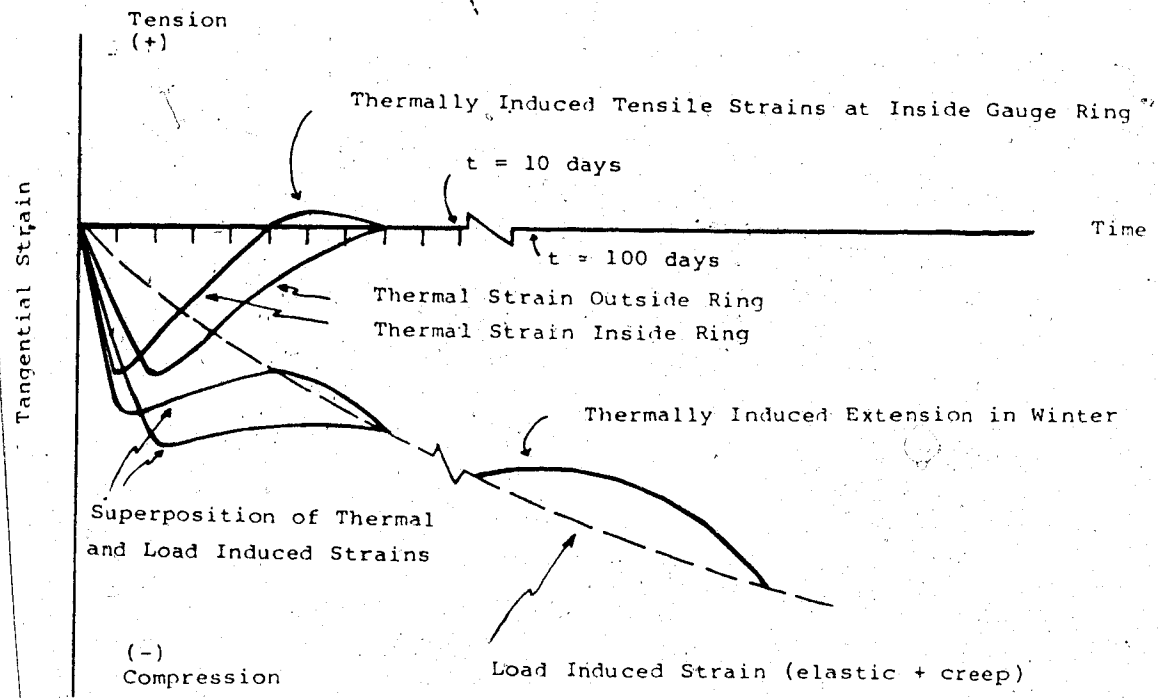


Figure 6.15 Schematic Representation of Thermal Strain Development in Concrete Lining

compressive strains vary significantly, but show maximum compressive strains are developed after one day on the inside ring, and two days on the outside ring. strains which develop on cooling of the lining at the inside gauge ring are between 1.5 and 3 times the strains which develop on the outside gauge ring over the period between one and six days. Tensile strains were measured on the inside gauge rings at the 108 and 109 m levels. It appears that thermally induced strains are largely self compensating after a period of about 7 days. The compressive strains remaining on the gauges after 6 days of cooling should represent strains due to loading of the lining.

The response of the gauges at the 180 m level is different from that observed at the upper two levels. The lining thickness at the 180 m level is about 0.81 metres compared to 0.61 and 0.66 m at 108-109m and 152 m depth, respectively. Figures B.32 and B.33 show compressive strains developing steadily over the first three days, followed by slight tensile straining over the next 16 days. It appears that the maximum thermal contraction developed at about 3 days, followed by extension on cooling over the next 13 days. During the winter of 1980-81, (readings taken about 100-200 days after installation) measurements showed tensile straining as a result of the colder temperature of the lining.

6.4.3.3 Interpretation of Lining Stresses

The short and long term elastic strains in the lining must be determined prior to calculation of the external rock loads. Creep of concrete was discussed in section 6.4.2.5, and the estimated creep function was developed in Appendix C.3. Regardless of how close the creep function approximates reality, time dependent deformations must occur if the lining is under load. The time-strain plots for the 108 and 109 m levels (Figures B.18 to B.21) effectively show no load buildup from 6 days to about 450 days with the exception of the east outside gauge at the 108 m level. This observation indicates the lining at the 108-109 m level is not loaded, or the loads are so small that the gauges are insensitive to the resultant creep. The performance of the gauges at the 108-109 m level also indicates that the zero load strain level is not fixed, but shifts in a positive or negative strain direction within the first week after installation.

Two approaches have been taken in the analysis of the lining strain measurements at the 152 and 180 m levels. The first assumes the majority of the lining strains developed at the end of the first week are due to shift of the zero load reading and do not represent strains from external loading. The second assumes that no shift of the zero load reading has occurred.

The tensile strains developed on the inside ring at the 152 m level (Figure B.30) may indicate zero compressive stress in the lining, and possibly thermally generated

moments due to a cooler inner zone of concrete adjacent to the opening. With the slower cooling of the outer margin, the thermal moments would relax, resulting in a relative increase in compressive strains on the inside gauge ring as shown in Figure B.30 for the period of 5 to 10 days after installation. This also occurs on the inside gauge rings for the 108-109 m levels but not on the 180 m level (Figures B.26, B.28 and B.32). The relatively flat response of all the gauges at the 152 and 180 m levels, after about 10 to 30 days indicates that significant short term load did not develop on the lining. If the majority of the strains at 6 days were due to external loading of the lining, then creep strains should be observed over the next month. For the initial analysis of the elastic strains in the lining at the most recent readings ($t=450$ days), the strains after 10 days were assumed to represent the zero load strains. Total strains and the tangential stress at each gauge at 450 days was calculated using equation C.3.12 and C.3.14. Gradual loading of the lining was assumed to begin at 10 days for both levels.

The second analysis assumed there were no zero point shifts of the gauges. The short term loads were calculated on the basis of the strains measured at 10 days. Creep strains were calculated for 450 days for the short term load by assuming the load was applied after 10 days. Tables 6.3 and 6.4 present the results of both analyses. The equivalent elastic strain at 450 days from the gradual loading as

Table 6.4 Evaluation of Strains at 152 m Depth, Assuming Zero Strain at 10 Days

Ring Location	Gauge Location	Case No. 1			Case No. 2		
		Measured Strain, ϵ_{450}	ϵ_{10}	$\epsilon_{450} - \epsilon_{10}$ (microstrain)	σ_{450} [MPa] (1)	ϵ_{450} (microstrain) (2)	$\epsilon_{450} - \epsilon_{(10,450)}$ (microstrain) (3)
Inside	North	-66	-6	-60	-1.19	-36	-17
	South	-21	+9	-30	-0.60	-18	-26
	East	-26	-10	-16	-0.32	-10	-29
	West	-55	-9	-46	-0.92	-28	-29
Outside	North	-86	-46	-40	-0.80	-24	-132
	South	-40	-18	-22	-0.44	-13	-52
	East	-109	-62	-47	-0.94	-28	-178
	West	-119	-50	-69	-1.38	-41	-144

Notes:

(1) σ_{450} calculated from Equation C.3.13 and C.3.14; Appendix C.3.

(2) $\epsilon_{450} = 30$ GPa (Assumed)

(3) $\epsilon_{(10,450)}$ = total strain (elastic + creep) at $t = 450$ days from commencement of ramp loading at $t = 10$ days

Table 6.5 Evaluation of Strains at 180 m Depth, Assuming Zero Strain at 10 Days

Ring Location	Measured Strain, ϵ (microstrain)			Case No. 1		Case No. 2		
	ϵ_{450}	ϵ_{10}	$\epsilon_{450} - \epsilon_{10}$	σ_{450} [MPa] (1)	ϵ_{450} (equiv) (microstrain) (2)	$\epsilon_{(10,450)}$ (microstrain) (3)	$\epsilon_{450} - \epsilon_{(10,450)}$ (microstrain)	
Inside	North	-355	-85	-270	-5.38	-161	-244	-111
	South	-176	-60	-116	-2.31	-69	-172	-4
	East	-94	-55	-39	-0.77	-23	-158	+64
	West	-123	-60	-63	-1.26	-37	-172	+49
Outside	North	-150	-65	-85	-1.69	-51	-187	+37
	South	-74	-57	-17	-0.33	-10	-164	+90
	East	-163	-74	-89	-1.77	-53	-212	+49
	West	-256	-98	-158	-3.14	-94	-281	+25

Notes:

- (1) σ_{450} calculated from Equation C.3.13 and C.3.14, Appendix C.3.
- (2) $\epsilon_{450} = 30$ GPa (Assumed)
- (3) $\epsilon_{(10,450)} =$ total strain (elastic + creep) at $t = 450$ days from commencement of ramp loading at $t = 10$ days

determined in the first analysis is presented in Column 7. The total strain at 450 days as calculated in the second analysis is presented in Column 8. The difference between the measured strain and the calculated total strain (elastic + creep) for the second analysis is presented in Column 9. A positive value indicates the calculated strain was larger than the measured strain. With the odd exception, the second analysis indicated that if the measured 10 day strains represented real elastic strains, and the creep function, appropriately described the lining behavior, then the measured strains at 450 days could be entirely accounted for by loading within the first 10 days.

The equivalent elastic strains at 450 days for gradual loading from the first analysis are not on average significantly different than the uncorrected 10 day strains. Both methods estimate similar rock pressure on the shaft lining. The analysis of embedment gauge data does not clearly show whether the loads developed within the first 10 days, or if the shaft is experiencing time dependent loading, with the loads developing gradually over a period of 450 days.

There are several indicators which support the theory that there is no significant time-dependent loading of the lining: a) the lining was generally placed within 2 radii of the shaft bottom, therefore elastic theory would predict some short term loading and b) the radial stress change gauges show little or no stress increase with time

indicating the lining loading between about day 10 and 100 is very small.

Stressmeter plots B.12 to B.14 show an increase in radial stress and reduction of tangential stress at about 100 days, after a period of quiescence. Embedment gauges at the 152 and 180 m levels also show a marked change in tangential strain at about the same time (about Dec. 1, 1980), but somewhat masked by thermal strains in the initial period. These measurements indicate an increase in lining loads as a result of ground subsidence due to raise drilling of the ventilation shaft nearby, or from driving access to the ventilation shaft or mining of test chambers through the coal seam at 209 m depth. A longer period of monitoring is needed to determine the long term rock loading on the lining.

6.4.4 Analysis of Field Stress on Lining

6.4.4.1 Introduction

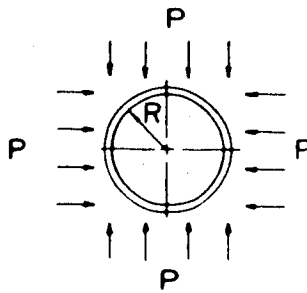
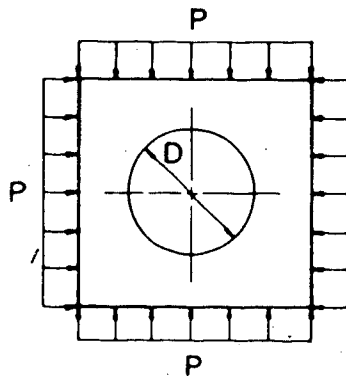
This section discusses the two methods used in calculating the field stress acting on the shaft lining. Both analyses are based on a linear elastic two dimensional plane strain model. The results of both methods of analysis, are presented as plots of tangential concrete strain, normalized to the major principal field stress. The normalized curves show the predicted strain for both the inner and outer gauge rings for $N=0.5$ to 1.0 and a 90 degree

arc of the field stress orientation, (See Figure 6.18).

6.4.4.2 Relative Stiffness Solution

The relative stiffness solution was developed as a simplified method for analyzing ground-structure interaction in tunnels (Einstein and Schwartz, 1979; Schwartz and Einstein, 1980). The method provides a closed form two dimensional linear elastic solution which is suited for time independent rock behavior and closed ring support systems in circular tunnels. The tunnel support is modeled after a thick walled elastic cylinder, but assumes uniform thrust across the cylinder under hydrostatic external load conditions. This assumption is more or less justifiable where the lining thickness is less than 20% of the external tunnel radius (Schwartz and Einstein, 1980). Lamé's equation for the tangential stresses developed across an externally loaded thick walled cylinder shows tangential stresses increase from the outer to inner wall of the cylinder (Timoshenko and Goodier, 1970). At the 180 m level in the shaft the $t/R = 0.27$, and the tangential stress differential at the inside gauge ring would be about 14% higher than the outside gauge ring, according to Lamé.

The relative stiffness of the rock to the liner is expressed by two dimensionless terms: the compressibility and flexibility ratios. Figure 6.16 presents the compressibility and flexibility ratios. The compressibility ratio reflects the relative stiffness of the tunnel liner to



E, E_s = Elastic moduli for ground and support

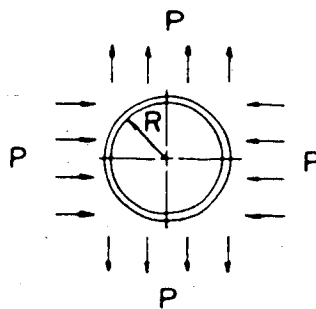
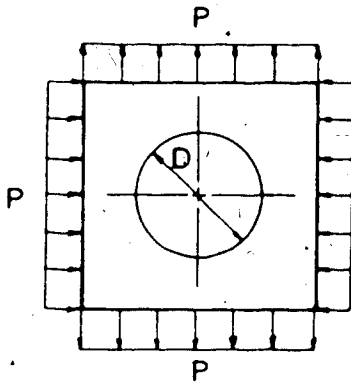
ν, ν_s = Poisson's ratios for ground and support

A_s = Cross-sectional area of support per unit length of tunnel

$$\frac{P}{\Delta D/D} \propto \frac{E}{(1-\nu^2)}$$

$$\frac{P}{\Delta D/D} = \frac{E_s A_s}{(1-\nu_s^2) R}$$

$$C^* = \text{Compressibility Ratio} = \frac{ER(1-\nu_s^2)}{E_s A_s (1-\nu^2)}$$



I_s = Moment of inertia of support per unit length of tunnel

$$\frac{P}{\Delta D/D} \propto \frac{E}{(1-\nu^2)}$$

$$\frac{P}{\Delta D/D} \propto \frac{E_s I_s}{(1-\nu_s^2) R^3}$$

$$F^* = \text{Flexibility Ratio} = \frac{ER^3(1-\nu_s^2)}{E_s I_s (1-\nu^2)}$$

Figure 6.16 Development of the Dimensionless Stiffness Ratios for the Relative Stiffness Solution (Schwartz and Einstein, 1980)

the ground mass for uniform load conditions Figure 6.16(a). The flexibility ratio reflects the relative stiffness of the tunnel liner-ground mass under asymmetric loading conditions as shown in Figure 6.16(b), (Schwartz and Einstein, 1980). The method was developed for "excavation unloading" conditions simulating the true behavior in tunnels (shafts) excavated at depth. The "excavation unloading" condition implies that the *in situ* stresses are applied initially, followed by excavation of the tunnel and installation of the liner. Because the analysis is elastic the lining load is proportional to the percentage of radial displacement allowed to occur before installing the liner. If no displacement is considered, then stresses in the lining will be due to the full applied field stress.

The boundary conditions at the interface between the rock/lining is presented by Schwartz and Einstein (1980) for the two limiting cases, "full slip" and "no-slip". The no-slip case, which assumes full transfer of shear stresses from the ground to the support, was chosen for the shaft lining analysis. The uneven blasted surface eliminates slip at the interface in intact rock. Figure 6.17 presents the formulas used for the no-slip case, and the general notation for the solution.

The following values of compressibility and flexibility ratios were used for the relative stiffness analysis of the shaft lining at the 152 and 180 m levels:

$$C_{152} = 0.214, F_{152} = 46.7, C_{180} = 0.183, F_{180} = 29.8.$$

$$\frac{u_s^E}{PR(1+\nu)} = \frac{1}{2}(1+\kappa)a_0^* + (1-\kappa)[2(1-\nu)b_2^* - a_2^*]\cos 2\theta \quad \text{Eq. 6.5}$$

$$\frac{v_s^E}{PR(1+\nu)} = - (1-\kappa)[a_2^* + (1-2\nu)b_2^*]\sin 2\theta \quad \text{Eq. 6.6}$$

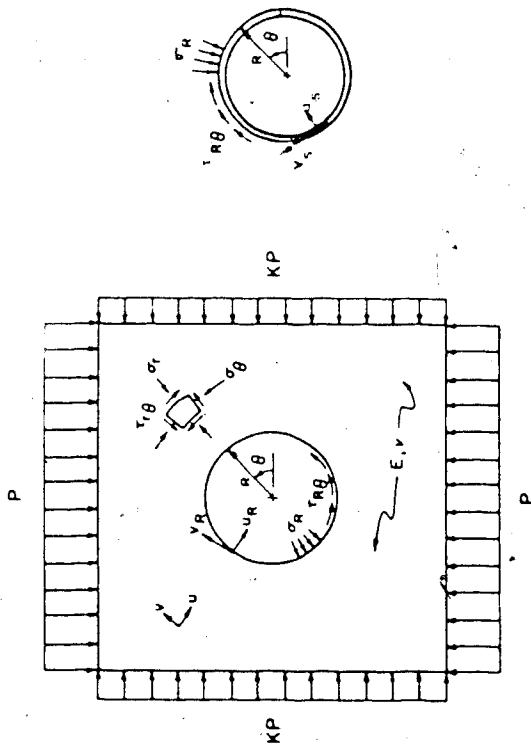
in which:

$$a_0^* = \frac{C^* F^* (1-\nu)}{C^* + F^* + C^* F^* (1-\nu)} \quad \text{Eq. 6.7}$$

$$b_2^* = \frac{C^* (F^* + 6)(1-\nu) + 2F^* \nu}{3F^* + 3C^* + 2C^* F^* (1-\nu)} \quad \text{Eq. 6.8}$$

$$b_2^* = \frac{C^* (1-\nu)}{2[C^* (1-\nu) + 4\nu - 6b - 3bC^* (1-\nu)]} \quad \text{Eq. 6.9}$$

$$a_2^* = bb_2^* \quad \text{Eq. 6.10}$$



For the no-slip case:

$$\frac{T}{PR} = \frac{1}{2}(1+\kappa)(1-a_0^*) + \frac{1}{2}(1-\kappa)(1+2a_2^*)\cos 2\theta \quad \text{Eq. 6.3}$$

$$\frac{M}{PR^2} = \frac{1}{4}(1-\kappa)(1-2a_2^* + 2b_2^*)\cos 2\theta \quad \text{Eq. 6.4}$$

Figure 6.17 Notation and Formulas for No-Slip Case of Relative Stiffness Solution (Schwartz and Einstein, 1980)

The modulus of elasticity of the lining and rock mass were taken as 30 GPa and 1.5 GPa respectively. Poisson's ratio was assumed to be 0.25 for both concrete and rock. Figures 6.18 and 6.20 present the results of the relative stiffness analysis for the two levels in terms of N and the radii of the inside and outside gauge rings. Stresses were converted into concrete strains for a concrete modulus of 30 GPa, and normalized to the major principal biaxial stress.

6.4.4.3 Finite Element Analysis of Lining Stresses

To study the effect of neglecting the non-uniform tangential stresses in a thick walled hollow cylinder under non-uniform loads, a series of plane strain finite element analyses were performed. The analysis simulated an "excavation unloading" condition. The general purpose, multi-dimensional and non-linear finite element program ADINA (Automatic Dynamic Incremental Nonlinear Analysis) was used for the analyses (Bathe, 1978). Figure 6.22 shows the element mesh used in the analyses. Because of the dual symmetry of the problem (about the vertical Y axis, and the horizontal Z axis), the problem was modelled by evaluating one quadrant only. The mesh extends for 8.3 radii in the Y and Z directions, to reduce the influence of boundary conditions on the lining stresses, and contains 119 elements, of which 36 are lining elements. Eight node isoparametric elements were used in the lining and four and three node isoparametric elements were used in the rock

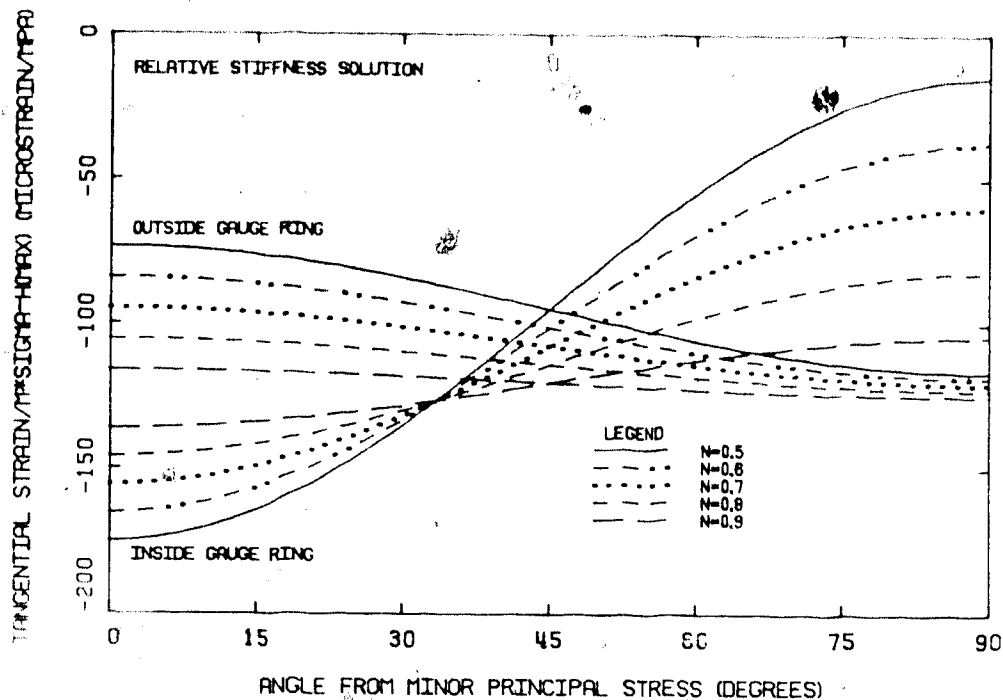


Figure 6.18 Plot of Tangential Lining Strains Normalized to the Maximum Principal Stress vs. Orientation of the Minor Principal Stress, for the Relative Stiffness Solution at 152 m Depth

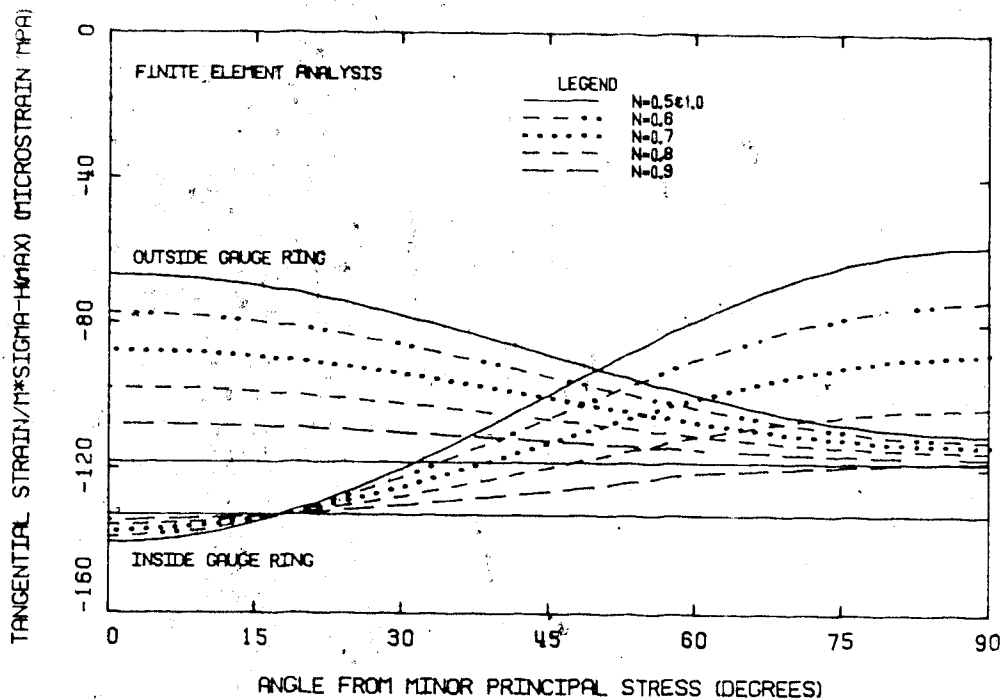


Figure 6.19 Plot of Tangential Lining Strains Normalized to the Maximum Principal Stress vs. Orientation of the Minor Principal Stress, for the Finite Element Analysis at 152 m Depth

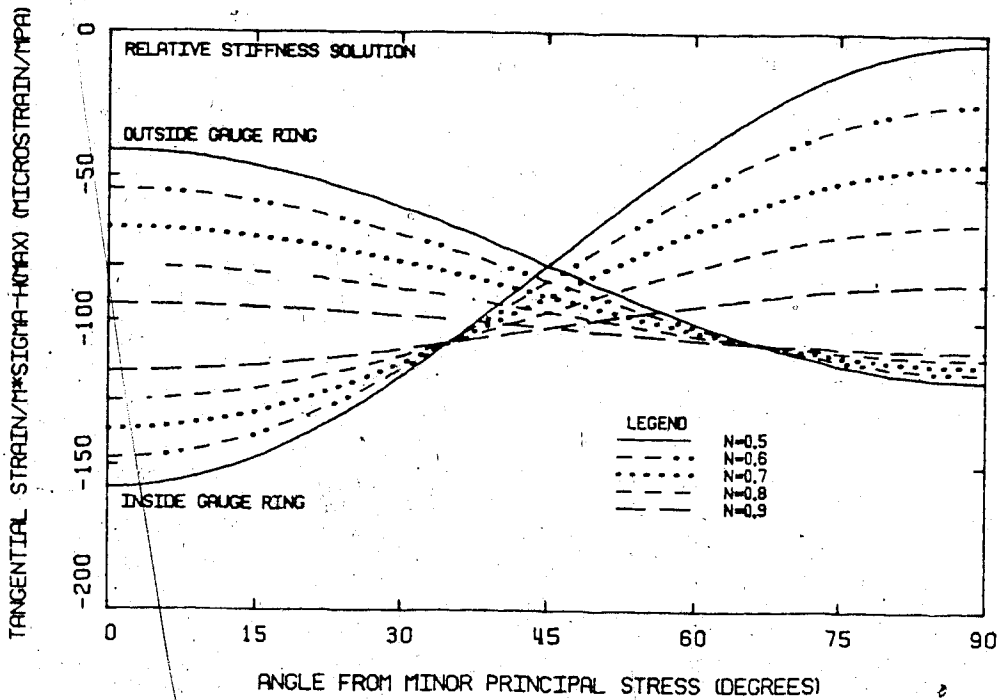


Figure 6.20 Plot of Tangential Lining Strains Normalized to the Maximum Principal Stress vs. Orientation of the Minor Principal Stress, for the Relative Stiffness Solution at 180 m Depth

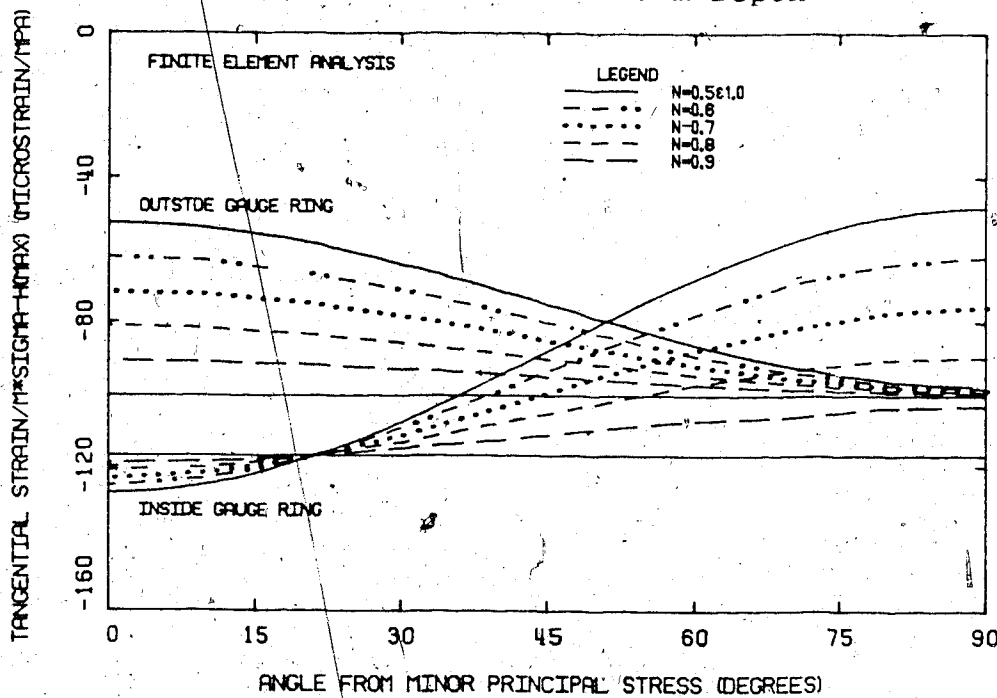


Figure 6.21 Plot of Tangential Lining Strains Normalized to the Maximum Principal Stress vs. Orientation of the Minor Principal Stress, for the Finite Element Analysis at 180 m Depth

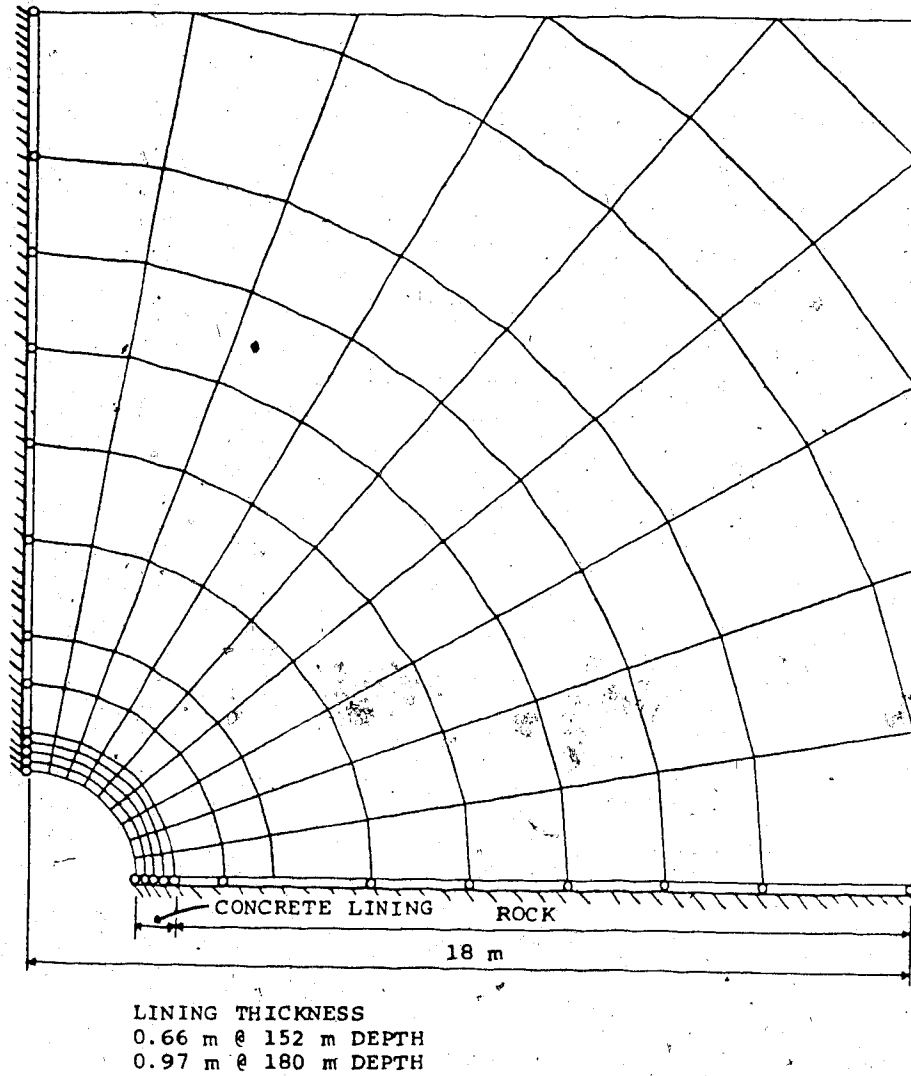


Figure 6.22 Finite Element Mesh for Lining Strain Analysis

mass. Five node isoparametric elements formed the boundary elements in the rock mass adjacent to the lining. The external mesh boundaries, and inside boundary of the shaft had two degrees of freedom. The left and bottom boundaries of the mesh had one degree of freedom each, modelled by frictionless rollers. The "excavation unloading" sequence was modelled by applying nodal forces calculated from the initial *in situ* stress field along the lining-shaft interface. The initial lining stress was zero and the single run of the program gives the final lining stress. The final rock mass stresses are the sum of the initial stresses (rock mass without tunnel) plus the incremental stresses generated when the field stress was applied on the lining. The rock and concrete properties were assumed to be the same as in section 6.4.4.2 for the relative stiffness solution. The mesh for the 152 and 180 m levels differed in the radii to the lining-rock interface, and the proportional distances to the element boundaries at 0.25, 0.5 and 0.75 of the lining thickness. The tangential stress was calculated at the element boundaries lying one quarter and three quarters of the distance through the lining, corresponding approximately to the locations of the inside and outside gauge rings. The results of the analysis are presented in Figures 6.19 and 6.21, for $N=0.5$ to 1.0, in the same manner of presentation as for the results of the relative stiffness solution (Figures 6.18 and 6.20).

6.4.4.4 Comparison of Finite Element Solution to Relative Stiffness Solution

Comparison of the normalized tangential strains predicted by the two methods, at the two depths shows similar response at both inside and outside gauge rings. The outside gauge ring strains are, however, about 5 percent higher for the relative stiffness solution ($N=1$). At the inside gauge ring, strains are about 10 percent lower for the relative stiffness solution ($N=1$). The two solutions start to deviate more if the angle from the major principal stress approaches 0 or 90 degrees, and if N approaches 0.5. The correspondence between the two solutions is particularly poor for the inside gauge ring curves, with the relative stiffness solution predicting much greater sensitivity of the lining strains to a non-uniform stress field. This may result in part from the size of the finite element mesh modelling the shaft lining.

6.4.5 Prediction of the Orientation and Magnitude of Stresses on the Shaft Lining

The average maximum external radial lining stress for each solution (Case 1 and Case 2) as shown on Tables 6.4 and 6.5 for each depth was estimated by dividing the averaged strains for each measurement ring by the normalized strain from the respective solution for $N = 1.0$. Estimations of these parameters should be considered as indicators rather than reliable quantities. The estimated values of the

stresses acting on the shaft lining are about 0.2 Mpa at the 152m level, and 0.6 Mpa at the 180m level for both the Case1 and Case2 assumptions. The difference between the finite element and the relative stiffness solutions was not significant.

6.4.6 Practical Implications from Lining Strain Measurements

Interpretation of the lining strain measurements was difficult because creep, shrinkage, and thermal strains were of the same order of magnitude as the elastic strains. Each of these quantities could be evaluated quantitatively. Creep tests on samples of the mix concrete loaded at various ages will allow fitting of the creep function to test data. Shrinkage effects could possibly be evaluated from an instrumented unloaded test ring cured under similar environmental conditions. The best location for such a test section in a shaft lining, is at a shallow depth, such as the 108-109 m depth ring where very low loads were measured. Extensometer measurements allow calculation of radial contraction of the lining during curing. The difference in the coefficients of thermal expansion of the gauge and mix can be evaluated by installing a gauge in a sample of the mix, and measuring the differential strain response with varying temperatures. Thermistors are necessary with each gauge to interpret thermal effects. The gauges could be placed directly in the mix. The initial purpose of casting the gauges in blocks was to minimize the effect of larger

aggregates adjacent to the gauge on strains. Direct placement of the gauges in the mix would eliminate the problem of shift of the zero point.

Location of the gauges could be optimized both with respect to the radial position from the inside margin, and the orientation of the gauge position with respect to the estimated major principal stress. Placement of gauges at two radial positions should be the minimum criterium for a thick walled lining. The inside gauge should be as close as possible to the inner wall, to optimize measurement of the maximum tangential strain in the section. The outside gauge should be within the outer 25% of the lining. Positions of the gauges at both diameters should be accurately measured with respect to the shaft centre.

A large number of gauges should be installed at each instrumented section. If 16 gauges are used, 4 diameters can be instrumented with inside and outside gauge pairs at each diametral end. The orientation of the 4 diameters could be at 0° , 30° , 60° and 90° to the estimated principal stress direction.

6.5 Piezometers

Data from the vibrating wire piezometers installed at 111 and 140 m was reduced from the frequency reading to water pressure by the use of tables in the operating manual and applying the gauge calibration factor. The piezometers

have confirmed that there are no significant water pressures acting on the shaft lining as a result of seepage from the aquifer at a depth of about 70 m. Pressures on the shaft lining at 111 and 140 m in December 1980 were 17 and 11 KPa respectively. In November 1981 the pressures at the same levels were -7 and -14 KPa respectively. The water pressures can therefore be effectively considered as zero.

The shaft liner acts as a slotted casing, with circumferential cracks formed at the intersection for successive lining pours (cold joints). Seepage from these joints in the vicinity of the aquifer at about 70 m demonstrates the drainage effect of the cracks.

6.6 Conclusions from Instrumentation Analysis

Analyses of extensometer, stressmeter and embedment gauge data has been presented in this chapter. All analyses have been based on two dimensional linear elastic models, with the exception of the analysis of the influence of the advancing face on stressmeter data. Normalized curves have been developed for each of the models used in the analysis to evaluate the influence of a number of independent variables simultaneously. Optimal location of each type of instrument may be selected through the use of normalized curves combined with an estimation of the orientation and magnitude of the field stresses.

The overall evaluation of the shaft performance is possible through presentation of the measured and estimated parameters on a convergence-confinement plot, developed in Chapter 7. The *in situ* testing and instrumentation has yielded sufficient data to develop the complete convergence and confinement curves with reasonable confidence. Data from each of the three major types of instruments has been used to evaluate the regional stress field estimation developed in Chapter 5. Success in evaluating the orientation of the major principal horizontal stress has been limited with extensometers and embedment gauges. Reasonable agreement was obtained from the stressmeter analysis. The most conclusive evidence on the ratio of the horizontal principal stresses was obtained from the extensometers at the 180 m level, which indicated that N was about 0.6 to 0.7. Stressmeters have been used to calculate the tangential and radial stress change associated with the advance of shaft bottom, the percentage of the total measured stress change which occurred below the shaft bottom, and prior to installing the shaft lining. Extensometers have been used to measure the radial displacement which occurred between the shaft bottom and lining installation, and the radial contraction which accompanies the initial lining shrinkage and cooling. From an estimation of the *in situ* deformation modulus of the rock the radial displacements were related to a percentage change in stress with shaft bottom advancement.

Analysis of embedment gauge data has allowed assessment of the external lining loads at the three instrumented levels. Measurements show there is little or no loading at the upper level (108-109 m). Calculation of the loads at the 152 and 180 m levels is complicated by zero gauge shift and concrete creep. The two extreme conditions assumed for analysis have yielded about the same stresses for the most recent measurements, but differ in the predictions of long term loads. Indirect evidence that the continued compressive straining of the embedment gauges is largely a result of concrete creep comes from the stressmeter measurements at the 152 m level. Figures B.9 to B.11 show a slight increase in radial stresses and decrease in tangential stresses up to about 200 days, indicating some load increase in the lining. The response of the stressmeters from about 100 to 450 days showed either a reversal of the earlier response or no change, indicating a short period of load buildup on the lining from about 100 to 200 days followed by no buildup and even possibly a load decrease. The load increase at about 100 days appears to be related to driving roadways in the coal seam at the 209 m level. Approximately 80m of roadway were cut between Dec. 16 and 22, 1980, which corresponds to the time the load increase occurred. Continued monitoring of the embedment gauges and stressmeters will allow determination of the time dependent loading of the lining.

7. EVALUATION OF SHAFT LINING PERFORMANCE

7.1 Introduction

This chapter presents the evaluation of the shaft lining performance. The results of the instrumentation and *in situ* stress analysis are used to develop convergence-confinement curves for the 152, 180 and 230 m levels of the shaft. The performance of the shaft lining is evaluated, and compared to an alternate support system of shotcrete.

7.2 The Convergence-Confinement Method

The convergence-confinement method, or characteristic lines method has received considerable attention in recent years (Gesta *et al*, 1978), both as a conceptual framework for understanding the ground-structure interaction in tunnels and as a quantitative tool for the evaluation of the performance tunnel support systems.

The method is applied by calculating two characteristic curves of radial displacement vs. radial stress, the ground convergence curve and the support reaction curve. The support interaction point which is found at the intersection of the two curves, describes the radial support pressure on the lining at equilibrium, as shown schematically on Figure 7.1.

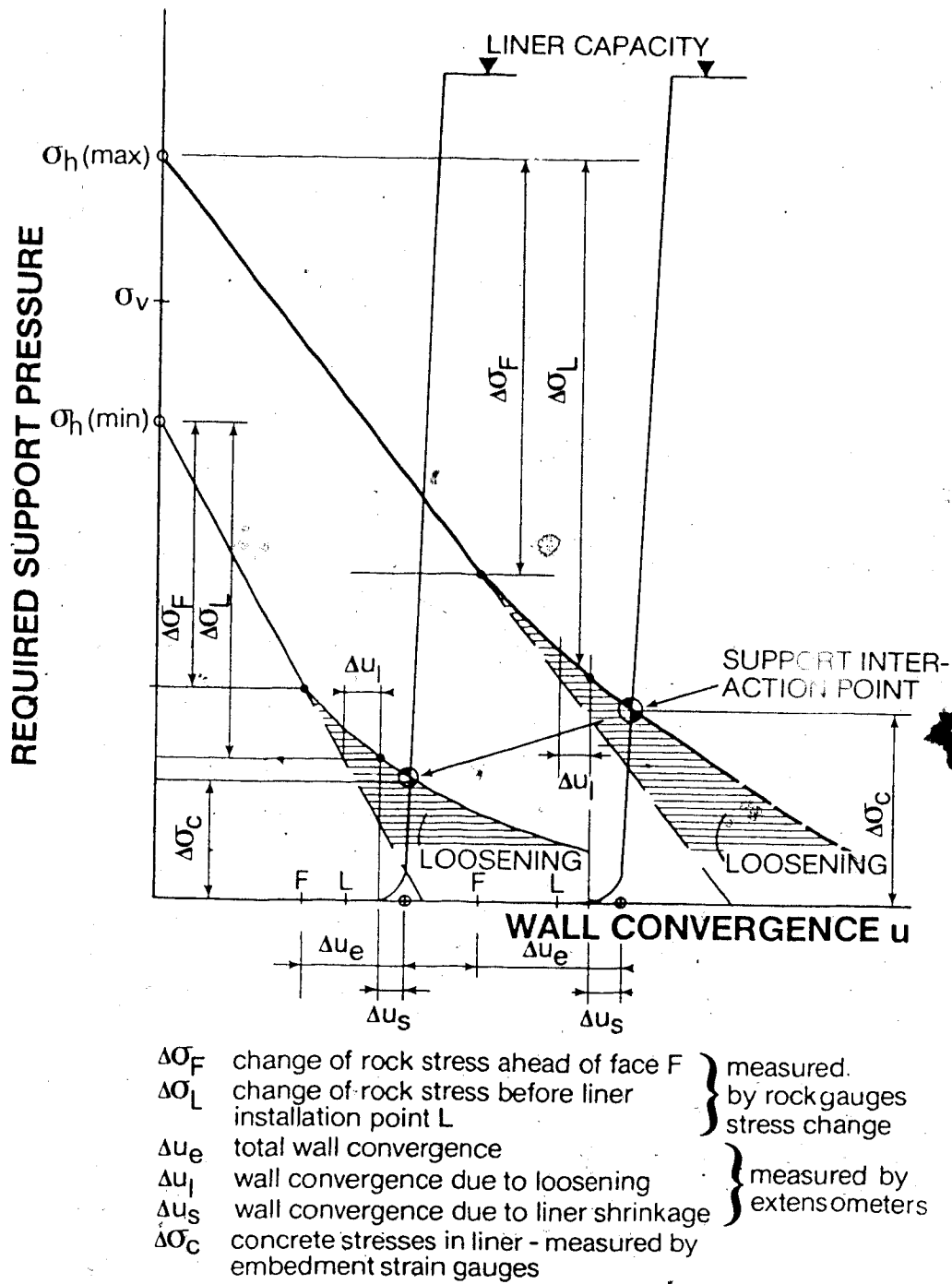


Figure 7.1 Schematic Convergence-Confinement Curves for a Nonuniformly Loaded Circular Shaft (Kaiser et al., 1982)

7.2.1 The Ground Convergence Curve

The ground convergence curve gives the relationship between the radial displacements at the wall, and the radial support pressure. The zero radial displacement point corresponds to the radial support pressure in the *in situ* virgin stress field. The three dimensional effects associated with the advancing face of an underground opening are considered as equivalent radial displacements or stress changes in a plane strain model. The radial wall displacements in a linear elastic material are a linear function of the equivalent radial support pressure. Where the *in situ* stresses are nonuniform, two ground convergence curves can be developed, limiting the range of radial wall displacements for points between 0 and 90° to the major principal biaxial field stress, as shown in Figure 7.1.

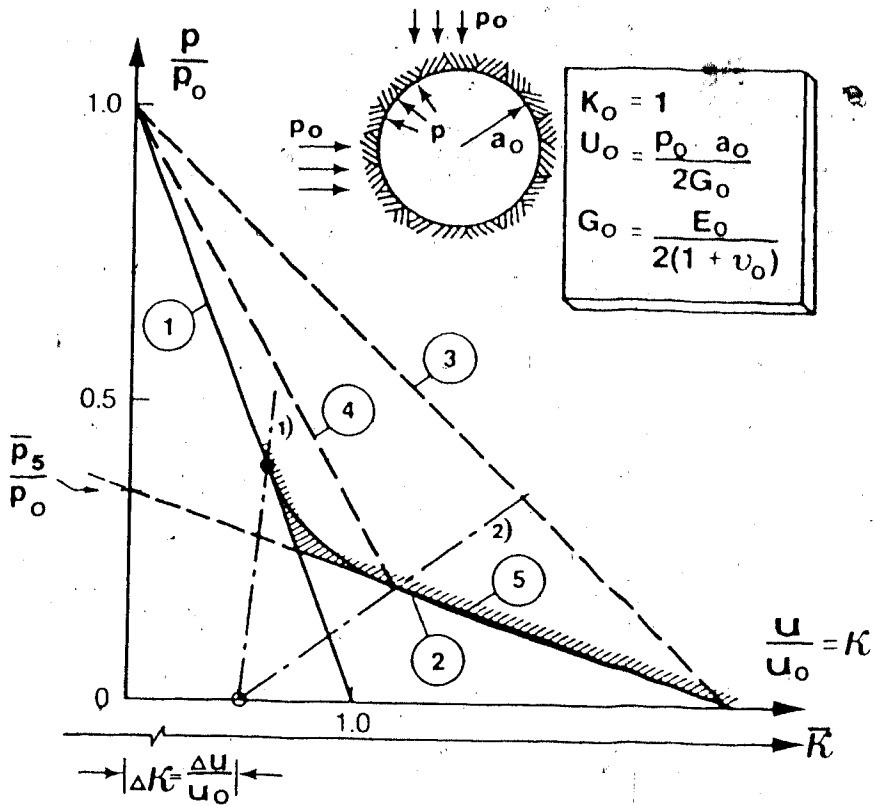
Nonlinear ground convergence curves may be associated with yielding or softening of the rock mass. The shape of the ground convergence curve in yielding ground is a function of the extent of the yielded zone and the assumed dilational characteristics of the yielded rock. Kaiser (1981) has shown that the extent of the yielded zone is controlled by the peak and ultimate failure criterion, the internal radial support pressure and the initial field stress.

Closed form solutions for predicting the ground convergence curve in a strain weakening brittle-plastic rock mass have been presented by Kaiser (1980) and Hoek and Brown

(1980). Both solutions assume an instantaneous drop in cohesion from peak to ultimate behavior at failure. Kaiser assumes a Coulomb failure criterion with a constant internal friction angle. Hoek and Brown assume an empirical parabolic strength criterion, which is presented in Section 3.3.5.4 for the mudstone at the Kipp site. Both solutions neglect time dependent behavior.

Nonlinear ground convergence may also develop in nonyielding ground, as a result of loosening or softening of the rock mass adjacent to the opening. Loosening develops if dilation of the rock occurs on preexisting or blast induced discontinuities, and softening is a result of a time independent or a time dependent local reduction of the stiffness of the rock mass. Kaiser (1981) has developed the equivalent stiffness or equivalent opening concept for evaluation of radial displacements in softening and yielding ground.

Figure 7.2 shows a schematic linearized ground reaction curve after Kaiser (1981), where the support pressure, p is normalized to the *in situ* field stress, p_0 , and the radial wall displacements u are normalized to the elastic wall displacements u_0 for zero support pressure. Curves 1 and 2 show the ground convergence curves for linear elastic and yielding ground respectively. The displacements for the unsupported yielding ground may be modelled as an equivalent linear elastic material, (Curve 3) by varying the opening size or the modulus of deformation. The support reaction



① Elastic ground; $P_0/\sigma_c \leq 1/2$; $a^* = a_0$; $G = G_0$

② Non-elastic ground; $P_0/\sigma_c \geq 1/2$; $a = a_0$

Unsupported opening:

③ Elastic ground with equivalent stiffness

$G_3^* = G_0/\kappa_3$; $a = a_0$; e.g. $\kappa_3 = 2.5$

or Equivalent opening with radius

$a_3^* = \kappa_3 a$; $G = G_0$

Supported opening: $P_s = (1-\lambda_s) P_0 = 0.12 P_0$

④ Same as ③ but $\kappa_4 < \kappa_3$; e.g. $\kappa_4 = 1.5$

⑤ Opening with variable support pressure

in elastic ground with equivalent stiffness

$\bar{G}_5 = G_0/\bar{\kappa}$; $a = a_0$; $p = \bar{p}_5$

Figure 7.2. Schematic Linear Ground Convergence Curves (Kaiser, 1981)

curves, 1) and 2) reach different support interaction points as a function of the stiffness of the support. Curve 4 shows the equivalent linearized ground convergence curve for equilibrium with support reaction curve 2). The total ground convergence curve may be linearized over segments, for example where the initial radial wall displacements are described by curve 1 and the final radial wall displacements are described by Curve 5. Curve 5 may be defined by varying either the modulus of deformation, the equivalent opening radius, or the stress field. Kaiser (1981) has used this concept to evaluate the nonlinear radial wall displacements observed in the Kielder Experimental Tunnels (after Ward et al., 1976), and has shown that it is not necessary to assume a large zone of yielded rock with low ultimate strength to explain the displacements measured in excess of those predicted by linear elasticity.

7.2.2 The Support Reaction Curve

The support reaction curve defines the relationship between radial support pressure and radial displacement at the support-ground interface. Hoek and Brown (1980) present solutions for a number of support systems. Equation 6.4 presents the closed form solution for the radial displacement-support pressure relationship for a closed ring concrete liner assuming no-slip at the tunnel/liner interface, (Schwartz and Einstein, 1980).

The maximum support pressure of a concrete ring under uniform external compression may be determined from Equation 7.1 (Hoek and Brown, 1980).

$$P_{sc(max)} = \frac{1}{2} \sigma_{c.conc} \left[1 - \frac{(r_i - t_c)^2}{r_i^2} \right] \quad \text{Eq. 7.1}$$

where

- $P_{sc(max)}$ = the maximum support pressure
- $\sigma_{c.conc}$ = unconfined compressive strength of concrete
- r_i = radius of the tunnel/liner interface.
- t_c = thickness of lining.

7.3 Application of the Convergence-Confinement Method to the Lethbridge Shaft

Figure 7.1 shows schematically the input parameters used to develop the convergence-confinement curves for the shaft. The initial horizontal stresses were estimated from *in situ* overcore testing and stressmeter measurements. Interpretation of extensometer and stressmeter data indicated the probable orientation of regional horizontal stresses. The major principal horizontal stress has been estimated with the most confidence, and is expected to be within $\pm 10\%$ of the actual stresses. The minor principal horizontal stress, used for the ground convergence curves is considered as the minimum reasonable value. The modulus of deformation of the rock mass was selected from the median

range between the low values determined in the laboratory and the high values calculated from *in situ* stress measurements. The actual average *in situ* modulus could vary by $\pm 30\%$. The linear ground convergence curves were obtained from Equation C.1.2, for the radial wall displacements at 0 and 90° to the major principal horizontal stress direction. The slopes of the two curves are not equal.

Stressmeter measurements have also been used to obtain the percentage of total stress change occurring ahead of the face, and prior to installing the liner. The measured stress change percentage was averaged from the response of tangential gauges. As discussed in Section 6.3.4, the tangential stress change vs. distance from the advancing face curve has the same shape as the corresponding curve for radial wall displacements in elastic ground. The percentage of the total stress change at any distance from the face was assumed to be constant around the shaft perimeter and the same at the 180 and 230 m levels as measured at the 152 m level. The radial wall displacements which occurred between the face and liner installation were measured with extensometers.

Comparison of extensometer measurements to stressmeter measurements taken over the same interval can be used to estimate the *in situ* modulus of deformation of the rock mass. Measurements of liner contraction due to shrinkage and thermal contraction were also measured with the extensometers (at 111 m). The support reaction curves were

calculated for the no-slip case of the relative stiffness solution from Equation 6.4. The measured lining strains were analyzed with the relative stiffness solution and a finite element model to obtain an estimate of the support interaction points described in Section 6.4.5. Tables 7.1 and 7.2 present the input data and sources for constructing the ground convergence and support reaction curves.

7.4 Discussion of Convergence-Confinement Curves

Figures 7.3 to 7.5 present the convergence-confinement curves for the 152, 180 and 230 m levels. For this analysis the ground convergence and support reaction curves were assumed to be linear. The figures show the percentage stress change and the corresponding radial displacements occurring below the shaft bottom, and before installation of the liner. The additional radial displacement due to thermal and shrinkage contraction of the installed liner was assumed to occur prior to the initial reaction of the liner. The actual stress-strain behavior of the liner would be nonlinear during the initial loading as the concrete cured. The predicted support reaction curves from the relative stiffness solution for the installed liner has a positive slope in the direction of the major principal stress (inward displacement with increasing load) and a negative slope in the direction of the minor principal stress (outward displacement with increasing load). The negative slope of

Table 7.1 Input Parameters for Ground Convergence Curve

Parameter	152 m	180 m	230 m	Source
Shaft radius a, (r:) [m]	2.82	2.97	2.91	Figure 4.6, 4.8, Construction log
Lining thickness, t_c [m]	0.66	0.81	0.75	"
Sigma-H(max) $P_{O(max)}$ [MPa]	4.5	5.25	6.9	Figure 5.5
Sigma-H(min) $P_{O(min)}$	3.0	3.5	4.6	"
$P_{O(max)}/P_{O(min)} = 1/N$	1.5	1.5	1.5	"
E_h [GPa]	2.5	2.5	2.5	Table 5.3
$u_{e(max)}$ [mm]	7.40	9.10	11.7	Equation C.1
$u_{e(min)}$ [mm]	3.17	3.90	5.02	"
Tangential stress change shaft bottom [%]	54*	55**	55**	Table 6.3
Tangential stress change before liner installed [%]	68*	70**	70**	"
Extensometer displacement u_{ext} [mm]		0.5-0.65		Figure B.3, B.4
Shrinkage & thermal contraction $u_{s,tc}$ [mm]	0.6	0.8	0.7	Figure B.1, B.2 Section 6.4.2.4
Measured lining load, P_i MPa				
Case 1: 10 days	0.2	0.6	--	Section 6.4.5
Case 2: 450 days	0.2	0.65	--	"
Initiation of yielding in rock mass [MPa]	0.71	1.08	1.62	Rock support interaction analysis (Hoek & Brown, 1980)

* Average measured value.

** Assumed to be similar measured stress change to 152 m level.

**Table 7.2 Input Parameters for Support Reaction Curves
Calculated from Relative Stiffness Solution**

Parameter → Depth →	Cast in Place liner			5 cm Thick Shotcrete			15 cm Thick Shotcrete		
	152 m	180 m	230 m	152 m	180 m	230 m	152 m	180 m	230 m
$u_s/p @ 0^\circ$ [mm/MPa]	-0.18	-0.16	-0.17	0.95	1.11	1.05	0.44	0.50	0.45
$u_s/p @ 90^\circ$ [mm/MPa]	0.82	0.77	0.79	2.36	2.61	2.5	1.81	1.91	1.83
$P_s(\max)$ [MPa]	7.2	8.2	7.9	0.5	0.5	0.5	1.55	1.5	1.5

Notes → Thickness of cast-in-place lining given in Table 7.1.
 E = 30 GPa for cast in place lining.
 E = 25 GPa for Shotcrete lining.

$u_s/p @ 0^\circ$ = normalized radial support displacement in direction of minor principal stress.

$u_s/p @ 90^\circ$ = normalized radial support displacement in direction of major principal stress.

$P_s(\max)$ = maximum support pressure.

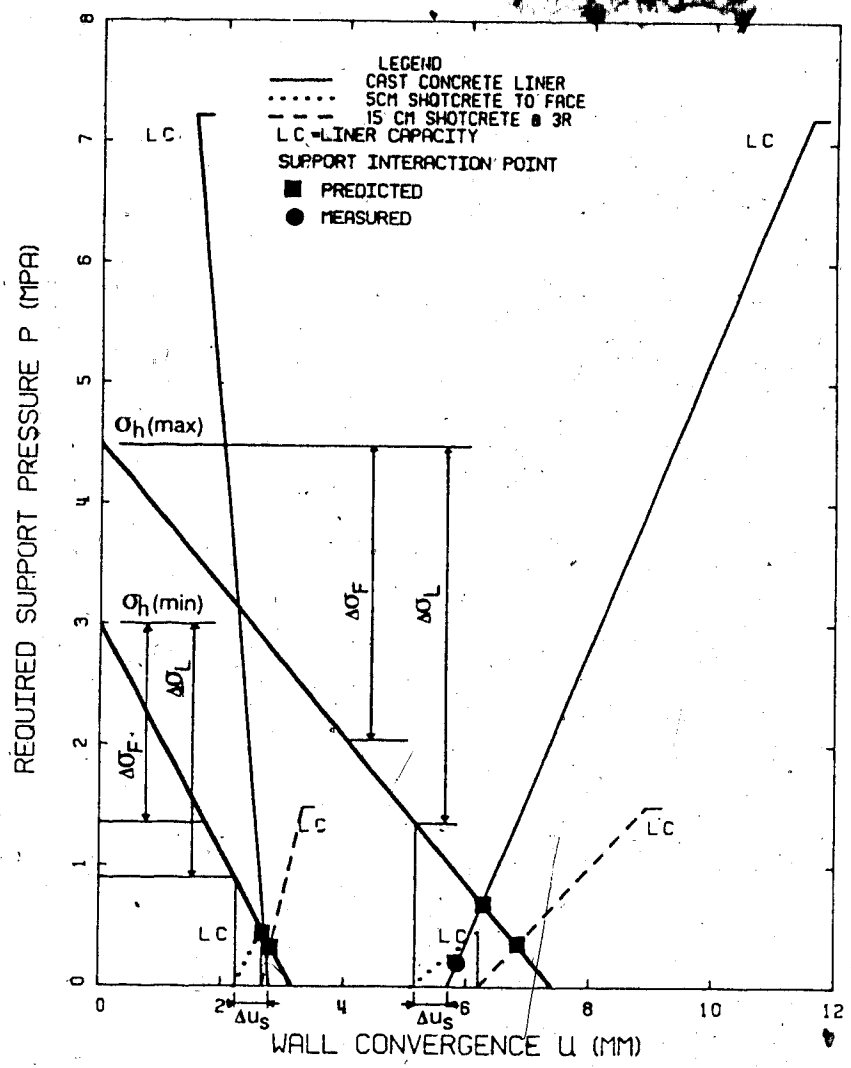


Figure 7.3 Convergence-Confinement Curves for Shaft at 152 m Depth

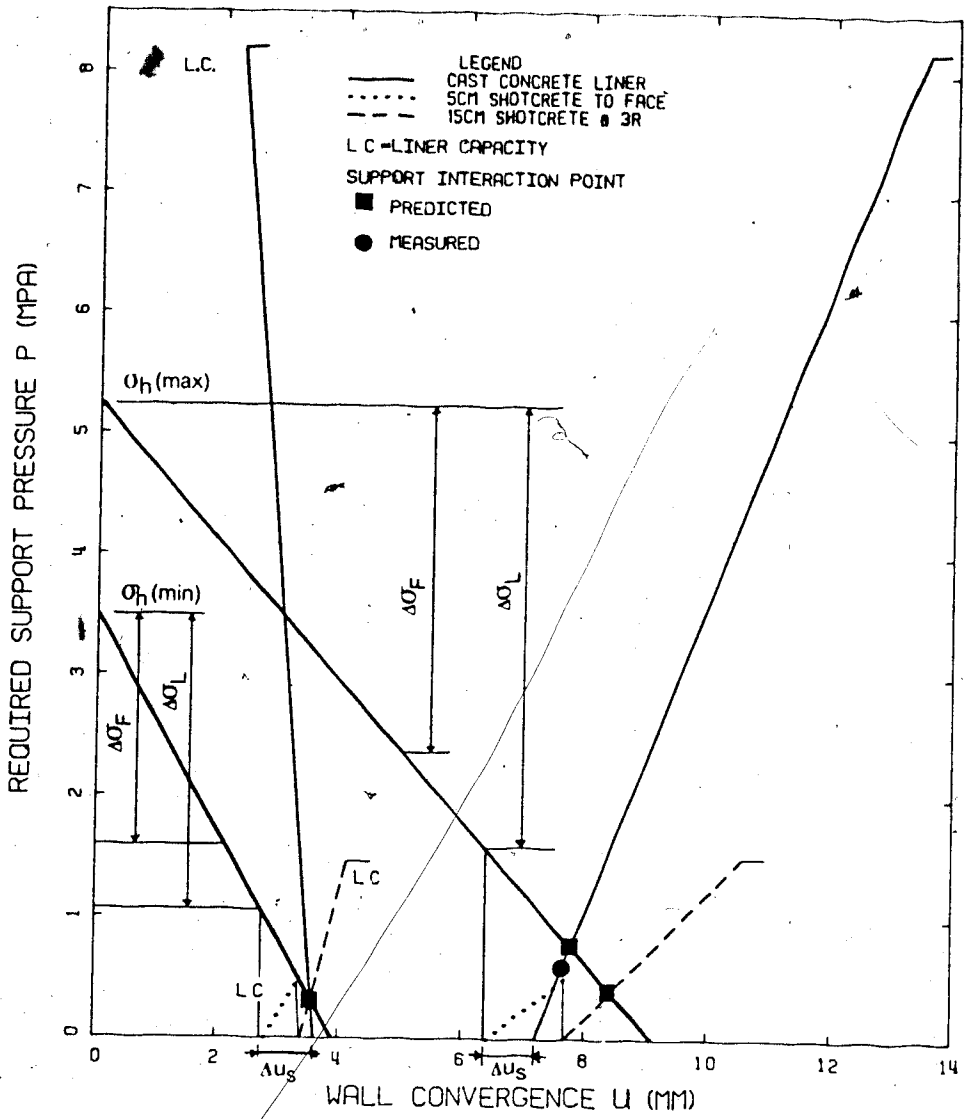


Figure 7.4 Convergence-Confinement Curves for Shaft at 180 m Depth

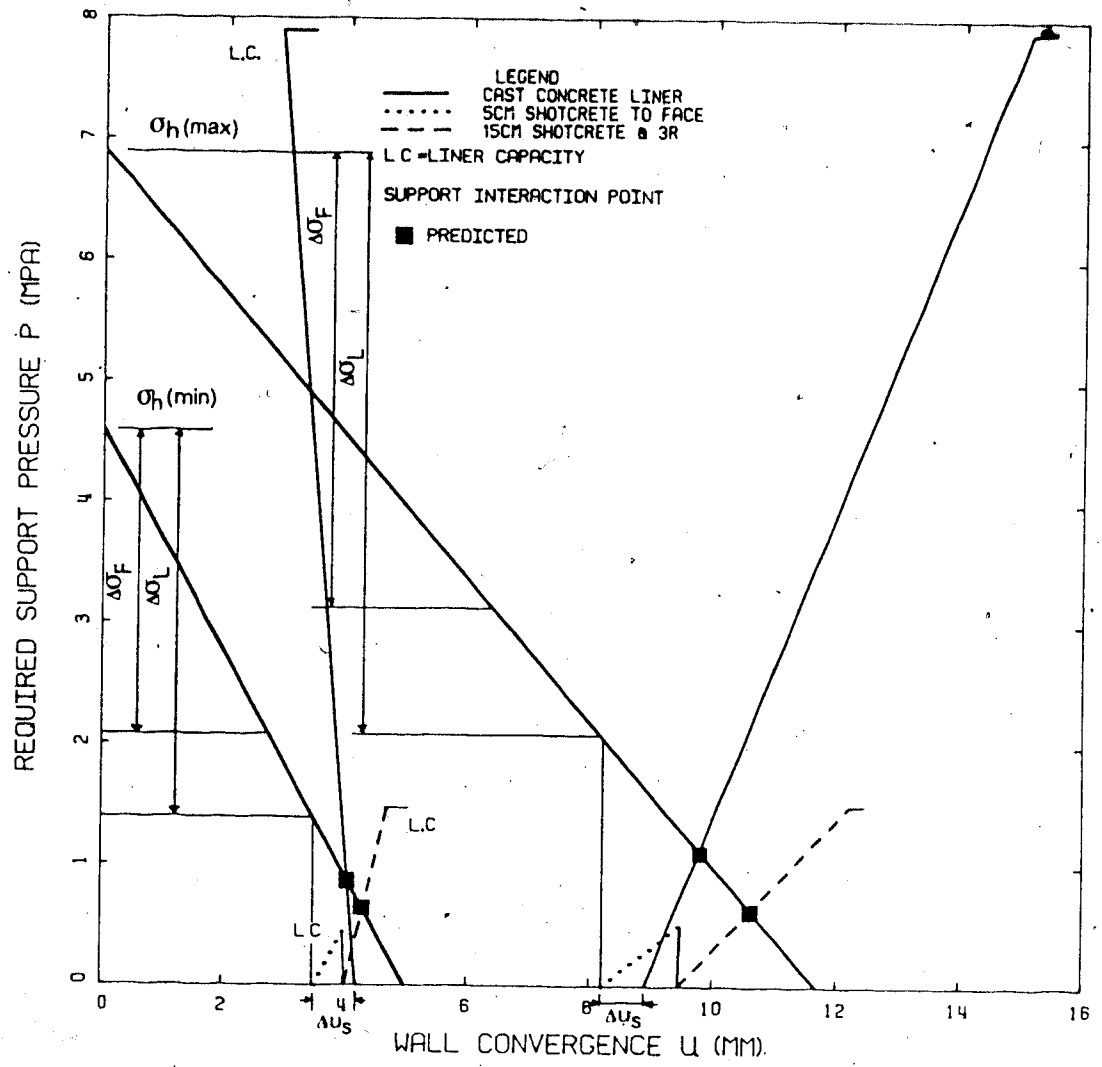


Figure 7.5 Convergence-Confinement Curves for Shaft at 230 m Depth

the support reaction curve predicts a higher load in the lining in the direction of the minor principal stress than would be predicted by using an equation for a uniformly loaded ring. The predicted support interaction point in the direction of the minor principal stress at the 180 m level is lower than the corresponding point for the 152 m level. This has developed because the increase in the estimated thermal contraction and shrinkage of the lining at the 180 m level by 0.2 mm decreases the required support pressure when the lining reaction occurs.

The convergence-confinement curves show reasonable agreement of the predicted and calculated support interaction points for the 152 and 180 m levels. The support interaction points calculated from the measured lining strains are about 30% and 80% of the values predicted by the relative stiffness solution for the 152 and 180 m levels respectively.

If the predicted support interaction points are taken as the lining loads, and the Factor of Safety of the lining is defined simply as the ratio of the maximum support pressure to the present support pressure, then the lining would have a F.S. of about 10 at 152 and 180 m and 7 at 230 m.

The difficulties in calculating the lining support pressures have been discussed in Section 6.4. The only clear evidence that there is not significant time dependent loading of the lining comes from the stable response of the

stressmeters at 152 m depth. Because the instruments have continued to function, it will be important to obtain stressmeter and embedment gauge measurements several times a year over the next few years to allow evaluation of the performance of the shaft lining under long term operating conditions.

As discussed in Section 7.2.1 the equivalent opening concept (Kaiser, 1981) may be used to develop linear ground convergence curves by considering the initial and final equilibrium conditions, without quantitatively assessing yielding, loosening or softening. The reasonable agreement which was obtained between the measured and predicted support interaction points for the installed liner indicates the assumption of linearity may be sufficient for the present analysis.

Figures 7.1 and 7.2 show qualitatively the development of nonlinearity in ground convergence curves. Nonlinear behavior may be assessed directly through measurement of loosening of the rock mass with extensometers, or by indirect assessment of yielding on the basis of the stress level compared to the rock mass strength. Loosening of the blast damaged rock adjacent to the shaft wall was not significant at the two levels of extensometer measurements. Hutchinson (1982) has shown that blast induced softening of the rock mass adjacent to the shaft wall may be undetectable from extensometer measurements if there is a linear increase in stiffness of the damaged rock away from the opening, to

the rock mass stiffness at the damaged/intact rock interface.

Closed form solutions are not available to evaluate yielding around circular openings in nonuniformly loaded ground. However, as a first approximation, yielding around the shaft at the three levels was assessed with a closed form solution for a circular opening in uniformly loaded ground, presented by Hoek and Brown (1980). The solution was described briefly in Section 7.2.1. The major principal horizontal stress at each level was assumed to be the uniform field stress. As recommended by Hoek and Brown (1980) the strength obtained from intact samples in the laboratory was reduced to approximate the rock mass strength. Figure 3.6 gives the peak and ultimate strength failure criterion for the laboratory tested samples. The peak strength of the rock mass was estimated by reducing the parameters M to 5.0 and S to 0.1 and assuming the ultimate strengths of the laboratory samples and the rock mass were equal. The ground-support interaction analysis indicated some yielding may have occurred locally below 152 m depth. The last row of Table 7.1 gives the calculated support pressure where yielding would occur. At the 180 m level, the ground-support interaction analysis predicted for the unsupported opening, 0.8 mm of radial wall displacements in the yielded rock mass a total of 8.8 mm of radial wall displacements and a radius of yielded rock equal to 1.08 times the shaft radius.

Support reaction curves for a 5 cm thick shotcrete lining installed immediately near the face and 15 cm thick shotcrete lining installed after the initial 5 cm support has yielded have been included on the convergence-confinement plots to show these support systems may be feasible alternatives for supporting the shaft wall up to depth of 230 m. There should be little doubt as to the suitability of shotcrete as a support in the upper reaches of the shaft, where no loading of the lining was observed at a depth of 108-109 m.

An initial 5 cm thick ring of shotcrete applied near the shaft bottom would yield at a support pressure of about 0.5 MPa, which, as shown on all of the convergence-confinement curves, is lower than the equilibrium support interaction point. The purpose of installing a thin shotcrete ring adjacent to the shaft bottom is to minimize loosening and damage of the wall rock during blasting of the next few benches, and thus minimize radial displacements and yielding. It is also required for safety reasons.

The maximum support pressure and post yielding characteristics of the 5 cm shotcrete ring may be enhanced slightly by placing a ring of wire mesh on the shaft wall prior to shotcreting. Its main benefit would be to prevent falling of spalling shotcrete or rock. Installation of a second coat of shotcrete to increase the thickness of the liner by 15 cm should be delayed until the shaft bottom has

advanced by 2-3 radii to allow the radial displacements to reach equilibrium. If the final intact support of 15 cm of reinforced shotcrete lining has a maximum support pressure of 1.5 MPa, and is installed when the initial 5 cm of shotcrete has yielded, as shown on Figures 7.3 to 7.5, then the lining would have a Factor of Safety of about 3.

In addition to requiring less materials for support, a shotcrete lined shaft would require a smaller excavated radius, allowing a significant saving on the excavation volume, and thus time and cost. The average lining thickness of the shaft was about 0.6 m. By reducing the lining thickness to 15 cm, and assuming 10 cm radial overbreak, the excavated volume of the shaft could be reduced by about 25%.

The above analysis is only valid for a dry shaft, where water pressures on the lining can be neglected. The piezometer measurements have shown that the shaft is dry. A shotcrete lined shaft would require drainage tubes to ensure relief of any water pressure.

7.5 Conclusions from Convergence-Confinement Analysis

The performance of the shaft lining has been analysed at depths of 152, 180 and 230 m using convergence-confinement curves. The linear ground convergence curves were developed on the basis of the interpretation of the measured *in situ* stresses and modulus of deformation. Stress changes ahead of the face and before

liner installation were measured with stressmeters at 152 m and were assumed to be representative for all other levels. Extensometers at 111 m measured radial shrinkage and contraction at the rock-lining interface.

Reasonable agreement was obtained from the convergence-confinement analysis at the 152 and 180 m levels between the measured and predicted support interaction points. Given the range of variability in the measured values of the parameters used to construct the convergence-confinement curves, the observed agreement may simply be somewhat fortuitous.

Based on the predicted support interaction point and maximum support pressure it appears the installed lining of 0.6 to 0.81 m has a Factor of Safety of about 7 to 10 at depths below 152 m.

An alternate shotcrete support ring from 15 to 20 cm thick would provide a maximum support pressure of about 1.5 MPa. Application of the initial 5 cm thickness of shotcrete to the shaft bottom would minimize blast overbreak and subsequent loosening but would likely fail by shear and need increased thickness after wall displacements have terminated. The feasibility of a shotcrete lining for the shaft depends on other factors such as cost, and also on the estimated long term load build up.

The evaluation of long term load build up was not conclusive in this study, even though the embedment gauges at the 152 and 180 m levels show a long term straining which

could indicate loading.

At least one more year of measurements will be needed to arrive at a more conclusive answer related to the long term loads.

8. CONCLUSIONS

8.1 Introduction

This thesis has examined the performance of a circular concrete lined shaft in weak bedrock (Bearpaw Formation). An extensive *in situ* testing and instrumentation program was conducted to determine the *in situ* stress field, radial wall displacements and stress changes associated with the advancing shaft bottom and the lining loads at 3 levels. A series of triaxial tests were performed on samples of the Bearpaw Formation siltstone from the shaft, to determine the peak and ultimate strength characteristics, and the loading rate dependence of the elastic deformation modulus. The performance of the shaft lining was evaluated using the convergence-confinement method.

The following sections of this chapter present the conclusions of this research program and implications for the design of future mine adits.

8.2 Laboratory Testing

Two series of triaxial tests were conducted on samples of siltstone from the shaft. Multiple failure state tests were run to obtain several points on both the peak and ultimate failure surfaces for each sample. Multiple failure state tests are easily performed and can provide a maximum of information from a single triaxial sample. Multiple

strain rate tests were conducted to determine the dependence of the elastic modulus of deformation on loading rate. The peak and ultimate strength results were fitted to the empirical Hoek and Brown (1980) failure criterion. The deformation modulus of the samples varied between 1.1 and 2.2 GPa, with the samples from the multiple failure state tests having a modulus range from 1.9 to 2.2 GPa, and the samples from the multiple strain rate tests having a modulus range from 1.1 to 1.7 GPa. The overall range in modulus is from 1.1 to 3.5 GPa. Modulus variation in the multiple strain rate tests did not show a consistent increase in modulus with increased strain rate as measured by Bieniawski (1970). Back calculation of the *in situ* modulus of deformation from overcore test data gave a range of E from 2.4 to 3.5 GPa. This implies that sampling disturbance may be a significant factor in altering the material properties of this weak argillaceous rock.

8.3 *In situ* Stress Field

In situ stresses were measured in 5 tests in a single horizontal drillhole at 91 m depth. With 4 out of 5 tests completed, the method was shown to be practical for good quality weak rock.

Analysis of stressmeter data at a depth of 152 m yielded an estimation of the orientation and magnitude of the principal horizontal stresses. The results from the

overcoring tests and stressmeter analysis support the hypothesis of Gough and Bell (1981) that the orientation of the major principal horizontal stress is northeast-southwest.

The vertical stress component is assumed to be equal to the overburden pressure, the major principal horizontal stress is estimated to be about 1.4 times the vertical stress and the ratio of the major to minor principal horizontal stress is estimated to be about 1.5.

8.4 Rock Mass Response to Shaft Sinking

Radial and tangential stress changes associated with the advancing shaft bottom were measured with stressmeters. The shape of the measured stress changes at $r/a = 1.5$ were in close agreement with those predicted by Hutchinson (1982), using an axisymmetric finite element analysis to model the advancing face of a tunnel. The radial stress change occurs suddenly near the advancing face, whereas the tangential stress change develops more gradually, reaching steady conditions several radii beyond the face. On average about 54% of the tangential stress change occurred below the shaft bottom, and 68% occurred before installation of the lining about 2 radii above the shaft bottom. About 78% of the radial stress change occurred below the shaft bottom and 85% occurred before installation of the liner. The longterm stressmeter measurements from about 100 to 200 days as shown

on Figures B.12 to B.14 indicates a slight increase in tangential stresses and a decrease or little change in the radial stresses. In terms of an elastic model, these stress changes indicate there is no increase of loads on the lining.

Extensometers were used to obtain the radial displacement distribution adjacent to the shaft. Loosening was not considered to be a significant factor in the measured radial displacements. Spalling of the wall rock at the 180 m level adjacent to the extensometers was probably not measured because of the depth of embedment of the extensometer head. Shrinkage and contraction of the lining at the 111 m level was measured from the extensometers as about 0.5 mm.

Combination of the stressmeter and extensometer measurements is essential for interpreting the radial wall displacements prior to installing the extensometers. Both extensometer and stressmeter measurements are needed for the development of the ground convergence curves.

The gradual development of tangential stresses has practical implications for the installation of rock anchors. If installed close to the face, the increase in tangential stresses will result in the development of a better bond of the anchor to the rock, as compared to installing the anchor at some distance from the face.

8.5 Development of Lining Loads

The complexity of interpreting lining loads from embedment gauge measurements has been discussed. Creep and zero shift are significant factors to be evaluated prior to determining the elastic strains. Interpretation of tangential lining strains at the upper level of the gauges (108-109 m) indicates that the loads on the lining at that depth are negligible. Interpretation of the tangential lining strains at the 152 and 180 m levels indicates about 0.2 and 0.6 MPa of external loads are acting on the lining at those respective depths. The loading at the 152 m and 180 m levels appears to have occurred during two separate and distinct periods. The first loading period closely followed lining installation and although difficult to interpret clearly because of shift of the zero strain levels, and initial thermal effects, it is a logical assumption based on the elastic response of an opening to shaft sinking as demonstrated by the convergence-confinement curves (Figures 7.3 and 7.4). The second loading period is identifiable as an increase in the lining strains from the embedment gauges at the 152 and 180 m levels and a reversal in the slope of the radial and tangential stressmeter curves at the 152 m level at about 100 days after installation (about Dec. 1, 1980), and resulted in an increase in the tangential lining strain rate for about 3 months. This second loading event may be associated with driving of the initial drifts in the coal or raise boring the ventilation shaft.

Section 6.4.6 suggests possible methods of improving lining strain measurements using embedment gauges. It appears that the most critical factors are measurement of the temperature in the concrete concurrently with strain measurements, installation of the gauges directly during pouring, and conducting creep tests on cylinders of the concrete to evaluate its creep properties.

8.6 Rock-Support Interaction Analysis

The key parameters necessary for construction of the convergence-confinement curves were obtained from analysis of the shaft instrumentation and *in situ* testing data. Reasonable agreement was obtained between the measured and predicted support interaction points. The present factor of safety of the lining at the 152 and 180 m depths is estimated to be between 7 and 10. Extrapolation of results to the 230 m level indicates the factor of safety is about 7. A shotcrete liner 15-20 cm thick installed with 2 to 3 radii delay would be sufficient for short term stability. A longer period of monitoring lining strains is needed to evaluate the long term lining support requirements.

8.7 Implications for the Design of Future Adits

Full development of the Kipp mine will require additional adits. Whether these adits are declines, or shafts, several recommendations for the support designs can be obtained from this study. The application of the convergence-confinement curves to evaluate alternate support systems shows that a 15 to 20 cm thick (possibly wire mesh reinforced) shotcrete ring would provide sufficient support for the shaft under present conditions. A decline to the coal seam, driven from the surface, should be oriented in the direction of the major principal horizontal stress (northeast-southwest) to minimize radial elastic wall displacements and yielding. The effect of gravitational forces would have to be considered when evaluating the roof stability of a decline. Shotcrete should be applied near the face in either a shaft or a decline to minimize deterioration and loosening of the exposed rock. A decline should be excavated through the bedrock preferably with a road header to minimize rock damage and hence opening convergence.

8.8 Implications for Future Monitoring Programs

Evaluation of the performance of an underground opening requires synthesis of a number of independently measured parameters. Convergence-confinement curves provide the conceptual framework for this evaluation. This project has

demonstrated that necessary parameters may be evaluated and analyzed with an appropriate material model to give reasonable agreement between the predicted and measured performance.

To maximize the results from any type of instrumentation or *in situ* testing, the expected response should be estimated, based on the best assessment of the *in situ* conditions. Optimal orientations and installation locations for each of the instruments used in the shaft have been presented with the gauge analysis.

REFERENCES

- American Concrete Institute, 1980. Mass Concrete for Dams and Other Massive Structures, Manual of Concrete Practice, Part 1, pp. 207.1-207.37.
- Babcock, E.A. 1978. Measurement of subsurface fractures from dipmeter logs, The American Association of Petroleum Geologists Bulletin, Vol. 62, No. 7, pp. 1111-1126.
- Bathe, K.J. 1978. ADINA, A Finite Element Program for Automatic Dynamic Incremental Nonlinear Analysis, Massachusetts Institute of Technology, Report 82448-1.
- Becker, R.M. 1968. An anisotropic elastic solution for the testing of stress relief core, U.S. Bureau of Mines Report of Investigations 7143, 15 pp.
- Becker, R.M. and Hooker, V.E. 1969. A method of determining *in situ* stress in anisotropic rock, Transactions AIME, Vol. 244, pp. 436+445.
- Bell, J.S. and Gough, D.I. 1979. Northeast-southwest compressive stress in Alberta: Evidence from oil wells, Earth and Planetary Science Letters, Vol. 45, pp. 475-482.
- Bieniawski, Z.T. 1970. Time-dependent behavior of fractured rock, Rock Mechanics, Vol. 2, pp. 123-137.
- Blackwood, R.L. 1978. Diagnostic stress-relief curves in stress measurement by overcoring, Int. J. Rock Mech., Min. Sci. & Geomechanics Abstr., Vol. 15, pp. 205-209.
- Branson, D.E. 1977. Deformation of Concrete Structures.

- McGraw-Hill, New York, 546 p.
- Byrne, P.J.S. and Farvolden, R.N. 1959. Clay Mineralogy and Chemistry of the Bearpaw Formation of Southern Alberta, Alberta Research Council, Bulletin #4.
- Comite Euro-International du Beton 1978. Bulletin d'Information N. 124/125-E, Vol. 11, CEB-FIP Model Code for Concrete Structures, (English Translation), 346 p.
- Cording, E.J., Hendron, A.J., MacPherson, H.H., Hansmire, W.H., Jones, R.A., Mahr, J.W. and O'Rourke, T.D. 1975. Methods for Geotechnical Observations and Instrumentation in Tunneling, Vol. 1 and 2, Report prepared for U.S. National Science Foundation, Washington, D.C., NTIS No. PB252585-PB252586.
- Crawford, I.D. 1947. The Geology and Structure of the Lethbridge Coal Field. M.Sc. Thesis, Department of Geology, University of Alberta, Edmonton, Alberta, 133 p.
- Dames and Moore, 1978. Report on Geotechnical Review of Applicability of Shortwall Mining in the Lethbridge Coal Field. Unpublished report prepared for Pacific Petroleum Ltd. (now Petro-Canada) and the Federal Government, 96 p.
- Dames and Moore, 1979. Report on Geotechnical Assessment for Shaft, Lethbridge Coalfield, Lethbridge, Alberta, unpublished report prepared for Pacific Petroleum Limited, (now Petro-Canada), 20 p.
- Einstein, H.H. and Schwartz, C.W. 1980. Simplified analysis

- for tunnel supports, Journal of the Geotechnical Engineering Division, A.S.C.E., No. GT4, pp. 499-518.
- Franklin, J.A. and Hoek, E. 1970. Developments in triaxial testing technique, Rock Mechanics, Vol. 2, pp. 223-228.
- Geiger, K.W., Brown, R.E., Withers, D.W. and de Vries, P.H. 1965. Water-well Records Southern Alberta, Townships 1-10, Alberta Research Council, Preliminary Report 65.4, 131 p.
- Gesta, M.P., Kerisel, M.J., Londe, M.P., Louis, M.C., and Panet, M.M. 1978. Tunnel stability by convergence-confinement method. General Report to Conference on Analysis of Tunnel Stability by the Convergence-Confinement Method, Paris, Underground Space, Vol. 4, No. 4, pp. 225-232.
- Gough, D.I. and Bell, J.S. 1981. Stress Orientations from oilwell fractures in Alberta and Texas. Canadian Journal of Earth Sciences, Vol. 18, No. 3, pp.638-645.
- Grob, H., Kovari, K. and Amstad, C. 1975. Sources of error in the determination of *in-situ* stresses by measurements, Tectonophysics, Vol. 29, pp. 29-39.
- Hawkes, I. and Bailey, W.V. 1973. Low Cost Cylindrical Stress Gage. Report prepared for U.S. Bureau of Mines, Washington, D.C., NTIS No. PB243347, 142 p.
- Hawkes, I. and Hooker, V.E. 1974. The vibrating wire stressmeter, Proceedings of the Third I.S.R.M. Congress, Denver, Colorado, Vol. 2, Part A, pp. 439-444.
- Hoek, E. and Brown, E.T. 1980. Underground Excavations in

- Rock. Institution of Mining and Metallurgy, London, U.K., 527 p.
- Hoek, E. and Franklin, J.A. 1968. A simple triaxial cell for field and laboratory testing of rock, Transactions of the Institute of Mining and Metallurgy Vol. 77 pp. A22-A26.
- Holter, M.E. and Chu, M. 1977. Geology and Coal Resources of Southeastern Alberta, Alberta Research Council, Open File Report 1978-13, 23 p.
- Hooker, V.E. and Bickel, D.L. 1974. Overcoring Equipment and Techniques used in Rock Stress Determination, U.S. Bureau of Mines Information Circular 8618, 32 p.
- Hooker, V.E., Aggson, J.R. and Bickel, D.L. 1974. Improvements in the Three-Component Borehole Deformation Gage and Overcoring Techniques, U.S. Bureau of Mines Report of Investigations 7894, 29 p.
- Hornby, I.W. and Noltingk, K.B.E. 1974. The application of the vibrating-wire principle for the measurement of strain in concrete, Experimental Mechanics, March, pp. 123-128.
- Hutchinson, D.E. 1982. Effects of Construction Procedures on Tunnel and Shaft Performance. M.Sc. Thesis, Department of Civil Engineering, University of Alberta, Edmonton, Alberta.
- Irad Gage Inc. 1977. Vibrating Wire Stressmeter Instruction Manual , 33 p.
- Irad Gage Inc. 1979. Instruction Manual for EM-5 Vibrating

- Wire Embedment Strain Gage, 15 p.
- Irish, E.J.W. 1971. The Southern Plains of Alberta, Geological Survey of Canada, Bedrock Geology Map 1286A, Scale 1:500,000.
- Jones, K. 1961. Calculation of stress from strain in concrete. U.S. Dept. of Interior, Bureau of Reclamation Eng. Monograph No. 29, 17 p.
- Kaiser, P.K. 1980. Effect of stress history on the deformation behavior of underground openings. 13th Canadian Rock Mechanics Symposium, Toronto, CIM Special Volume No. 22, pp. 133-140.
- Kaiser, P.K. 1981. A new concept to evaluate tunnel performance - influence of excavation procedure. 22nd U.S. Symp. on Rock Mech. , pp. 264-271.
- Kaiser, P.K. and Hutchinson, D.E. 1982. Effects of construction procedure on tunnel performance. 4th International Conference on Numerical Methods in Geomechanics, Edmonton, Alberta, 9 p. (to be published).
- Kaiser, P.K., MacKay, C.H. and Morgenstern, N.R. 1982. Performance of a shaft in weak rock (Bearpaw Shale). ISRM Symposium on Caverns and Pressure Shafts, Aachen, 10 p. (in press)
- Kovari, K. and Tisa, A. 1975. Multiple failure state and strain controlled triaxial tests, Rock Mechanics, Vol. 7, pp. 17-33.
- Kruse, G.K. 1969. Deformability of rock structures, California State Water Project, ASTM Special Technical

- Publication No. 477, Determination of the *In Situ* Modulus of Deformation of Rock, pp. 58-88.
- McCrossan, R.G. and Galister, R.P., Editors, 1966. Geological History of Western Canada, Alberta Society of Petroleum Geologists, 2nd Ed., 232 p.
- Merrill, R.H. and Peterson, J.R. 1961. Deformation of a borehole in rock. U.S. Bureau of Mines Report of Investigations 5881, 32 p.
- Mindess, S. and Young, J.F. 1981. Concrete. Prentice Hall, Toronto, 671 pp.
- Neville, A.M. 1970. Creep of Concrete: Plain, Reinforced and Prestressed. North-Holland Publishing Company, Amsterdam, 622 pp.
- Neville, A.M. 1973. Properties of Concrete. Pitman, London, 686 p.
- Noonan, D.K.J. 1972. Fractured rock subjected to direct shear, M.Sc. thesis, University of Alberta, Edmonton, Alberta.
- Obert, L. 1966. Determination of Stress in Rock - A State-of-the-Art Report, Am. Soc. Testing Mats., Special Technical Publication 429, 56 p.
- Obert, L. and Duvall, W.I. 1967. Rock Mechanics and the Design of Structures in Rock, John Wiley and Sons Inc., New York, 650 p.
- Orchard, D.F. 1979. Concrete Technology, Vol. 1: Properties of Materials. 4th ed., Applied Science Publishers Ltd., London, 487 pp.

- Pariseau, W.G. and Eitani, I.M. 1977. Post-elastic vibrating wire stress measurements in coal, Proceedings of the Int. Symp. on Field Measurements in Rock Mechanics, Zurich, pp. 255-273.
- Pender, M.J. 1980. Elastic solutions for a deep circular tunnel, Geotechnique, Vol. 30, No. 2, pp. 216-222.
- Peterson, R. 1954. Studies of the bearpaw shale at a damsite in Saskatchewan, Journal of the Soil Mechanics and Foundation Division, A.S.C.E., Vol. 80, Paper 476.
- Peterson, R. and Peters, N. 1963. Heave of spillway structures on clay shales, Canadian Geotechnical Journal, Vol. 1, No. 1, pp. 5-15.
- Robinson, Dames and Moore, 1980. Review of Groundwater Hydrology Conditions, Lethbridge Coal Project, Unpublished Report to Petro-Canada Ltd.
- Russell, L.S. and Landes, R.W. 1940. Geology of the Southern Alberta Plains, Geological Survey of Canada, Memoir 221, 223 p.
- Schwartz, C.W. and Einstein, H.H. 1980. Improved design of tunnel supports: Volume 1 - Simplified analysis for ground-structure interaction in tunneling, Report No. UMTA-MA-06-0100-80-4, U.S. Dept. of Transportation, Urban Mass Transportation Administration, Washington, D.C. 427 p.
- Sellers, J.B. 1977. The measurement of stress changes in rock using the vibrating wire stressmeter, Proc. Int. Symp. on Field Measurements in Rock Mechanics, pp.

275-288.

Stalker, A. Macs. 1963. Surficial Geology of the Blood Indian Reserve, Geological Survey of Canada, Paper 63-25 and Map 40-1963.

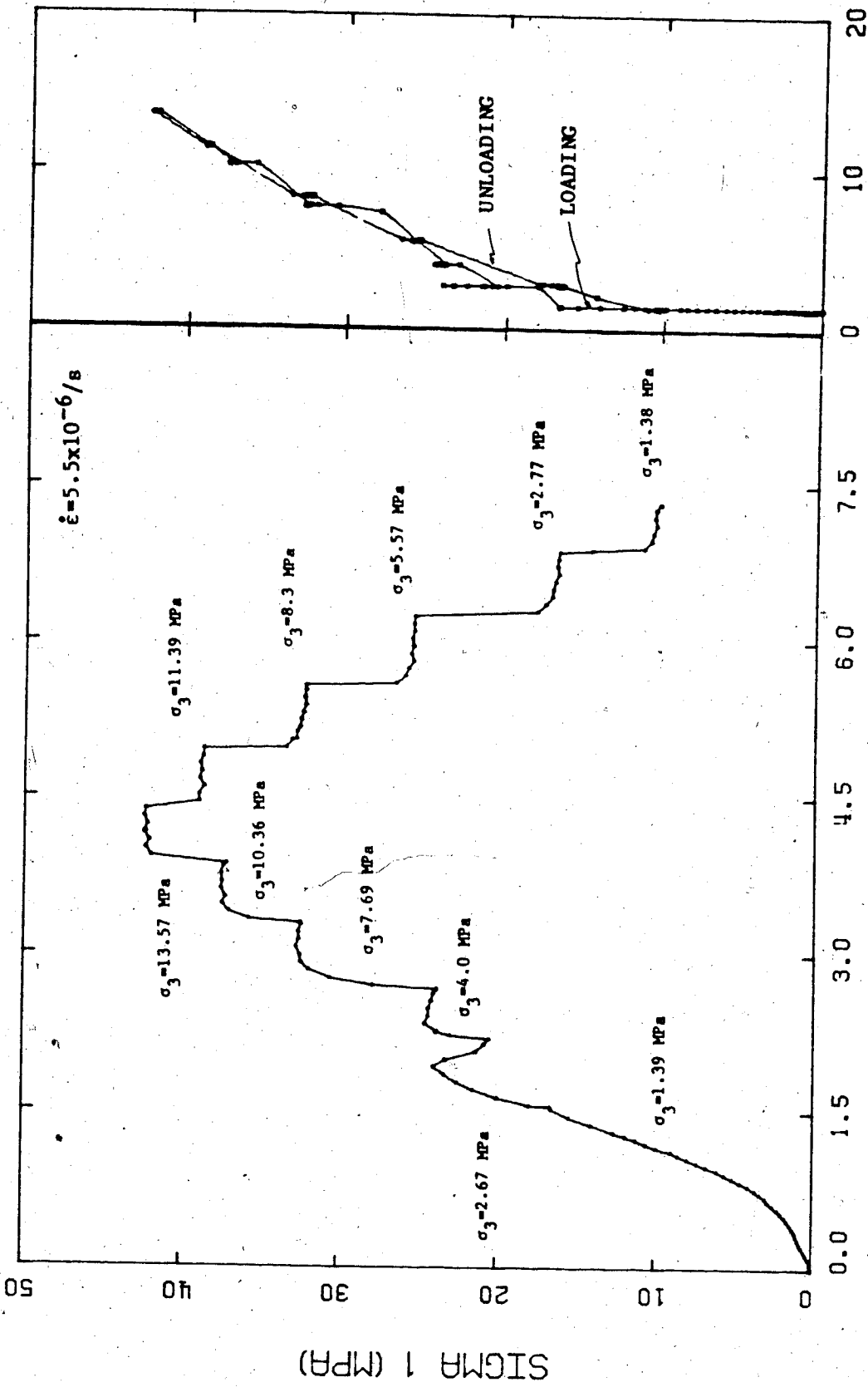
Timoshenko, S.P. and Goodier, J.N. 1970. Theory of Elasticity, 3rd Ed., McGraw Hill, New York, 567 p.

Vardar, M. 1977. Zeiteinfluss auf das Bruchverhalten des Gebirges in der Umgebung von Tunneln. Veröffentlichungen des Institutes für Bodenmechanik und Felsmechanik der Universität Fridericiana in Karlsruhe, 118 p.

Ward, W.H., Coats, D.J. and Tedd, P. 1976. Performance of tunnel support systems in the Four Fathom Mudstone, Building Research Establishment Current Paper CP 25/76, Building Research Station, Garston, U.K.

Zoback, M.L. and Zoback, M. 1980. State of stress in the conterminous United States, J.G.R., Vol. 85, pp. 6113-6156.

APPENDIX A



SIGMA 3 (MPa)

AXIAL STRAIN (%)

Figure A.1 Axial Strain and Confining Stress vs. Axial Stress for Triaxial Test No. 1

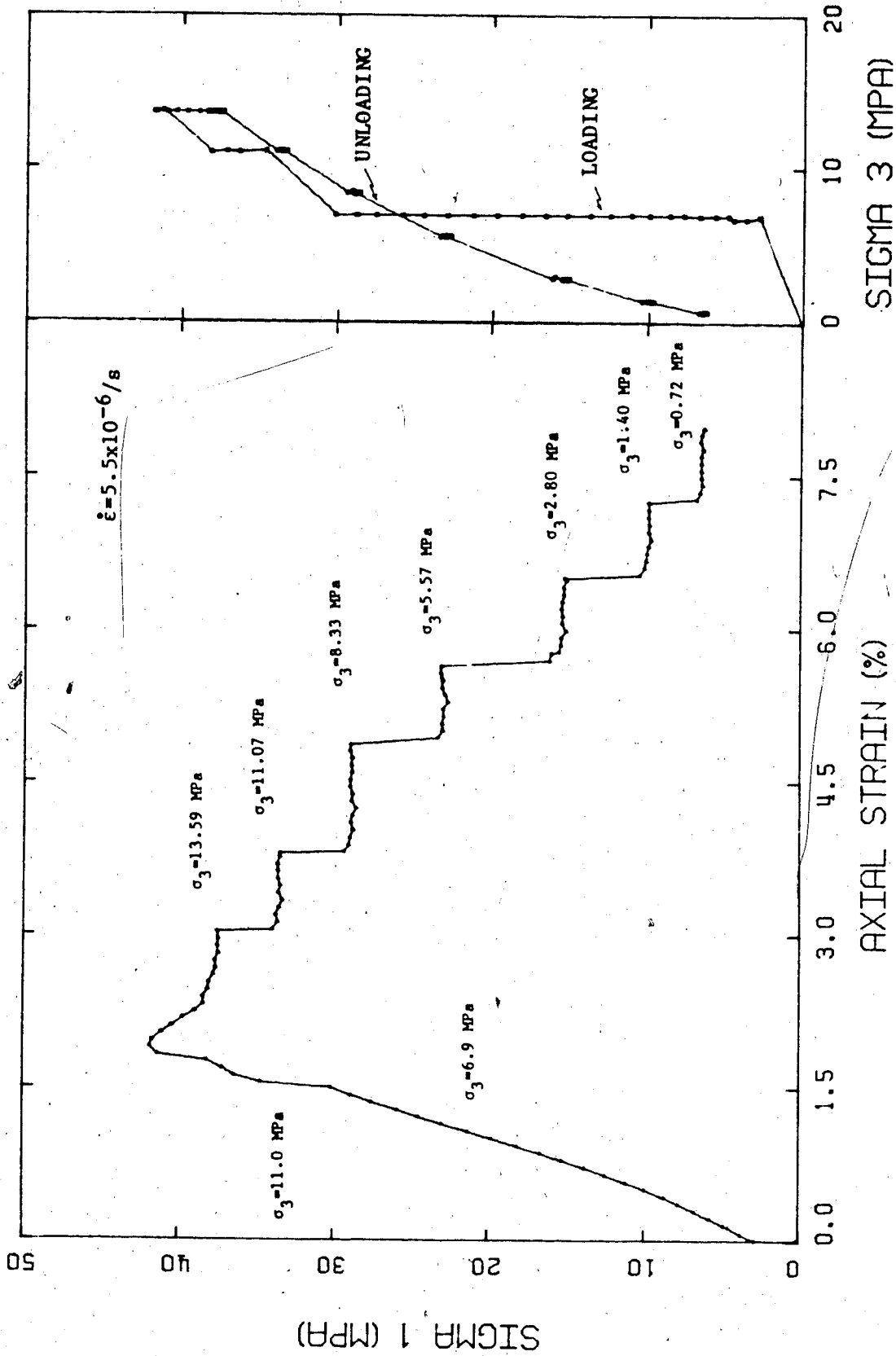


Figure A.2 Axial Strain and Confining Stress vs. Axial Stress for Triaxial Test No. 2

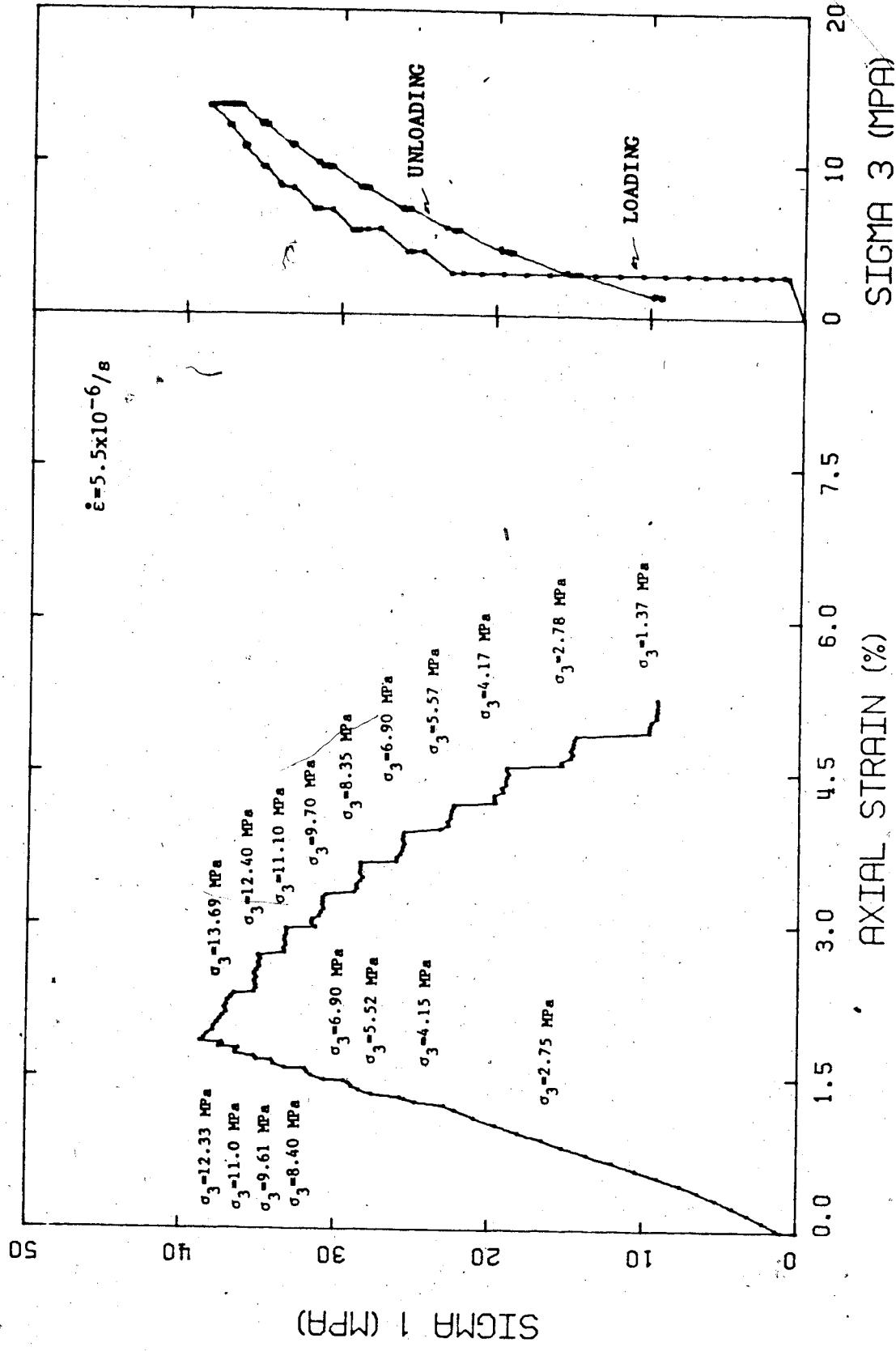


Figure A.3 Axial Strain and Confining Stress vs. Axial Stress for Triaxial Test No. 3

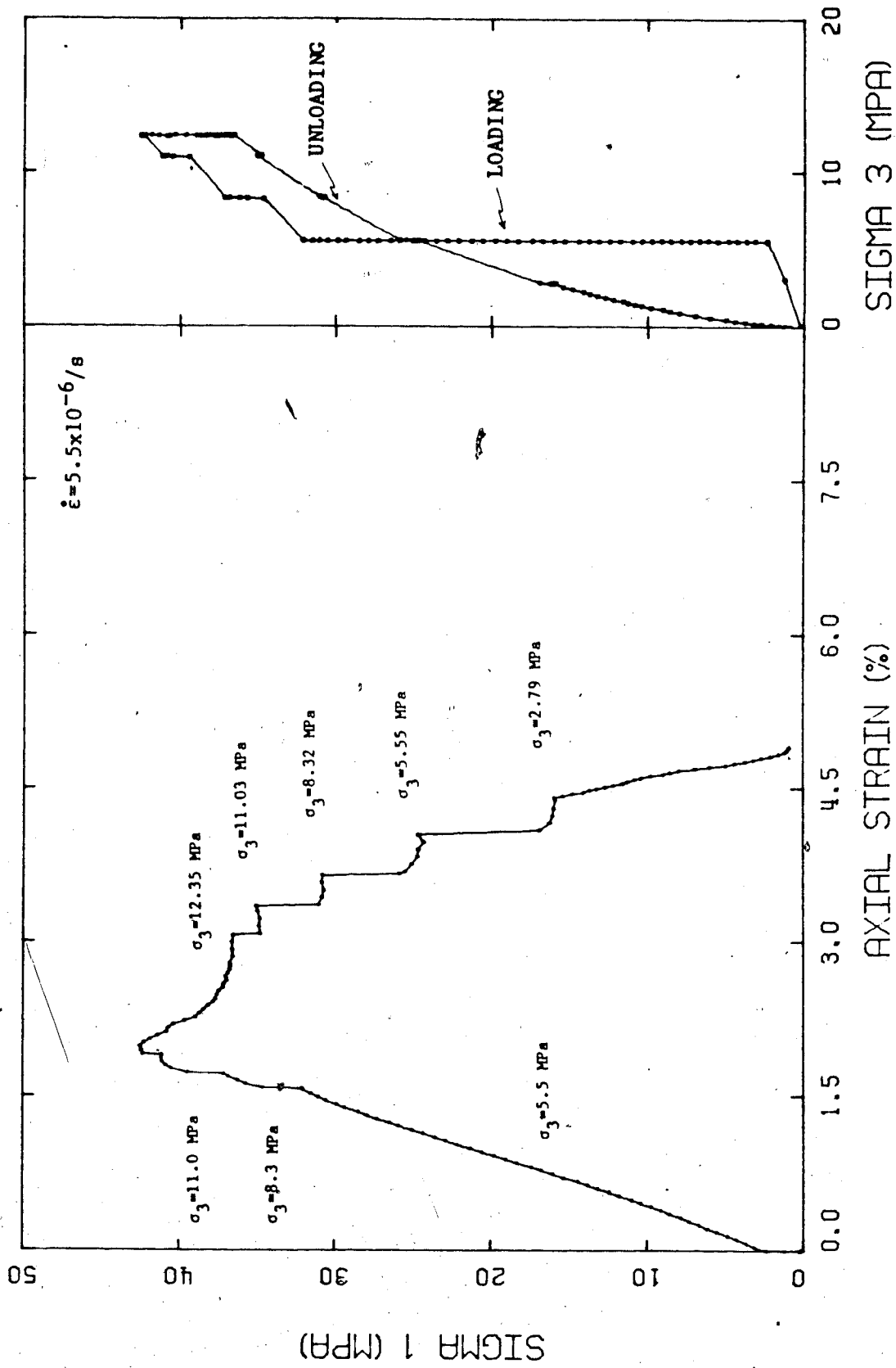


Figure A.4 Axial Strain and Confining Stress vs. Axial Stress for Triaxial Test No. 4

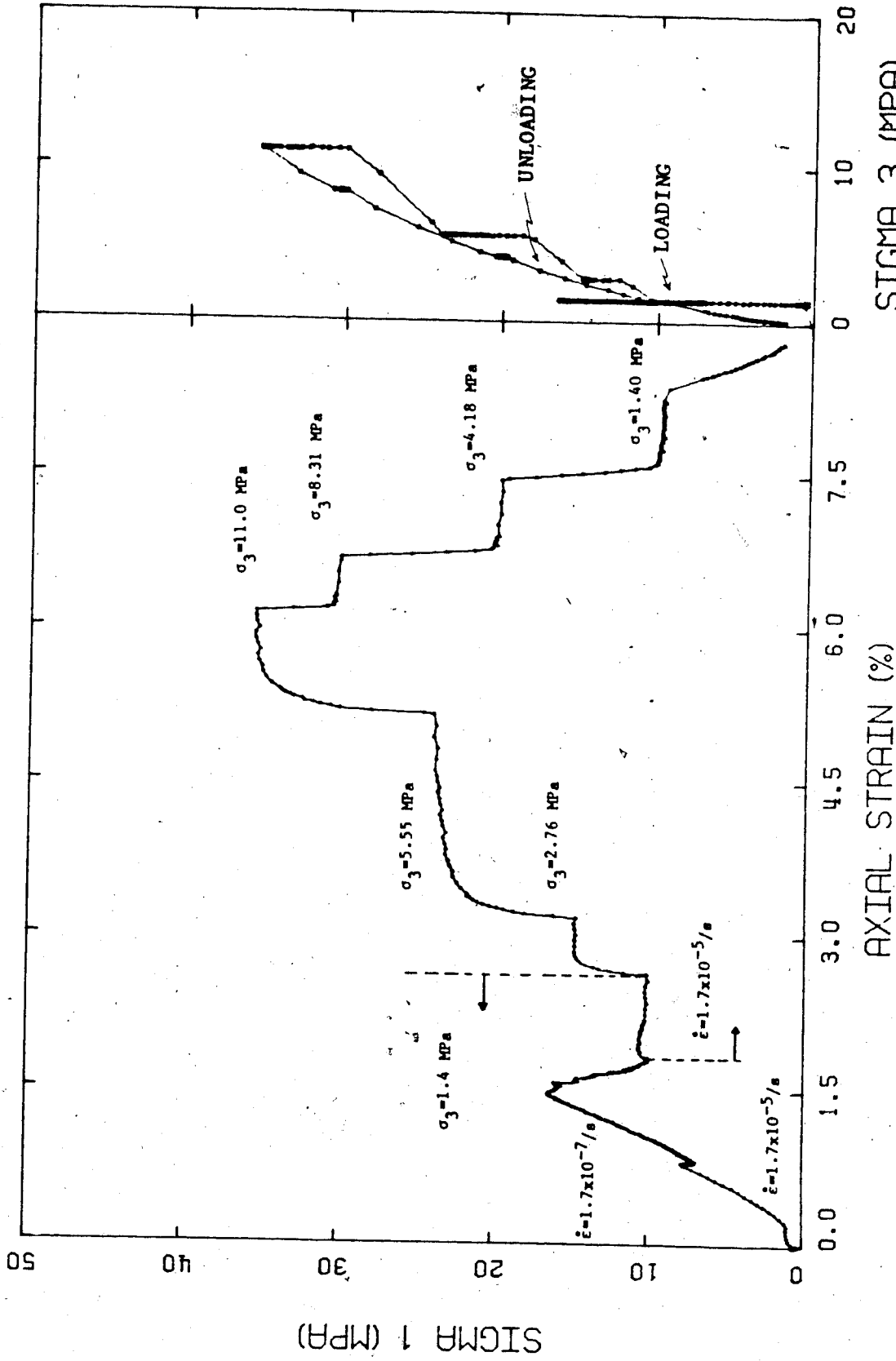


Figure A.5 Axial Strain and Confining Stress vs. Axial Stress for Triaxial Test No. 5

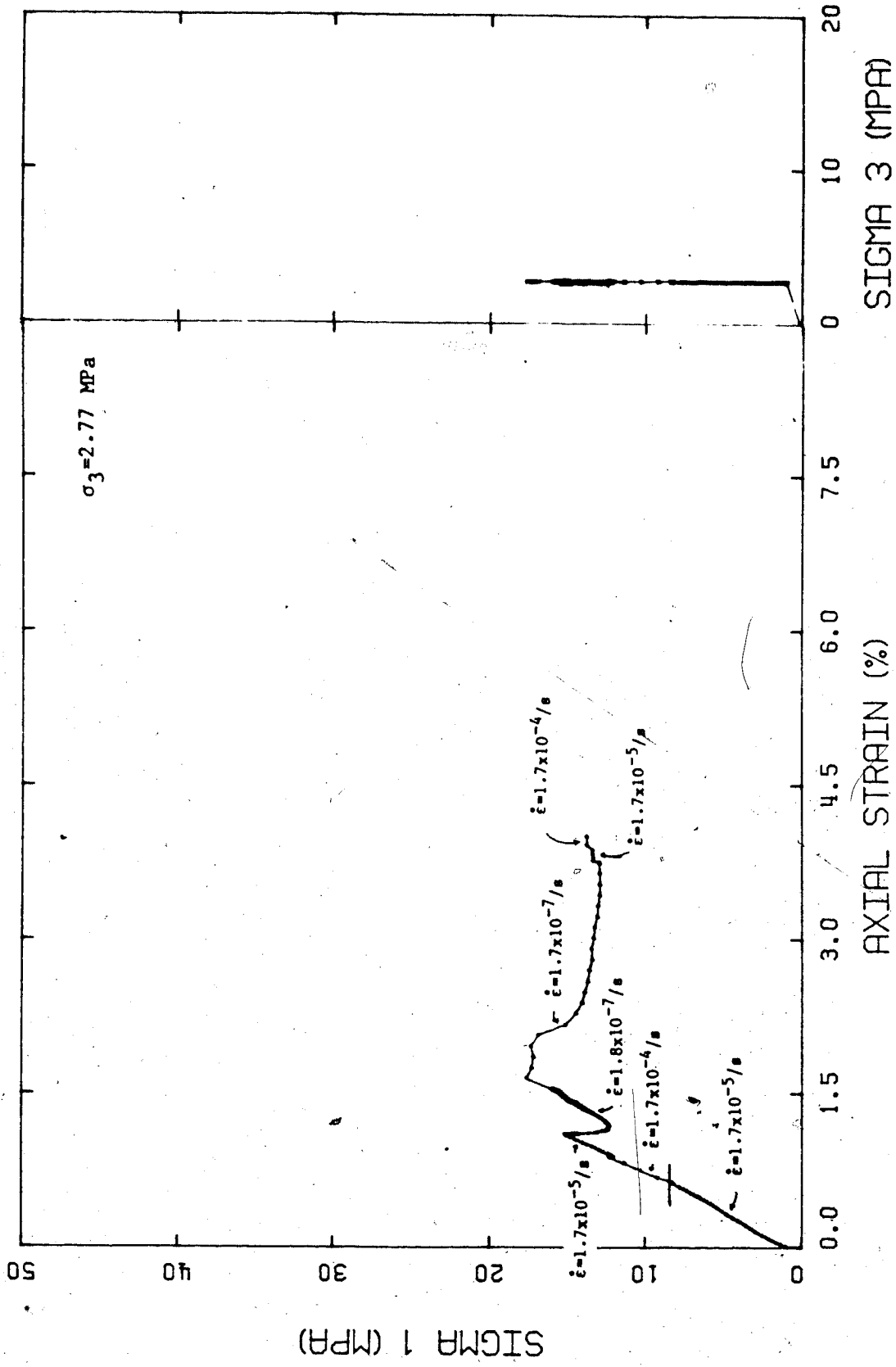


Figure A.6 Axial Strain and Confining Stress vs. Axial Stress for Triaxial Test No. 6

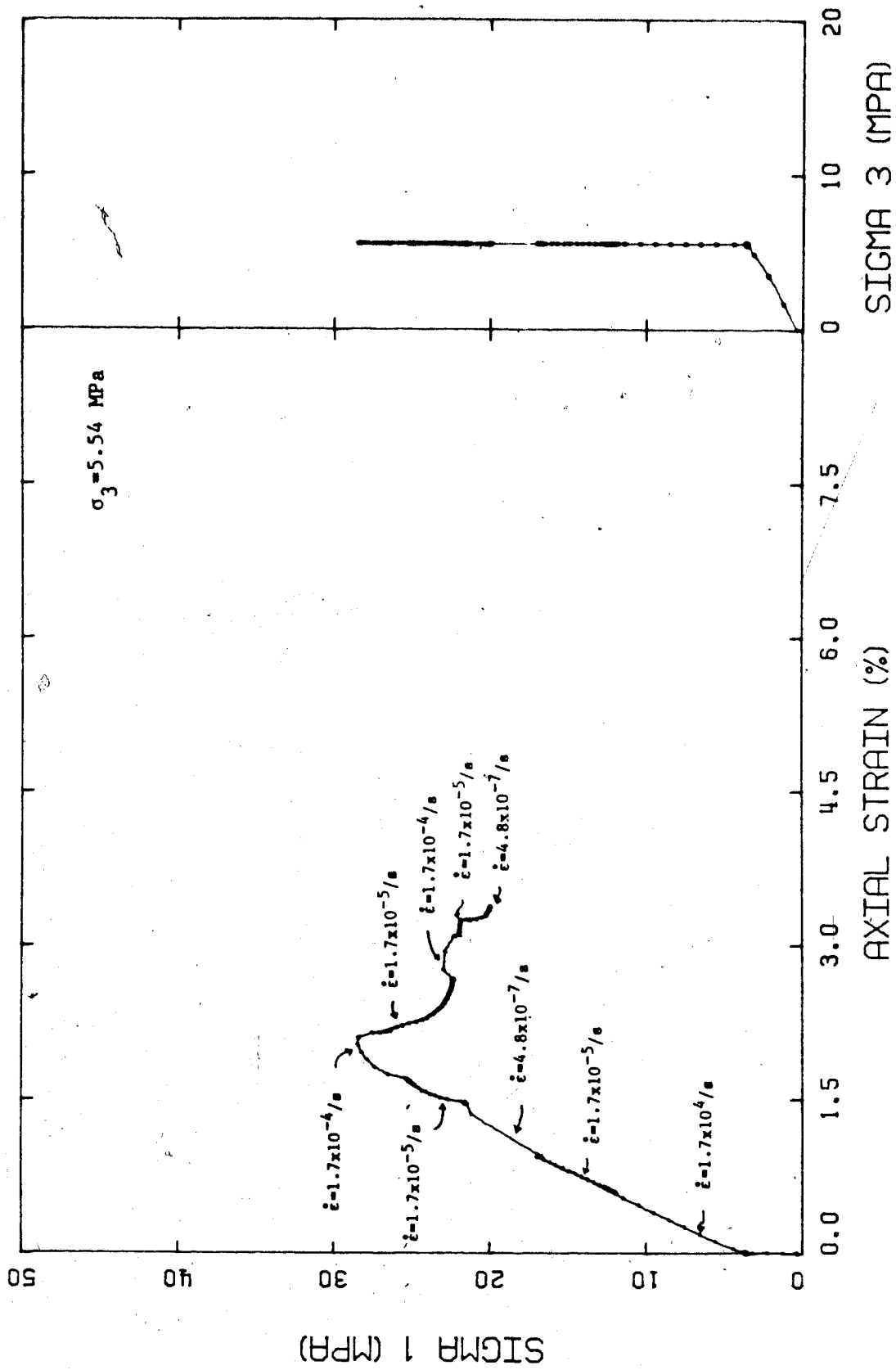


Figure A.7 Axial Strain and Confining Stress vs. Axial Stress for Triaxial Test No. 7

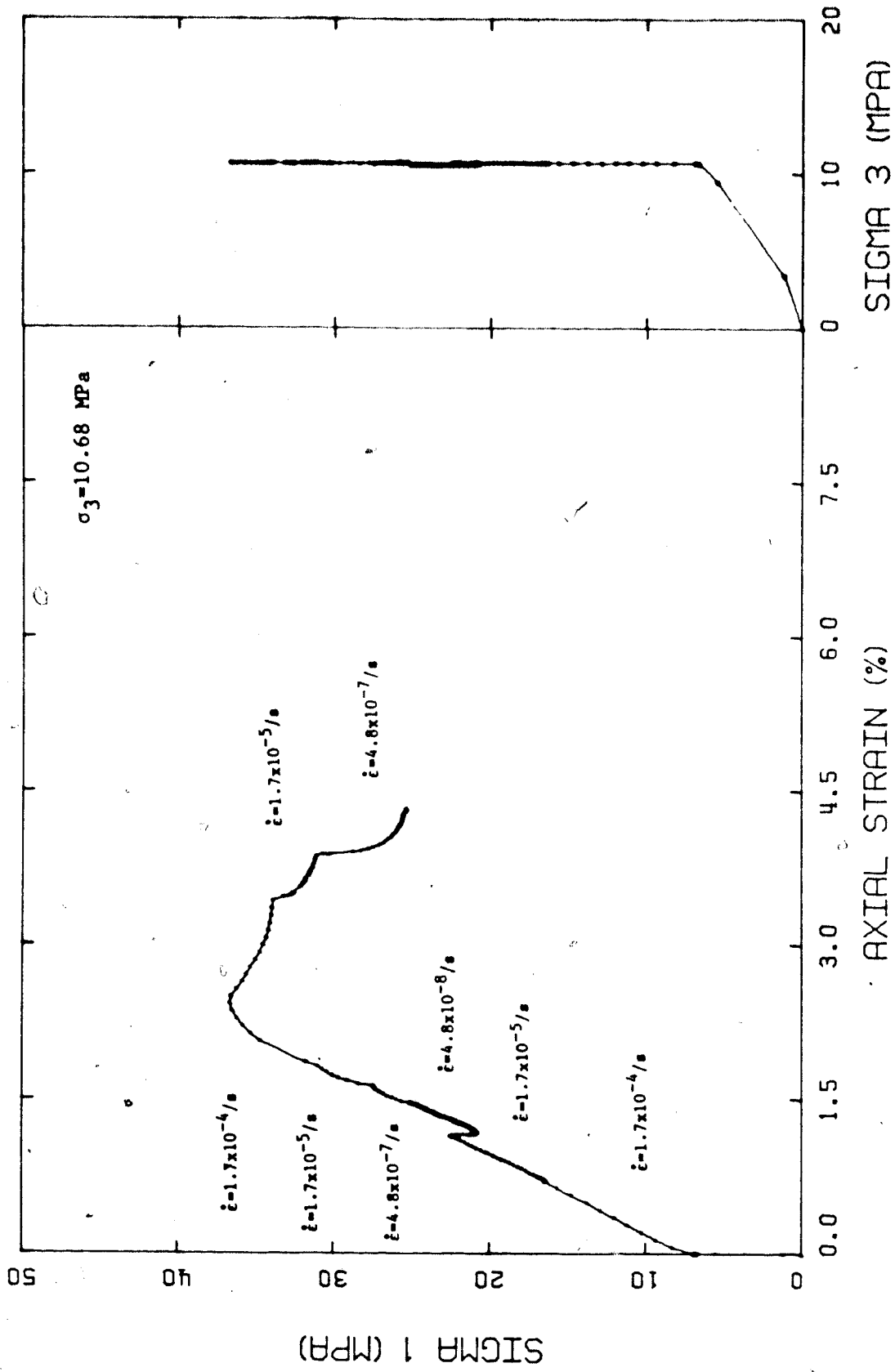


Figure A.8 Axial Strain and Confining Stress vs. Axial Stress for Triaxial Test No. 8

APPENDIX, B

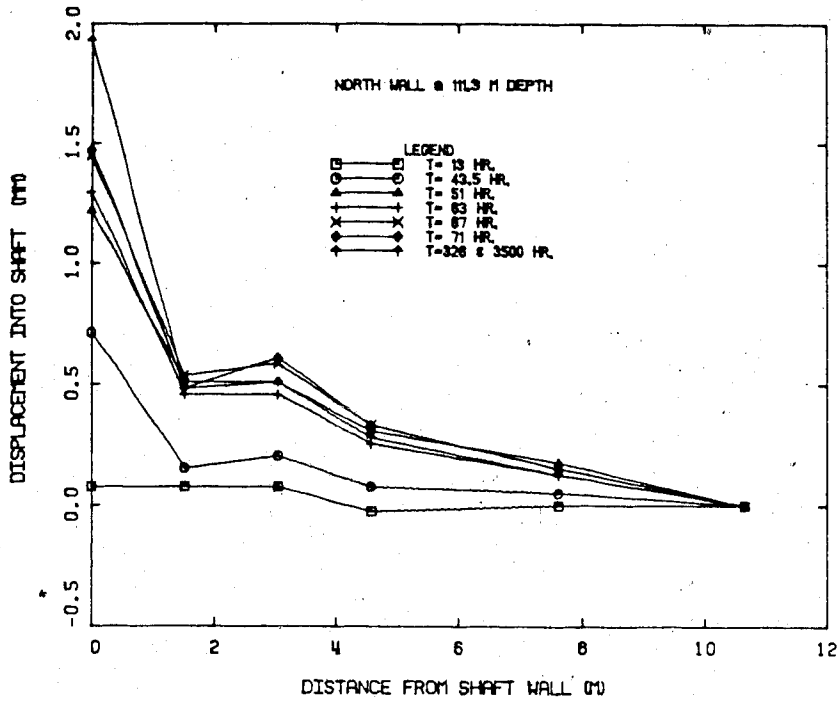


Figure B.1 Depth-Displacement Plot for N. Wall Extensometer at 111 m Depth

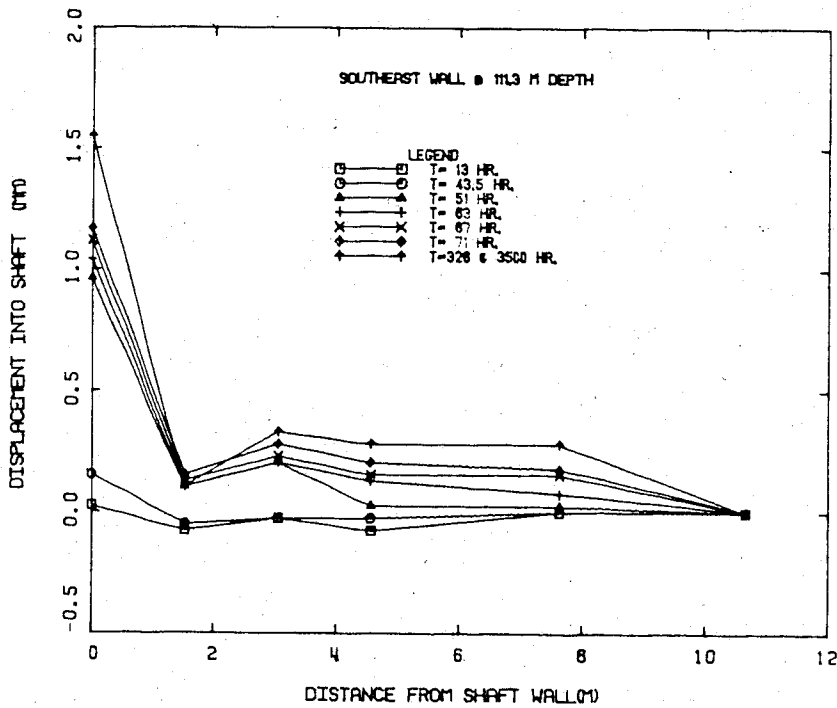


Figure B.2 Depth-Displacement Plot for S.E. Wall Extensometers at 111 m Depth

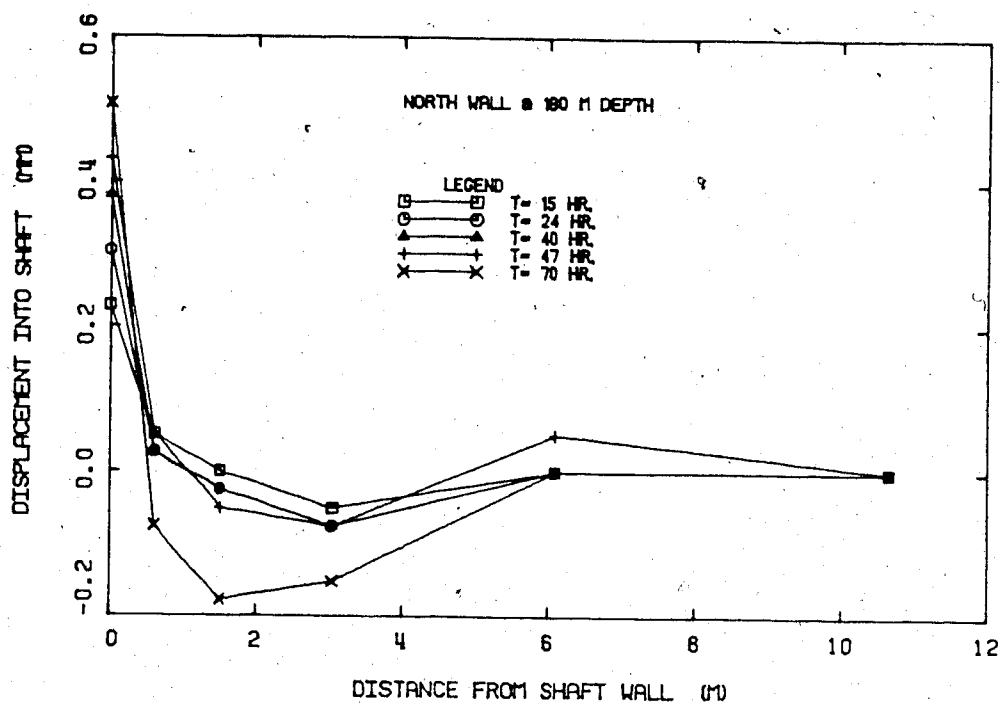


Figure B.3 Depth-Displacement Plot for N. Wall Extensometer at 180 m Depth

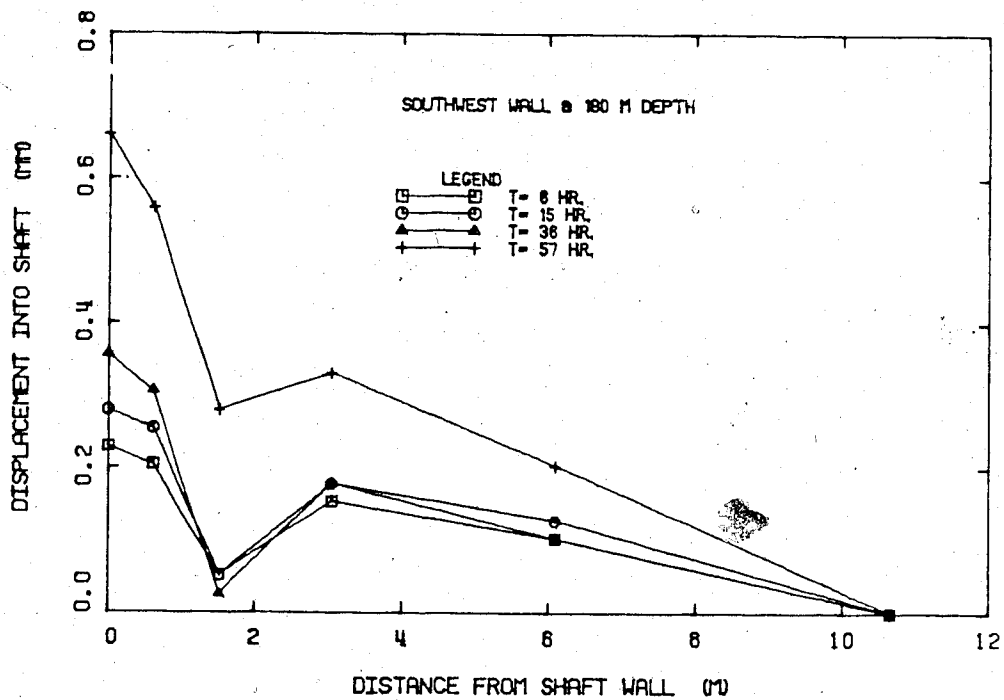


Figure B.4 Depth-Displacement Plot for S.W. Extensometer at 180 m Depth

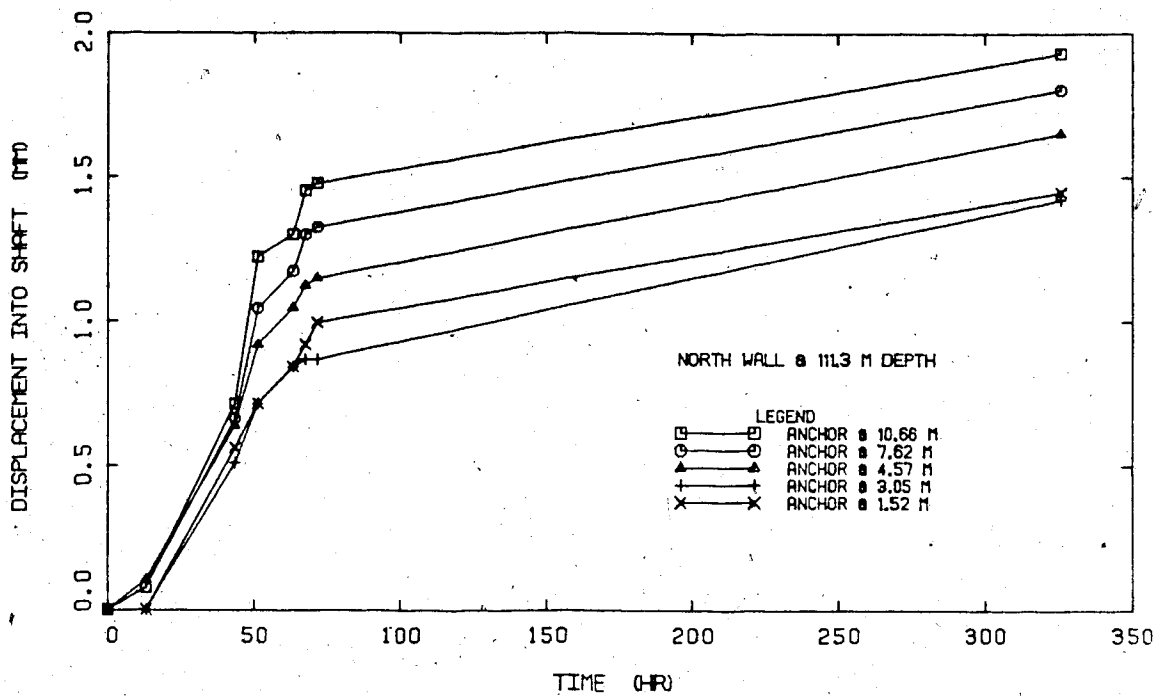


Figure B.5 Time-Displacement Plot for N. Wall Extensometer at 111 m Depth

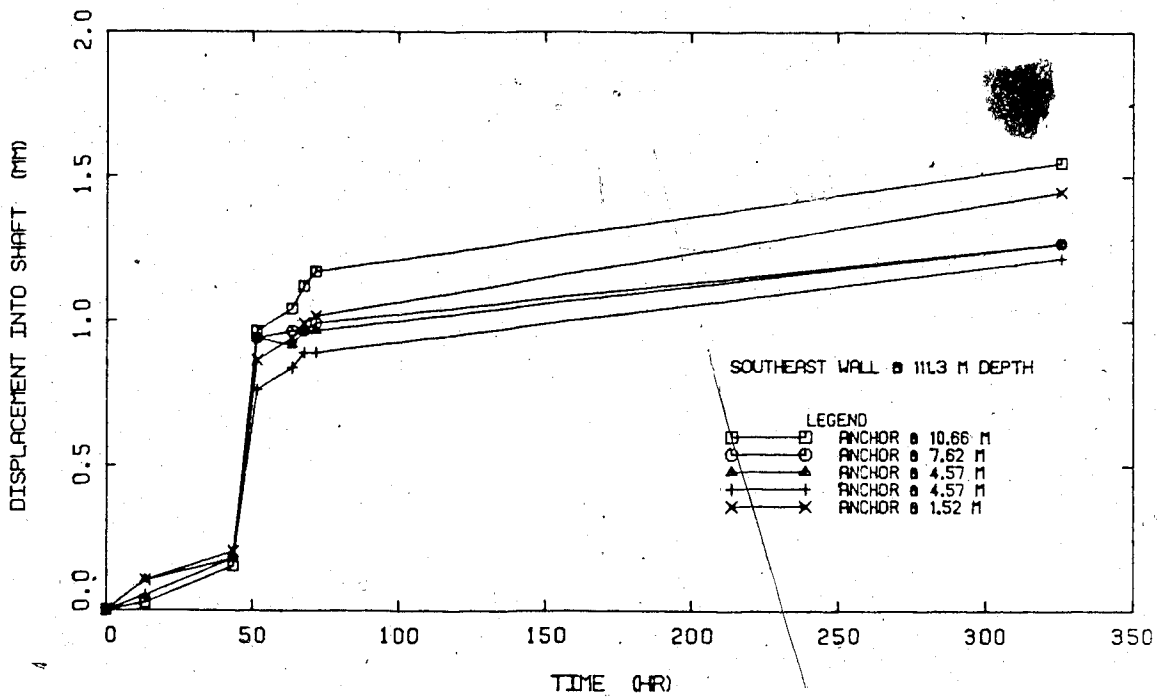


Figure B.6 Time-Displacement Plot for S.E. Wall Extensometer at 111 m Depth

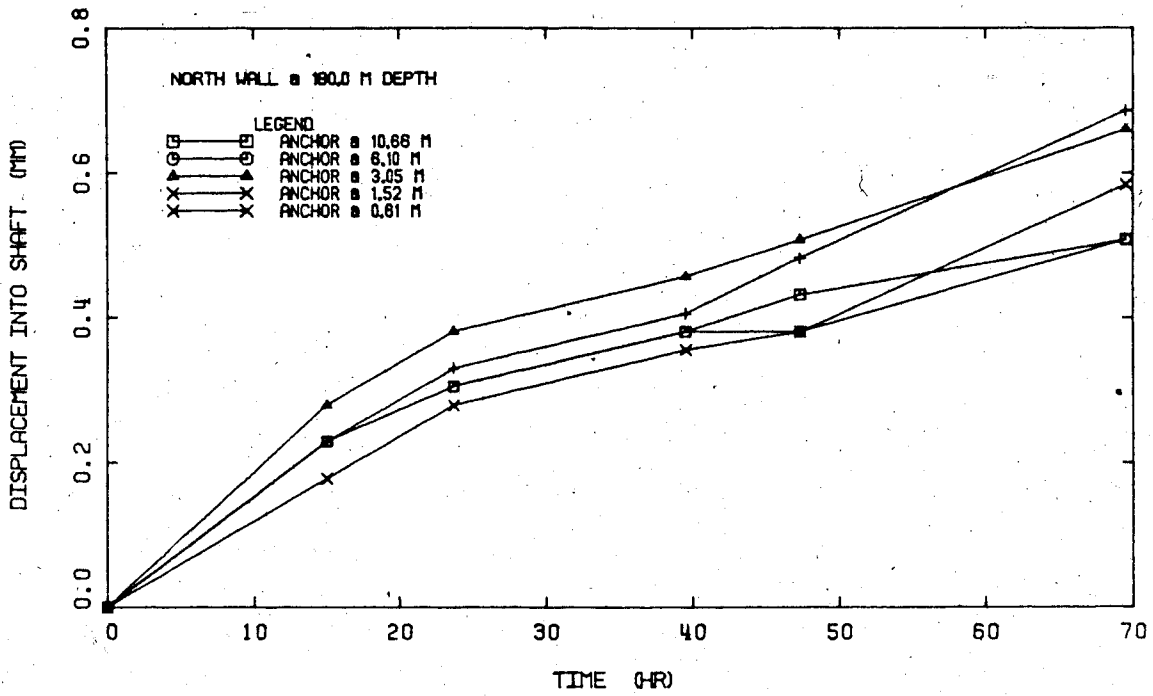


Figure B.7 Time-Displacement Plot for N. Wall Extensometer at 180 m Depth

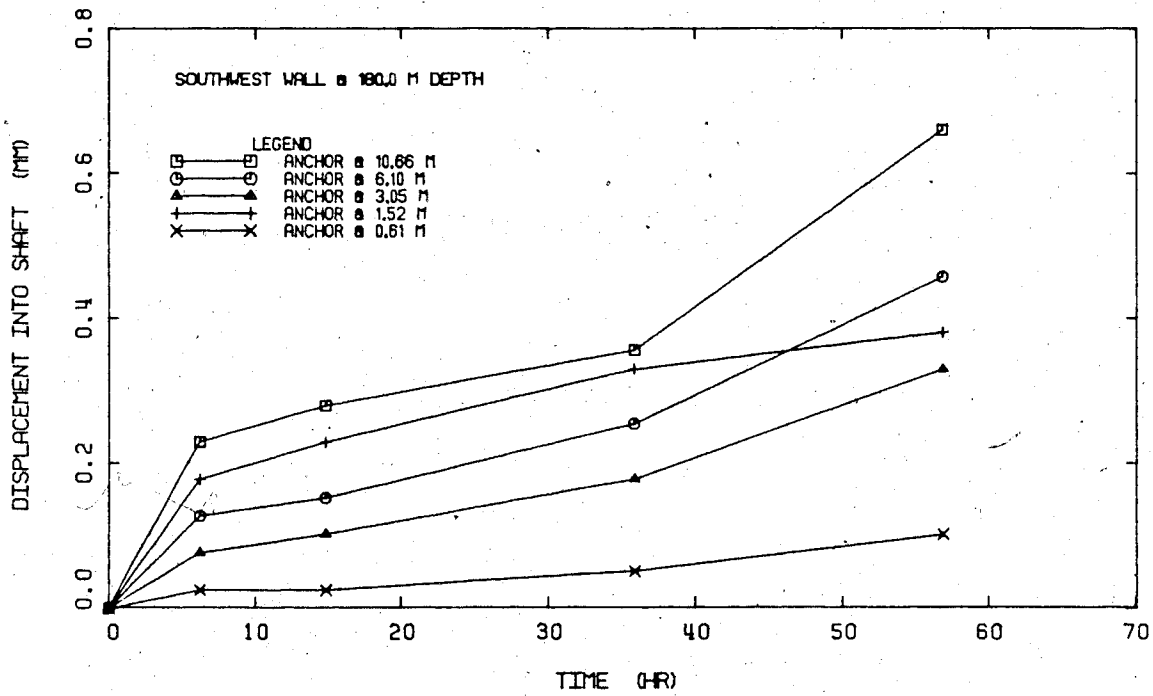


Figure B.8 Time-Displacement Plot for S.W. Extensometer at 180 m Depth

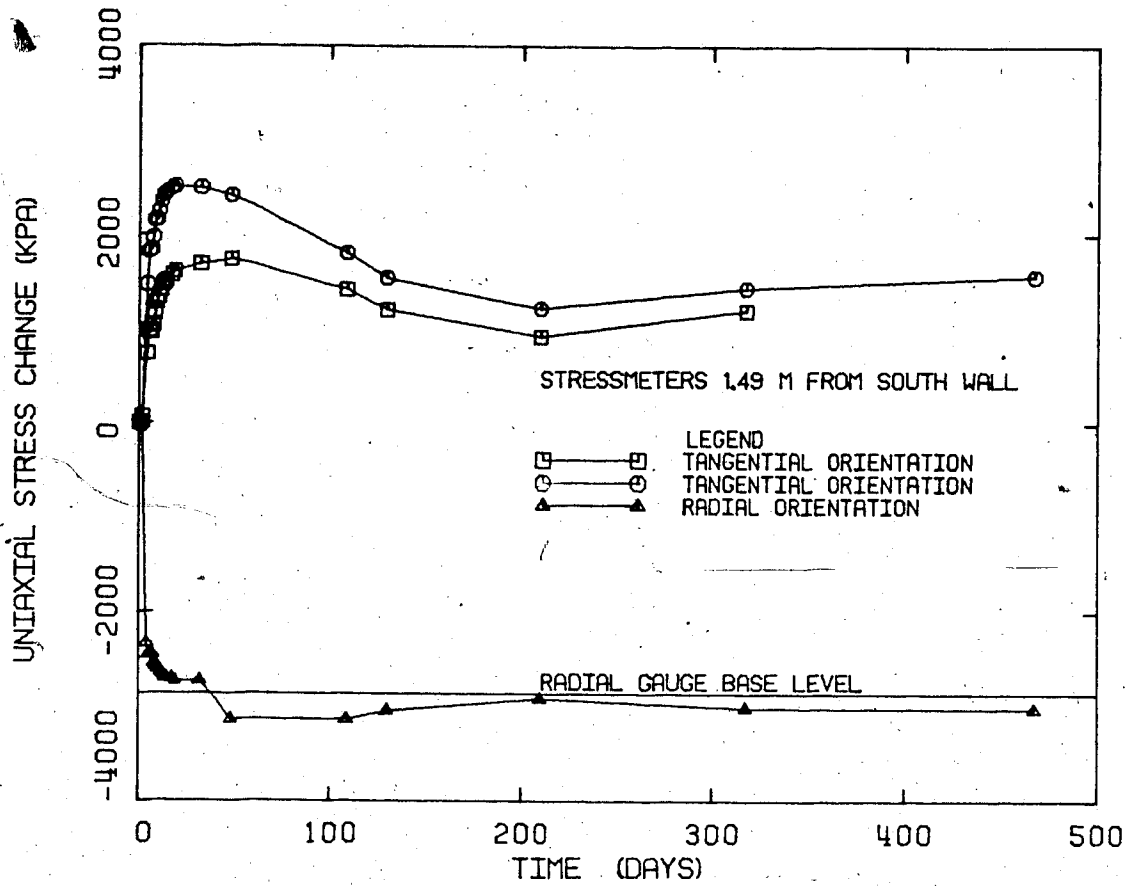


Figure B.9 Stress Change-Time Plot for Stressmeters at 1.49 m from South Wall

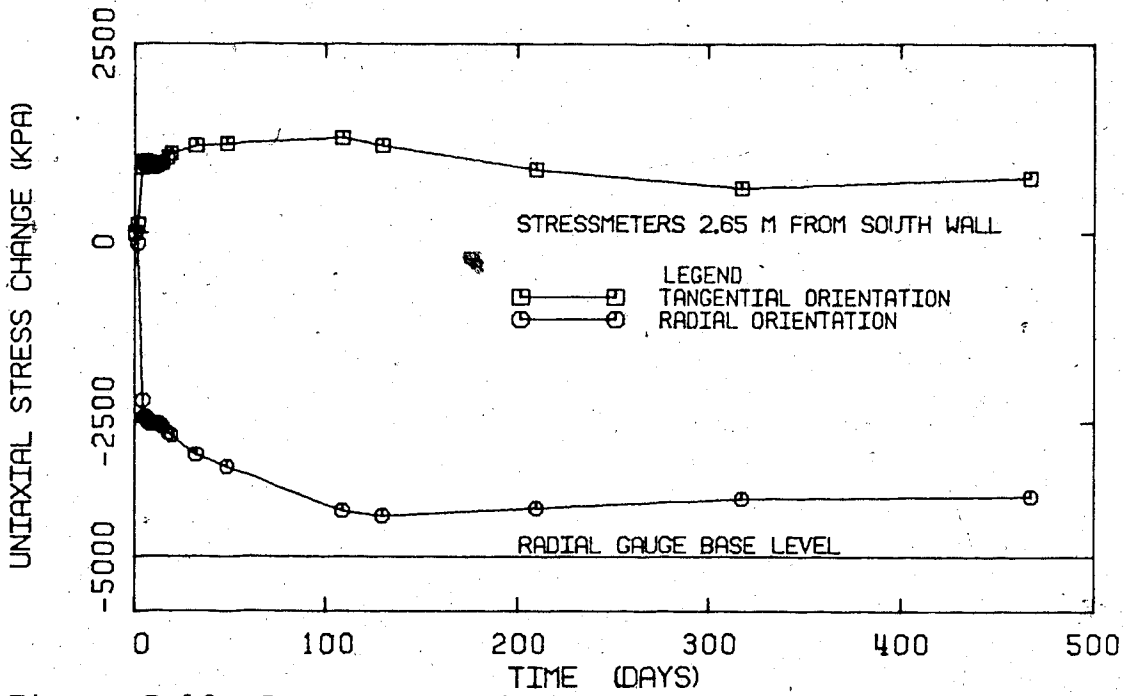


Figure B.10 Stress Change-Time Plot for Stressmeters at 2.65 m from South Wall

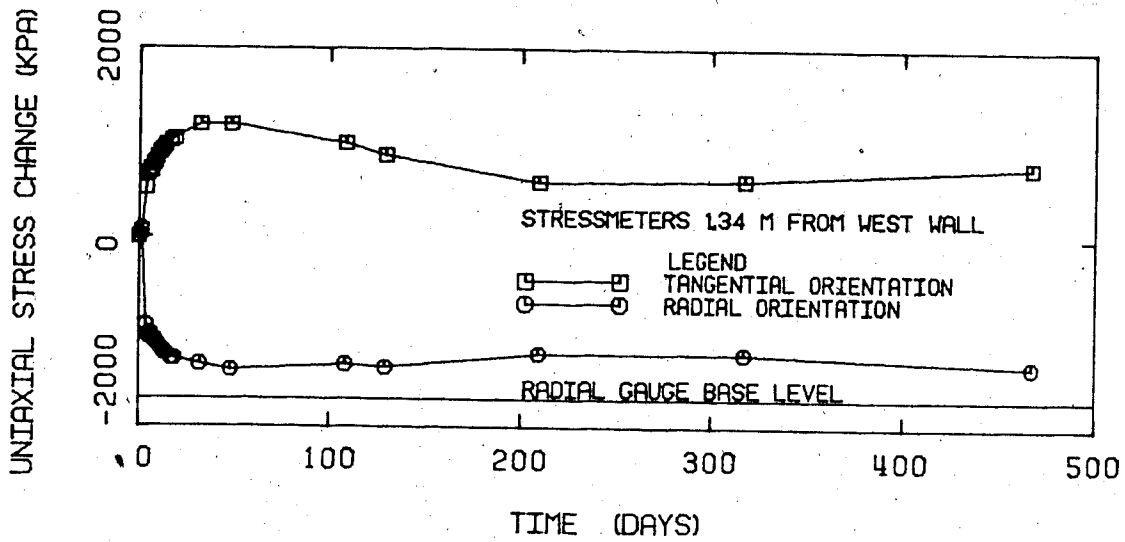


Figure B.11 Stress Change-Time Plot for Stressmeters at 1.34 m from West Wall

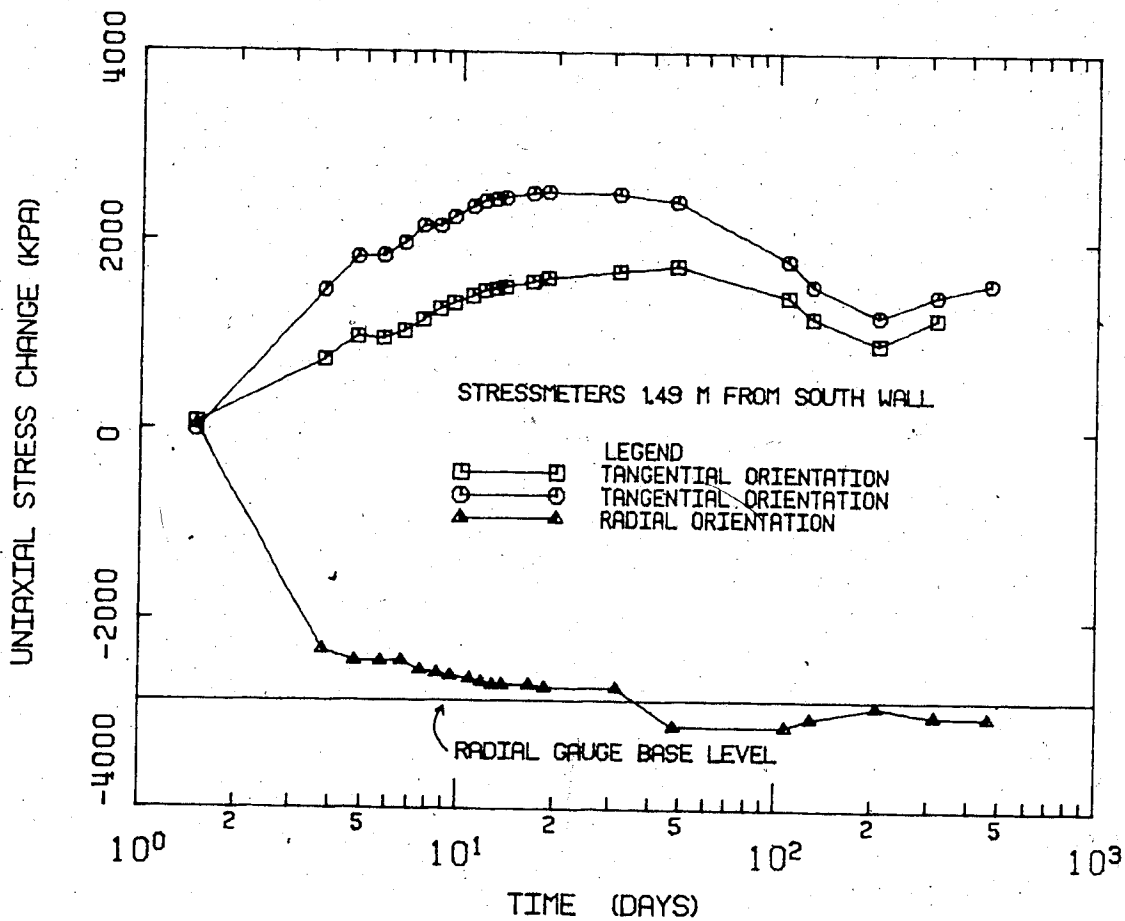


Figure B.12 Stress Change-Log Time Plot of Stressmeters at 1.49 m from South Wall

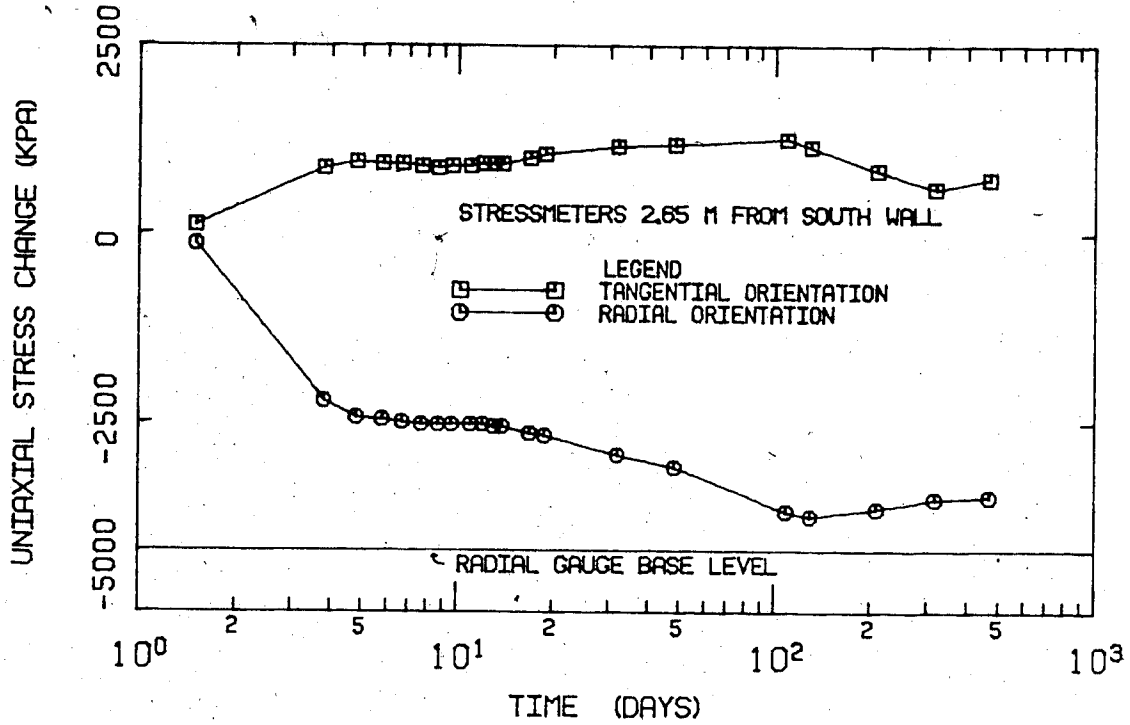


Figure B.13 Stress Change-Log Time Plot of Stressmeters at 2.65 m from South Wall

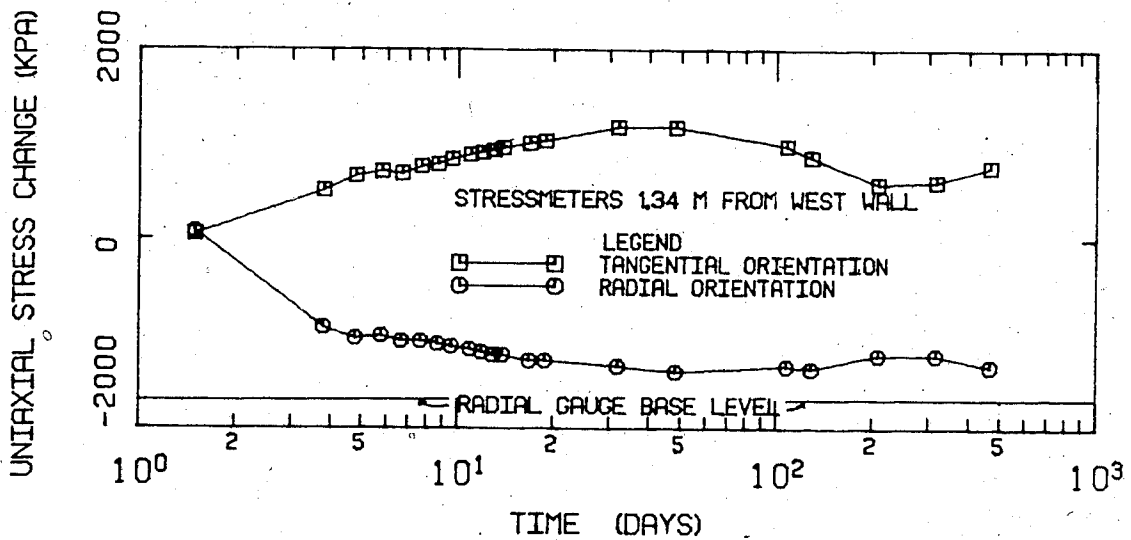


Figure B.14 Stress Change-Log Time Plot of Stressmeters at 1.34 m from West Wall

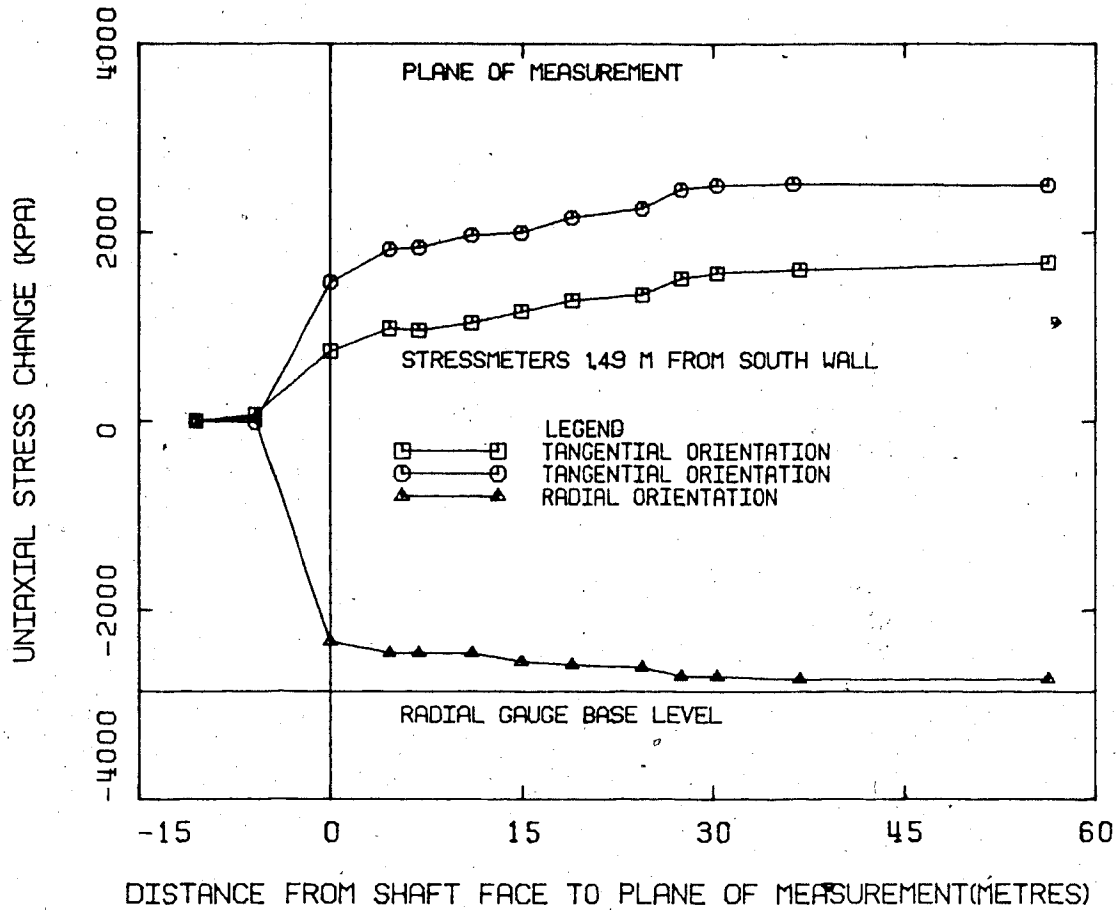


Figure B.15 Stress Change-Depth Plot for Stressmeters at 1.49 m from South Wall

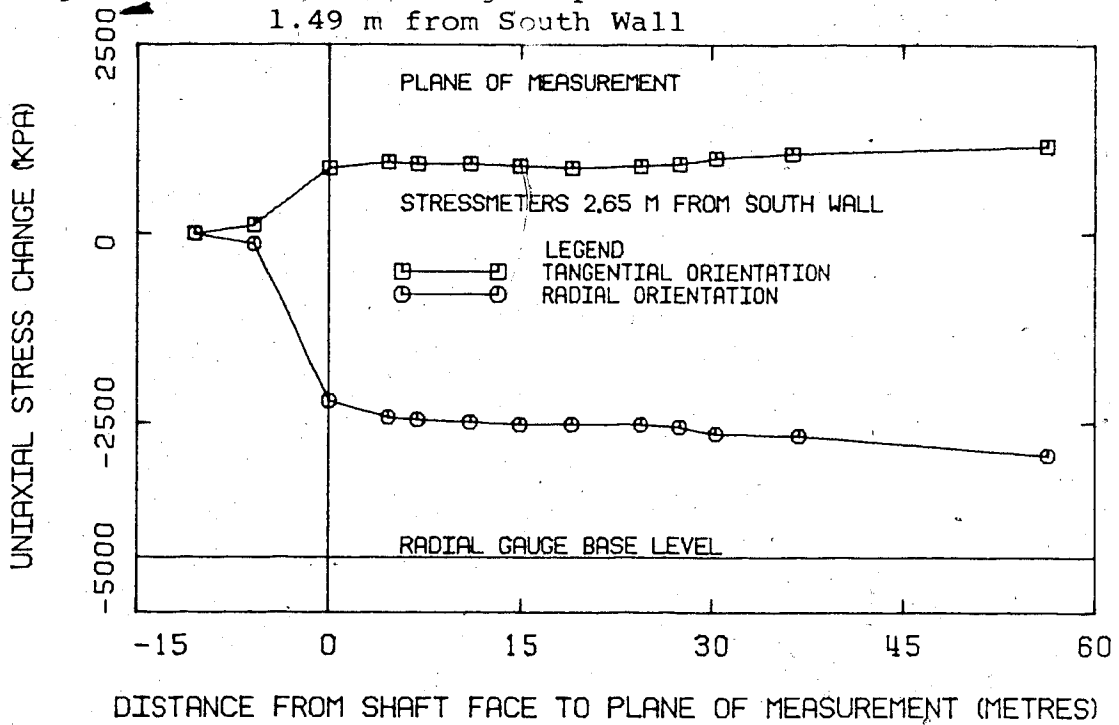


Figure B.16 Stress Change-Depth Plot for Stressmeters at 2.65 m from South Wall

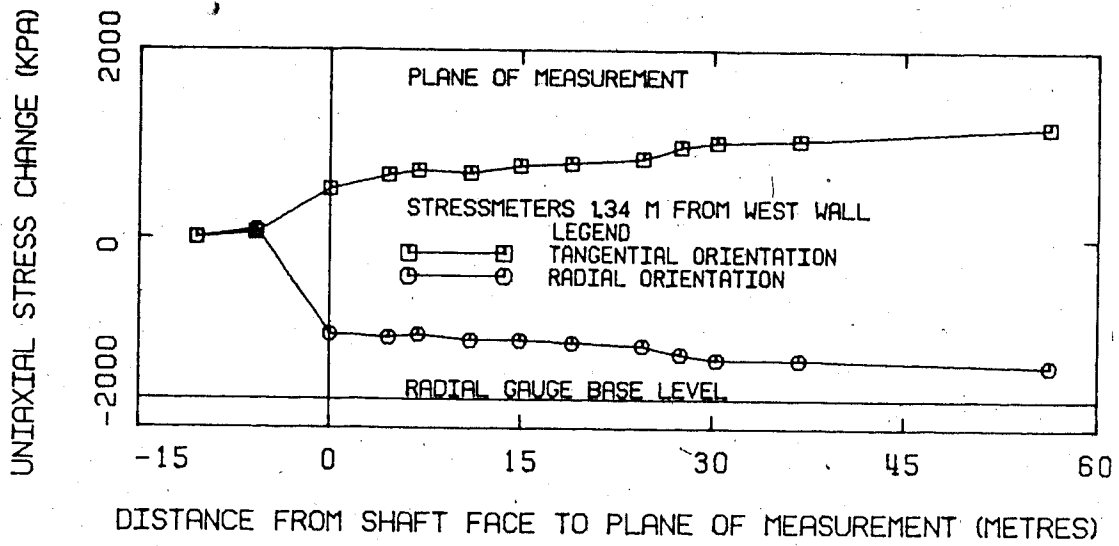


Figure B.17 Stress Change-Depth Plot for Stressmeters at 1.34 m from West Wall

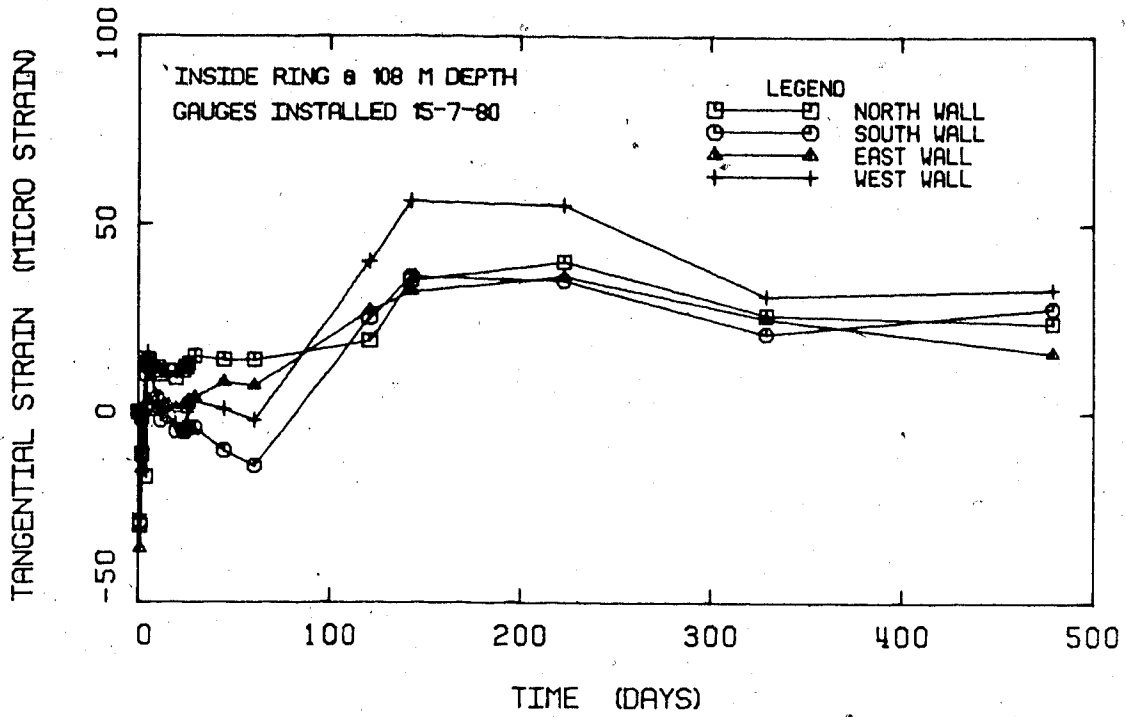


Figure B.18 Tangential Strain-Time Plot for Inside Gauge Ring at 108 m Depth

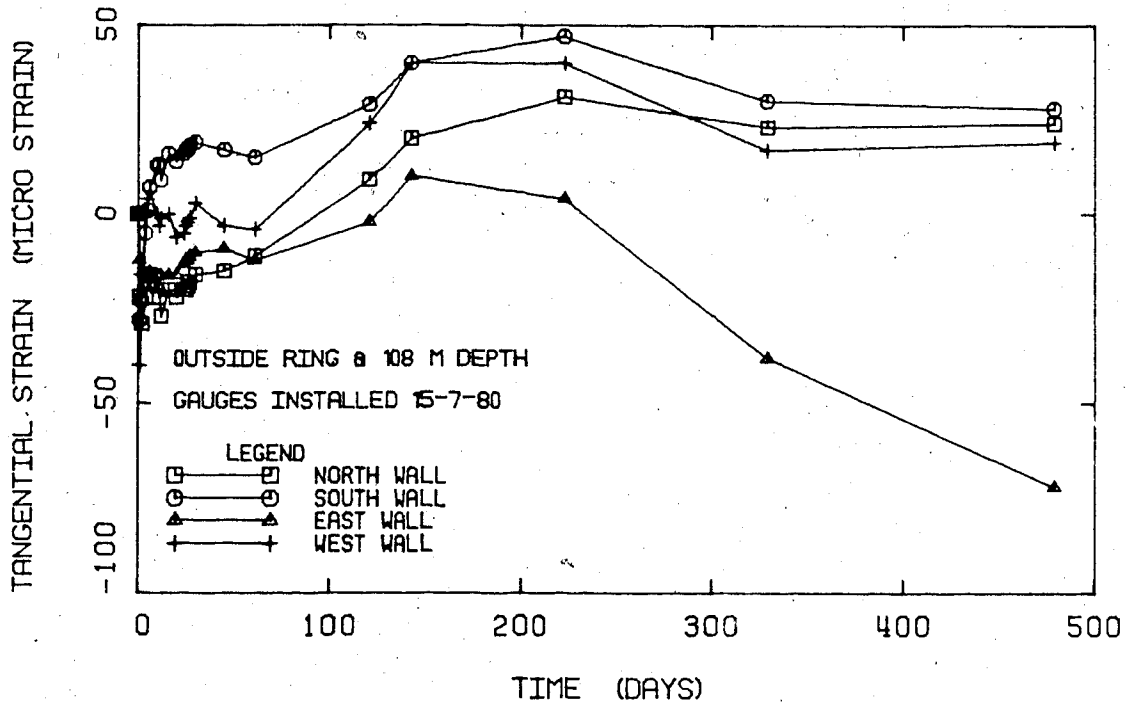


Figure B.19 Tangential Strain-Time Plot for Outside Embedment Gauge Ring at 108 m Depth

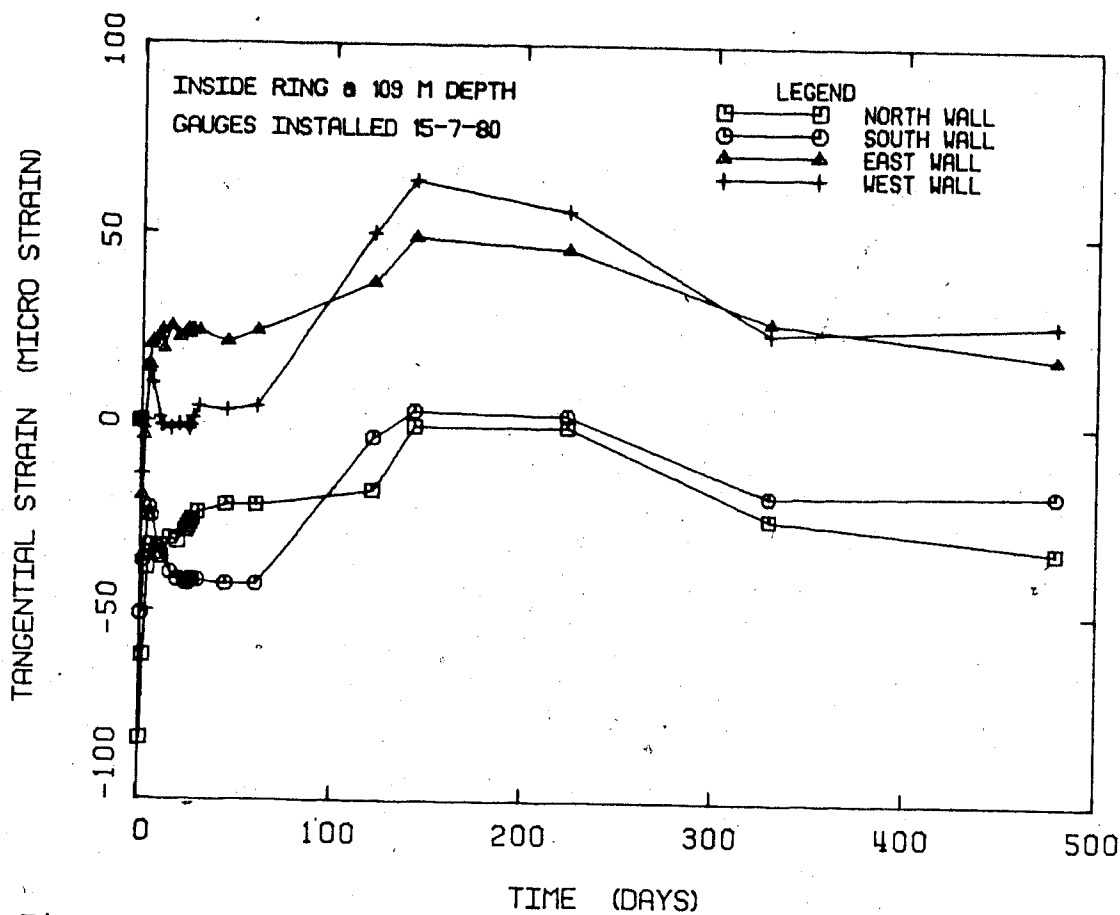


Figure B.20 Tangential Strain-Time Plot for Inside Embedment Gauge Ring at 109 m Depth

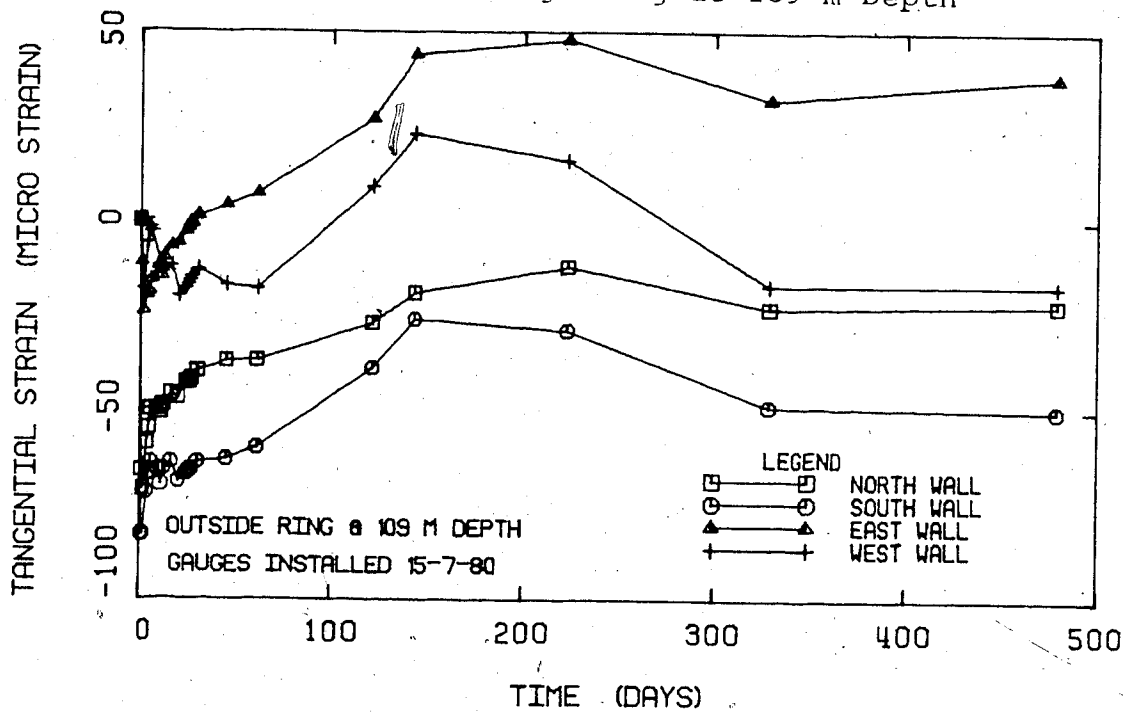


Figure B.21 Tangential Strain-Time Plot for Outside Embedment Gauge Ring at 109 m Depth

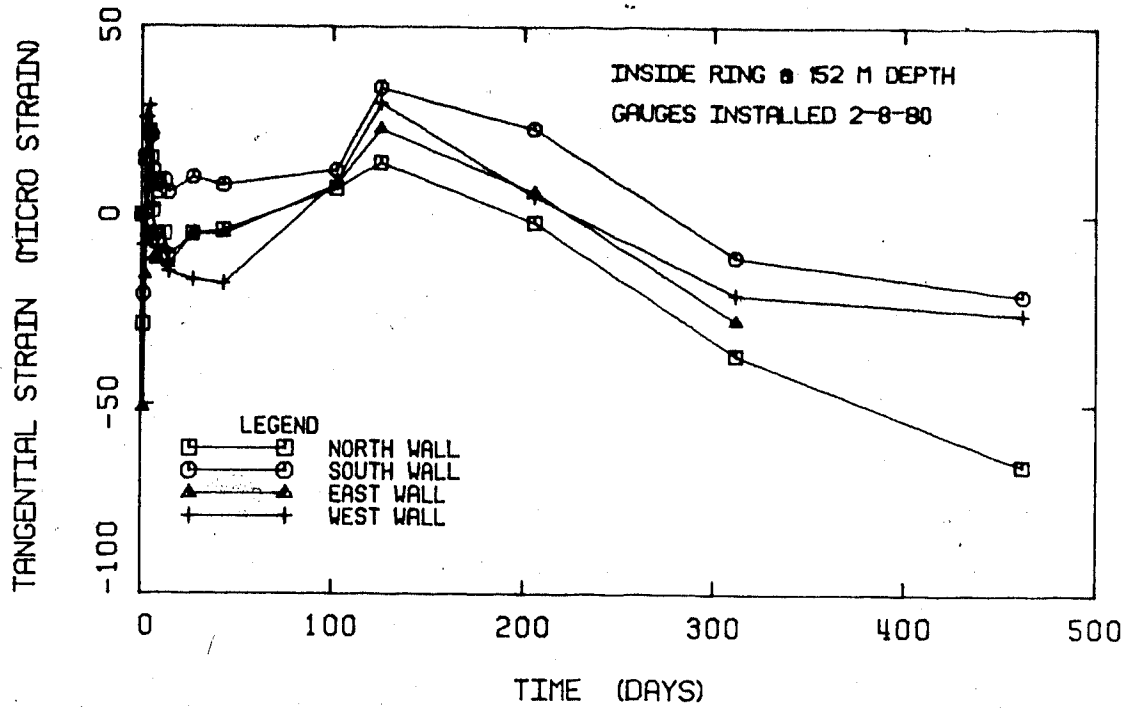


Figure B.22 Tangential Strain-Time Plot for Inside Embedment Gauge Ring at 152 m Depth

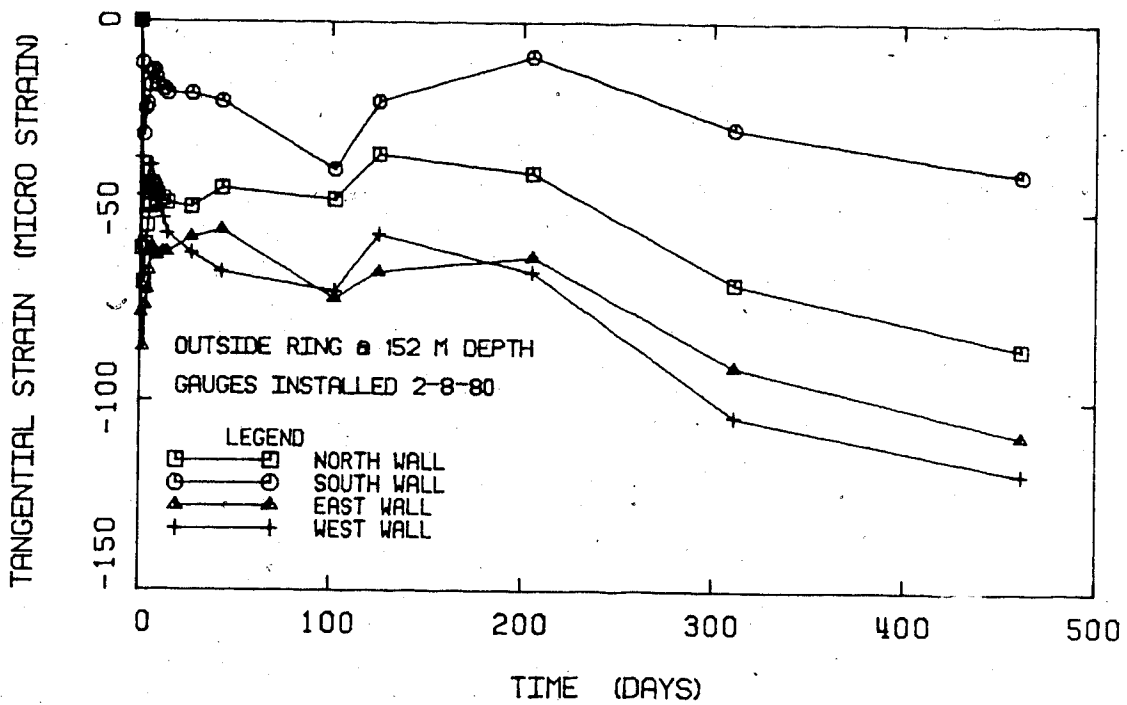


Figure B.23 Tangential Strain-Time Plot for Outside Embedment Gauge Ring at 152 m Depth

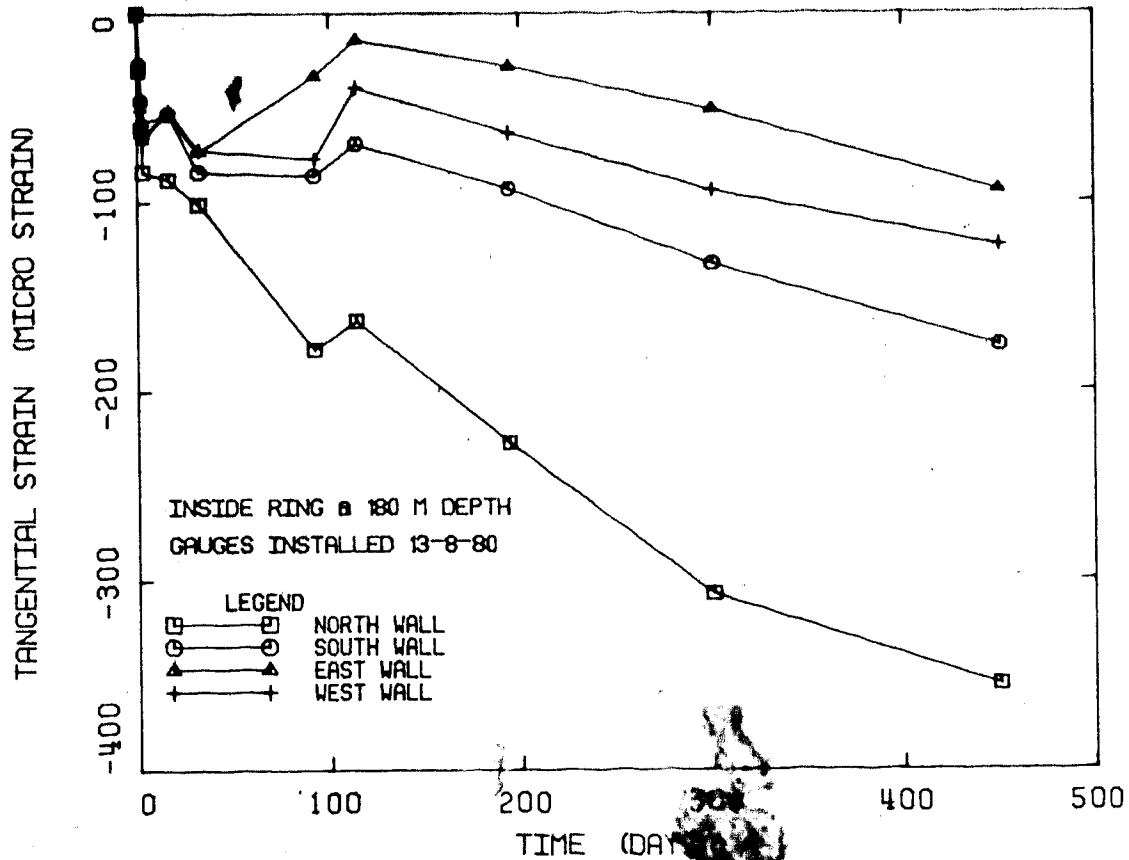


Figure B.24 Tangential Strain-Time Plot for Inside Embedment Gauge Ring at 180 m Depth

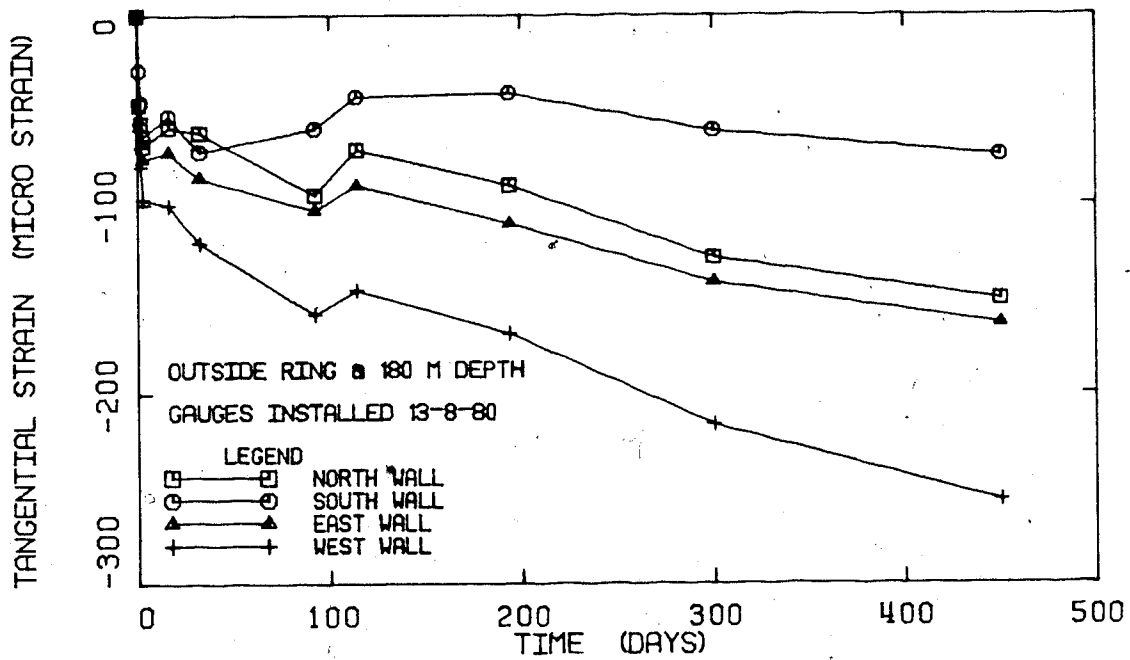


Figure B.25 Tangential Strain-Time Plot for Outside Embedment Gauge Ring at 180 m Depth

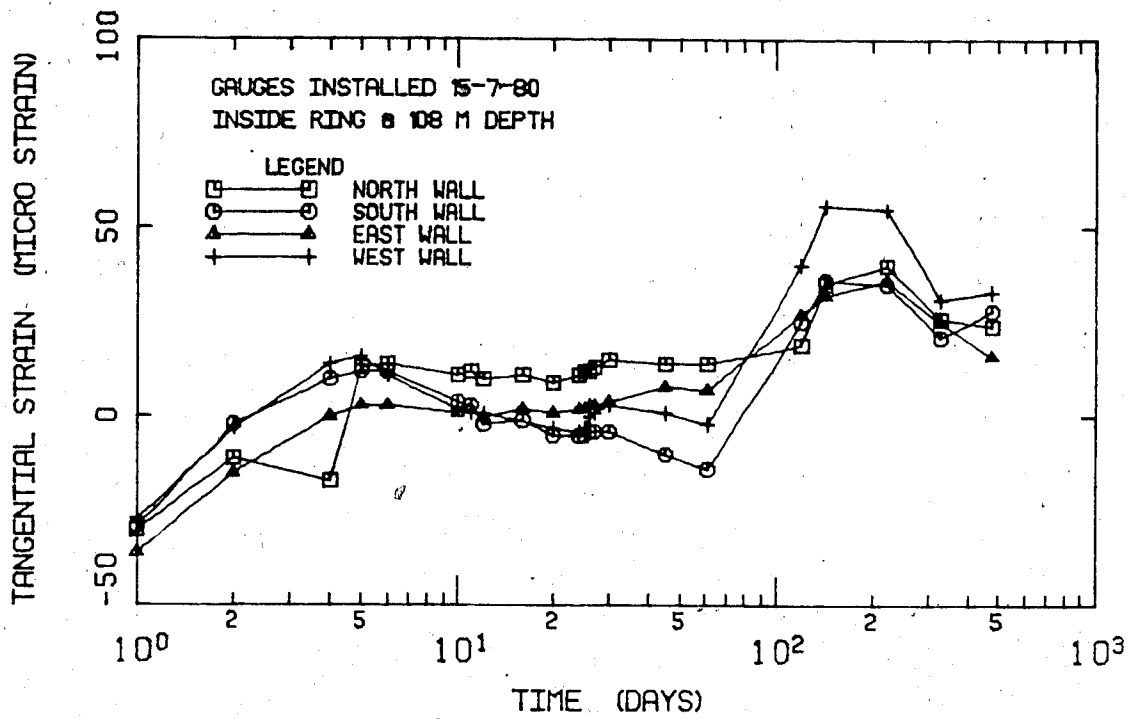


Figure B.26 Tangential Strain-Log Time Plot for Inside Embedment Gauge Ring at 108 m Depth

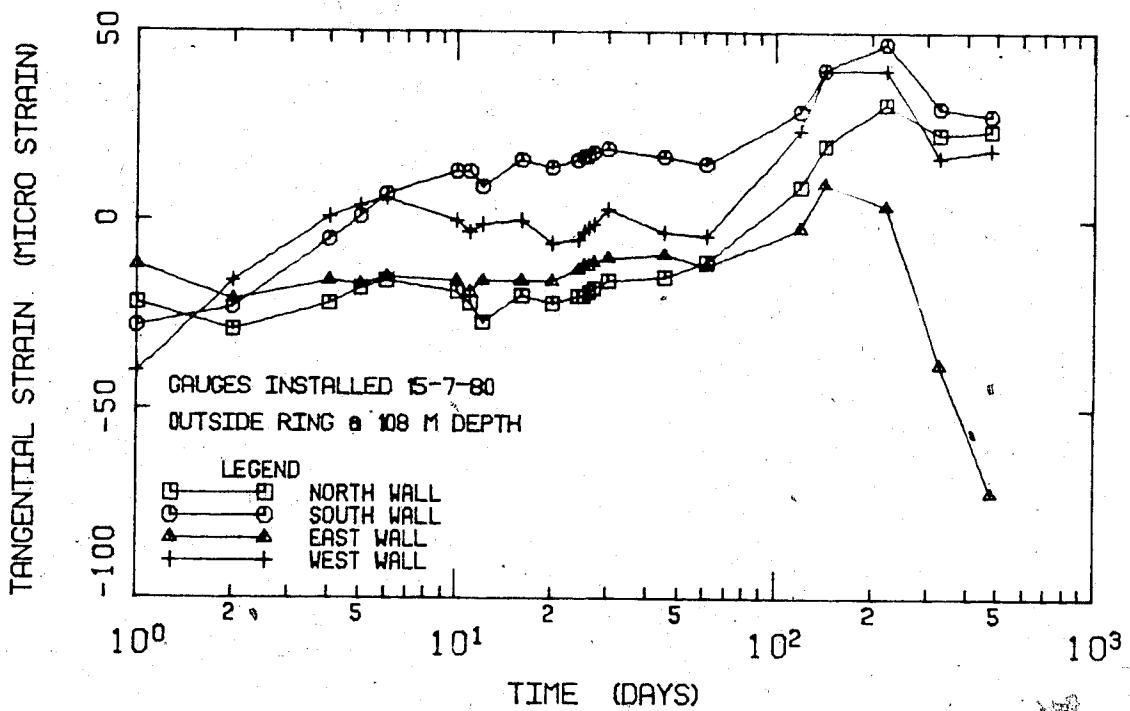


Figure B.27 Tangential Strain-Log Time Plot for Outside Embedment Gauge Ring at 108 m Depth

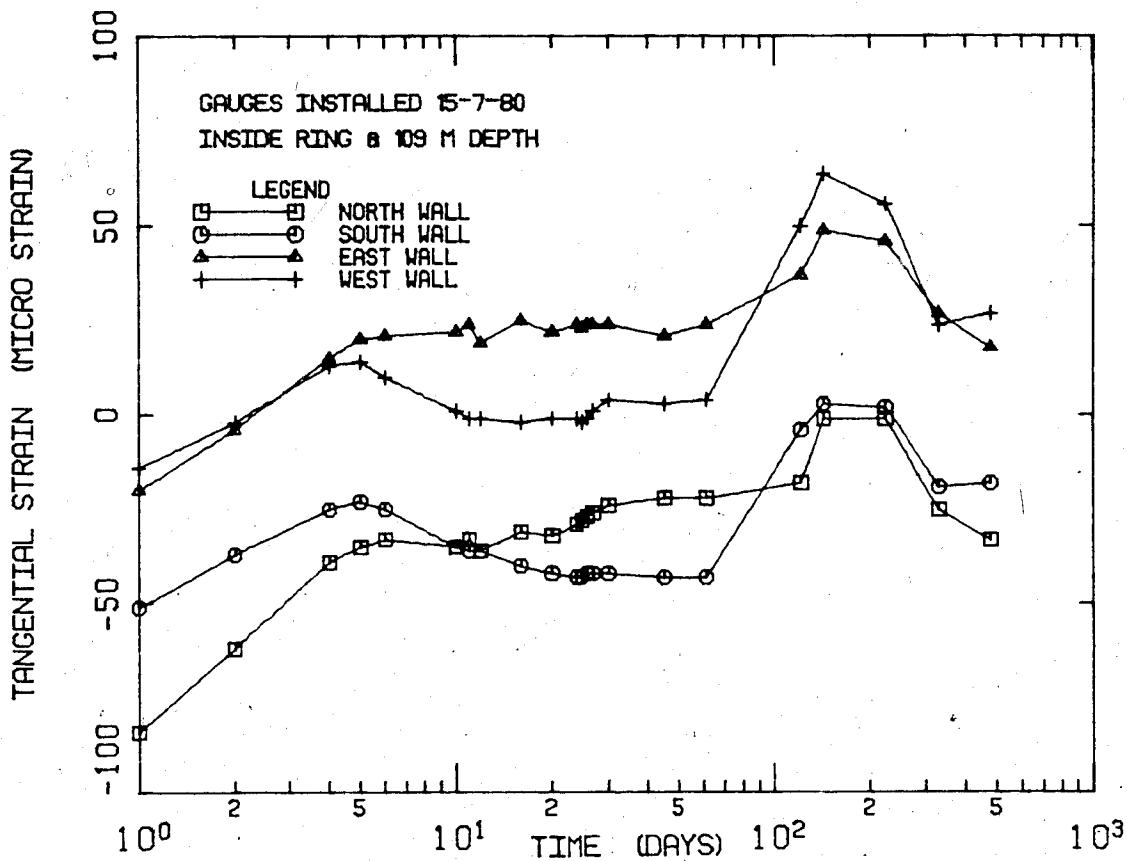


Figure B.28 Tangential Strain-Log Time Plot for Inside Embedment Gauge Ring at 109 m Depth

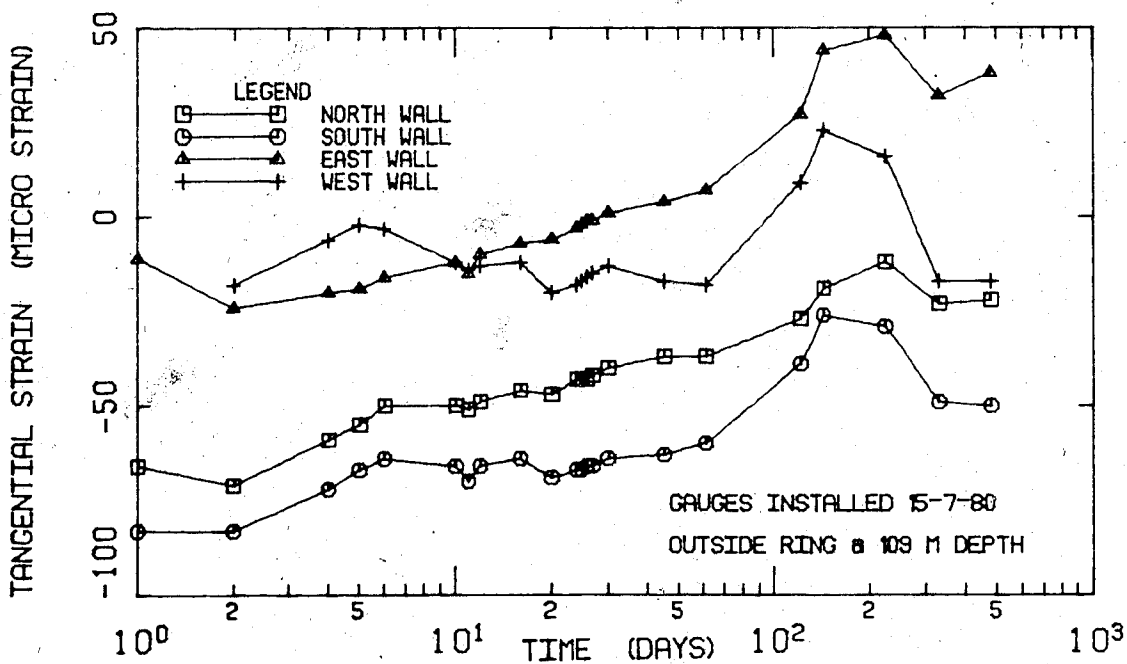


Figure B.29 Tangential Strain-Log Time Plot for Outside Embedment Gauge Ring at 109 m Depth

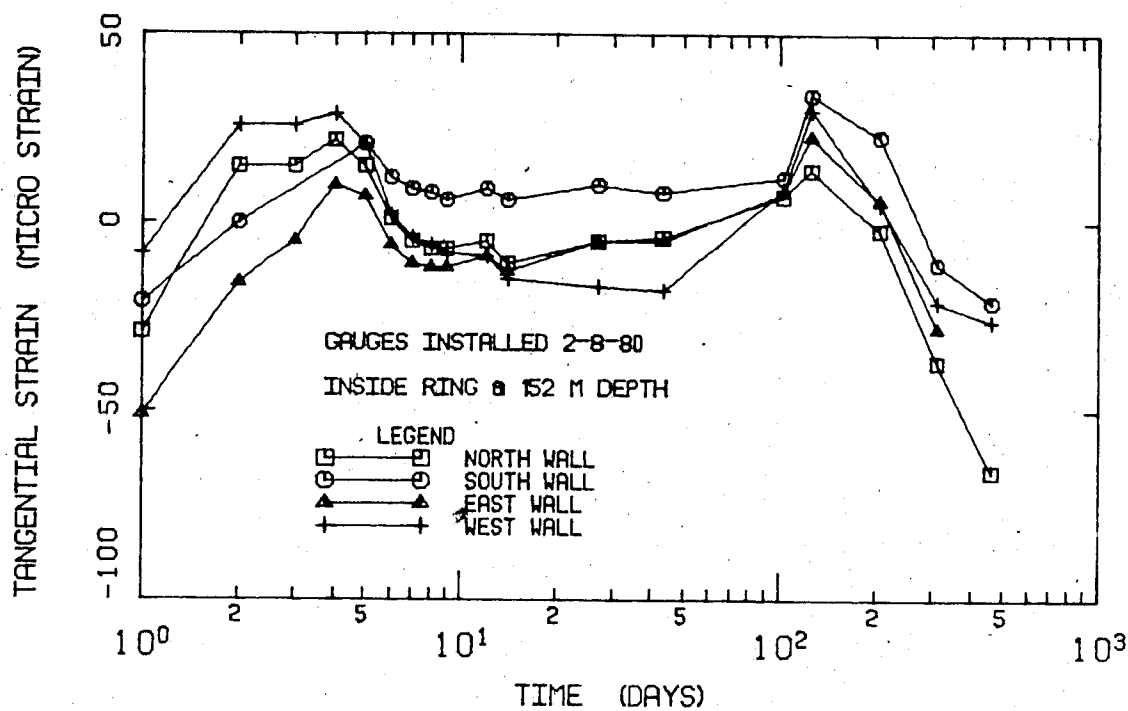


Figure B.30 Tangential Strain-Log Time Plot for Inside Embedment Gauge Ring at 152 m Depth

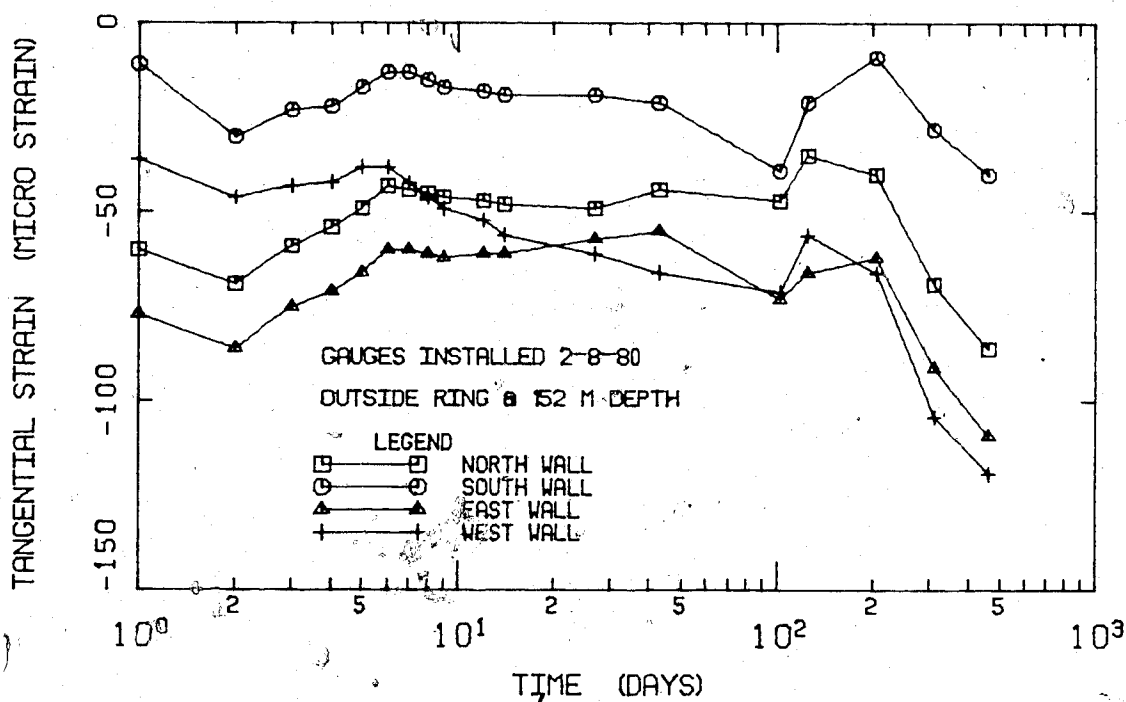


Figure B.31 Tangential Strain-Log Time Plot for Outside Embedment Gauge Ring at 152 m Depth

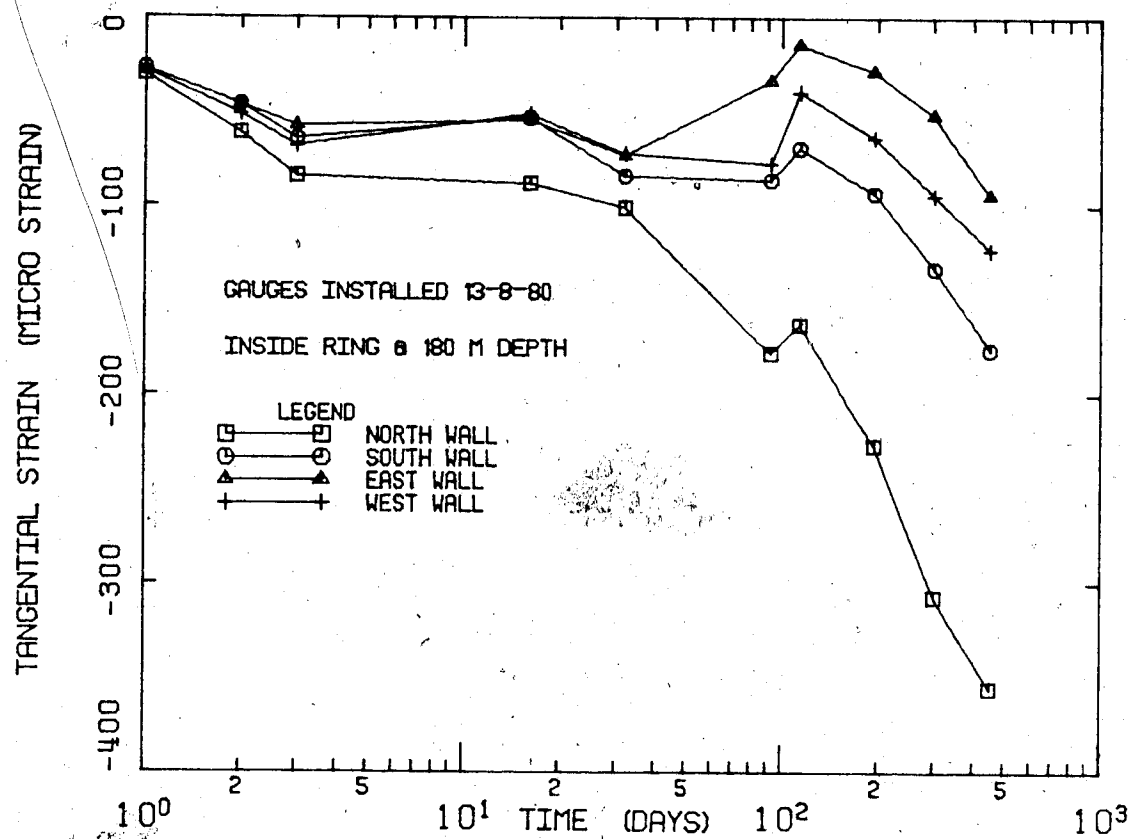


Figure B.32 Tangential Strain-Log Time Plot for Inside Embedment Gauge Ring at 180 m Depth

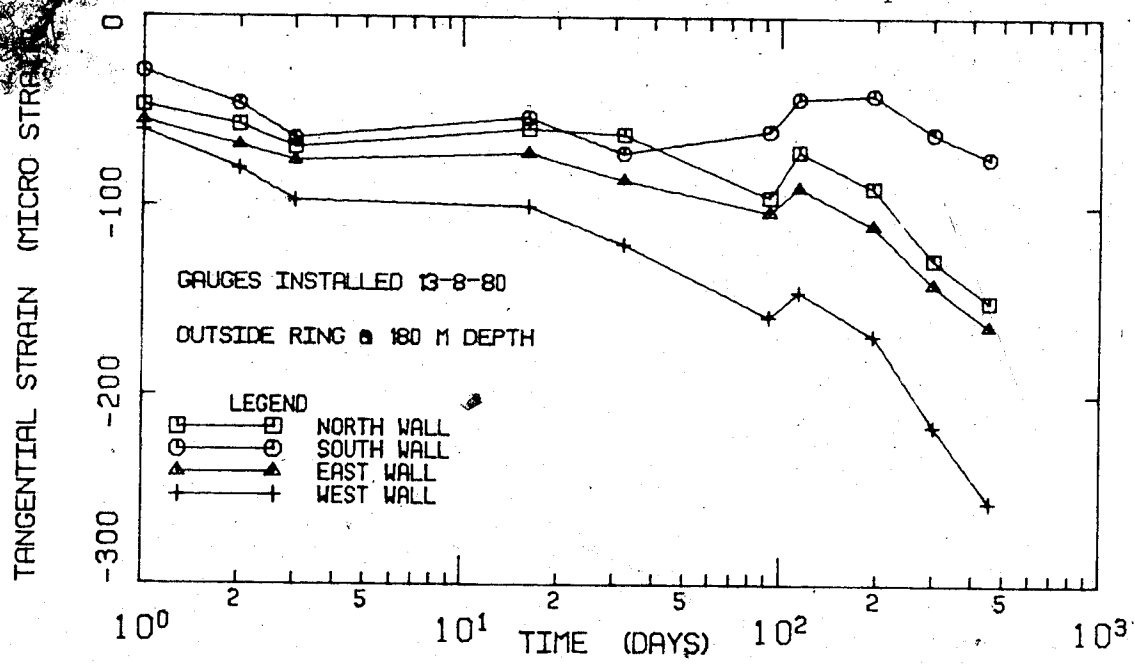


Figure B.33 Tangential Strain-Log Time Plot for Outside Embedment Gauge Ring at 180 m Depth

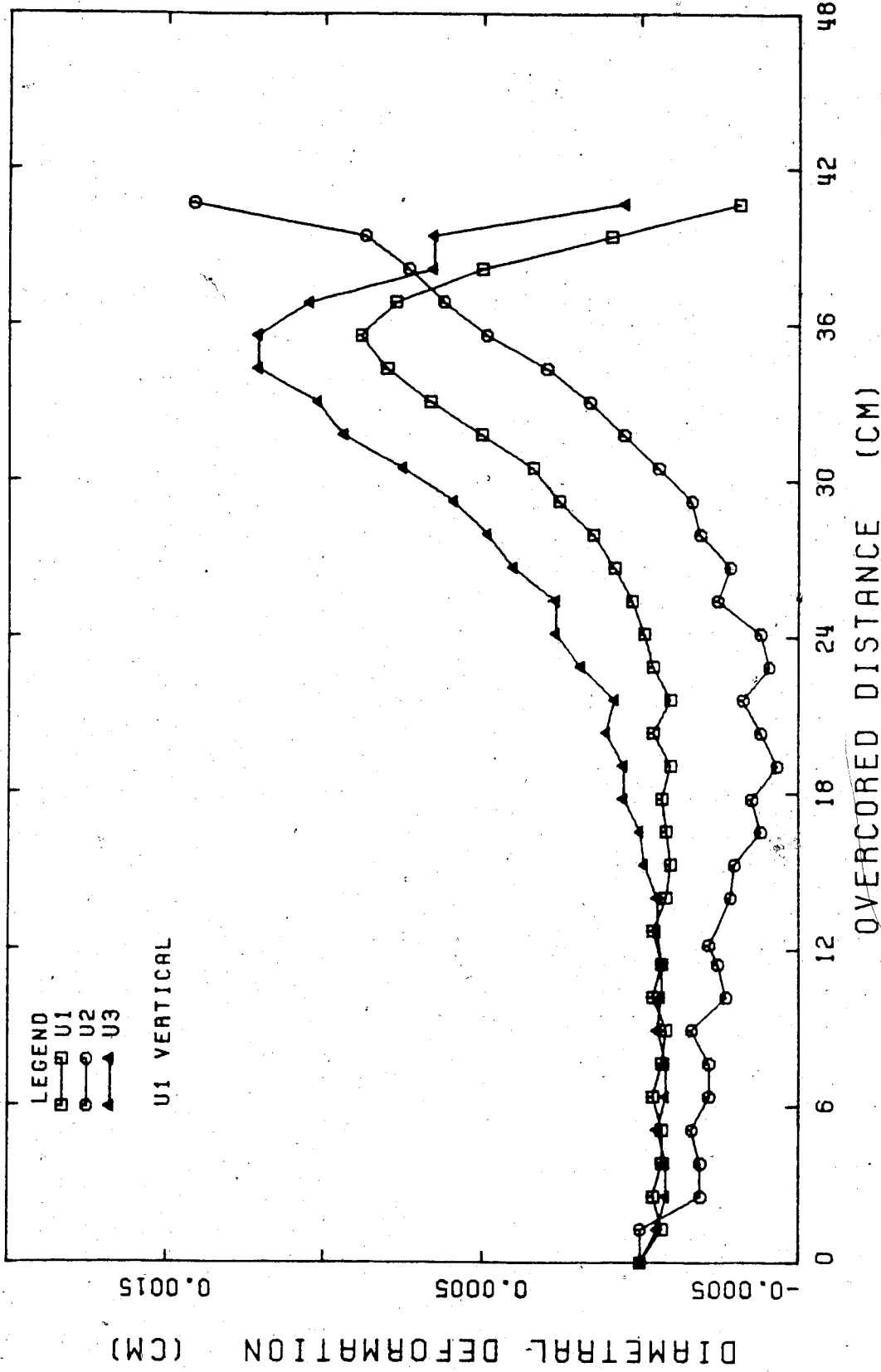


Figure B.34 Plot of Diametral-Deformation vs. Overcored Depth for Overcore Test No. 1

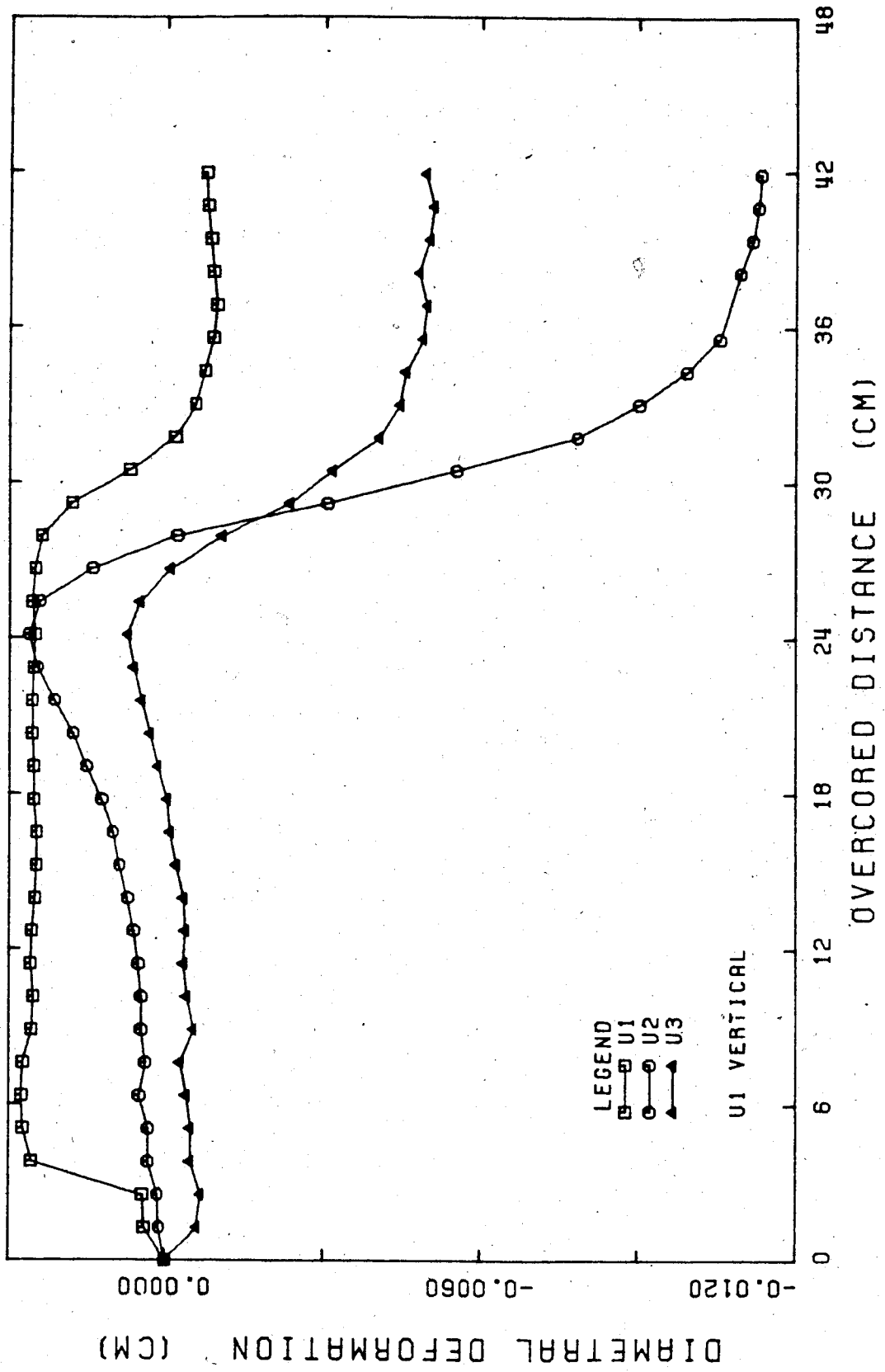


Figure B.35 Plot of Diametral-Deformation vs. Overcored Depth for Overcore Test No. 2

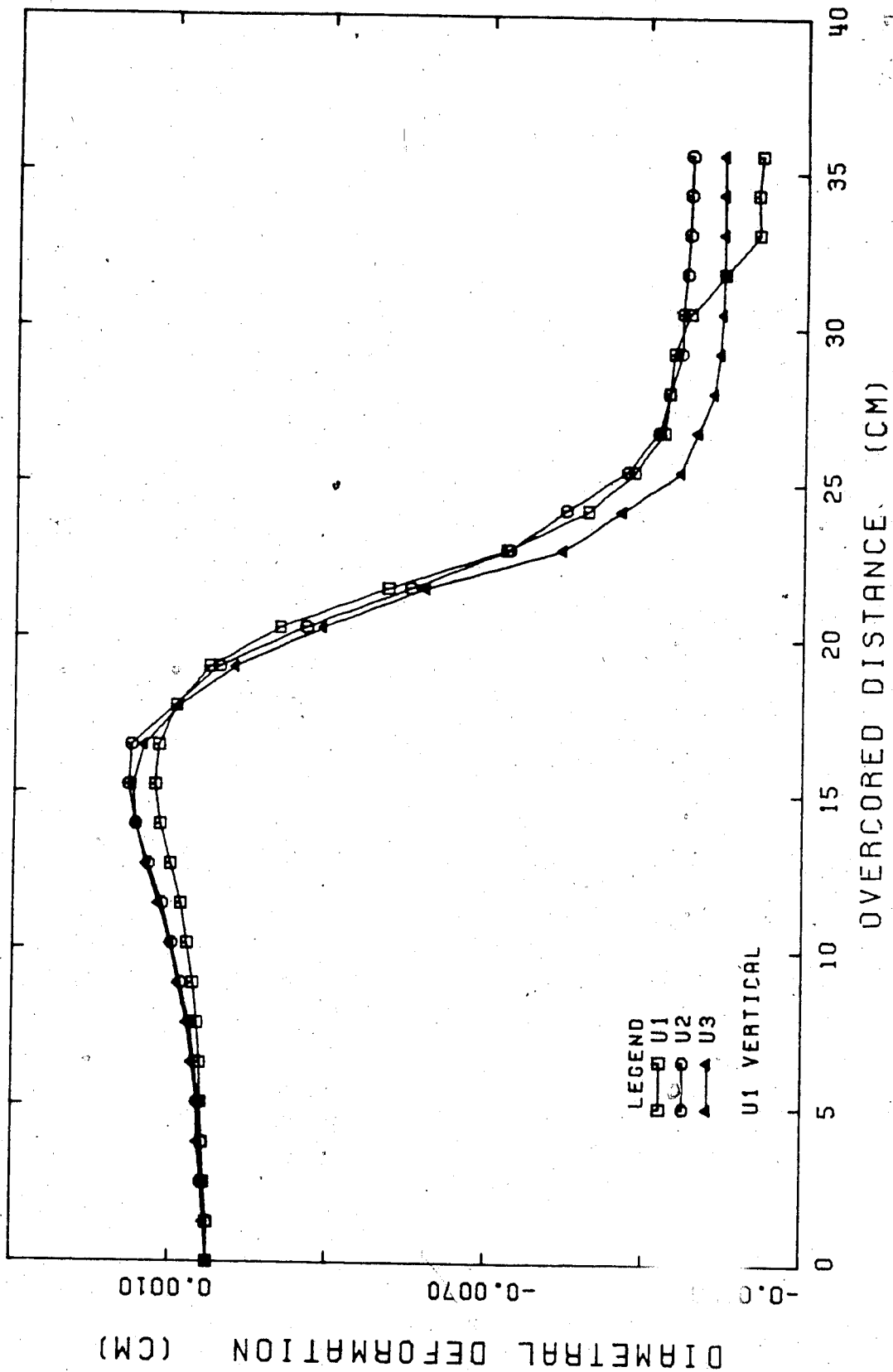


Figure B.36 Plot of Diametral-Deformation vs. Overcored Depth for Overcore Test No. 3

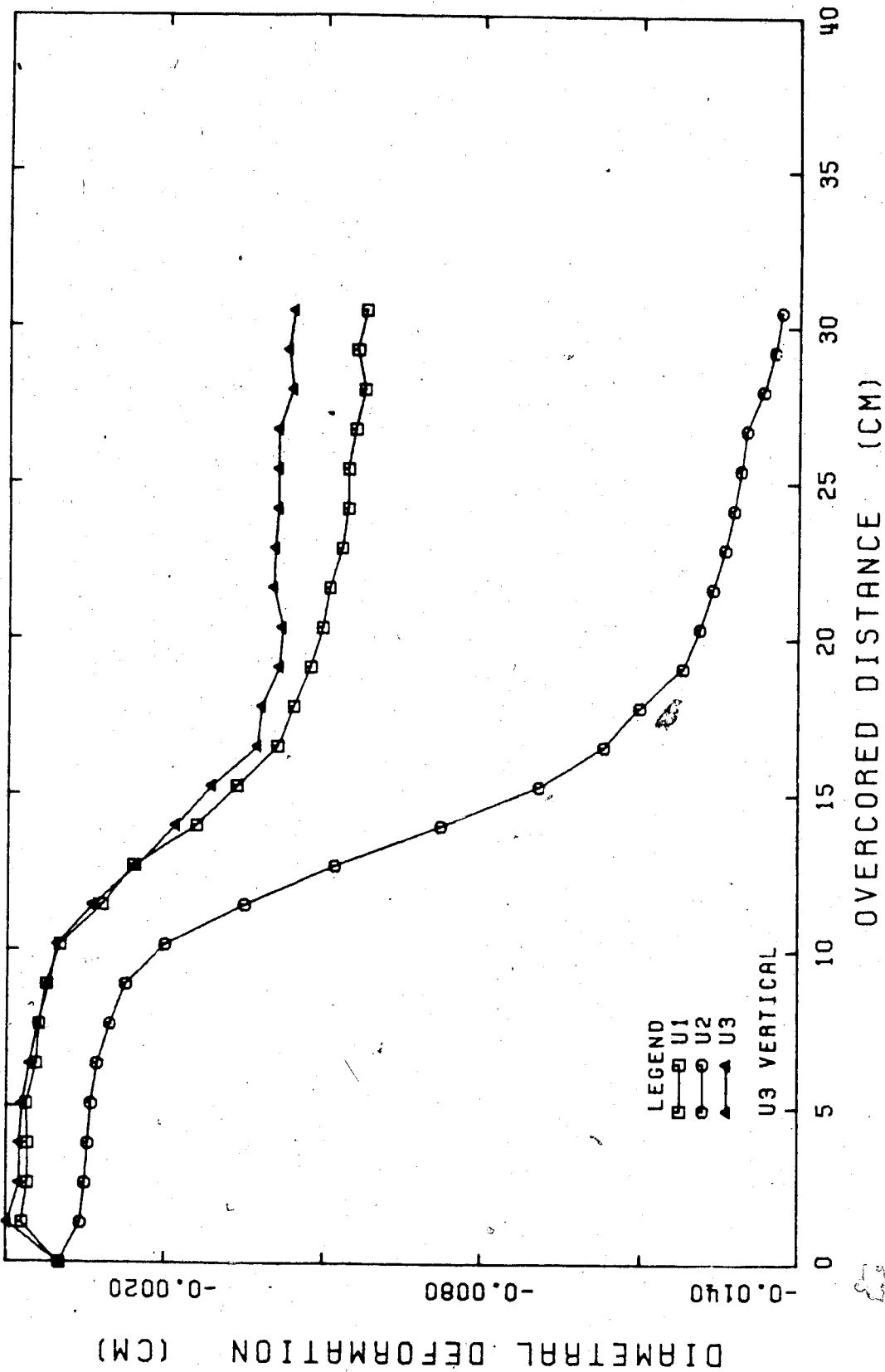


Figure B.37 Plot of Diametral-Deformation vs. Overcored Depth for Overcore Test No. 4

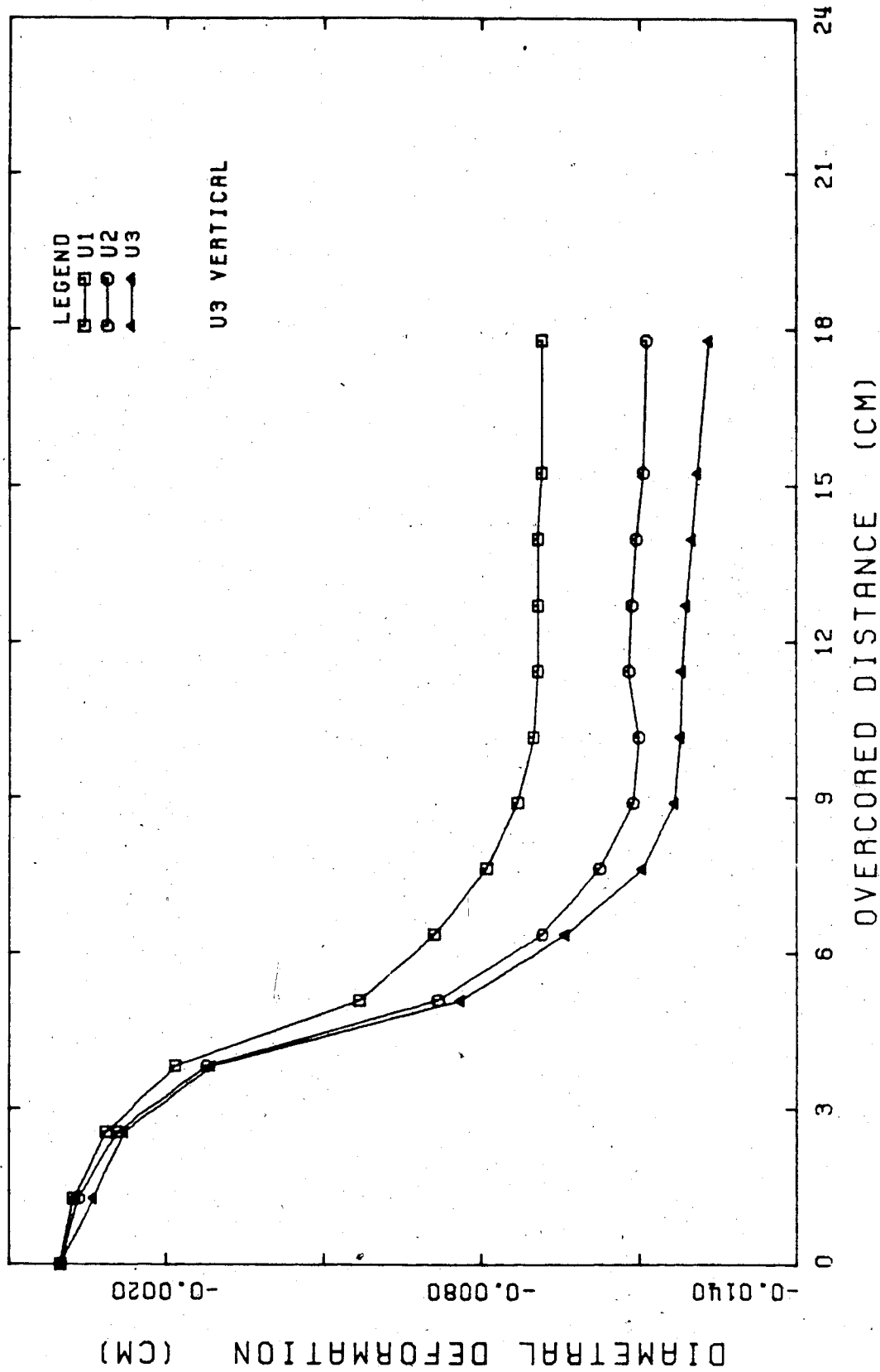


Figure B.38 Plot of Diametral-Deformation vs. Overcored Depth for Overcore Test No. 5

APPENDIX C.1

Radial Displacement Around a Circular Hole Formed in a
Prestressed Thin Plate.

Merill and Peterson (1961) derive the equations for radial displacements around a circular hole formed in a prestressed plate loaded under conditions of plane strain. Kruse (1969) presents the equations for radial displacement from the principle of superposition. Equation C.1.1 relates the radial displacement u_r , which would occur around a circular opening formed in a prestressed plate, to the deformation, u , which would occur in a plate with a hole, subsequently loaded biaxially, and the deformation u_0 which would occur in a biaxially loaded plate without a hole.

$$u_r = u - u_0 \quad \text{Eq. C.1.1}$$

where:

$$u = \frac{1-\nu^2}{E} \left[\frac{S+Q}{2} \left(r + \frac{a^2}{r} \right) + \frac{S-a}{2} \left(r + \frac{4a^2}{r} - \frac{a^4}{r} - \frac{a^4}{r^3} \right) \cos 2\theta \right] \\ - \frac{\nu(1+\nu)}{E} \left[\frac{S+Q}{2} \left(r - \frac{a^2}{r} \right) - \frac{S-a}{2} \left(r - \frac{a^4}{r} \right) \cos 2\theta \right]$$

Eq. C.1.2

Find u_0 from equation C.1.2 for $a=0$.

$$u_o = \frac{1-v^2}{E} \left[\frac{S+Q}{2} r + \frac{S-Q}{2} r \cos 2\theta \right] \\ - \frac{v(1+v)}{E} \left[\frac{S+Q}{2} r - \frac{S-Q}{2} r \cos 2\theta \right]$$

Eq. C.1.3

Substitute equations C.1.2 and C.1.3 into C.1.1 and simply

$$u_r = \frac{Sa^2}{2Er} \left[(1+v) \left(1 - \frac{a^2}{r^2} \cos 2\theta \right) + 4(1-v^2) \cos 2\theta \right] \\ + \frac{Qa^2}{2Er} \left[(1+v) \left(1 + \frac{a^2}{r^2} \cos 2\theta \right) - 4(1-v^2) \cos 2\theta \right]$$

Eq. C.1.4

If $N = Q/S$,

$$u_r = \frac{Sa^2}{2Er} \left\{ \left[(1+v) \left(1 - \frac{a^2}{r^2} \cos 2\theta \right) + 4(1-v^2) \cos 2\theta \right] \right. \\ \left. + N \left[(1+v) \left(1 + \frac{a^2}{r^2} \cos 2\theta \right) - 4(1-v^2) \cos 2\theta \right] \right\}$$

Eq. C.1.5

where:

S = major principal compressive stress

$Q = NxS$ = minor principal compressive stress

a = radius of opening

v = Poisson's ratio of material

E = Young's modulus of elasticity of material

θ = angle between direction of radial displacement and

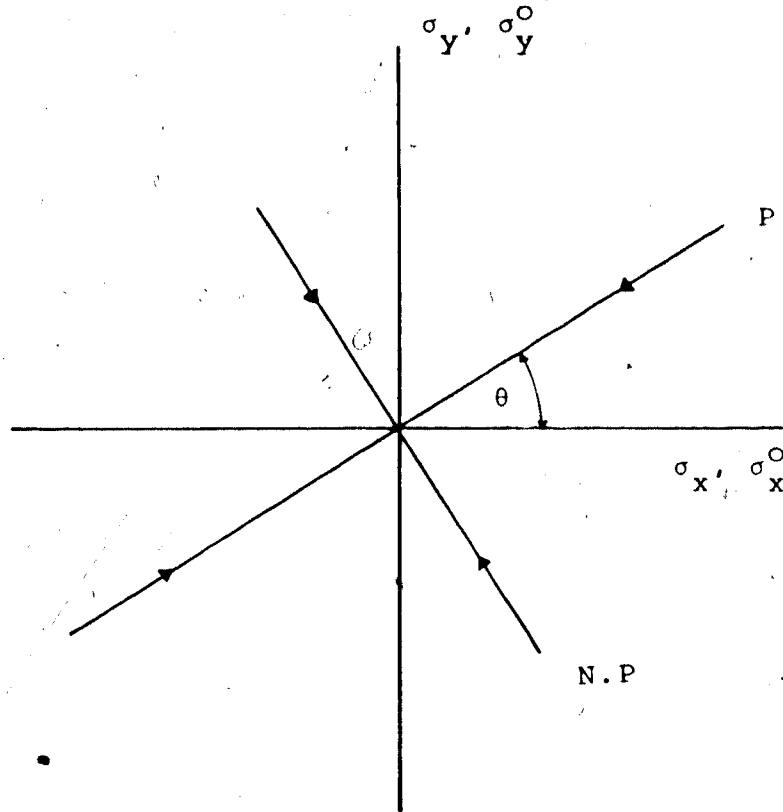
the direction of the major principle compressive stress.

APPENDIX C.2

Analysis of Stress Change Measurements Adjacent to Shaft

This appendix deals with the interpretation of vibrating wire stress change measurements adjacent to a circular opening excavated in a prestressed material. The material is assumed to be isotropic and linearly elastic. For simplicity plane stress conditions will be assumed. Pariseau (1978) states that the plane stress case is within 6% of the plain strain case for $\nu = 0.25$. Figure C.1 shows the reference coordinates and notation used in the solution.

Pariseau (Ibid) presents an analysis of stress change measurements for both soft and hard gauges. Soft gauges, such as the U.S.B.M. deformation probe do not influence the deformations the borehole experiences due to stress changes in the rock. Hard gauges such as the vibrating wire stressmeter, act as a rigid inclusion in the borehole because of the high stiffness ratio of the gauge to the rock. The principle of operation of the gauges is described in section 4.3.4.3. Calibration of the uniaxial response of the soft rock model of the gauges across the loaded diameter, during multiaxial compression tests in coal has closely matched the manufacturers suggested reduction factors (Pariseau and Eitanni, 1977). Three gauges installed in the same borehole may be used to determine the biaxial stress change. It is assumed that the uniaxial stress change is measured in a given orientation at each



$\sigma_x^0, \sigma_y^0 =$ Initial Stresses

$\sigma_x, \sigma_y =$ Final Stresses

$\sigma_1^0 = P =$ Major Principal Stress

$\sigma_3^0 = \text{N.P.} =$ Minor Principal Stresses

Figure C.1 Initial Biaxial Stress Conditions

gauge independent of the adjacent gauge(s), i.e. the gauges are not a co-planar array. This allows the interpretation of each gauge separately.

In terms of global x-y coordinate system, as shown in Figure A.1, the stress change in the x and y direction is

$$\Delta \sigma_x = \sigma_x(\text{final}) - \sigma_y^0(\text{initial})$$

$$\Delta \sigma_y = \sigma_y(\text{final}) - \sigma_y^0(\text{initial}) \quad \text{Eq. C.2.1}$$

Initial stress condition, before excavation of shaft:

$$\sigma_x^0 = \frac{1}{2} (\sigma_1^0 + \sigma_3^0) + (\sigma_1^0 - \sigma_3^0) \cos 2\theta$$

$$\sigma_y^0 = \frac{1}{2} (\sigma_1^0 + \sigma_3^0) - (\sigma_1^0 - \sigma_3^0) \cos 2\theta \quad \text{Eq. C.2.2}$$

or

$$\sigma_x^0 = \frac{1}{2} (P + N.P.) + (P - N.P.) \cos 2\theta$$

$$\sigma_y^0 = \frac{1}{2} (P + N.P.) - (P - N.P.) \cos 2\theta \quad \text{Eq. C.2.2a}$$

Adjacent to the shaft, the final stresses following shaft construction are given by Kirsch's Equations (Timoshenko & Goodier, 1970), following the notation shown in Figure C.2.

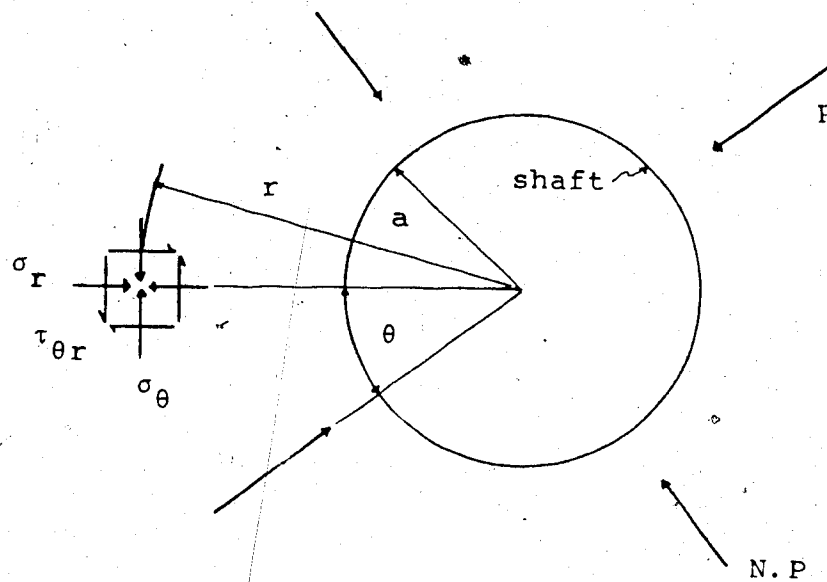


Figure C.2 Notation for Biaxial Stresses Adjacent to Shaft in Isotropic Elastic Ground

$$\sigma_r = \frac{P}{2} [(1+N)(1-\alpha^2) + (1-N)(1 + 3\alpha^4 - 4\alpha^2)] \cos 2\theta$$

$$\sigma_\theta = \frac{P}{2} [(1+N)(1+\alpha^2) - (1-N)(1 + 3\alpha^4)] \cos 2\theta$$

Eq. C.2.3

Where: $\alpha = a/r$ If: $\sigma_r^0 = \sigma_x^0$ $\sigma_\theta^0 = \sigma_y^0$

And insert equation C.2.3 and equation C.2.2.a into equation C.2.1:

$$\Delta\sigma_r = \Delta\sigma_x = \frac{P}{2} [(1+N)(1-\alpha^2) + (1-N)(1 + 3\alpha^4 - 4\alpha^2)] \cos 2\theta$$

$$- \left[\frac{1}{2} (P+N.P.) + (P - N.P.) \cos 2\theta \right]$$

$$\Delta\sigma_\theta = \Delta\sigma_y = \frac{P}{2} [(1+N)(1+\alpha^2) - (1-N)(1 + 3\alpha^4)] \cos 2\theta$$

$$- \left[\frac{1}{2} (P+N.P.) - (P-N.P.) \cos 2\theta \right]$$

Eq. C.2.4

After simplifying:

$$\frac{\Delta\sigma_r}{P} = \frac{1}{2} \{ (1+N)(1-\alpha^2) + (1-N)(1 + 3\alpha^4 - 4\alpha^2) \cos 2\theta \\ - [(1+N) + (1-N) \cos 2\theta] \}$$

$$\frac{\Delta\sigma_\theta}{P} = \frac{1}{2} \{ (1+N)(1+\alpha^2) - (1-N)(1+3\alpha^4) \cos 2\theta \\ - [(1+N) - (1-N) \cos 2\theta] \}$$

Eq. C.2.5

APPENDIX C.3

Evaluation of Elastic and Creep Strains
in the Concrete Lining

The Comité Euro-International Du Béton (1978) presents an empirical method which allows evaluation of creep strains in concrete cured under normal conditions. A 20 percent margin of uncertainty is suggested for the method. The method is based on the assumptions that the principle of superposition is valid, that is, creep deformations which result from stresses applied at different times or at variable rates, are additive. A detailed description of the method is presented in the C.E.B. (Ibid), and will not be repeated here. Basically the method uses a series of empirical curves which relate the age of the concrete when initially loaded, the age when the strain is measured, the structure geometry and drying conditions to a creep coefficient. The creep coefficient divided by the 28 day modulus of elasticity of the concrete is the creep strain per unit stress which occurs at time t when the concrete is loaded at time t_0 . All times are with respect to the day of pouring. The total strain in the concrete at a time t , for a constant stress σ_0 applied at t_0 is given in equation C.3.1.

$$\epsilon(t, t_0) = \sigma_0 \times \left(\frac{1}{E_c(t_0)} + \frac{\rho(t, t_0)}{E_{c28}} \right) \quad \text{Eq. C.3.1}$$

where: $\epsilon(t, t_0)$ is the total strain at time t
 σ_0 is the stress applied at time t_0
 $E_c(t_0)$ is the instantaneous modulus of elasticity
of the concrete at t_0
 E_{c28} is the instantaneous modulus of elasticity
at $t = 28$ days
 $\rho(t, t_0)$ is the creep coefficient
 $\frac{1}{E_c(t_0)}$ is the instantaneous elastic strain at t_0
 $\frac{\rho(t, t_0)}{E_{c28}}$ is the creep strain at time t .

The creep function, $\phi(t, t_0)$ is defined by equation C.3.2.

$$\phi(t, t_0) = \frac{1}{E_c(t_0)} + \frac{\rho(t, t_0)}{E_{c28}} \quad \text{Eq. C.3.2}$$

By application of the principle of superposition, the total strain of the concrete at some time t , may be calculated for a uniform stress variation from equation C.3.3.

$$\epsilon(t, t_0) = \epsilon_n(t) + \sigma_0 \phi(t, t_0) + \int_{t_0}^t \phi(t, \tau) d[\sigma(\tau)] \quad \text{Eq. C.3.3}$$

where: $\epsilon_n(t)$ is strain independent of stress (shrinkage, thermal expansion)

$\phi(t, \tau)$ is the creep function

$d[\sigma(\tau)]$ is the variation of stress at the time interval $d\tau$

In analyzing the shaft strain data, the following assumptions will be applied:

- the loading of the shaft by the rock mass may be approximated by a constant linear function with an initial constant stress σ_0
- shrinkage and thermal strains may be evaluated separately prior to creep and elastic strain analysis,

Therefore equation C.3.3 may be simplified to give equation C.3.4

$$\varepsilon(t, t_0) = \sigma_0 \phi(t, t_0) + \int_{t_0}^t \phi(t, \tau) d[\sigma(\tau)] \quad \text{Eq. C.3.4}$$

The first term in equation C.3.4 is the total strain (elastic + creep) at time t due to the constant stress σ_0 applied at time t_0 . The second term in equation C.3.4 is the total strain at time t due to the linearly increasing stress, commencing from zero stress at time t_0 . The two load histories may be considered as separate events, occurring at a different time t_0 .

Evaluation of the creep function $\phi(t, t_0)$ for $t_0 = 3$ to 400 days and for $t = 450$ days, the concrete age at the time of the most recent reading, is presented in Table C.1.

Equation C.3.5 is the C.E.B. equation for calculating the creep coefficient, $\rho(t, t_0)$.

Table C.1 Parameters for Development of Creep Function for
Concrete Lining at t=450 Days

t_0 [days]	3	5	10	20	40	70	100	200	300	400
$t-t_0$ [days]	447	445	440	430	410	380	350	250	150	50
$E_c(t_0)$ [GPa]	16.8	20.2	24.6	28.2	30.8	32.1	32.7	33.4	33.6	33.8
f'_c [MPa]	11.4	16.3	24.1	31.8	37.8	41.2	42.7	44.6	45.3	45.6
$1/E_c \times 10^6$	59.4	49.6	40.7	35.5	32.5	31.2	30.6	30.0	29.7	29.6
$\rho(t, t_0)$	2.07	1.87	1.63	1.38	1.15	1.02	0.90	0.67	0.49	0.31
$\phi(450, t_0)$ [Microstrain/MPa]	129.5	112.9	95.7	82.1	71.5	65.5	61.1	52.5	46.3	40.1

$$\rho(t, t_0) = \beta_a(t_0) + \rho_d \beta_d(t-t_0) + \rho_F [\beta_F(t) - \beta_F(t_0)]$$

Eq. C.3.5

For the Lethbridge shaft, equation C.3.5 reduces to

$$\rho(t, t_0) = \beta_a(t_0) + 0.4\beta_d(t-t_0) + 2.8 [0.5 - \beta_F(t_0)]$$

Eq. C.3.6

The values of the various coefficients of equations C.3.5 and C.3.6 are given on pages 333 to 338, Appendix E, VII, after C.E.B. report (Ibid) N.124/125.

$$F'_{c_t} = f'_{c_{28}} \left(\frac{4}{3 + \frac{28}{t}} \right)$$

Eq. C.3.6

$$E_{c_i} = 5000 \sqrt{F'_{c_t}} \text{ [MPa]}$$

Eq. C.3.7

where: F'_{c_t} is the instantaneous unconfined compressive strength of the concrete at time t .

E_{c_i} is the instantaneous modulus of elasticity of the concrete at time t .

Equations C.3.6 and C.3.7 are empirical equations expressing the development of strength and modulus of elasticity of concrete with time, (Neville, 1970). The concrete used in the shaft has an average 28 day compressive strength of 35 MPa. Figure C.3.1 is the plot of the creep function $\phi(450, t_0)$ vs \log_e time. Equation C.3.8 gives a good fit to

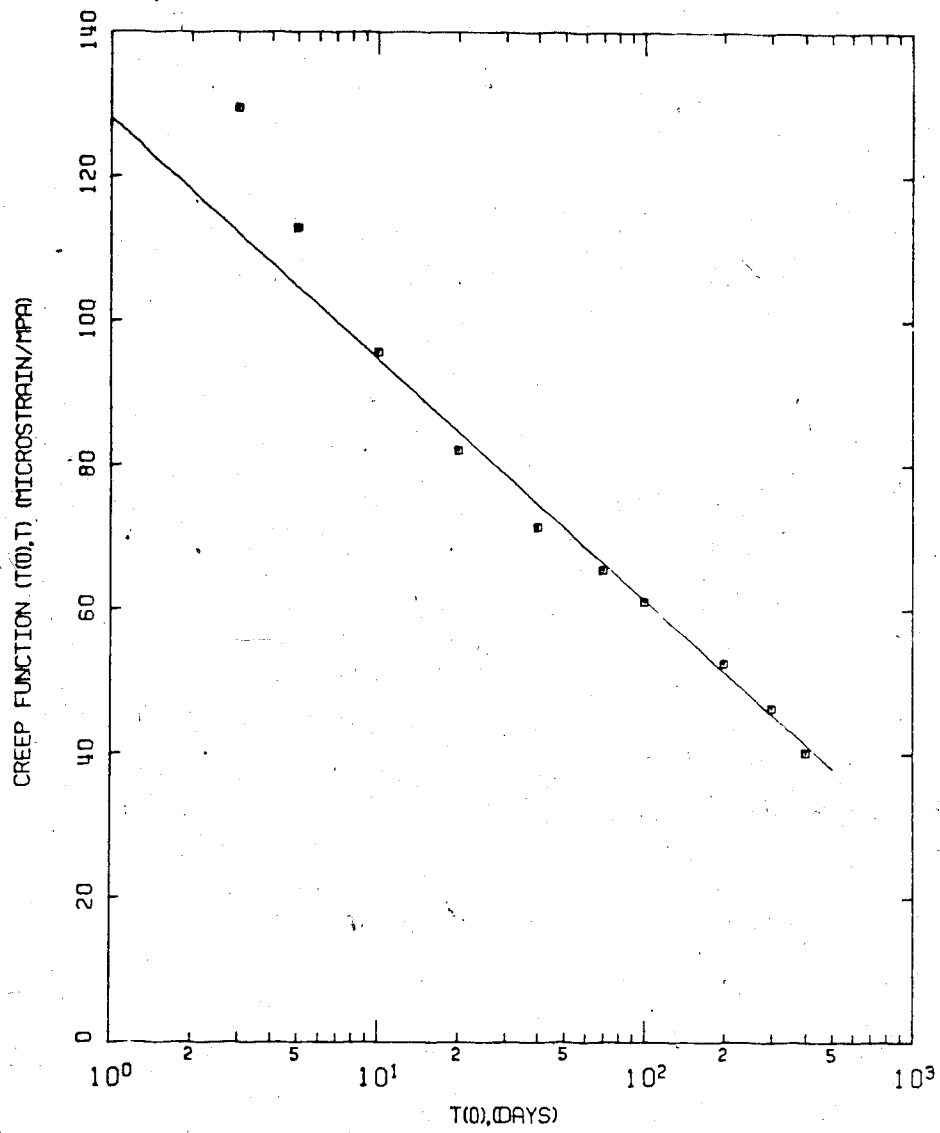


Figure C.3 Creep Function vs. Time for $t=450$ days

the points for $10 < t_0 < 450$ days

$$\phi(450, t_0) = 128 - 14.76 \ln(t_0) \text{ [microstrain/MPa]}$$

Eq. C.3.8

The significant deviation of $\phi(450, t_0)$ for $t_0 = 3$ and 5 days is probably related to the difficulty in predicting $\phi(t, t_0)$ for very low values of t_0 . This is not important as it will be assumed that loading of the liner commenced on or after $t_0 = 10$ days. A creep function similar to equation C.3.8 must be calculated for each time t at which lining strains are analyzed. Substitution of equation C.3.8 into the second term of equation C.3.4 yields:

$$\epsilon(450, t_0) = \int_{t_0}^{450} (128 - 14.76 \ln(t_0)) d[\sigma(\tau)]$$

Eq. C.3.9

Since a constant linear loading function will be assumed, the term $d[\sigma(\tau)]$ in equation C.3.9 becomes $K \cdot dt$ where K is the constant increase of stress with time, (MPa/day).

Equation C.3.9 becomes:

$$\epsilon(450, t_0) = \int_0^{450} (128 - 14.76 \ln(t_0)) \cdot K \cdot dt$$

Eq. C.3.10

Integration of equation C.3.10 yields:

$$\epsilon(450, t_0) = K \left[128t \Big|_{t_0}^{450} - 14.76 (t/nt - t) \Big|_{t_0}^{450} \right]$$

Eq. C.3.11

and after simplification

$$\epsilon(450, t_0) = K \left[128(450 - t_0) - 14.76(2299 - t_0(\ln t_0 - 1)) \right]$$

Eq. C.3.12

The constant loading of the lining at both the 152 and 180 m levels was considered to begin at $t=10$ days because of the observed strain increase at the 180 m level after 10 days. Solution of equation C.3.12 for 10 days yields

$$\epsilon(450, 10) = 22,579 K \text{ [microstrain]}$$

Eq. C.3.13

A value of K was calculated from equation C.3.13 for each measured $\epsilon(450, 10)$. Stress from gradual loading was then calculated from equation C.3.14.

$$\sigma_{450} = K \times 450 \text{ [MPa]}$$

Eq. C.3.14

Results are shown in tables 6.4 and 6.5.

APPENDIX C.4

Formulas for Determining in situ Stresses in Isotropic Rock

The diametral deformation of a borehole on overcoring is related to a biaxial stress field in the plane normal to the borehole, by a closed form elastic solution. For the borehole shown in Figure C.4, the diametral deformation U is related to the principal biaxial stresses, P and Q by equations C.4.1 (Obert, 1966).

For Plane Stress:

$$U = \frac{d}{E} [(P+Q) + 2(P-Q) \cos 2\theta]$$

For Plane Strain:

$$U = \frac{d(1-\nu^2)}{E} [(P+Q) + 2(P-Q) \cos 2\theta] \quad \text{Eq. C.4.1}$$

where: d = borehole diameter

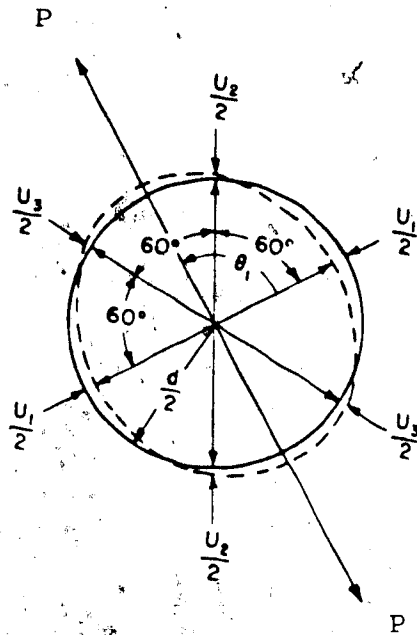
E = Young's modulus

ν = Poisson's ratio

θ = is measured as shown in Figure C.4

For a borehole overcored in a 3-dimensional stress field, the deformations of the core along the core axis are a function of the axial stress, σ_z , and are given by equation C.4.2 (Obert, 1966).

$$\epsilon_z = \frac{1}{E} [\sigma_z - \nu (P + Q)] \quad \text{Eq. C.4.2}$$



P = major principal biaxial stress

Figure C.4 View down borehole of a 60 degree deformation rosette (Obert, 1966)

The principal biaxial stresses in the plane normal to the borehole axis may be determined by assuming a plane strain model and by adding the strain component due to the axial stress using the principle of superposition (Obert, 1966). The contribution of the axial deformation to the diametral deformation (the Poisson effect) is $-v\epsilon_z d$ the total diametral deformation is given by equation C.4.3 (Obert, 1966).

$$U = \frac{d(1-\nu^2)}{E} [(P-Q) + 2(P-Q) \cos 2\theta] - v\epsilon_z d$$

Eq. C.4.3

Where three diametral deformation measurements, U_1 , U_2 and U_3 are taken at 60° intervals around the borehole, the plain strain solution for the principal stresses are given by equation C.4.4 (Obert, 1966).

$$P = \frac{E(1-\nu^2)}{6d} \left\{ (U_1 + U_2 + U_3) + \frac{\sqrt{2}}{2} [(U_1 - U_2)^2 + (U_2 - U_3)^2 + (U_3 - U_1)^2]^{1/2} \right\}$$

$$Q = \frac{E(1-\nu^2)}{6d} \left\{ (U_1 + U_2 + U_3) - \frac{\sqrt{2}}{2} [(U_1 - U_2)^2 + (U_2 - U_3)^2 + (U_3 - U_1)^2]^{1/2} \right\}$$

$$\theta_1 = \frac{1}{2} \tan^{-1} \frac{3(U_2 - U_3)}{2U_1 - U_2 - U_3}$$

Eq. C.4.4

where θ_1 is shown on Figure C.4.

For the horizontal borehole in the shaft wall, σ_z is approximately equal to σ_r , the radial stress near the shaft. A first approximation of the in situ stresses is obtained by neglecting the deformation component due to axial strain. Sample calculations assuming a value of σ_z equal to the horizontal field stress and including the diametral deformation due to axial strain showed less than a 2 percent change over the stresses calculated by neglecting the axial strain contribution.

APPENDIX C5

Formulas for Determining in situ Stresses
in Anisotropic Rock

Formulas are presented for evaluating the in situ stresses in anisotropic rock. The solution is for plane stress boundary conditions and assumes the rock is homogeneous, linearly elastic and is orthotropic and transversely isotropic, and the borehole axis is aligned with the orthogonal axis of elastic symmetry, as shown in Figure C.5 (Becker and Hooker, 1969).

The radial diametral deformations from overcoring, U_1 , U_2 , U_3 are obtained at 60° intervals. The elastic axis E_1 is assumed to coincide with the direction of U_1 . Theta (θ) is measured counterclockwise from E_1 to U_2 and U_3 as 60° and 120° respectively. E_1 and E_2 are the orthotropic elastic modulus.

Let: $A = U_1$

$$B = \frac{2}{\sqrt{3}} (U_2 - U_3)$$

$$C = \frac{1}{3} [2 (U_2 + U_3) - U_1] \quad \text{Eq. C.5.1}$$

The angle δ (see Figure C.5) measured counterclockwise from E_1 to the major principal biaxial stress, ρ is calculated from equation C.5.2.

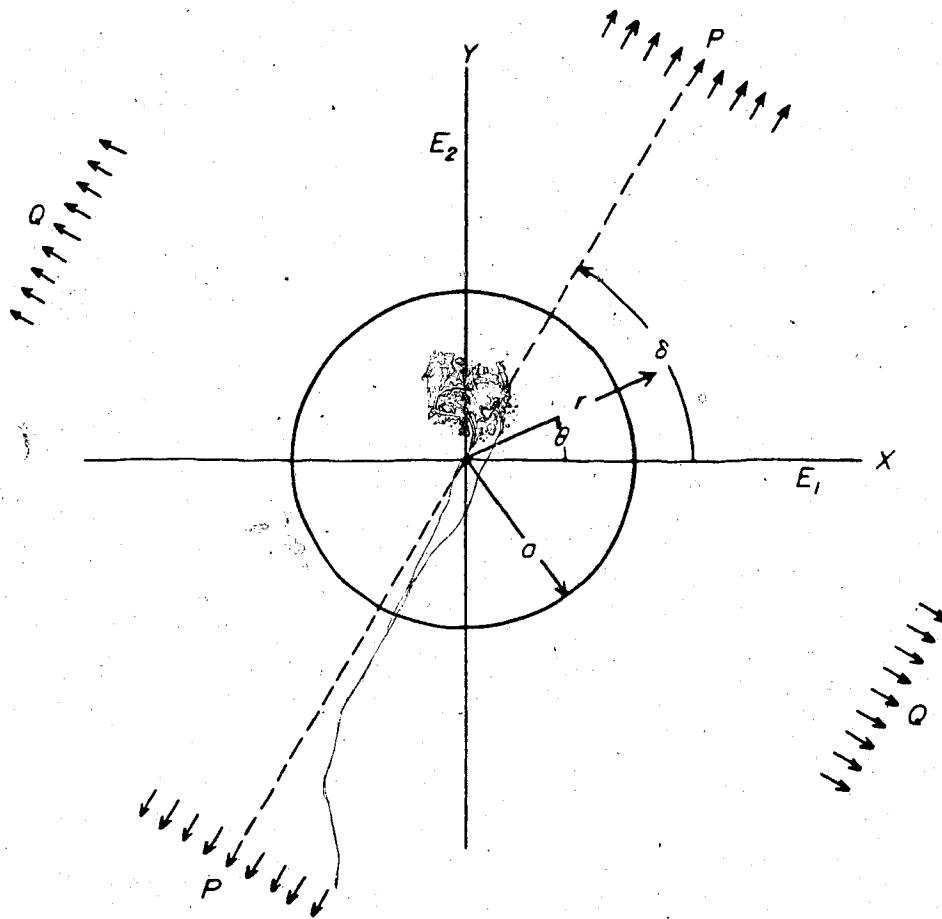


Figure C.5 A Circular Hole in an Orthotropic Solid
Subject to a Biaxial Field

$$\delta = \tan^{-1} \left[\frac{2L-K}{M} \pm \sqrt{\left(\frac{2L-K}{M}\right)^2 + 1} \right] \quad \text{Eq. C.5.2}$$

where the quantity $\frac{2L-K}{M}$ is calculated in equation C.5.3

$$\frac{2L-K}{M} = \frac{CE_2 - AE_1}{B \sqrt{E_1 E_2}} \quad \text{Eq. C.5.3}$$

The values of K and M are determined from equations C.5.4 and C.5.5:

$$K = \frac{A E_1 \sqrt{E_2/E_1} + C E_2}{(1 + \sqrt{E_2/E_1})} \quad \text{Eq. C.5.4}$$

$$M = \frac{B E_2}{d (1 + \sqrt{E_2/E_1})^2} \quad \text{Eq. C.5.5}$$

where: d is the diameter of the probe hole (nominally 3.81 cm).

The major and minor principal biaxial stresses P and Q respectively are determined as functions of δ , K and M from equations C.5.6 and C.5.7.

$$P = \frac{1}{2} \left(K + \frac{M}{\sin 2\delta} \right) \quad \text{Eq. C.5.6}$$

$$Q = K - P \quad \text{Eq. C.5.7}$$